

Achim Kimmerle

# **Diffused Surfaces for High Efficiency Silicon Solar Cells**

Process Development, Characterization,  
and Modeling

DIFFUSED SURFACES FOR  
CRYSTALLINE SILICON SOLAR CELLS –  
PROCESS DEVELOPMENT,  
CHARACTERIZATION, AND MODELING



Dissertation  
zur Erlangung des Doktorgrades  
der Technischen Fakultät  
der Albert-Ludwigs-Universität Freiburg im Breisgau

vorgelegt von

Achim Kimmerle

angefertigt am  
Fraunhofer Institut für Solare Energiesysteme ISE  
Freiburg im Breisgau

2015

Dekan:	Prof. Dr. Georg Lausen
Referent:	Prof. Dr. Eicke R. Weber
Koreferent:	Prof. Dr. Leonhard Reindl
Prüfungskommission	Prof. Dr. Eicke R. Weber Prof. Dr. Leonhard Reindl Prof. Dr. Oliver Paul Prof. Dr. Oliver Ambacher
Datum der Prüfung:	9.7.2015

Schriftenreihe der Reiner Lemoine-Stiftung

**Achim Kimmerle**

**Diffused Surfaces for High Efficiency  
Silicon Solar Cells**

Process Development, Characterization, and Modeling

Shaker Verlag  
Aachen 2015

**Bibliographic information published by the Deutsche Nationalbibliothek**

The Deutsche Nationalbibliothek lists this publication in the Deutsche Nationalbibliografie; detailed bibliographic data are available in the Internet at <http://dnb.d-nb.de>.

Zugl.: Freiburg, Univ., Diss., 2015

Copyright Shaker Verlag 2015

All rights reserved. No part of this publication may be reproduced, stored in a retrieval system, or transmitted, in any form or by any means, electronic, mechanical, photocopying, recording or otherwise, without the prior permission of the publishers.

Printed in Germany.

ISBN 978-3-8440-3820-0

ISSN 2193-7575

Shaker Verlag GmbH • P.O. BOX 101818 • D-52018 Aachen

Phone: 0049/2407/9596-0 • Telefax: 0049/2407/9596-9

Internet: [www.shaker.de](http://www.shaker.de) • e-mail: [info@shaker.de](mailto:info@shaker.de)

## Abstract

This work investigates the formation, application, and analysis of highly doped near surface regions in crystalline silicon solar cells.

The standard method to extract the recombination parameter  $J_0$  and the carrier lifetime in the base substrate from lifetime measurements of samples exhibiting diffused surfaces is revised, adapted and tested on simulation and measurement data sets. A method is developed that applies updated physical models, is in well agreement with modern simulation tools, extends the application on a wider range of base substrates, and enables the comparability of  $J_0$  analyzed by different authors and on different base substrates.

An analytical model for solar cells with locally contacted passivated rear side is adapted to account for injection dependent effects and tested against numerical simulations. The adaption enables modeling devices which are, on the one hand, influenced by injection dependent material parameters and, on the other hand, leave the low-level injection regime.

The effective surface recombination velocity of holes at highly phosphorus-doped surfaces is evaluated and parameterized in dependence of the surface dopant concentration for two industrially relevant passivation schemes, both for planar and alkaline textured surfaces. The results show increased recombination at textured surfaces in respect to planar surfaces for low dopant concentrations. The parameterization is applicable in simulation tools that apply Fermi-Dirac statistics together with a well-accepted model for band-gap narrowing.

New processes to form deep driven-in phosphorus diffusions with low surface concentrations in one single process step are developed. Low recombination activity of  $J_0 = (18 \text{ to } 38) \text{ fA/cm}^2$  is achieved, promising for the application in crystalline silicon solar cells. A simulation of the recombination behavior in dependence of the process parameters gives additional insight for further development of diffusion processes.

A lean, industrially feasible sequence to produce back-contact back-junction solar cells featuring a non-passivated aluminum alloyed emitter is developed. The presented solar cell process requires only one high temperature diffusion step without the need of further dopant sources or diffusion masks. The contacts are applied by screen-printing and the emitter is formed by aluminum-alloying. A first experimental evaluation is presented that leads to a conversion efficiency of 20.1 %. A simulation study based on experimentally achieved recombination parameters shows a potential conversion efficiency of 22.6 % and the impact of the developed strategy to reduce the recombination at the aluminum alloyed emitter.

## Zusammenfassung

Diese Arbeit untersucht die Herstellung, Anwendung und Analyse von hoch-dotierten Oberflächen in kristallinen Silicium-Solarzellen.

Die Standardmethode zur Bestimmung der Dunkelsättigungsstromdichte  $J_0$  und der Basislebensdauer aus quasistatischen Lebensdauermessungen wird untersucht, angepasst und anhand von Simulationen und Messdaten evaluiert. Die Weiterentwicklung verwendet aktuelle physikalische Parameter, stimmt dadurch mit aktuellen Simulationsprogrammen überein, erweitert die Anwendbarkeit auf verschiedene Basissubstrate und erhöht die Vergleichbarkeit der erhaltenen Werte zwischen verschiedenen Autoren und Experimenten.

Ein analytisches Modell zur Beschreibung von Solarzellen mit lokalen Kontakten auf der Rückseite wird auf injektionsabhängige Effekte angepasst und mit numerischen Simulationen verglichen. Das neue Modell ermöglicht die Modellierung von Solarzellen, die von injektionsabhängigen Parametern beeinflusst werden bzw. sich nicht in Niedriginjektion befinden.

Die effektive Oberflächenrekombinationsgeschwindigkeit der Defektelektronen an hoch phosphordotierten Oberflächen wird für zwei industrielle Passivierschichten auf sowohl planen als auch texturierten Oberflächen in Abhängigkeit der Oberflächenkonzentration bestimmt und parametrisiert. Die Ergebnisse zeigen eine erhöhte Rekombination an texturierten gegenüber planen Oberflächen bei niedrigen Dotierkonzentrationen. Die Parametrisierung ist für die Verwendung in Simulationsprogrammen geeignet.

Neue Prozesse zur Erzeugung tief eingetriebener Phosphorprofile mit niedrigen Oberflächenkonzentrationen in einem einzigen Prozessschritt werden entwickelt. Niedrige Rekombinationsparameter von  $J_0 = (18 \text{ bis } 38) \text{ fA/cm}^2$  werden erreicht, vielversprechend für die Anwendung in kristallinen Silicium-Solarzellen. Die Simulation des Rekombinationsverhaltens in Abhängigkeit der Prozessparameter ermöglicht ein erweitertes Verständnis für die Weiterentwicklung der Prozesse.

Ein kurzer, industriell umsetzbarer, Herstellungsprozess für rückseitig kontaktierte und –sammelnde Solarzellen mit Aluminium legiertem Emitter wird entwickelt. Der vorgestellte Prozess benötigt lediglich einen Hochtemperaturschritt zur Dotierung ohne weitere Diffusionsquellen oder –Masken. Die Kontakte werden mittels Siebdruck aufgebracht und der Emitter direkt aus der Aluminiumpaste legiert. Eine erste experimentelle Realisierung führt zu einem Solarzellenwirkungsgrad von 20.1 %. Eine Simulationsstudie basierend auf experimentellen Daten zeigt ein Effizienzpotential von 22.6 % und den Einfluss der entwickelten Methode zur Verringerung der Ladungsträgerrekombination am Emitter.



# Table of Contents

<b>1</b>	<b>Introduction</b>	<b>1</b>
	1.1 Background.....	1
	1.2 Thesis Outline.....	3
<b>2</b>	<b>Fundamentals</b>	<b>5</b>
	2.1 Applied Physical Models.....	5
	2.2 Characterization Methods.....	12
	2.3 Recombination Properties of Diffused Surfaces.....	14
	2.4 Analysis of the Surface Recombination by QSSPC.....	19
	2.5 Analytical Model for PERC Solar Cells.....	21
	2.6 Preliminary Solar Cell Concept.....	24
<b>3</b>	<b><math>J_0</math>-analysis of QSSPC-Measurements</b>	<b>30</b>
	3.1 Introduction.....	30
	3.2 Surface Recombination Velocity from QSSPC Measurements.....	32
	3.3 $J_0$ -analysis Methods.....	39
	3.4 Impact on the $J_0$ -Analysis of Symmetrical Samples.....	43
	3.5 Experimental Comparison on Symmetrical Lifetime Samples.....	52
	3.6 Impact on $J_0$ -Analysis of Asymmetrical Samples.....	56
	3.7 Experimental Comparison on Asymmetrical Lifetime Samples.....	60
	3.8 Conclusion.....	65
<b>4</b>	<b>Analytical Modeling of locally contacted Solar Cells</b>	<b>67</b>
	4.1 Introduction.....	67
	4.2 Injection Dependent Model.....	67
	4.3 High-Level Injection Effects.....	70
	4.4 Comparison to Numerical Simulations.....	71
	4.5 Results.....	72
	4.6 Conclusion.....	79
<b>5</b>	<b>Recombination Velocity of Phosphorus Diffused Surfaces</b>	<b>80</b>
	5.1 Introduction.....	80
	5.2 Experimental Setup.....	81
	5.3 Results.....	82

---

5.4	Conclusion.....	93
<b>6</b>	<b>In-Situ Oxidation for Advanced Doping Processes</b>	<b>94</b>
6.1	Introduction.....	94
6.2	Experimental Setup.....	94
6.3	Results.....	95
6.4	Predictive Modeling.....	101
6.5	Conclusion.....	103
<b>7</b>	<b>Back-Contact Back-Junction Solar Cell with Al-Alloyed Emitter</b>	<b>104</b>
7.1	Introduction.....	104
7.2	Proof of Concept Cell Batch.....	104
7.2.1	Desired Solar Cell Process Sequence.....	104
7.2.2	Analysis of Different Process Steps.....	111
7.2.3	Parallel Resistance.....	118
7.2.4	Solar Cell Characteristics.....	122
7.3	Simulation of Solar Cell Parameters.....	131
7.3.1	Simulation Setup.....	131
7.3.2	Consideration of Contact and Metal Resistivity.....	133
7.3.3	Influence of Pitch Contact Distance.....	138
7.3.4	Influence of Emitter Structuring.....	139
7.3.5	Influence of Base Resistivity.....	142
7.4	Conclusion.....	144
<b>8</b>	<b>Summary</b>	<b>147</b>
	<b>Appendix: Carrier Statistics in Highly Doped Silicon</b>	<b>150</b>
	<b>Bibliography</b>	<b>153</b>
	<b>List of Publications</b>	<b>163</b>
	<b>List of Constants, Symbols, and Acronyms</b>	<b>166</b>
	<b>Acknowledgment</b>	<b>173</b>



# 1 Introduction

## 1.1 Background

Providing energy and simultaneously reducing the emission of greenhouse gases is one of the major technical challenges of today [1]. Photovoltaics (PV) has the potential to contribute significantly in this task [2]. For example, during the period of writing this thesis, the average prices of crystalline silicon PV-modules produced in Germany could be reduced from 1.3 €/W<sub>peak</sub> in October 2011 to 0.59 €/W<sub>peak</sub> in February 2015 (average prices offered on the international spot exchange, [3]).

The solar cell production can contribute dominantly in two ways in reducing the costs per generated power unit: on the one hand, the production costs per module area can be reduced by reducing the costs alongside the production chain of solar cells. On the other hand, the output power of the module can be increased by increasing the solar cell's conversion efficiency. Increasing the conversion efficiency is presumably the most effective way, although this increase often comes with an increase in process complexity and costs per solar cell, not least because of the additionally applied technologies often have not reached the same level of maturity and market volume as the existing standard solutions. The dominating crystalline silicon solar cell technology of today is the so-called aluminum back surface-field (Al-BSF) solar cell. One limitation of its conversion efficiency lies in the fully aluminum alloyed rear side which shows high recombination activity and low internal light reflection [4]. A solution to overcome this limitation is the electrical passivation of the rear side while the Al-BSF is formed locally at point- or line-shaped contact openings, known as passivated emitter and rear cell (PERC) approach. Another approach is to form the *p-n*-junction and all electrodes at the rear-side of the device, which is known as back-contacted back-junction (BC-BJ) and shows the additional advantages of avoiding optical shading due to the front side electrodes and the possibility of optimizing the front side for preventing recombination without further restrictions regarding electrical contacts or lateral conductivity. Forming the contact and doping structure at one side of the wafers raises the challenge to avoid additional costs due to structuring and multiple doping of the solar cell. In this work, an example of a BC-BJ technology is developed under the rigorous regime of minimizing additional costs. Therefore it is restricted to one high-temperature doping process, to avoid additional deposition of dielectrics apart from the passivation layers, to the application of technologies that are already in industrial mass-production, and to screen-printing of the metallization.

Analytical modeling provides a fast and easy accessible possibility of evaluating the influence of different solar cell constituencies on the device performance. The increasing complexity when leaving the Al-BSF structure increases the challenge of modeling the device performance analytically. As an example, the PERC approach is

chosen. The carrier flows in the resulting device are, due to the non-uniform rear-side, more complex than in Al-BSF devices. However, analytical solutions exist in literature. Regarding the electrical output characteristics of the solar cell, increasing the conversion efficiency means increasing the voltage or the current of the device. Increasing voltage increases the excess carrier density, which is regarded to be much smaller than the dopant concentration by most analytical models. In this work, a well-known analytical model is adapted to take effects into account which occur from leaving this low-injection regime, to make it applicable to solar cells which reach higher voltages. Additionally, the consideration of the injection density enables the application of injection dependent material properties, increases the applicability of the model even further, and gives a base of describing other solar cell structures analytically.

In the recent years, the commercially available products of screen printing paste used for the front-side of Al-BSF solar cells underwent dramatic improvements regarding the formation of highly conductive electrical contacts to surfaces exhibiting lower dopant concentrations [5]. Additionally, the alternative solar cell structures, such as BC-BJ, exhibit different surface areas which have to fulfill different sets of requirements at the same time. In consequence, the doping processes are adapted constantly to produce optimized doping profiles. In this work, the focus lies on high temperature phosphorus doping from gaseous phosphor-oxychloride ( $\text{POCl}_3$ ) as dopant source. As an example, a process is developed leading to moderate dopant concentrations, as are desirable for the front-side of BC-BJ solar cells or for front-contacted solar cells with alternative metallization techniques.

The constant development of the diffusion processes leads to an increase in process complexity. In this work it is shown, at the example of the developed doping process, how predictive modeling of the emitter properties as a function of process parameters can aid and consequently accelerate the experimental development of new processes.

Finally, characterizing the recombination properties of the newly devised, highly doped surfaces is crucial for the improvement of the processes, the simulative prediction of the solar cells performance, and for the comparison between different technologies and results from different authors or institutes. In this work, the commonly applied method to obtain the recombination parameter  $J_0$  from lifetime measurements on test samples is investigated and improved for higher reliability, compatibility with modern simulation tools and extended applicability.

## 1.2 Thesis Outline

Chapter 2 introduces fundamental mechanisms, characterization techniques, and gives the status of the developments prior to this thesis as they are important for the following chapters.

In Chapter 3 the commonly applied method to extract the recombination parameter  $J_0$  from quasi-steady-state carrier lifetime measurements is investigated. On the one hand, commonly accepted physical models are applied to ensure applicability of the analyzed  $J_0$  in modern simulation tools. On the other hand, the method is adapted for increased reliability on different substrates and for high excess carrier densities. The changes are evaluated with experimental and simulated data sets. Finally, the method is adapted and tested for samples exhibiting only one diffused surface - as often occur at early stages in solar cell production or in the development of single-side doping techniques.

In Chapter 4 an analytical model for solar cells with locally contacted rear surface is investigated for its applicability beyond the low-level injection regime. Several adaptations are introduced taking into account the effects of excess carriers on the physical material parameters as well as high-level injection effects. The outcome of the model is tested against numerical simulations of devices of which the performance limitation is dominated by the rear surface structure and the base substrate.

Chapter 5 describes the experimental evaluation of the effective surface recombination velocity (SRV) at the phosphorus doped silicon-dielectric surface for two passivation schemes. A broad range of surface dopant concentration is covered by means of incremental back-etching the surface. The SRV is obtained by both, analytical and numerical modeling the emitter recombination and parameterized in dependence of the surface dopant concentration for planar and alkaline textured surfaces.

In Chapter 6 the development of a phosphorus diffusion process is described featuring in-situ oxidation under oxygen gas ambient at elevated temperatures. The resulting doping profiles are parameterized in dependence of process parameters. The parameterization is applied to predictively simulate the electrical properties of the highly doped regions.

In Chapter 7 the development of a back-contact back-junction solar cell featuring an aluminum alloyed emitter is described. The process sequence is shortened and simplified in respect to the preliminary existing technology in order to reach relevance for industrial production of solar cells and to overcome several restrictions of the preliminary solar cell concept. The solar cell manufacturing is described together with chosen characterization results of process steps and final solar cells. In the second part of Chapter 7, a numerical simulation study shows the impact of the chosen rear-side on the device performance.



## 2 Fundamentals

*In this chapter, basic fundamentals needed to understand the development and results of the thesis are stated. The applied physical models are given in Section 2.1. Section 2.2 introduces the applied characterization methods. Section 2.3 describes the recombination properties of diffused surfaces and gives an analytical solution for the calculation of the dark saturation current density. The commonly applied analysis method to extract the dark saturation current density from quasi steady-state photo conductance decay measurements is introduced in Section 2.4. In Section 2.5, an analytical model for solar cells with locally point-contacted rear that is taken as a starting point for further extensions is given. The preliminary solar cell concept as a basis for the development reported in this thesis is introduced in Section 2.6.*

### 2.1 Applied Physical Models

In this work, simulations, analytical calculations, and analysis of measurement data are carried out with the help of physical models for carrier statistics, recombination, and transport. This section states the applied models implemented in the characterization and simulation tools. The focus lies on stating the implemented models as they are applied, detailed derivations and explanations can be found in literature, e.g. textbooks [6, 7]. Unless specified otherwise, the same set of physical models is applied for all calculations in this work.

#### Carrier concentrations

The product of the electron concentration  $n_0$  and the hole concentration  $p_0$  in equilibrium defines the square of the intrinsic carrier density for undoped silicon

$$n_{i,0}^2 \equiv n_0 \cdot p_0 = N_C F_{1/2} \left( \frac{E_i - E_C}{k_B T} \right) \cdot N_V F_{1/2} \left( -\frac{E_i - E_V}{k_B T} \right). \quad (2.1)$$

Here,  $F_{1/2}$  denotes the Fermi integral of order 1/2,  $N_C$  and  $N_V$  the effective densities of states, and  $E_C$  and  $E_V$  the edges of the conduction and the valence band, respectively.  $E_i$  denotes the intrinsic Fermi level. The device temperature is denoted as  $T$  and the Boltzmann constant  $k_B$ . For doped silicon, the  $p$ - $n$ -product becomes

$$np = N_C F_{1/2} \left( \frac{E_{f_n} - E_C}{k_B T} \right) \cdot N_V F_{1/2} \left( -\frac{E_{f_p} - E_V}{k_B T} \right). \quad (2.2)$$

Here,  $E_{f_n}$  and  $E_{f_p}$  denote the quasi Fermi levels of electrons and holes, respectively.

Many calculations presented in this work are carried out for silicon with dopant concentrations well below  $10^{18} \text{ cm}^{-3}$ . Thus, the following implementation is based on Maxwell-Boltzmann statistics since it allows for a simpler calculation procedure than

Fermi-Dirac statistics and both statistics accurately describe such materials (compare Figure 2.1). In the case of Maxwell-Boltzmann statistics, Eq. (2.1) reads

$$n_{i,0}^2 \equiv n_0 p_0 = N_C N_V \exp\left(-\frac{E_{g,0}}{k_B T}\right). \quad (2.3)$$

The band-gap  $E_{g,0} = E_C - E_V$  is the smallest potential difference between the conduction and the valence band. The band-gap for undoped silicon  $E_{g,0}$  is given by Green *et al.* [8]

$$E_{g,0} = \left(1.206 - 2.73 \cdot 10^{-4} \frac{T}{\text{K}}\right) \text{eV}. \quad (2.4)$$

In the present work,  $N_C$  and  $N_V$  are not evaluated explicitly in case of the Boltzmann approximation; instead a parameterization of  $n_{i,0}(T)$  is applied based on a temperature dependent evaluation of  $n_{i,0}$  from 77 to 300 K by Sproul *et al.* [9]

$$n_{i,0}(T) = f_{\text{corr}} \cdot 1.64 \cdot 10^{15} \left(\frac{T}{\text{K}}\right)^{1.706} \exp\left(-\frac{E_{g,0}}{2k_B T}\right) \text{cm}^{-3}. \quad (2.5)$$

The correction factor  $f_{\text{corr}}$  is introduced as in Ref. [10] to match the well accepted value of  $n_{i,0} = 9.65 \cdot 10^9 \text{cm}^{-3}$  at  $T = 300 \text{K}$ , proposed by Altermatt *et al.* [11]. We apply  $f_{\text{corr}} = 0.9677$ . This leads to  $n_{i,0} = 8.26 \cdot 10^9 \text{cm}^{-3}$  at  $T = 25 \text{°C}$ .

In the presence of dopants [12] or excess carriers [13], the effective band-gap is reduced by  $\Delta E_g = \Delta E_C + \Delta E_V$ , composed by the absolute shifts of the conduction band  $\Delta E_C$  and valence band  $\Delta E_V$ . They are calculated in this work by the parameterization of Schenk [14]. Eq. (2.3) still holds by introducing an effective intrinsic carrier density

$$n_{i,\text{eff}}^2 \equiv n_0 p_0 = N_C N_V \exp\left(-\frac{E_{g,0} - \Delta E_g}{k_B T}\right). \quad (2.6)$$

All analytical calculations presented in this work assume negligible electric fields, which leads to local charge neutrality:

$$n_0 + N_A = p_0 + N_D, \quad (2.7)$$

with the ionized acceptor concentration  $N_A$  and donor concentration  $N_D$ . This relationship together with Eq. (2.6) allows for the calculation of the carrier concentrations in equilibrium which apply to the case of  $p$ -type ( $N_A > N_D$ )

$$p_0 = \frac{1}{2} \left( N_A - N_D + \sqrt{(N_A - N_D)^2 + 4n_{i,\text{eff}}^2} \right) \approx N_A - N_D$$

$$n_0 = \frac{n_{i,\text{eff}}^2}{p_0}. \quad (2.8)$$

The approximation on the right hand side is valid for  $N_A - N_D \gg n_{i,\text{eff}}$ , which is given for most practical cases – to avoid unrealistic behavior in limiting cases the approximation is not applied in this work and the full Eq. (2.8) is used instead. In the presence of excess carriers of concentration  $\Delta n$  (it is assumed that  $\Delta n = \Delta p$ ) the carrier concentrations are calculated by  $p = p_0 + \Delta n$  and  $n = n_0 + \Delta n$ .

For dopant concentrations exceeding  $10^{18} \text{ cm}^{-3}$ , Pauli-blocking reduces the  $p$ - $n$ -product and hence Fermi-Dirac statistics is applied. To evaluate Eq. (2.2) the quasi Fermi levels have to be calculated. Therefore we use the parameterization of the densities of states by Green [8]

$$\begin{aligned} N_C &= 2.86 \cdot 10^{19} \text{ cm}^{-3} \left( \frac{T}{300\text{K}} \right)^{1.58} \\ N_V &= 3.1 \cdot 10^{19} \text{ cm}^{-3} \left( \frac{T}{300\text{K}} \right)^{1.85}. \end{aligned} \quad (2.9)$$

From Eq. (2.2) and the reduction of the band gap follows

$$\begin{aligned} E_C - E_{\text{fn}} &= k_B T F_{\frac{1}{2}}^{-1} \left( \frac{n_0}{N_C} \right) - \Delta E_C \\ E_{\text{fp}} - E_V &= k_B T F_{\frac{1}{2}}^{-1} \left( \frac{p_0}{N_V} \right) - \Delta E_V. \end{aligned} \quad (2.10)$$

Here  $n_0$  and  $p_0$  are evaluated for undoped silicon by Eq. (2.8) applying  $n_{i,0}$  from Eq. (2.5), which is accurate for all regarded cases in this work. Multiplication of Eq. (2.2) and Eq. (2.3) leads to the effective intrinsic carrier density

$$n_{i,\text{eff}}^2 \equiv n_{i,0}^2 \frac{n_0}{N_C} \exp \left( \frac{E_C - E_{\text{fn}}}{k_B T} \right) \cdot \frac{p_0}{N_V} \exp \left( \frac{-E_V + E_{\text{fp}}}{k_B T} \right). \quad (2.11)$$

A comparison between Fermi-Dirac and Maxwell-Boltzmann statistics as applied in this work is shown in Figure 2.1. The resulting energy levels in respect to the intrinsic Fermi level are shown in Figure 2.2.

The implementation applied in this work is also implemented in the Sinton lifetime tester software [15, 16], with a slight adaption in PC1Dmod [17, 18] and its results are in excellent agreement with the numerical emitter simulator EDNA [19] and the numerical device simulator Sentaurus [20], as shown by Haug *et al.* [17]. For the difference of the implementation mostly applied in this work to the implementation in PC1Dmod, the reader is referred to the Appendix.

Note that to the date of publication of this work it is unclear if silicon with dopant concentrations exceeding  $3 \cdot 10^{19} \text{ cm}^{-3}$  is more accurately described by Fermi-Dirac

statistics with Schenk's BGN model [14] or Maxwell-Boltzmann statistics with an apparent band-gap parameter. Yan and Cuevas [21, 22] found evidence, that Fermi-Dirac statistics together with Schenk's BGN does not describe the observed recombination behavior of highly doped, effectively non-passivated surfaces correctly whereas they are able to accurately describe their data with an apparent BGN model and Maxwell-Boltzmann or Fermi-Dirac statistics. However there is no evidence that

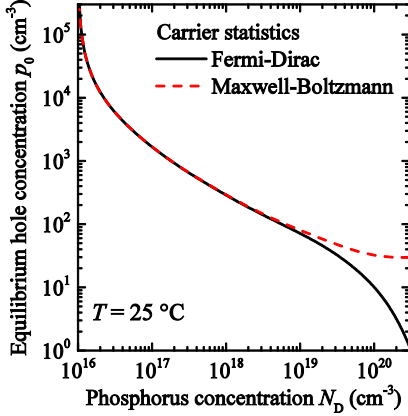


Figure 2.1 Equilibrium minority carrier concentration over phosphorus dopant concentration as calculated in this work by Fermi-Dirac and Maxwell-Boltzmann statistics.

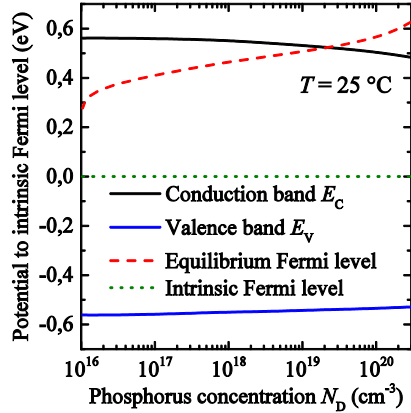


Figure 2.2 Edges of the conduction and valence band and the equilibrium Fermi level calculated with Eq. (2.10) for highly phosphorus doped silicon.

Fermi-Dirac statistics with an adaption of Schenk's model is not able to describe the data as well. In this work, Fermi-Dirac statistics and Schenk's model are chosen not to give a statement in the debate but for reasons of simplicity: for all regarded dopings ( $p$ -type,  $n$ -type, moderately- or highly doped) and influences (BGN due to doping or injected carriers) one single model can be applied and any transition between regions of qualitatively different BGN-influences is smooth.

### Intrinsic recombination

The sum of the Auger- and radiative recombination is often referred to as intrinsic recombination. In this work a parameterization by Richter *et al.* [23] is applied for the intrinsic recombination rate

$$R_{\text{intr}} = \frac{np - n_{i,\text{eff}}^2}{\text{cm}^{-3}\text{s}} \left[ 2.5 \cdot 10^{-31} g_{\text{eeh}} \frac{n_0}{\text{cm}^{-3}} + 8.5 \cdot 10^{-32} g_{\text{ehh}} \frac{p_0}{\text{cm}^{-3}} + 3 \cdot 10^{-29} \left( \frac{\Delta n}{\text{cm}^{-3}} \right)^{0.92} + B_{\text{low}} \right], \quad (2.12)$$

with the radiative recombination coefficient  $B_{\text{low}} = 4.73 \cdot 10^{-15}$  [24] and the Coulomb-enhancement factors [23]

$$g_{\text{eeh}} = 1 + 13 \left( 1 - \tanh \left[ \left( \frac{n_0}{3.3 \cdot 10^{17} \text{cm}^{-3}} \right)^{0.66} \right] \right) \quad (2.13)$$

$$g_{\text{ehh}} = 1 + 7.5 \left( 1 - \tanh \left[ \left( \frac{p_0}{7 \cdot 10^{17} \text{cm}^{-3}} \right)^{0.63} \right] \right).$$

For a given recombination rate  $R$ , a carrier lifetime  $\tau$  can be defined by assuming an exponential decay of excess carriers with time constant  $\tau$ , which leads to

$$\tau = \frac{\Delta n}{R}. \quad (2.14)$$

### Recombination via defect states

Recombination via defect states in the volume or at the surface can be described by the Shockley-Read-Hall formalism firstly introduced by Shockley and Read [25] and Hall [26] in the same year. In the volume, one finds the SRH-recombination rate to be

$$R_{\text{SRH}} = \frac{np - n_{i,\text{eff}}^2}{\tau_{n0}(p + p_1) + \tau_{p0}(n + n_1)} \quad (2.15)$$

with the capture time constants  $\tau_{n0}$  and  $\tau_{p0}$ . The SRH-densities are defined by

$$n_1 \equiv N_C \exp\left(-\frac{E_C - E_t}{k_B T}\right) \quad (2.16)$$

$$p_1 \equiv N_V \exp\left(\frac{E_V - E_t}{k_B T}\right),$$

where  $E_t$  denotes the energy position of the defect state.

In this work, the recombination at boron-oxygen defects is applied for several analytical and numerical calculations. The SRH-recombination rate is calculated analogously to Rüdiger [27]: the lifetime  $\tau_d$  is applied, evaluated by Bothe *et al.* [28] at an injection density of  $\Delta n/N_{\text{dop}} = 0.1$ , and adapted by Bothe *et al.* [28] and Glunz *et*

*al.* [29] by a factor 2 in order to take permanent improvement of the carrier lifetime due to high temperature processes in solar cell processing into account:

$$\tau_d = 2 \cdot 7.675 \cdot 10^{45} \cdot \left( \frac{[B_s]}{\text{cm}^{-3}} \right)^{-0.824} \cdot \left( \frac{[O_i]}{\text{cm}^{-3}} \right)^{-1.748} \text{ s}, \quad (2.17)$$

with the boron concentration  $[B_s]$ , here assumed equal to  $N_A$ , and the interstitial oxygen concentration  $[O_i]$ . This leads to a low-level injection lifetime for electrons of  $\tau_{n0} = 1.1/2.03 \tau_d$ . According to Rein *et al.* [30],  $\tau_{p0} = 9.3 \tau_{n0}$  and  $E_C - E_t = 0.41 \text{ eV}$  is chosen. This leads to the SRH-lifetime

$$\tau_{\text{SRH}} = \frac{\Delta n}{np - n_{i,\text{eff}}^2} [\tau_{n0}(p + p_1) + \tau_{p0}(n + n_1)] \approx \tau_{n0} \frac{N_A + 10.3 \cdot \Delta n}{N_A + \Delta n}. \quad (2.18)$$

The right hand side of this equation is valid under illumination for injection conditions  $\Delta n \gg n_{i,\text{eff}}$ , and dopant concentrations  $N_A \gg n_{i,\text{eff}}$ .

Analogous to the recombination via defect centers in the bulk, the recombination rate at the surface can be described by the SRH formalism leading to [31]

$$R_{\text{surface}} = \frac{np - n_{i,\text{eff}}^2}{\frac{p + p_1}{s_n} + \frac{n + n_1}{s_p}}, \quad (2.19)$$

where  $s_n$  and  $s_p$  denote the low-level injection surface recombination velocities of electrons and holes, respectively. The surface recombination velocity is given in units of cm/s and is defined by

$$S = \frac{R_{\text{surface}}}{\Delta n_{\text{surface}}}. \quad (2.20)$$

It can be interpreted as the average velocity of the excess carriers flowing towards an infinitely recombining surface.

### Carrier mobility

The current density  $j_n$  of a carrier concentration  $n$  caused by an electric field  $E$  reads [6]

$$j_n = \sigma_n E. \quad (2.21)$$

The proportionality factor  $\sigma_n$  is the specific conductivity. The carrier mobility  $\mu$  is defined as

$$\sigma_n = nq \mu_n. \quad (2.22)$$

The carrier mobility is influenced by scattering of the carriers at the crystal lattice, ionized dopants, and free carriers. In this work, the parameterization of Klaassen [32] [33] adapted by Schindler [34] is applied for electron and hole mobilities. The implementation also considers the correction of the factor  $r_5 = -0.01552$  in Ref. [32] to  $r_5 = -0.8552$ , as proposed by Ref. [20]. For diffusive carrier transport, the diffusion coefficient  $D$  of a type of carriers can be calculated from the mobility by the Einstein relation

$$D_{n/p} = \frac{k_B T}{q} \mu_{n/p}. \quad (2.23)$$

### Ambipolar diffusion

The mobility of electrons  $\mu_n$  in general exceeds the mobility of holes  $\mu_p$ . If the injected excess electrons and holes diffuse to their point of recombination, their current densities equal because of an electric field that forms due to a nonzero electrical current. This effect is called ambipolar diffusion [35] which is particularly important in the high injection regime and must be considered when electrical fields are neglected, e.g. in the analytical calculations in this work. The ambipolar diffusion coefficient is given by Kane and Swanson [36]

$$D_{\text{amb}} = \frac{k_B T}{q} \frac{\mu_n \mu_p (n + p)}{n \mu_n + p \mu_p}. \quad (2.24)$$

Thus the electric field enhances the diffusive propagation of holes and reduces the same for electrons. Obviously,  $D_{\text{amb}}$  equals the diffusion coefficient of the minority carriers at low level injection conditions and converges to the harmonic mean of  $\mu_n$  and  $\mu_p$  for high-level injection conditions  $\Delta n \gg N_{\text{dop}}$ .

Klaassen's mobility model takes into account lattice scattering, scattering at ions and at free-carriers. Kane and Swanson [36] proposed to neglect free-carrier scattering when evaluating the ambipolar diffusion coefficient due to the parallel electron and hole particle flows. In contrast, Li and Thurber [37] showed that free-carrier scattering influences the carrier mobility even for carriers with the same average momentum, indicating that the injection density influences the carrier mobility also for zero net current densities. Neglecting this discussion by applying the full Klaassen model including free-carrier scattering leads to an underestimation of  $D_{\text{amb}}$ , independently on whether quasi-neutrality is applied (e.g. the analytical calculations in this work) or not (e.g. the numerical calculations). Thus the comparison between numerical device simulations and analytical calculations is not affected by this discussion. The difference comes into effect by comparing calculations to measured data and will be discussed there (Chapter 3).

## 2.2 Characterization Methods

This section states briefly the applied characterization techniques and gives more detailed literature references. The quasi-steady-state photo conductance decay (QSSPC) method to determine the excess carrier lifetime is described in Section 2.4.

### Electrochemical capacitance-voltage measurement (ECV)

The ECV method is applied to determine the depth dependent charge carrier concentration close to the surface of a sample. In the regarded highly doped regions, the measured carrier concentration at a given point equals approximately the dopant concentration, which is why the outcome of the ECV measurement is also denoted as *doping profile* in this work. The ECV technique has been introduced by Bremner *et al.* [38] and later refined by Ambridge *et al.* [39] and by Blood [40] to the evaluation method used in this work. A detailed description of the technique for the application on Si-surfaces and its limitations can be found in Ref. [41].

The near surface carrier concentration  $n$  is evaluated via capacitance-voltage measurements by

$$n = \frac{2}{q\epsilon_{\text{Si}}A^2 \frac{d}{dV} C^{-2}}, \quad (2.25)$$

with the elementary charge  $q$ , the permittivity of silicon  $\epsilon_{\text{Si}}$ , the contact area between the sample and the electrolyte  $A$  and the capacitance  $C$  measured by a periodical variation of the voltage  $V$  between the electrolyte and the semiconductor. One major source of uncertainty is the assumed contact area  $A$  which depends on the surface topography of the sample and the area of the sealing ring  $A_0$ :

$$A = f_A A_0, \quad (2.26)$$

with the area factor  $f_A$ , which denotes the ratio of the surface area of the sample to an ideally planar surface. Typically one applies  $f_A = 1$  to 1.1 for saw damage etched surfaces and  $f_A = 1.6$  to 1.7 for alkaline textured surfaces. In this work,  $f_A$  is adapted so that the calculated sheet resistance of the profile matches the measured sheet resistance at the profiling position prior to the ECV measurement. To determine  $A_0$ , the etch crater after ECV-measurements of planar surfaces is characterized by optical microscopy.

The carrier-depth profile is obtained by iteratively back-etching and C-V-measurements of the sample in the automated system WEP CVP21, which applies ammonium bifluoride  $\text{NH}_4\text{HF}_2$  for both, back-etching and electrolyte.

### **Spectrally resolved light beam induced current measurements (SR-LBIC)**

SR-LBIC measurements evaluate the local external quantum efficiency EQE at short circuit conditions of silicon solar cells applying lasers of different wavelength for the local excitation. The locally induced current is obtained by scanning the light beam over the short circuited solar cell and evaluating its current response. The locally induced current can be scaled to the external quantum efficiency EQE by an additional spectral response measurement. SR-LBIC was introduced by Warta *et al.* [42]. In this work, the commercially available LOANA solar cell analysis system by pv-tools GmbH is applied, featuring laser diodes with wavelengths of  $\lambda = 405, 532, 670, 780, 940,$  and  $1060$  nm. Interpolating between the nodes of the local EQE of different wavelength, and spectral integration gives maps of local short-circuit current densities  $J_{SC}$ , as introduced by Padilla *et al.* [43].

### **Transfer length method (TLM)**

TLM is applied for the determination of the electrical contact resistance of line contacts. It was firstly introduced by Shockley [44] and further developed for the determination of metal contact resistivity on Si-samples by Berger [45]. Relevant information for the application in this work can be found in Ref. [41].

### **Scanning electron microscopy (SEM)**

The SEM was firstly introduced by von Ardenne [46]. An electron beam is focused on a spot of the sample and causes the emission of electrons and photons. A modern introduction to the method and to its application on Si-samples can be found in Ref. [41]. SEM is applied for characterizing the microstructure of a given sample. In the applied configuration, the electrons are detected and the beam is scanned over the sample surface in order to reveal the sample topography or other spatial variations. In this work, an acceleration voltage for the electron beam of 5 kV is chosen which allows to distinguish between areas of different dopant densities and thus to evaluate the local thickness of highly doped regions.

### **Inductive coupling sheet resistance measurement**

The sheet conductivity of the samples is measured by inductive coupling, which was firstly introduced by Miller *et al.* [47]. In the applied setup, the sample moves linearly over 3 coils with a diameter of approximately 2.5 cm each. This results in approximately 70 measurement spots for each wafer. A detailed description of the applied system is given by Spitz *et al.* [48]. The typical measurement positions of the coils on a wafer of 156 mm edge length are shown in Figure 2.3.

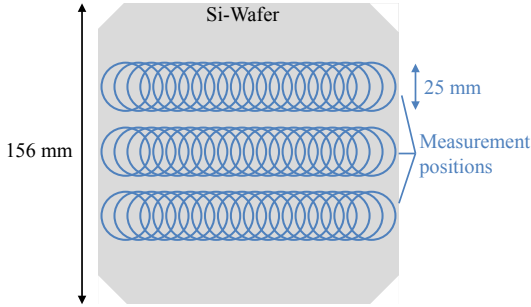


*Figure 2.3 Typical pattern of the inductive coupling sheet resistance measurement, adapted from [49].*

A measure of the uniformity of the wafer's conductivity gives the standard deviation over the different measurement positions. Note that this value is typically lower than other uniformity measurements which are based on homogeneously distributed measurements over the whole wafer surface.

The sheet resistance  $R_{sh}$  of a highly doped surface region is evaluated by subtracting the measured sheet conductivity of the base substrate  $\Sigma_{sh}$  (e.g. measured before the doping process) from the measured conductivity after the doping process. In addition, the system evaluates the wafer thickness  $W$  by differential capacitance probe as described in Ref. [41]. For homogeneously doped samples, the specific conductivity  $\sigma_0$  of the material is determined by  $\sigma_0 = \Sigma_{sh} / W$ .

### 2.3 Recombination Properties of Diffused Surfaces

In this work, the recombination properties of near surface regions exhibiting high dopant concentrations play an important role. Carrier recombination within the highly doped region occurs mainly via the Auger mechanism, recombination assisted by defect states in the volume, and recombination at the surface of the semiconductor, e.g. the interface to a dielectric passivation layer or a metal contact. Recombination via defect states in the volume or at the surface can be described by the Shockley-Read-Hall formalism. Thus the former is described by the Shockley-Read-Hall lifetime  $\tau_{SRH}$  while the latter is simply denoted as surface recombination velocity  $S$ .

Furthermore, the recombination of carriers in the diffused region depends on the local minority carrier density and thus also the carrier mobility  $\mu$ , as the carriers need to diffuse to the location of recombination.

#### Impact on the recombination properties of a device

For the investigations in this work, it is important to note that the injection density (which approximately equals the minority carrier density) even under illumination, are

always very low compared to the local dopant concentration in the diffused region. This is referred to as low-level injection regime. For low-level injection, the relevant parameters introduced in Section 2.1,  $\tau_{\text{intr}}$ ,  $\tau_{\text{SRH}}$ ,  $S$ , and  $\mu$  are independent from the injection density. Furthermore, the doping of the base substrate of all regarded devices is much lower than the dopant concentration in the dominant parts of the diffused region. This leads to the important fact that the probability of recombination for a given minority carrier in the diffused region does not depend on the injection density or the doping of the base substrate. Thus a recombination parameter  $J_0$  for a diffused region is defined independent from substrate doping or injection density [50]

$$J_{\text{rec}} = J_0 \frac{pn - n_{i,\text{eff}}^2}{n_{i,\text{eff}}^2}. \quad (2.27)$$

In the case of a  $p$ -type substrate,  $J_{\text{rec}}$  is the electron recombination current from the substrate into the diffused region,  $n$  the electron and  $p$  the hole density at the edge of the space charge region in the base substrate, and  $n_{i,\text{eff}}$  the effective intrinsic carrier density at the same location.

For an ideal diode, one finds [6]

$$\frac{np}{n_{i,\text{eff}}^2} = \exp\left(\frac{V_{\text{junction}}}{V_{\text{th}}}\right), \quad (2.28)$$

with the junction voltage  $V_{\text{junction}}$  which is defined as the difference of the quasi Fermi potentials of electrons and holes at the pn-junction. The thermal voltage is defined as  $V_{\text{th}} = k_{\text{B}}T/q$ . This leads to the recombination current at the junction

$$J_{\text{rec}} = J_0 \left( \exp\left(\frac{V_{\text{junction}}}{V_{\text{th}}}\right) - 1 \right). \quad (2.29)$$

This equation is another common definition of the dark saturation current density  $J_0$ , which equals the introduced recombination parameter in Eq. (2.27) for all practical purposes.

To quantify the recombination at a diffused surface-region, one can introduce a virtual interface and an effective recombination velocity  $S_{\text{eff}}$  at the edge of the space charge region in the base substrate

$$J_{\text{rec}} =: q\Delta n S_{\text{eff}}. \quad (2.30)$$

Replacing the majority carrier density in the substrate by  $N_{\text{dop}} + \Delta n$  and the minority carrier density by  $\Delta n$ ,  $J_0$  can then be expressed as a function of  $S_{\text{eff}}$  [51]

$$J_0 = S_{\text{eff}} \frac{qn_{i,\text{eff}}^2}{N_{\text{dop}} + \Delta n}. \quad (2.31)$$

From Eq. (2.31) follows that the effective recombination velocity at a diffused surface depends on substrate doping and injection density. In contrast,  $J_0$  is in good approximation independent from those variables and therefore an appropriate quantity to describe the recombination properties of diffused surfaces. Throughout this work,  $J_0$  represents the recombination parameter of one diffused surface, e.g. one side of the wafer.

### Analytical calculation of $J_0$ for diffused surface regions

A. Cuevas *et al.* [52] calculate the dark saturation current density  $J_0$  and the photo current at the junction  $J_{\text{ph}}$ , resulting from the generation of carriers in the diffused region, in an analytical, iterative way. The result in the third order reads for  $J_0$  [52]

$$\begin{aligned}
 J_0^{\text{3rd}} &= q \frac{S_p p_0(x_j)(1 + B_2) + A_1 + A_3}{1 + B_2 + S_p p_0(x_j)(A_1 + A_3)} \\
 A_1(x_j) &= \int_0^{x_j} \frac{dx}{D_p(x) p_0(x)} \\
 \overline{A_1}(x_j) &= \int_0^{x_j} \frac{p_0(x)}{\tau_p(x)} dx \\
 B_2(x_j) &= \int_0^{x_j} \frac{\overline{A_1}(x)}{D_p(x) p_0(x)} dx \\
 \overline{B_2}(x_j) &= \int_0^{x_j} A_1(x) \frac{p_0(x)}{\tau_p(x)} dx \\
 A_3(x_j) &= \int_0^{x_j} \frac{\overline{B_2}(x)}{D_p(x) p_0(x)} dx \\
 \overline{A_3}(x_j) &= \int_0^{x_j} B_2(x) \frac{p_0(x)}{\tau_p(x)} dx,
 \end{aligned} \tag{2.32}$$

with the SRV of the minority carriers  $S_p$ . Note that the minority carriers are denoted as  $p$  here. The depth variable  $x$  varies from  $x=0$  at the Si-surface to  $x=x_j$  at the  $p$ - $n$ -junction. For the photo current, the solution reads [52]

$$\begin{aligned}
 J_{\text{ph}}^{3\text{rd}} &= q \frac{C_1 + S_p p_0(x_j) C_2 + C_3}{1 + B_2 + S_p p_0(x_j) (A_1 + A_3)} \\
 C_1(x_j) &= \int_0^{x_j} G_L(x) dx \\
 C_2(x_j) &= \int_0^{x_j} \frac{C_1(x)}{D_p(x) p_0(x)} dx \\
 C_3(x_j) &= \int_0^{x_j} \frac{p_0(x)}{\tau_p(x)} C_2(x) dx,
 \end{aligned} \tag{2.33}$$

with a slight adaption of the nomenclature by the author. The current loss due to the loss of carriers generated in the volume of the highly doped region is often referred to as *short circuit current loss*  $\Delta J_{\text{SC}}$  and can be calculated by  $\Delta J_{\text{SC}} = qC_1 - J_{\text{ph}}^{3\text{rd}}$ .

Eq. (2.32) allows for the calculation of an effective SRV  $S_p$  from a doping profile and given  $J_0$  [52]

$$S_p^{3\text{rd}} = \frac{1}{p_0(x_j)} \frac{\frac{J_0}{q} (1 + \overline{B_2}) - (\overline{A_1} + \overline{A_3})}{1 + B_2 - \frac{J_0}{q} (A_1 + A_3)}. \tag{2.34}$$

Note that in the presence of surface charge, e.g. as a property of the passivation layer, the calculated  $S_p$  must be regarded as an effective value if this charge is not taken into account. In this work, for the evaluation of Eq. (2.32) to (2.34) the surface charge density of the passivation layers is not investigated and any calculations assume charge neutrality. Thus  $S_p$  is referred to as *effective* SRV. As e.g. shown by Richter *et al.* [53] care must be taken even at high doping densities when the surface charge acts attractive to minority carriers and thus shows a voltage dependent  $S_p$ . However, this work exclusively deals with passivation layers exhibiting positive fixed charges, applied on *n*-doped surfaces. Thus, no voltage dependent  $S_p$  is expected.

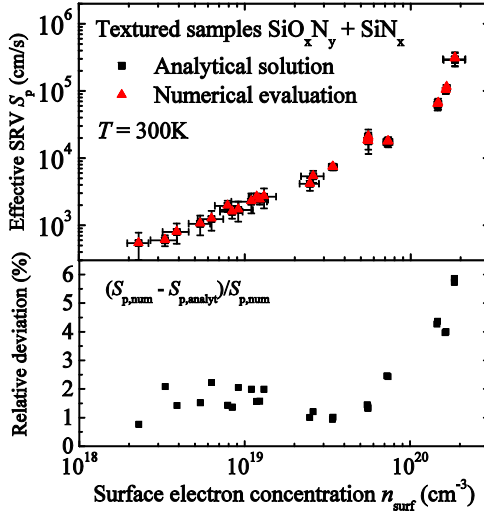


Figure 2.4 Extracted  $S_p$  from the measured  $J_0$  and doping profiles over surface electron concentration  $n_{\text{surf}}$  evaluated in Chapter 6. The values are calculated with Eq. (2.24) and with the numerical device simulator PC1Dmod. Below: relative deviation of the numerical simulation and the analytical model.

To evaluate the accuracy of the analytical solution, experimentally determined  $J_0$ -values and doping profiles (compare Chapter 6) are used to extract  $S_p$  with Eq. (2.24) and with the numerical device simulator PC1Dmod [17], applying the same  $n_{i,\text{eff}}$  (see Appendix). The resulting  $S_p$  as well as the relative deviation between the two evaluation methods are plotted over the surface electron concentration in Figure 2.4.

The analytical solution differs up to 6 % for the profiles exhibiting the highest surface concentration and in the range of 2 % for surface dopant concentrations below  $6 \cdot 10^{19} \text{ cm}^{-3}$ . On the one hand, this deviation lies well within the uncertainty of the evaluated data. On the other hand, the analytical solution overestimates  $J_0$  for all regarded cases. In this work, Eq. (2.34) is used to calculate  $S_p$  which is then parameterized and used in Eq. (2.32) and Eq. (2.33) to predict the recombination behavior of highly doped surfaces. Thus the underestimation of  $S_p$  is partly compensated by the overestimation of the re-calculated  $J_0$  and the relative deviation shown in Figure 2.4 represents an upper limit for the uncertainty of the analytical model. In conclusion, the analytical model is well suited for the application in this work.

## 2.4 Analysis of the Surface Recombination by QSSPC

QSSPC measurements are commonly applied to determine the effective minority carrier lifetime  $\tau_{\text{eff}}$  of a given sample. The QSSPC technique was firstly introduced by Sinton and Cuevas [54]. An excellent description is given in the PhD thesis of Mark Kerr [55]. The excess carriers are optically generated with a photographic flash-lamp and the resulting time-dependent photo conductance of the sample is measured by an inductive coil, located underneath the wafer. Two operating regimes, depending on the illumination, can be applied:

The transient regime is based on a short optical excitation and the subsequent evaluation of the excess carrier density without illumination. Its application is restricted to samples with high carrier lifetimes. The (quasi-) steady-state regime applies an illumination intensity which is varying slowly with time so that the change can be considered negligible and the sample to be under steady-state conditions at each measurement. This allows for the evaluation of different operating points in one measurement. All measurements shown in this work are taken in the quasi-steady-state regime, although the steady-state condition is not strictly assumed but the generalized analysis Eq. (2.37) is applied.

This section gives a brief derivation of the relationship between the measured effective lifetime  $\tau_{\text{eff}}$  and the recombination velocity at the surface of the substrate  $S_{\text{eff}}$ . In this work, the focus lies on the analysis of QSSPC measurements on lifetime samples featuring diffused surfaces. In this context, the surface of the quasi-neutral substrate is defined as the edge of the space charge region at the base-side.

The diffusion equation for the injected carrier density  $\Delta n$  in the bulk of a wafer with parallel surfaces is [56]

$$\frac{\partial \Delta n(x,t)}{\partial t} = D \frac{\partial^2 \Delta n(x,t)}{\partial x^2} - \frac{\Delta n(x,t)}{\tau_b(x)} + G_L(x,t), \quad (2.35)$$

with the local photo generation rate  $G_L$ , the dimension perpendicular to the surface  $x$  ( $x=0$  in the center of the wafer), the diffusion coefficient of the minority carriers  $D$ , and the bulk lifetime  $\tau_b$ . Assuming a diffusion of the carriers towards the surfaces and a recombination current density  $J_{\text{rec}} = q \cdot \Delta n \cdot S$  at those leads to the following boundary conditions [56]

$$\mp D \left. \frac{\partial \Delta n(x,t)}{\partial x} \right|_{x=\pm \frac{W}{2}} = S_{1/2} \Delta n \left( \frac{\pm W}{2}, t \right), \quad (2.36)$$

with the wafer thickness  $W$  and the (effective) recombination velocities at the surfaces  $S_1$  at the front and  $S_2$  at the rear side. Assuming uniform photo generation, negligible

electric fields, and neglecting the spatial variation of  $D$  and  $\tau_b$  due to their injection dependence leads to the generalized solution by Nagel *et al.* [56]

$$\frac{\partial \Delta n_{av}(t)}{\partial t} = G_{av}(t) - \frac{\Delta n_{av}(t)}{\tau_{eff}(\Delta n_{av})}, \quad (2.37)$$

where the subscript *av* denotes averaging over the wafer thickness. The effective lifetime  $\tau_{eff}$  is composed of the recombination in the substrate characterized by  $\tau_b$  and the recombination at the (effective) surfaces, which can be characterized by a surface lifetime  $\tau_s$ , simply defined by [57]

$$\frac{1}{\tau_{eff}} = \frac{1}{\tau_b} + \frac{1}{\tau_s}. \quad (2.38)$$

To separate the two components, Luke and Cheng [58] proposed the solution for Eq. (2.35) considering the boundary conditions (2.36), to be

$$\tan(\alpha_i W) = \frac{\alpha_i D(S_1 + S_2)}{\alpha_i^2 D^2 - S_1 S_2}, \quad (2.39)$$

with  $\alpha_i$  being the time-modes of the decay.

After excitation has stopped (transient case) the measured effective lifetime is identified as the lifetime of the fundamental mode  $i = 0$  and can be expressed by [58]

$$\frac{1}{\tau_s} = \alpha_0^2 D. \quad (2.40)$$

Eq. (2.39) is transcendental in  $\alpha_i$ . It can be solved numerically, but for two important cases analytical approximations exist, proposed by Sproul *et al.* [59]: for symmetrical lifetime samples  $S_1 = S_2$  holds [59]

$$S = \frac{W}{2} \left[ \tau_s - \frac{W^2}{D\pi^2} \right]^{-1}. \quad (2.41)$$

For the case where the recombination at one side of the wafer can be neglected (e.g.  $S_2 = 0$ ) the approximation reads [59]

$$S = W \left[ \tau_s - \frac{4W^2}{D\pi^2} \right]^{-1}. \quad (2.42)$$

In the quasi-steady state case with uniform generation,  $\pi^2$  has to be replaced by 12 [60] in Eq. (2.41) and (2.42). However, Sinton *et al.* [61] showed that the factor 12 only holds for extremely high diffusion length in the bulk of the wafer which are not given for the regarded case of high injection densities. Additionally, since the difference

between  $\pi^2$  and 12 seems minor compared with the remaining uncertainty of the method, e.g. regarding the uniformity of the generation rate, and for reasons of simplicity,  $\pi^2$  is applied in all cases in this work.

For the evaluation of those equations to determine  $S$ , the bulk-lifetime  $\tau_b$  has to be known. The recombination in the bulk can be calculated as the sum of the recombination at defect centers, described by  $\tau_{\text{SRH}}$ , and intrinsic recombination, described by  $\tau_{\text{intr}}$  [25]:

$$\frac{1}{\tau_b} = \frac{1}{\tau_{\text{intr}}} + \frac{1}{\tau_{\text{SRH}}}. \quad (2.43)$$

The SRH recombination depends on material defects and contamination and is generally not known for the substrate in use. For  $\tau_{\text{intr}}$  we use the parameterization Eq. (2.12) and subtract it from the effective recombination for the following considerations leading to the Auger-corrected effective lifetime  $\tau_{\text{corr}}$ :

$$\frac{1}{\tau_{\text{corr}}} = \frac{1}{\tau_{\text{eff}}} - \frac{1}{\tau_{\text{intr}}}. \quad (2.44)$$

Thus the definition of  $\tau_s$  becomes

$$\frac{1}{\tau_s} = \frac{1}{\tau_{\text{corr}}} - \frac{1}{\tau_{\text{SRH}}}. \quad (2.45)$$

## 2.5 Analytical Model for PERC Solar Cells

In this section, the equations used for modeling PERC silicon solar cells with locally point contacted rear side are given. The implementation of the analytical model adapted in this work is called *Pitchmaster* and described in detail by Wolf *et al.* [10].

The basis is the two diode model [62] that describes the illuminated current-voltage curve of the device by

$$J = -J_{\text{col}} + J_{01} \left[ \exp \left\{ \frac{V_{\text{ext}} - JR_S}{V_{\text{th}}} \right\} - 1 \right] + J_{02} \left[ \exp \left\{ \frac{V_{\text{ext}} - JR_S}{2V_{\text{th}}} \right\} - 1 \right] + \frac{V_{\text{ext}} - JR_S}{R_p}. \quad (2.46)$$

Here,  $J_{\text{col}}$  is the photogenerated and collected current density,  $J_{01}$  and  $J_{02}$  are the first and second diode dark saturation current densities,  $R_S$  and  $R_p$  the global series and parallel resistances, respectively. The following working points of the device are of interest: open circuit (OC) with zero external current  $J = 0$ , short circuit (SC) with zero external voltage between the contacts  $V_{\text{ext}} = 0$  and the maximum power point (MPP) with maximum output power  $J \cdot V_{\text{ext}}$ . Respectively, the characteristic quantities of a device are denoted as open circuit voltage  $V_{\text{OC}}$ , short circuit current density  $J_{\text{SC}}$  and fill factor

$$FF = \frac{J_{\text{mpp}} V_{\text{mpp}}}{J_{\text{sc}} V_{\text{OC}}}. \quad (2.47)$$

The conversion efficiency  $\eta$  is defined as the ratio between the maximum output power density  $J_{\text{mpp}} V_{\text{mpp}}$  and the power density of the incident illumination  $P_{\text{light}}$ . In this work, the standard test conditions  $P_{\text{light}} = 1000 \text{ W/m}^2$ , a device temperature of  $T = 25 \text{ }^\circ\text{C}$  and the solar spectrum AM1.5g are applied.

Assuming uniform injection density,  $J_{01}$  is composed by the saturation current densities of the emitter  $J_{0e}$  and of the base  $J_{0b}$  by  $J_{01} = J_{0e} + J_{0b}$ . The second diode saturation current density  $J_{02}$  describes non-ideal behavior mainly caused by recombination in the space charge region [62, 63]. In the model (low-level injection approximation), the base dark saturation current density [64]

$$J_{0b} = \frac{qDn_{i,\text{eff}}^2}{N_{\text{dop}}L_{\text{eff,OC}}} \quad (2.48)$$

is calculated from the effective diffusion length  $L_{\text{eff,OC}}$  for open circuit conditions. The other relevant parameters are the diffusion coefficient of the minority carriers  $D$ , the dopant concentration  $N_{\text{dop}}$  and the effective intrinsic carrier concentration  $n_{i,\text{eff}}$ . The effective diffusion length is defined as [64]

$$L_{\text{eff}} = L \frac{1 + \frac{S_{\text{eff}}L}{D} \tanh\left(\frac{W}{L}\right)}{\frac{S_{\text{eff}}L}{D} + \tanh\left(\frac{W}{L}\right)}, \quad (2.49)$$

with the device thickness  $W$  and the effective SRV at the rear surface  $S_{\text{eff}}$ . The bulk diffusion length  $L$  is calculated from the carrier lifetime in the bulk by  $L = \sqrt{\tau_b D}$ .

So far, the model describes one-dimensional transport in the device.  $S_{\text{eff}}$  is defined to lead to a correct saturation current density  $J_{0b}$  when applied in combination with the equations for one-dimensional transport. To consider devices with non-uniform rear side, such as point or line contacted solar cells, there are various parameterizations for  $S_{\text{eff}}$  in literature [10, 65, 66]. In this work, the parameterization by Fischer [65] is applied:

$$S_{\text{eff}} = \frac{D}{W} \left( \frac{R_{\text{S,back}}}{\rho W} + \frac{D}{fWS_{\text{met}}} - 1 \right)^{-1} + \frac{S_{\text{pass}}}{1-f}. \quad (2.50)$$

Here,  $f$  denotes the metallization fraction of the rear side and  $S_{\text{pass}}$  and  $S_{\text{met}}$  the SRV of the passivated and metallized area, respectively.  $R_{\text{S,back}}/(\rho W)$  denotes the global, normalized dark series resistance of the rear contact with the base resistivity  $\rho$ . The

model assumes an infinite  $L$ ,  $S_{\text{pass}} \ll S_{\text{met}}$  and an equipotential front surface, e.g. a highly conductive emitter. The applied model calculates  $R_{S,\text{back}}$  by [10]

$$R_{s,\text{back}} = R_{\text{spread}} + \left( \frac{\rho W}{L_p^2} - R_{\text{spread}} f \right) \cdot \left( 1 - \exp \left\{ -\frac{1}{2} \sqrt{\frac{W}{L_p(1-f)}} \right\} \right), \quad (2.51)$$

with the point contact distance  $L_p$ . The spreading resistance  $R_{\text{spread}}$  for point contacts of radius  $r_{\text{cont}}$  is given by the expression by Cox and Strack [67]

$$R_{\text{spread}} = \frac{\rho}{2\pi r_{\text{cont}}} \arctan \left( \frac{2W}{r_{\text{cont}}} \right). \quad (2.52)$$

For the calculation of the photogenerated current density  $J_{\text{ph}}$ , the model applies the approach introduced by Fischer [65]: the cumulated generation depth profile in the illuminated device is approximated by

$$J_{\text{gen}}(x) = (1-M) \left[ J_{\text{gen,front}} + J_{\text{gen,exp1}} \left( 1 - \exp \left\{ -\frac{x}{L_1} \right\} \right) \right. \\ \left. + J_{\text{gen,exp2}} \left( 1 - \exp \left\{ -\frac{x}{L_2} \right\} \right) + J_{\text{gen,hom}} \frac{x}{W} \right]. \quad (2.53)$$

Here  $x$  denotes the dimension perpendicular to the device surface with  $x=0$  at the front and  $x=W$  at the rear surface.  $J_{\text{gen,front}}$  quantifies the generation at the front side at  $x=0$ ,  $J_{\text{gen,exp1}}$  and  $J_{\text{gen,exp2}}$  exponentially decreasing generation terms with absorption length  $L_1$  and  $L_2$ , respectively.  $J_{\text{gen,hom}}$  is a homogeneous generation term and  $M$  the optical shading (optical metallization fraction) of the front metallization grid. The generation terms and absorption lengths are obtained by fitting Eq. (2.53) to the result of numerical simulations as described in Ref. [10].

After Fischer [65], the collected current density

$$J_{\text{col}} = c(1-M) \left[ J_{\text{gen,front}} - \Delta J_{\text{SC,emitter}} + \frac{J_{\text{gen,exp1}} \left( 1 - \exp \left\{ -\frac{x}{L_1} \right\} \right)}{\left( 1 + L_1/L_{\text{eff,SC}} \right)} \right. \\ \left. + \frac{J_{\text{gen,exp2}} \left( 1 - \exp \left\{ -\frac{x}{L_2} \right\} \right)}{\left( 1 + L_2/L_{\text{eff,SC}} \right)} + J_{\text{gen,hom}} \frac{L_{\text{col}}}{W} \right] \quad (2.54)$$

follows from the reduction of the short circuit current density due to recombination of the minority carriers generated in the emitter  $\Delta J_{SC,emitter}$ , the effective diffusion length  $L_{eff,SC}$  and the collection diffusion length  $L_{col,SC}$ , both under SC conditions. The latter is described by [68]

$$L_{col} = L \frac{\frac{S_{eff}L}{D} \left( \cosh\left\{\frac{W}{L}\right\} - 1 \right) + \sinh\left\{\frac{W}{L}\right\}}{\frac{S_{eff}L}{D} \sinh\left\{\frac{W}{L}\right\} + \cosh\left\{\frac{W}{L}\right\}}. \quad (2.55)$$

The analytical model accounts for SC conditions by calculating  $S_{eff,OC}$  by Eq. (2.50) for OC conditions and scaling the outcome by an empirical injection factor  $\gamma_{inj}$  via  $S_{eff,SC} = \gamma_{inj} S_{eff,OC}$ .  $S_{eff,SC}$  is used to calculate  $L_{eff,SC}$  by Eq. (2.49), which is necessary for the calculation of  $J_{col}$  in Eq. (2.54).

## 2.6 Preliminary Solar Cell Concept

Preliminary investigations of the solar cell structure of interest were carried out in the PhD thesis of Robert Woehl [69]. In this chapter, central results of this previous work are repeated to give the background for the development of a new process sequence, which is presented in this work. Although several process sequences are investigated in Ref. [69], the focus is set on the process sequence which lead to the highest conversion efficiency of  $\eta = 20.0\%$  (denoted as *SymPro* in Ref. [69] initially published in Ref. [70], active cell area  $16.25 \text{ cm}^2$ ).

### Solar cell structure

The solar cell structure of interest is a back-contacted back-junction (BC-BJ) solar cell with an aluminum alloyed emitter. A schematic cross section is shown in Figure 2.5.

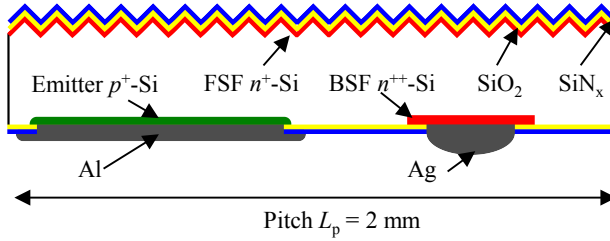


Figure 2.5 Cross section of the solar cell structure of interest. The base substrate is an  $n$ -type float-zone silicon wafer. The emitter is achieved by alloying of the aluminum while the FSF and BSF are formed in several high temperature diffusion steps featuring reactive gases.

For clarification of the shown cross sections, in this work, base substrate doping which typically exhibits dopant concentrations below  $10^{17} \text{ cm}^{-3}$  is denoted with  $n$  or  $p$ , respectively. Higher dopant concentrations are denoted with  $n^+$  or  $p^+$ , whereas for the highest phosphorus concentrations above  $10^{20} \text{ cm}^{-3}$ , as e.g. the contacted BSF of the solar cell,  $n^{++}$  is used.

In Ref. [69], the base substrate is phosphorus-doped float-zone (FZ) silicon. The front surface field (FSF) and the back surface field (BSF) are doped with phosphorus in thermal diffusion steps applying tube furnace diffusion in  $\text{POCl}_3$  containing gas ambient. All phosphorus diffusions in this work are carried out in the same tube furnace system. The reader may find an accurate description of the system and the influence of different gas flows and ambient temperatures in Ref. [49]. The respective process steps are simply denoted as  $\text{POCl}_3$  diffusion in this work. The FSF has a sheet resistance of  $R_{\text{sh}} = 120 \text{ } \Omega/\text{sq}$ , whereas the highly doped BSF features  $R_{\text{sh}} = 2 \text{ } \Omega/\text{sq}$ . The passivation stack at the front side is a thin thermally grown silicon dioxide ( $\text{SiO}_2$ ) layer, approx. 10 nm thick, covered with a silicon nitride ( $\text{SiN}_x$ ) anti-reflective coating (ARC) layer, approx. 60nm thick. The rear side is electrically passivated by a thick thermally grown  $\text{SiO}_2$  layer covered with the same  $\text{SiN}_x$ -ARC layer as the front-side. The  $n$ - and  $p$ -contacts are applied by screen-printing of commercially available silver- and aluminum pastes, respectively. The emitter region ( $p^+$ ) is formed by the alloying of the Al with Si during contact firing.

### Process sequence

The flow-chart of the solar cell's process sequence after Woehl [69] is depicted in Figure 2.6.



Figure 2.6 Process sequence for the fabrication of solar cells after Ref. [69]. The high temperature steps, which are carried out in a tube furnace are marked orange, the PECVD depositions blue, and the wet-chemistry steps green. All structures are defined by means of screen-printing.

After texturing in an alkaline etching solution, the wafers are exposed to a tube furnace POCl<sub>3</sub> diffusion step. Subsequently, the rear side is chemically polished. Consequently, the phosphosilicate glass (PSG) and the highly phosphorus-doped layer at this side are removed. After the removal of the PSG layer at the front-side, the wafers are coated with a SiO<sub>x</sub> layer in a reactor for plasma-enhanced chemical vapor deposition (PECVD). The SiO<sub>x</sub> layer masks the areas where no BSF-formation is

desired during the second  $\text{POCl}_3$  diffusion step. This is achieved by screen-printing of a masking resist, selective etching of the  $\text{SiO}_x$  layer, and subsequent removing the resist. After the removal of the formed PSG and the remaining  $\text{SiO}_x$ , the wafers are cleaned for the long thermal oxidation drive-in step, during which a  $\text{SiO}_2$  layer is formed. This layer serves as the rear side passivation. Now, the rear side is protected by a screen-printed mask for the removal of the  $\text{SiO}_2$  layer at the front. After removing the mask and wet-chemical cleaning, the surfaces are passivated in a short thermal oxidation step, resulting in a  $\text{SiO}_2$  layer thickness of approx. 10 nm, and are additionally coated with a  $\text{SiN}_x$  layer, which is deposited in a PECVD reactor on both sides. In order to form the opening for the emitter and the Ag-contacts, both sides are masked with a screen-printed resist once more with the respective pattern at the rear side. After removal of the dielectric in the mask's openings and the mask itself, the metal contacts are deposited by screen-printing. Contact formation and activation of the passivation layers takes place in a fast-firing furnace and a final anneal step on a hotplate at a temperature of approx. 400 °C.

### Properties of aluminum alloyed emitters

Here, the properties of aluminum alloyed emitters and the influence of the alloying process are discussed briefly as far as they are needed to understand the fundamental restriction of the regarded solar cell structure and the results of this thesis.

A detailed description of the alloying process of screen printed aluminum pastes can be found in Ref. [69, 71]. The peak temperature  $T_{\text{peak}}$  during alloy has an important influence on the Al doping profile as exemplarily shown in Figure 2.7, taken from Ref. [69].

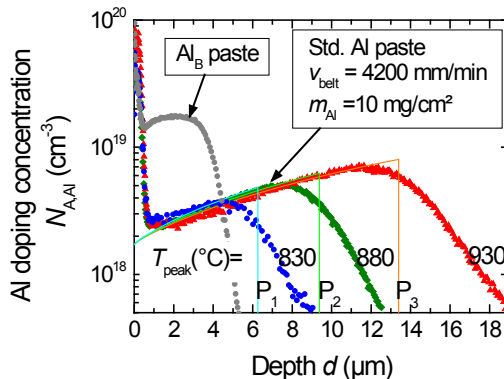


Figure 2.7 ECV measurements of doping profiles for different peak firing temperatures  $T_{\text{peak}}$  of fully aluminum-covered plane silicon surfaces and the corresponding theoretical fits. With permission taken from Woehl [69].

Figure 2.7 depicts the Al dopant concentration profile for three different peak firing temperatures. The firing process was carried out in the same fast firing furnace as used in this work at a belt velocity  $v_{\text{belt}}$  of 4.2 m/min. The Al paste is also applied in this work and denoted as paste B in Chapter 7. Higher peak temperatures increase the amount of dopants in two ways: on the one hand, the peak dopant concentration increases due to the increased equilibrium concentration of Al during recrystallization. On the other hand, the depth of the profile increases due to the increased exposure time and reaction speed, in particular the diffusivity in the liquid phase of the components.

The amount of incorporated aluminum has a strong influence on the dark saturation current density  $J_0$ . Figure 2.8 shows exemplarily the measured  $J_0$  over the emitter thickness of aluminum alloyed non-passivated (a) and passivated (b) surfaces for an aluminum paste and the same paste with aluminum-boride (AlB) additive, taken from Ref. [72].

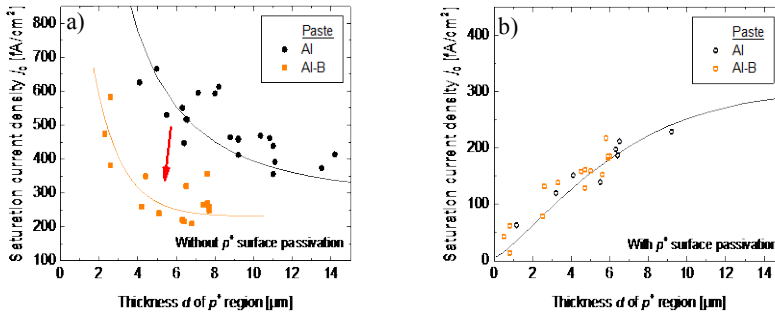


Figure 2.8 Measured saturation current densities  $J_0$  as a function of the  $p^+$ -region thickness  $d$ . The black line shows the numerical simulation result from Ref. [73] while the orange line serves as a guide to the eye. Shown are the results for non-passivated (a) and for passivated surfaces (b), both for aluminum paste without (black) and with (orange) AlB content. With permission taken from Rauer et al. [72].

$J_{0e}$  of the non-passivated emitter formed with the Al-paste without AlB additive increases strongly with decreasing thickness of the  $p^+$ -region  $d$  from approx.  $400 \text{ fA/cm}^2$  at  $d = 12 \mu\text{m}$  to approx.  $600 \text{ fA/cm}^2$  at  $d = 6 \mu\text{m}$ . The reason is that the highly recombination active surface is not effectively shielded by a shallowly doped region. The shielding effect of the doped region increases with increasing thickness and dopant density. On the other hand, if the surface is effectively passivated (b),  $J_0$  decreases with decreasing thickness because the amount of Al dopants and, in consequence, the recombination at the defect centers [74] is reduced. For this reason, Woehl [69] chose a firing process resulting in a peak firing wafer temperature of  $840 \text{ }^\circ\text{C}$ , a thickness of the  $p^+$ -layer of approx.  $10 \mu\text{m}$ , and a  $J_0$  of  $420 \text{ fA/cm}^2$ .

Also shown in Figure 2.8 is  $J_0$  over  $d$  for emitters formed from the same Al-paste with AlB additive. Schmidt et al. [74] and Rüdiger *et al.* [73] showed that Al-alloying leads to a strongly reduced minority carrier lifetime in the alloyed region well below the expected Auger-lifetime observed in regions doped with boron of the same concentration. Thus the additional incorporation of boron does not reduce this lifetime significantly but shields the non-passivated and thus recombination active surface effectively. The consequence is a reduced  $J_0$  for the same alloying conditions (compare data at the same  $d$ ) and a low  $J_0$  for comparably shallow profiles, e.g. nearly down to  $200 \text{ fA/cm}^2$  at  $d > 5 \text{ }\mu\text{m}$ . This particular finding is important for the development in this work and further addressed in Chapter 7.

### 3 $J_0$ -analysis of QSSPC-Measurements

Major results given in this chapter are published in Ref. [15, 16, 75]. In Section 2.4, a brief description of the relationship between the effective lifetime and the recombination at the surfaces is given. In Section 3.2, the equations to extract the surface recombination velocity of lifetime samples with known bulk-lifetime from QSSPC-measurements are stated as discussed in the literature and tested on simulation data. Section 3.3 states the commonly applied method to extract  $J_0$  of highly doped surfaces when the bulk-lifetime is not known and derives new methods accounting for band-gap narrowing due to injected carriers and for the finite carrier diffusion coefficient. The impact of the different methods for symmetrical lifetime samples is compared on simulation data in Section 3.4 and on measurement data in Section 3.5. For asymmetrical lifetime samples, the comparison on simulation data takes place in Section 3.6 and on measurement data in Section 3.7.

#### 3.1 Introduction

At the beginning of this thesis in 2011, the standard method for the extraction of  $J_0$  from QSSPC measurements was the so-called *slope-method* introduced by Kane and Swanson [76]. It is implemented in the measurement software of the QSSPC Systems by Sinton Instruments. For the method, several assumptions have to be made of which the following are under discussion in this work

- The method assumes uniform injection density  $\Delta n$  in the base substrate of the lifetime sample
- The Auger-lifetime  $\tau_{\text{Aug}}^{-1} = 1.66 \cdot 10^{-30} \Delta n^2 \text{ cm}^6/\text{s}$  is applied
- A constant  $n_i = 8.6 \cdot 10^9 \text{ cm}^{-3}$  is applied for all base substrate dopings and injection densities

Already in his original publication Kane pointed out that the method may underestimate  $J_0$  at high  $\Delta n_{\text{av}}$  for the non-uniform  $\Delta n$  in the base, shown by his simulation of the inverse carrier lifetime over injection density given in Figure 3.1.

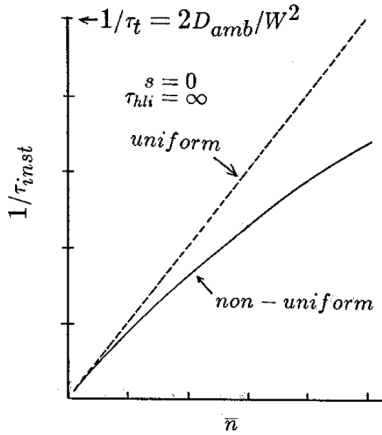


Figure 3.1 Original published simulated (solid line) and assumed (dashed line) inverse carrier lifetime over injection density taken from Kane and Swanson [76]. Clearly visible is the decreasing slope of the inverse lifetime leading to an increased apparent  $J_0$  in the applied standard method.

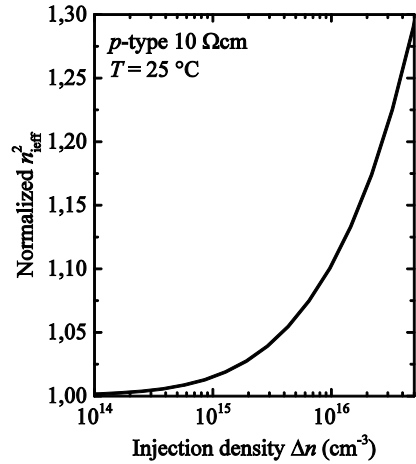


Figure 3.2  $n_{i,eff}^2$  normalized to  $n_{i,0}^2$  upon the injection density  $\Delta n$  for a p-type substrate with specific resistivity  $\rho_0 = 10 \Omega\text{cm}$  at  $T = 25 \text{ }^\circ\text{C}$  after Eq. (2.6).

As shown in Chapter 2.4, the origin of this decrease lies in the finite carrier diffusion coefficient or in other words that the carriers have to diffuse to the surface to recombine there. This limits the applicable injection density for the method depending on the  $J_0$  of the surfaces: for low  $J_0$ , higher  $\Delta n$  can be tolerated to avoid the influence of the carrier diffusion.

The second effect is the injection dependence of the effective intrinsic carrier density  $n_{i,eff}$ : from Eq. (2.6) follows the increase of  $n_{i,eff}$  with increasing  $\Delta n$  due to the plasmonic reduction of the band-gap (Figure 3.2). This leads on the one hand to a decrease of the apparent  $J_0$  for higher  $\Delta n$  because of the underestimation of  $n_{i,eff}$ . On the other hand the change of  $n_{i,eff}$  with injection density influences the slope of the  $1/\tau - \Delta n$  curve and thus leads to an additionally decreased apparent  $J_0$ . Finally the high-injection Auger-model limits the application of the method to the high-level injection regime.

Additional to the dependency on  $\Delta n$ , the choice of the models, the constant  $n_{i,eff}$  in particular, has two implications: The apparent  $J_0$  evaluated with the former implementation does not lead to the same surface recombination when applied in modern simulation tools that do mostly apply the injection dependent BGN as used in

this work. Finally the same highly doped surfaces can lead to different apparent  $J_0$  when evaluated on different base substrates of different dopant concentrations, thus the comparability between different authors or even different experiments is limited.

In this chapter, the former implemented method is adapted to ensure the compatibility with simulation tools, the comparability on different substrates and extends the applicable range of injection densities.

### 3.2 Surface Recombination Velocity from QSSPC Measurements

In this section, analytical methods to extract the effective surface recombination velocity (SRV) from QSSPC data under the assumption of a known SRH-lifetime in the bulk  $\tau_{\text{SRH}}$  are given. The methods are compared on simulated data sets. To calculate  $S_{\text{eff}}$ , Eq. (2.39) needs to be solved. Three methods are compared for symmetrical and asymmetrical lifetime samples:

The approximations Eq. (2.41) and Eq. (2.42) are denoted as *Sproul* in the following. Approximating Eq. (2.39) is not necessary for the analytical  $J_0$  analysis: in the symmetrical case  $S_1 = S_2 = S$ , the exact solution of Eq. (2.39) is

$$S = \alpha_0 D \tan\left(\frac{\alpha_0 W}{2}\right). \quad (3.1)$$

For asymmetrical samples ( $S_1 \neq S_2$ ), the effective surface recombination velocity is [77]

$$S_2 = \alpha_0 D \frac{-S_1 + \alpha_0 D \tan(\alpha_0 W)}{\alpha_0 D + S_1 \tan(\alpha_0 W)}. \quad (3.2)$$

In order to solve this equation, the recombination properties of surface 1 need to be known, either as  $J_{0,1}$  of a diffused surface or the  $S_1$  of a non-diffused surface. Eq. (3.1) and Eq. (3.2) are denoted as *general\_solution* in the following.

Historically, in the  $J_0$ -analysis that makes use of the injection dependent effective surface recombination velocity (often referred to as *slope-method*) the diffusion term in Eq. (2.41) is neglected, which is basically the assumption of a uniform  $\Delta n$  in the substrate [76], leading to

$$S = \frac{W}{2\tau_s}. \quad (3.3)$$

For asymmetrical lifetime samples, the same assumption enables to calculate the SRV of one side by simply subtracting the assumed value for the other side [51]

$$S_2 = \frac{W}{\tau_s} - S_1. \quad (3.4)$$

Eq. (3.1) and Eq. (3.2) are denoted as *uniform\_injection* in the following. An overview of the method applied to determine  $S_{\text{eff}}$  from the absolute recombination in the sample at known  $\tau_b$  is given in Table 3.1.

*Table 3.1 Overview of the compared methods for the analysis of the simulated data sets of symmetrical lifetime samples to determine  $S_{\text{eff}}$  from the absolute recombination at known bulk lifetime  $\tau_b$ . For the asymmetrical case, Eq. (3.3) and (3.1) have to be replaced by Eq. (3.4) and (3.2), respectively. For the special case of asymmetrical samples with one perfectly passivated side, Eq. (2.42) can be applied instead of Eq. (2.41).*

Short name	Applied equation (symmetrical case)	Central assumption
Uniform_injection	$S = \frac{W}{2\tau_s}$ (3.3)	$\Delta n(x) = \text{const.}$
Sproul	$S = \frac{W}{2} \left[ \tau_s - \frac{W^2}{D\pi^2} \right]^{-1}$ (2.41)	uniform generation
General solution	$S = \alpha_0 D \tan \left( \frac{\alpha_0 W}{2} \right)$ (3.1)	uniform generation

## Simulation setup

Numerical simulations are carried out using the simulation software QsCell 5.7, published by A. Cuevas [78]. The software has been adapted by the author of the present thesis to account for band-gap narrowing due to injected carriers, the Richter model for intrinsic recombination, and the mobility model as stated in Chapter 2.1. All the simulations in this section use a wafer thickness of  $W = 200 \mu\text{m}$ , textured surfaces, a  $\text{SiN}_x$ -ARC of thickness 75 nm, air ambient, and an additional SRH recombination defined by an injection independent  $\tau_{\text{SRH}} = 1 \text{ ms}$ . The simulation applies either the optical spectrum of the flash lamp (*flasher*) or the spectrum resulting of a combination of the lamp with a red-filter (*RG850*). The spectra are implemented in the original version of QsCell 5.7. The simulation creates data sets of  $\tau_{\text{eff}}$  over average injection density  $\Delta n_{\text{av}}$  in a very similar manner to the QSSPC measurement software [54] in the quasi-steady state:  $\Delta n_{\text{av}}$  is calculated by the total conductivity of the wafer divided by the sum of the carrier mobilities, the wafer thickness, and the elementary charge. The effective lifetime is calculated by dividing  $\Delta n_{\text{av}}$  by the total generation rate in the wafer. To allow for comparison with the  $J_0$ -analysis in the next sections, the surfaces are assumed to be highly doped, characterized by an applied  $J_0$ . The simulation transforms the input  $J_0$  by Eq. (2.31) into a  $S_{\text{eff}}$ , applying the local injection density at the given surface. Figure 3.3 depicts a schematic of a symmetrical lifetime sample.

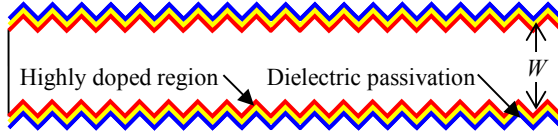


Figure 3.3 Schematic of a textured symmetrical lifetime sample featuring two identical highly doped and passivated surfaces.

### Evaluation

For calculating  $S_{\text{eff}}$  with the different methods,  $\tau_{\text{bulk}}$  is assumed to be known:  $\tau_s$  is calculated from  $\tau_{\text{eff}}$  and  $\tau_{\text{bulk}}$  by Eq. (2.45) applying  $\Delta n_{\text{av}}$  to calculate the intrinsic carrier lifetime and the applied value for  $\tau_{\text{SRH}}$ . The obtained  $S_{\text{eff}}$  is then transformed by Eq. (2.31) for each injection point, applying  $\Delta n_{\text{av}}$  to calculate an apparent  $J_0$  for comparison with the input data.

The objective is to compare the analyzed  $J_0$  with the input  $J_0$  to evaluate the validity of the made assumptions which are crucial for the following evaluation of the  $J_0$ -analysis methods, based on the injection dependent evaluation of the surface recombination velocity and restricted to the experimentally accessible average injection density  $\Delta n_{\text{av}}$ .

### Results

At first, symmetrical lifetime samples are simulated with an input value of  $J_0 = 100 \text{ fA/cm}^2$  at the surfaces, the RG850 spectrum and two different base substrates doped with  $N_A = 1.5 \cdot 10^{15} \text{ cm}^{-3}$  and  $N_D = 5 \cdot 10^{16} \text{ cm}^{-3}$ . The analyzed  $J_0$  over average injection density  $\Delta n_{\text{av}}$  is shown in Figure 3.4 in a range of low injection to  $\Delta n_{\text{av}} = 3 \cdot 10^{16} \text{ cm}^{-3}$ , which gives an applicable upper bound in practice.

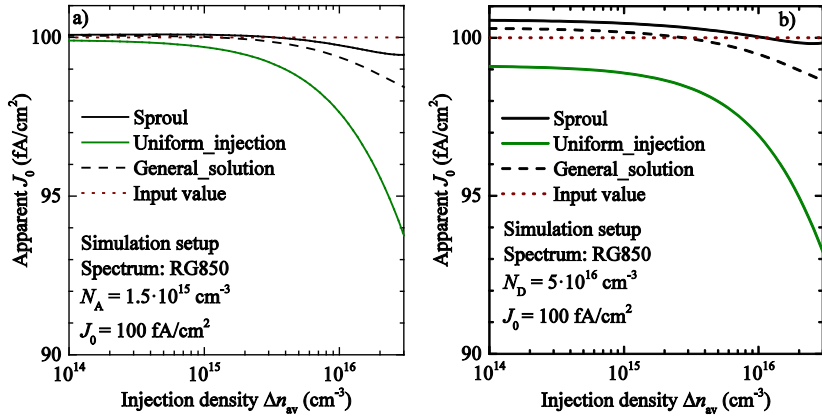


Figure 3.4 Apparent  $J_0$  for the different evaluation methods over injection density for symmetrical lifetime samples of lowly doped  $p$ -type material (a) and highly doped  $n$ -type material (b). The spectrum resulting from the usage of the red-filter RG850 is applied.

The extracted  $J_0$  deviates less than 7% of the input value of  $J_0 = 100 \text{ fA/cm}^2$ . However, the assumption of uniform  $\Delta n$  by Eq. (3.3) leads to an underestimation of  $J_0$  for high  $\Delta n$  and exhibits a high negative slope in this range due to a higher  $\Delta n$  in the bulk than at the surfaces. This effect is strongly reduced by the methods accounting for the finite carrier diffusion towards the surfaces (*Sproul* and *general\_solution*) leading to a deviation of less than 2%. This finding does not depend significantly on the applied base material as shown in the example for the two very different substrates. As a result, only  $p$ -type substrates with base-doping  $N_A = 1.5 \cdot 10^{15} \text{ cm}^{-3}$  are considered in the following, as they are assumed to be representative of many applied samples for the extraction of  $J_0$ .

A second simulation is carried out for asymmetrical lifetime samples featuring one non-recombination active surface ( $S = 0$ ) and one surface characterized by an input value of  $J_0 = 100 \text{ fA/cm}^2$  (Figure 3.5). The latter is located either at the illuminated front-side (a) or the non-illuminated rear side (b).

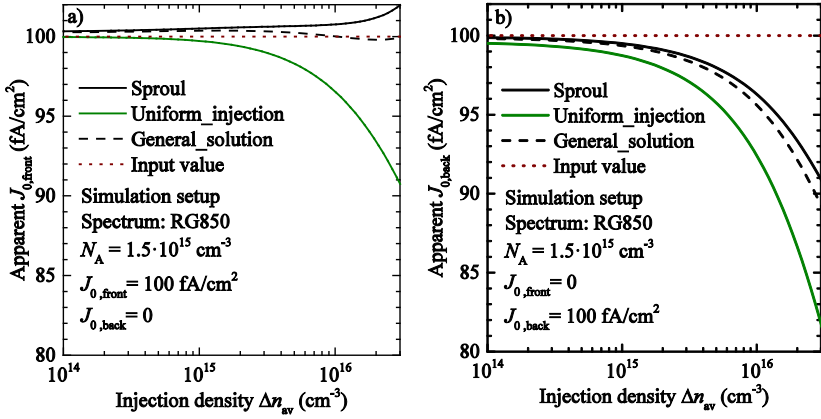


Figure 3.5 Apparent  $J_0$  for the different evaluation methods over injection density for the recombination active diffused surface located at the illuminated front-side (a), or the non-illuminated rear side (b). The spectrum of the red-filter RG850 is applied.

For the recombination active surface located at the front side (illuminated side, a), the assumption of a *uniform\_injection* results in an underestimation towards higher injection densities, which is even more pronounced compared to the analysis on the symmetrical samples (deviation of up to 10 %). The *general\_solution* and *Sproul* differ less than 1 % and 2 % from the input data, respectively.

However, when the recombination active surface is the non-illuminated side (b), the obtained  $J_0$  via all methods is strongly underestimated at high injection densities.

Before the explanation is given, the influence of the applied spectrum is evaluated in a third simulation: the implemented flasher spectrum without red-filter is applied (Figure 3.6) on a symmetrical sample (a) and an asymmetrical sample with the recombination active surface located at the illuminated front side (b).

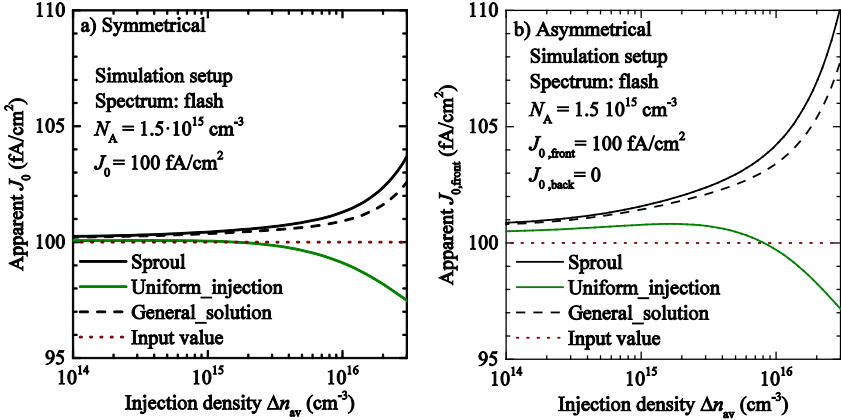


Figure 3.6 Apparent  $J_0$  over injection density for a symmetrical lifetime sample (a) and an asymmetrical sample with a recombination active front-side (b). The flasher spectrum without filter is applied.

The analysis with the *general\_solution* of Eq. (2.39) as well as *Sproull* Eq. (3.3) lead to an overestimation of  $J_0$  for high injection densities of up to 4 % for the symmetrical sample and up to 10 % for the asymmetrical sample at  $\Delta n_{av} = 3 \cdot 10^{16} \text{ cm}^{-3}$ . In this case, the analysis based on the assumption of *uniform\_injection* density leads to an underestimation of below 2.5 % for both samples.

The origin of this behavior lies in the non-uniform  $\Delta n$  over the wafer depth. Exemplarily, the  $\Delta n$  over the wafer depth is shown at an average injection density of  $\Delta n_{av} \approx 10^{16} \text{ cm}^{-3}$  in Figure 3.7 for both, the symmetrical and asymmetrical lifetime samples applying a) the spectrum of the red-filter RG850 and b) the flasher spectrum.

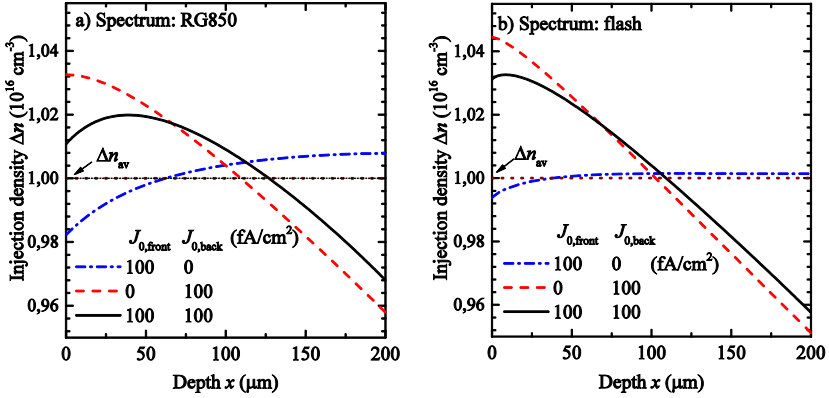


Figure 3.7 Injection density over depth for illumination at the front-side ( $x = 0$ ) for symmetrical samples and asymmetrical samples at an average injection density of  $\Delta n_{av} = 10^{16} \text{ cm}^{-3}$ . The simulation parameters are  $\tau_{SRH} = 1 \text{ ms}$ ,  $W = 200 \mu\text{m}$ , and  $N_A = 1.5 \cdot 10^{15} \text{ cm}^{-3}$ . a) spectrum of the red-filter RG850, b) flasher spectrum.

The analysis with Eq. (3.2) (*Sproul, general\_solution*) assumes uniform generation (in quasi-steady state mode) while the analysis with Eq. (3.3) assumes uniform  $\Delta n$ . However, the generation profile – even when applying a red-filter – is highly non-uniform and the generation at the front-side is pronounced in respect to the recombination at the rear side.

For asymmetrical samples, this leads to the following: When the recombination active surface is located at the front-side, the injection density becomes approximately uniform over the wafer depth (Figure 3.7) since the gradient towards a non-recombination active surface is small. Thus the assumption of uniform  $\Delta n$  is more accurate for the flasher spectrum than with the red-filter in this case. In the case of a recombination active rear side and non-recombination active front side, the majority of the injected carriers have to diffuse through the whole wafer which implements a high concentration gradient and violates both assumptions of uniform generation and uniform injection density.

For symmetrical samples (solid lines in Figure 3.7), both assumptions are violated as well. However, for the simulated samples, the application of a red-filter leads to a compensation of the different effects at the front and the rear side: the overall recombination current density at the surfaces  $J_{rec}/q = \Delta n_{front} S_{front} + \Delta n_{back} S_{back}$  is accurately described by  $\Delta n_{av} \cdot (S_{front} + S_{back})$  since the underestimated  $\Delta n_{front}$  is compensated for by the overestimated  $\Delta n_{back}$  if the additional reduction of  $\Delta n$  towards the surfaces (*Sproul, general\_solution*) is considered.

The analysis shows that for symmetrical lifetime samples, the red-filter RG850 together with an analysis accounting for the finite diffusion coefficient of the injected carriers enables the highest accuracy for the evaluation of the surface recombination. For measurement data obtained without red-filter or when the recombination active surface is located at the rear side, it is recommended to consider the different injection densities at the surfaces and therefore the generation profile – this can be done either analytically or numerically [79]. In this work, all measurements and further simulations apply the RG850 filter unless specified otherwise.

### 3.3 $J_0$ -analysis Methods

One assumption for the applicability of the method of the previous section is that the SRH recombination in the substrate is negligible,  $\tau_{\text{SRH}} \gg \tau_{\text{corr}}$ , or known. In reality, this is not always the case, thus another method is used more often:

In the standard analysis method, the approximation Eq. (3.3) is applied, inserting into Eq. (2.31) leads to the well-known expression introduced by Cuevas [80]

$$\frac{2J_0}{n_{i,\text{eff}}^2} \frac{(N_{\text{dop}} + \Delta n_{\text{av}})}{qW} = \frac{1}{\tau_s} = \frac{1}{\tau_{\text{corr}}} - \frac{1}{\tau_{\text{SRH}}}. \quad (3.5)$$

One method to extract the  $J_0$  of diffused surfaces on symmetrical samples from the measured Auger-corrected effective lifetime is differentiating Eq. (3.5) with respect to  $\Delta n$ :

$$J_0 = \frac{qW}{2} \frac{d}{d\Delta n_{\text{av}}} \left( \frac{n_{i,\text{eff}}^2}{\tau_{\text{corr}}} - \frac{n_{i,\text{eff}}^2}{\tau_{\text{SRH}}} \right). \quad (3.6)$$

Historically, band-gap narrowing (BGN) due to injected carriers in the substrate is neglected. This leads to an injection independent  $n_{i,\text{eff}}$ . Assuming the SRH-contribution to the base lifetime to be injection independent in the range of the data-evaluation (in the following denoted as *fit-range*) leads to the standard  $J_0$ -analysis originally implemented in the Sinton lifetime tester software (in this work referred to as *Kane&Swanson*) [76, 80]

$$J_0 = n_{i,\text{eff}}^2 \frac{qW}{2} \frac{d}{d\Delta n_{\text{av}}} \frac{1}{\tau_{\text{corr}}}. \quad (3.7)$$

The derivative  $d/d\Delta n(\tau_{\text{corr}}^{-1})$  is evaluated by a linear regression of  $\tau_{\text{corr}}^{-1}$  over  $\Delta n_{\text{av}}$  in a range where  $\tau_{\text{SRH}}$  is assumed to be injection independent, which is usually the case in the high injection regime  $\Delta n_{\text{av}} > 10 \cdot N_{\text{dop}}$ .

Eq. (3.7) represents the standard  $J_0$ -analysis method for QSSPC data. In the following, new methods are derived to overcome the restrictions listed in Section 3.1. All new

methods are designed to enable simple implementation and computation speed comparable with Eq. (3.7) to give the same applicability in practice, specifically for the Sinton lifetime-tester software's direct evaluation of measurements.

### Considering band-gap narrowing

Injected carriers in a substrate lead to band-gap narrowing [14] and thus an effective intrinsic carrier density  $n_{i,\text{eff}}$  that depends on  $\Delta n$  (see Figure 3.2). Together with the additional assumption

$$\frac{d}{d\Delta n} \frac{n_{i,\text{eff}}^2}{\tau_{\text{SRH}}} \ll \frac{d}{d\Delta n} \frac{n_{i,\text{eff}}^2}{\tau_{\text{corr}}}, \quad (3.8)$$

Eq. (3.6) leads to [15]

$$J_0 = \frac{qW}{2} \frac{d}{d\Delta n_{\text{av}}} \frac{n_{i,\text{eff}}^2}{\tau_{\text{corr}}}. \quad (3.9)$$

This equation is the result of collaboration of the author with R. A. Sinton and implemented in the Sinton lifetime tester WCT120 software, accessible as *BGN analysis after Kimmerle* there. Since it is based on Eq. (3.3), which assumes uniform injection density, it is denoted as *uniform\_injection* in this work.  $J_0$  must be evaluated in a range where Eq. (3.8) is valid, e.g. in high-injection conditions for high  $\tau_{\text{SRH}}$ . The obtained apparent  $J_0$  allows for the calculation of the surface recombination for arbitrary injection densities. The injection dependent SRH recombination in the substrate can thus be calculated by subtracting this surface recombination from  $\tau_{\text{corr}}^{-1}$  by Eq. (3.5) via [57]

$$\frac{1}{\tau_{\text{SRH}}(\Delta n)} = \frac{1}{\tau_{\text{corr}}(\Delta n)} - \frac{2J_0}{n_{i,\text{eff}}^2(\Delta n)} \frac{N_{\text{dop}} + \Delta n}{qW}. \quad (3.10)$$

In contrast to the *Kane&Swanson* method Eq. (3.7), the result of the method *uniform\_injection* Eq. (3.9) is not totally independent from a constant SRH-recombination; when condition (3.8) is not fulfilled, the obtained  $J_0$  from *uniform\_injection* overestimates  $J_0$  by

$$\Delta J_0 = \frac{qW}{2\tau_{\text{SRH}}} \frac{d}{d\Delta n_{\text{av}}} n_{i,\text{eff}}^2 + \frac{qW n_{i,\text{eff}}^2}{2} \frac{d}{d\Delta n_{\text{av}}} \frac{1}{\tau_{\text{SRH}}}. \quad (3.11)$$

The right hand side is the linear injection dependence of the SRH recombination in the base substrate. For all regarded methods, this influence cannot be separated from a contribution of  $J_0$  – thus the common way to avoid this is the data-evaluation in a range where the influence is assumed to be small (e.g. high or constant  $\tau_{\text{SRH}}$ ). This leaves

$$\Delta J_0 = \frac{qW}{2\tau_{\text{SRH}}} \frac{d}{d\Delta n_{\text{av}}} n_{i,\text{eff}}^2, \quad (3.12)$$

which can be calculated. This correction depends on the applied fit range in  $\Delta n$ , the base doping, and  $\tau_{\text{SRH}}$  but is independent from  $J_0$ . To show its influence on the analysis,  $\Delta J_0$  is given here for two different  $p$ -type substrates and a wide range of possible  $\tau_{\text{SRH}}$  and injection densities in Figure 3.8.

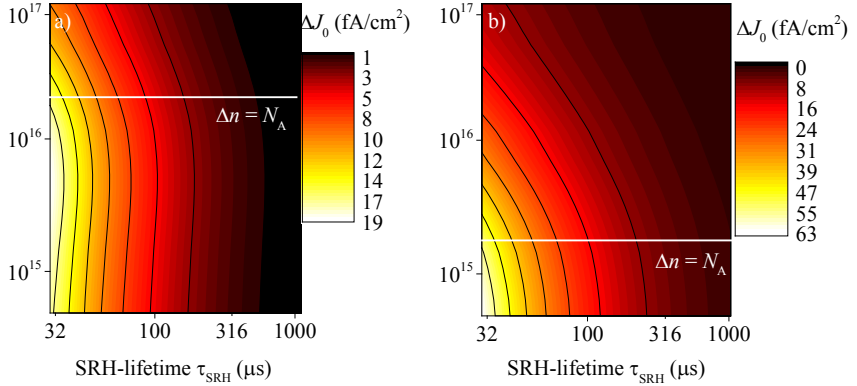


Figure 3.8 Correction for  $J_0$ -analysis  $\Delta J_0$  when assuming a constant SRH lifetime  $\tau_{\text{SRH}}$  in the substrate after Eq. (3.12), dependent on the center of the applied fit range. Examples are given for  $p$ -type wafers with specific resistance  $\rho_0 = 1 \text{ } \Omega\text{cm}$  (a) and  $\rho_0 = 10 \text{ } \Omega\text{cm}$  (b). The thickness of the wafer is  $200 \text{ } \mu\text{m}$ , and the fit range is chosen to  $\Delta n \pm 30 \%$ . For clarification of the relative position of the possible fit range, the  $\Delta n = N_{\text{dot}}$  lines are given.

On lowly doped  $p$ -type material (a) with high lifetime ( $\tau_{\text{SRH}} > 500 \text{ } \mu\text{s}$ ) and under high injection conditions ( $\Delta n = 10 \cdot N_{\text{dop}} \pm 30 \%$ ), the correction is negligible ( $\Delta J_0 < 3 \text{ fA/cm}^2$ ). However, for different dopant concentrations, applied fit ranges, or lower  $\tau_{\text{SRH}}$ , the influence of  $\Delta J_0$  may be significant for low  $J_0$  to be evaluated: and in some cases still realistic SRH recombination defined by  $\tau_{\text{SRH}} = 100 \text{ } \mu\text{s}$  leads to a deviation of up to  $20 \text{ fA/cm}^2$  on lowly doped and up to  $5 \text{ fA/cm}^2$  on highly doped  $p$ -type substrate.

The necessary input-parameters for Eq. (3.12) are experimentally available:  $\tau_{\text{SRH}}$  can be calculated by Eq. (3.10) and averaged over the fit range. This averaging is necessary since  $J_0$  and  $d/d\Delta n \tau_{\text{SRH}}^{-1}$  are not independent variables. Thus,  $J_0$  can be calculated by Eq. (3.9) and be corrected for the influence of a constant  $\tau_{\text{SRH}}$  by Eq. (3.12) as  $J_{0,\text{corrected}} = J_0 - \Delta J_0$  (in this work referred to as *uniform\_injection\_corr*). Such obtained  $J_0$  shows by design the same robustness against constant  $\tau_{\text{SRH}}$  as the *Kane&Swanson*

method but additionally takes band-gap narrowing into account. However, with all methods, care must be taken when violating high-injection conditions on a substrate with low SRH lifetime, since the latter is presumably injection dependent and may contribute significantly to the derivative of the recombination rate.

### Considering carrier diffusion

The standard *Kane&Swanson* evaluation method and the method *uniform\_injection (corrected)* apply the approximation Eq. (3.3), which is based on the assumption of a uniform  $\Delta n$  in the wafer. Thus, in agreement with the simulation results in Section 3.1, while analyzing QSSPC datasets to extract  $J_0$ , several authors observe a decrease of the slope and thus a decrease of obtained  $J_0$  towards higher injection levels [76, 81]. In Section 2.4 it is shown that the assumption of a homogeneous generation leads to Eq. (2.39) according to Luke [82]. Section 3.2 shows that it describes the surface recombination accurately for injection densities  $\Delta n > 5 \cdot 10^{15} \text{ cm}^{-3}$ . For this reason, a method is derived in the following combining Eq. (2.39) with the advantage of independency from an unknown (but injection independent) contribution of  $\tau_{\text{SRH}}$ .

The approximation Eq. (3.3) is not necessary for the analytical  $J_0$  analysis. A more general approach is to derive Eq. (2.31) for the injection density  $\Delta n$ . This leads to

$$J_0 = q \frac{d}{d\Delta n} (n_{i,\text{eff}}^2 S). \quad (3.13)$$

In the symmetrical case one may apply Sproul's approximation Eq. (2.41), which leads to

$$J_0 = \frac{qW}{2} \frac{d}{d\Delta n_{\text{av}}} \frac{n_{i,\text{eff}}^2}{\tau_s - \frac{W^2}{D\pi^2}} = \frac{qW}{2} \frac{d}{d\Delta n_{\text{av}}} \frac{n_{i,\text{eff}}^2}{\left( \frac{1}{\tau_{\text{corr}}} - \frac{1}{\tau_{\text{SRH}}} \right)^{-1} - \frac{W^2}{D\pi^2}}. \quad (3.14)$$

Comparing with *uniform\_injection* Eq. (3.9) or, in the assumption of a constant  $n_i$ , the *Kane&Swanson* method Eq. (3.7), it is obvious that in this case the surface lifetime is simply corrected by the diffusion term  $W^2/D\pi^2$ . Replacing  $\tau_s$  with  $\tau_{\text{corr}}$  in Eq. (3.14) may be a good choice in practice. However, for high SRH recombination, the problem reappears when evaluating Eq. (3.14), the result of the  $J_0$ -analysis is not exactly independent from a constant SRH-lifetime. In contrast, the constraint (3.8) is more limited because of the diffusion term in Eq. (3.14); in other words, the influence of even a constant  $\tau_{\text{SRH}}$  is extended not only on the influence of the BGN but also on the influence of the carrier diffusion.

Assuming that  $J_0$  is known, the SRH lifetime can be calculated from Eq. (2.31) and Eq. (2.41) by

$$\frac{1}{\tau_{\text{SRH}}} = \frac{1}{\tau_{\text{corr}}} - \frac{1}{\frac{W}{2S_{\text{eff}}} + \frac{W^2}{D\pi^2}} = \frac{1}{\tau_{\text{corr}}} - \frac{1}{\frac{W}{2J_0(N_{\text{dop}} + \Delta n_{\text{av}})} + \frac{W^2}{D\pi^2}}. \quad (3.15)$$

The obtained (averaged) value can be used to correct  $\tau_s$  in Eq. (3.14). An iteration of Eq. (3.14) and Eq. (3.15) leads to a self-consistent solution (in this work referred to as *diffusion\_corr*) and thus to a  $J_0$  and  $\tau_{\text{SRH}}$  which are in agreement with Eq. (2.31), Eq. (2.41) and injection dependent BGN in the substrate.

### General solution and asymmetrical samples

Applying an approximation to solve Eq. (2.31) is not necessary, and for asymmetrical samples an approximation is not available. In the previous section, the solutions of Eq. (2.31) are given for the asymmetrical case  $S_1 \neq S_2$ , Eq. (3.2) and for the symmetrical case  $S_1 = S_2$ , Eq. (3.1).  $J_0$  can be evaluated by applying Eq. (3.13) on these solutions.

Similar to *uniform\_injection\_corr* and *diffusion\_corr*, this procedure is not entirely independent from the contribution of a constant  $\tau_{\text{SRH}}$ . To evaluate  $\tau_{\text{SRH}}$  with the analyzed  $J_0$  and to get a robust method leading to an apparent  $J_0$  that is independent from a constant contribution of  $\tau_{\text{SRH}}$ , one can easily solve Eq. (3.2) and Eq. (3.1) numerically with negligible computation time to obtain the recombination parameter  $\alpha_0$  for an assumed  $S_{\text{eff}}$  calculated from the obtained  $J_0$ . In this work, this is implemented into a visual basic routine to be available directly for the QSSPC measurement sheet. The obtained value for  $\alpha_0$  is then used to calculate an injection dependent  $\tau_{\text{SRH}}$  by

$$\frac{1}{\tau_{\text{SRH}}} = \frac{1}{\tau_{\text{corr}}} - \alpha_0^2 D. \quad (3.16)$$

Here all quantities are injection dependent. The average value of  $\tau_{\text{SRH}}$  over the fit range can be applied to calculate a corrected  $\alpha_0$  and thus a corrected  $J_0$  analogously to the aforementioned case (referred to as *general\_solution*). This procedure leads by design to a  $J_0$  which is independent from a constant contribution of  $\tau_{\text{SRH}}$  (in the injection regime where  $J_0$  is evaluated) in agreement with Eq. (2.31), Eq. (2.41), and considering band-gap narrowing in the substrate for symmetrical and asymmetrical samples.

### 3.4 Impact on the $J_0$ -Analysis of Symmetrical Samples

In this section, the derived evaluation methods for the  $J_0$ -analysis are compared on simulated data sets; identical simulations were carried out in Section 3.1. To show the influence of the different applied methods, the obtained data sets are analyzed for  $J_0$  and  $\tau_{\text{SRH}}$ .  $J_0$  is evaluated differentially from the data of two successive illumination

intensities. The typical fit range of  $10 \cdot N_A \pm 30\%$  is applied for the averaging of  $J_0$ , which is then used for the calculation of  $\tau_{\text{SRH}}$ . For the  $\tau_{\text{SRH}}$ -corrected methods, the average of the obtained  $\tau_{\text{SRH}}$  in the fit-range is then applied for an updated  $J_0$ -analysis. The procedure is repeated twice. For all simulations shown in this section, a  $p$ -type base doping of  $N_A = 1.5 \cdot 10^{15} \text{ cm}^{-3}$  and a wafer thickness of  $W = 200 \text{ }\mu\text{m}$  is applied. The findings shown here do not differ qualitatively when applying other base dopant concentrations or  $n$ -type substrates.

An overview of the applied methods is given in Table 3.2.

Table 3.2 Overview of the compared methods for the analysis of the simulated data sets of symmetrical lifetime samples. For the asymmetrical samples, Eq. (3.1) has to be replaced by Eq. (3.2). All methods assume a negligible change of  $\tau_{\text{SRH}}$  in the fit range.

Short name	Applied equations (symmetrical case)	References	Central assumption (in fit-range)	Description
<i>Kane&amp;Swanson</i>	$J_0 = n_i^2 \frac{qW}{2} \frac{d}{d\Delta n} \frac{1}{\tau_{\text{corr}}} \quad (3.7)$	[76]	$\Delta n(x) = \text{const.}$ $n_{i,\text{eff}} = \text{const.}$	Original implemented slope method and models
<i>Kane&amp;Swanson_dated</i>				<i>Kane&amp;Swanson</i> with $n_{i,\text{eff}}^2(\Delta n)$ and Auger by Richter [23]
<i>Uniform_injection</i>	$J_0 = \frac{qW}{2} \frac{d}{d\Delta n} \frac{n_{i,\text{eff}}^2}{\tau_{\text{corr}}} \quad (3.9)$	[15]	$\Delta n(x) = \text{const.}$ $\tau_{\text{SRH}} \text{ high}$	Recently implemented method
<i>Uniform_injection_corr</i>	$\frac{1}{\tau_{\text{SRH}}(\Delta n)} = \frac{1}{\tau_{\text{corr}}} \frac{2J_0}{n_{i,\text{eff}}^2(\Delta n)} \frac{N_{\text{dop}} + \Delta n}{qW} \quad (3.10)$	[15]	$\Delta n(x) = \text{const.}$ $\tau_{\text{SRH}} = \text{const.}$	Above, corrected for $\tau_{\text{SRH}}$ (3 iterations)
<i>Diffusion_corr</i>	$J_0 = \frac{qW}{2} \frac{d}{d\Delta n} \frac{n_{i,\text{eff}}^2}{\tau_s} \frac{W^2}{D\pi^2} \quad (3.14)$			
	$\frac{1}{\tau_{\text{SRH}}} = \frac{1}{\tau_{\text{corr}}} \frac{W}{q n_{i,\text{eff}}^2} \frac{1}{2 J_0 (N_{\text{dop}} + \Delta n)} + \frac{W^2}{D\pi^2} \quad (3.15)$	[59, 82]	uniform generation symmetrical sample $\tau_{\text{SRH}} = \text{const.}$	Fit $n_{i,\text{eff}}^2 S_{\text{eff}}$ with $S_{\text{eff}}$ from Sproul <i>et al.</i> [59], corrected for $\tau_{\text{SRH}}$ (3 iterations)
<i>General_solution</i>	$S = \alpha_0 D \tan\left(\frac{\alpha_0 W}{2}\right) \quad (3.1) \quad J_0 = q \frac{d}{d\Delta n} \left(n_{i,\text{eff}}^2 S\right) \quad (3.13)$	[82]	uniform generation $\tau_{\text{SRH}} = \text{const.}$	Fit $n_{i,\text{eff}}^2 S_{\text{eff}}$ applying the solution of Eq. (2.39), corrected for $\tau_{\text{SRH}}$ (3 iterations)
	$\frac{1}{\tau_{\text{SRH}}} = \frac{1}{\tau_{\text{corr}}} - \alpha_0^2 D \quad (3.16)$			

## Injection dependency

The first part investigates the dependency of the analyzed results on the applied fit-range.

To investigate the influence and robustness against constant SRH recombination, symmetrical lifetime samples are simulated assuming  $J_0 = 100 \text{ fA/cm}^2$  and constant  $\tau_{\text{SRH}} = 500 \text{ }\mu\text{s}$  (Figure 3.9).

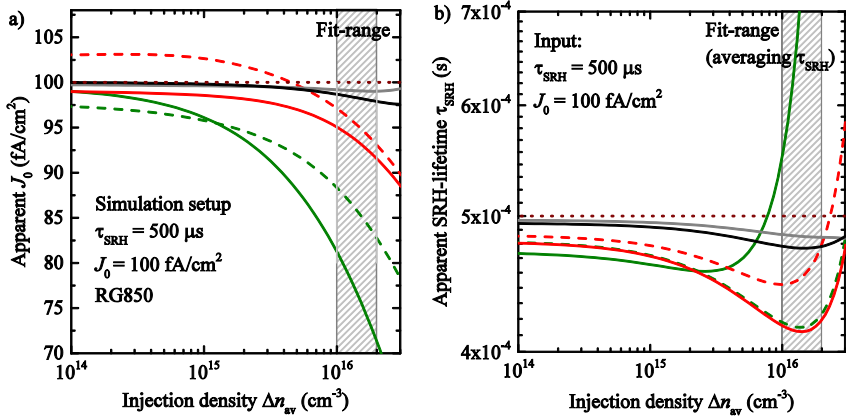


Figure 3.9 a) Differentially evaluated apparent  $J_0$  over  $\Delta n_{\text{av}}$  extracted from simulation data with the different methods. The data are simulated with  $p$ -type base doping  $N_A = 1.5 \cdot 10^{15} \text{ cm}^{-3}$ ,  $J_0 = 100 \text{ fA/cm}^2$  on both sides, and an additional recombination defined by  $\tau_{\text{SRH}} = 500 \text{ }\mu\text{s}$ . The spectrum of the red-filter RG850 is applied. The typical fit range of  $10 \cdot N_A \pm 30 \%$  is applied for the averaging of  $J_0$ , which is then applied for the calculation of  $\tau_{\text{SRH}}$ . b) calculated apparent  $\tau_{\text{SRH}}$ .

- Kane&Swanson
- - - Kane&Swanson\_updated
- - - Uniform\_injection
- - - Uniform\_injection\_corr
- Diffusion\_corr
- General\_solution
- · · Input value

It is shown that neglecting  $d/d\Delta n (n_{i,\text{eff}}^2)$  (neglecting BGN) by fitting  $1/\tau_{\text{corr}}$  (Kane&Swanson and Kane&Swanson\_updated) leads to a strong decrease of the apparent  $J_0$  for increasing injection density. In this case, the method Kane&Swanson\_updated is depicted additionally to show the influence of regarding the change of  $n_{i,\text{eff}}^2$  with  $\Delta n$ . However, fitting  $n_{i,\text{eff}}^2/\tau_{\text{corr}}$  (uniform\_injection) leads to a reduced increase but a  $J_0$  that is influenced by  $\tau_{\text{SRH}}$ . The iterative correction for  $\tau_{\text{SRH}}$  (uniform\_injection\_corr) reproduces  $J_0$  up to an injection density of  $\Delta n_{\text{av}} = 10^{16} \text{ cm}^{-3}$  very well (5% deviation). For the diffusion corrected methods, the iteration procedure (diffusion\_corr and general\_solution) leads to a deviation of  $J_0$  below 3% for the whole range up to  $\Delta n_{\text{av}} = 3 \cdot 10^{16} \text{ cm}^{-3}$  and 1.8% in the fit range.

The methods *diffusion\_corr* and *general\_solution* reproduce  $\tau_{SRH}$  with the highest accuracy (deviation < 5 %) – but consistently underestimate for  $\Delta n_{av} > 10^{16} \text{ cm}^{-3}$ . However, this deviation can be expected since, on the one hand, the effective lifetime is dominated by Auger- and surface recombination for high injection densities. On the other hand, an underestimation of  $J_0$  implies an underestimation of  $\tau_{SRH}$  to match with the total recombination in the sample. Thus every violation of the assumptions on  $\Delta n$  and the resulting inaccuracy in the calculated surface recombination leads to a strong influence on the analyzed  $\tau_{SRH}$ .

### Injection dependent base recombination

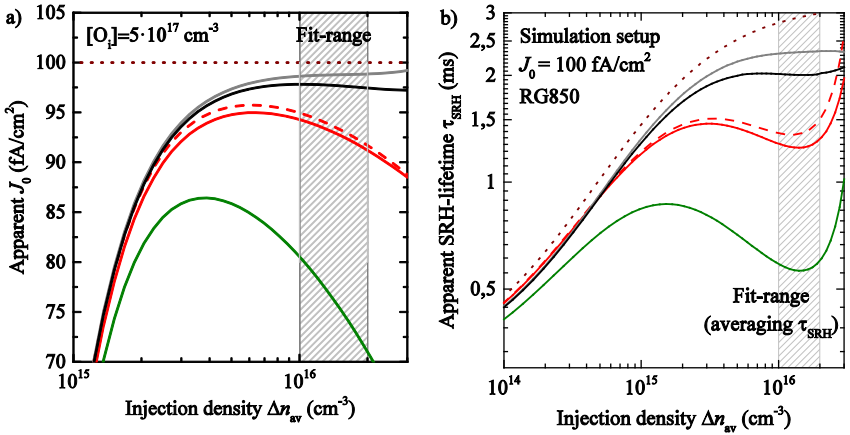


Figure 3.10 a) Differentially evaluated apparent  $J_0$  over  $\Delta n_{av}$  differentially extracted from simulation data with the different methods. The data are simulated with p-type base doping  $N_A = 1.5 \cdot 10^{15} \text{ cm}^{-3}$ ,  $J_0 = 100 \text{ fA/cm}^2$  on both sides, and an additional recombination in the substrate defined by  $[O_i] = 5 \cdot 10^{17} \text{ cm}^{-3}$ . The implemented spectrum of the red-filter RG850 is applied. The typical fit range of  $10 \cdot N_A \pm 10\%$  is applied for the averaging of  $J_0$ , which is then applied for the calculation of  $\tau_{SRH}$ . b) Calculated apparent  $\tau_{SRH}$ .

- Kane&Swanson
- - - Uniform\_injection
- Uniform\_injection\_corr
- Diffusion\_corrected
- General\_solution
- · - · - Input value

Experimentally,  $\tau_{SRH}$  is not expected to be independent from  $\Delta n$ . As an example, the parameterization of  $\tau_{SRH}$  for the recombination on boron-oxygen defects (degraded) of a concentration of  $[O_i] = 5 \cdot 10^{17} \text{ cm}^{-3}$  is chosen (given implementation in QsCell) for the simulations (Figure 3.10).

For all analysis methods, a strong decrease of the apparent  $J_0$  is observed for decreasing injection density in the range  $\Delta n < 5 \cdot 10^{15} \text{ cm}^{-3}$  due to the injection

dependence of the SRH-recombination. At high injection densities  $\Delta n > 5 \cdot 10^{15} \text{ cm}^{-3}$ , the *Kane&Swanson* method and *uniform\_injection* show an apparent  $J_0$  that decreases with injection density. Such behavior has been predicted by Kane and Swanson [76] (compare Figure 3.1) due to the non-uniformity of the injection density for samples with high surface recombination activity. Mäckel and Varner [81] observed the same on measured and simulated data sets. Min *et al.* [83] propose to use the maximum value of the apparent  $J_0$  over  $\Delta n_{av}$ . Finally Thomson *et al.* [84] apply numerical simulations to obtain the apparent  $J_0$  by fitting the outcome to the measured effective carrier lifetime.

In contrast, the methods taking into account the finite carrier diffusion coefficient (*diffusion\_corr* and *general\_solution*) lead to a good reproduction of the input  $J_0$  with a deviation below 2.4 % in the fit range. Interestingly, the approximation of Sproul seems to reproduce the data with higher accuracy than the general solution. The advantage of taking the finite diffusion coefficient into account is visible for this example: neglecting the carrier diffusion (*Kane&Swanson* and *uniform\_injection*), the apparent  $J_0$  decreases for higher injection densities leading to a maximum that is experimentally difficult to evaluate and still underestimates  $J_0$  by 15 % or 5 % for the *Kane&Swanson* method or *uniform\_injection*, respectively. In contrast, the diffusion corrected methods enable a broad fit-range for  $\Delta n_{av} > 7 \cdot 10^{15} \text{ cm}^{-3}$  with a deviation below 3 %.

Again,  $\tau_{SRH}$  is reproduced much better by the diffusion corrected methods *diffusion\_corr* and *general\_solution* than by the other methods. For high injection densities,  $\tau_{SRH}$  is underestimated for similar reasons as for the previous case (compare Figure 3.9 and discussion there)

### **$J_0$ - and $\tau_{SRH}$ -variation**

In the second part of this section the methods are compared using simulation data of symmetrical samples dependent on the applied  $J_0$  and  $\tau_{SRH}$ . For simplicity, only four methods are compared in the following: the *Kane&Swanson* method (which is in widespread use), the method *uniform\_injection* (which is in use to the time of writing this thesis), its correction for constant  $\tau_{SRH}$  *uniform\_injection\_corr*, and *diffusion\_corr*. *Diffusion\_corr* is selected because it varies only slightly from *general\_solution*, but shows a desirable simplicity and analytical functionality. The simulations are analyzed in a fit-range of  $\Delta n_{av} = (1 - 2) \cdot 10^{16} \text{ cm}^{-3}$  which is very close to  $10 N_{dop} \pm 30 \%$  for the applied  $p$ -type  $10 \text{ } \Omega\text{cm}$  substrate. The choice of the fit-range is crucial for the deviation of the methods: at lower injection densities, the methods assuming uniform injection deviate less. However, on the one hand high injection densities lead to high  $S_{eff}$  for a given  $J_0$  and thus a high surface recombination which is beneficial for its evaluation. On the other hand e.g. for recombination of boron oxygen defect centers, when Czochralski pulled silicon (Cz-Si) is applied,  $\tau_{SRH}$  increases with injection density and

the injection dependency of  $\tau_{\text{SRH}}^{-1}$  generally decreases for high injection densities. Thus it is beneficial to apply high  $\Delta n$ .

The first set of simulations applies a constant  $\tau_{\text{SRH}} = 500 \mu\text{s}$ , but varies  $J_0 = 1$  to  $500 \text{ fA/cm}^2$ . The four methods are used to extract the apparent  $J_0$  and  $\tau_{\text{SRH}}$ . Figure 3.11 depicts the relative deviation of the incrementally evaluated apparent  $J_0$  from the input  $J_0$  and the obtained  $\tau_{\text{SRH}}$  from the analysis.

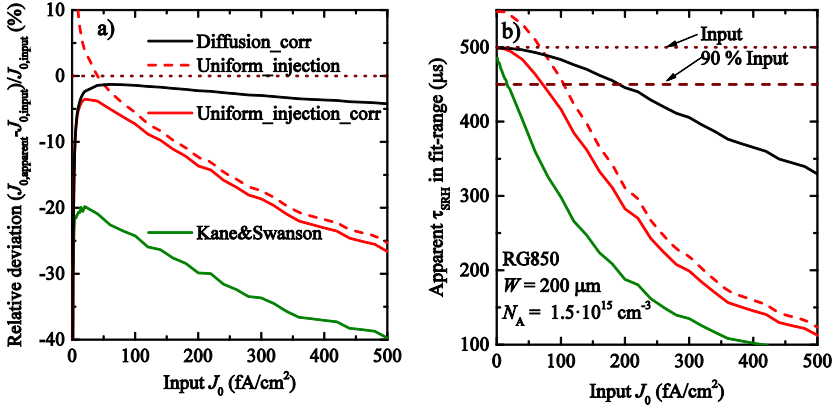


Figure 3.11 Results of the  $J_0$ -analysis on simulated data sets with different methods over input  $J_0$ . Each sample is simulated with a thickness of  $W = 200 \mu\text{m}$ , base doping  $N_A = 1.5 \cdot 10^{15} \text{ cm}^{-3}$ , constant  $\tau_{\text{SRH}} = 500 \mu\text{s}$ , and the implemented spectrum RG850. The analysis is carried out in a fit range of  $(1 \text{ to } 2) \cdot 10^{16} \text{ cm}^{-3}$ . The obtained  $J_0$  are applied for the calculation of  $\tau_{\text{SRH}}$ . a) Relative deviation of the obtained  $J_0$  from the input value. b) Average value of the analyzed  $\tau_{\text{SRH}}$  in the fit range.

The *Kane&Swanson* method underestimates  $J_0$  by more than 20 % for all applied sets of input data. Considering BGN and updated models (*uniform\_injection*) reduces the deviation by  $\sim 15$  % of the input  $J_0$ . The iteration procedure to correct for  $\tau_{\text{SRH}}$  is significant for  $J_0 < 20 \text{ fA/cm}^2$  in this case. The method *uniform\_injection\_corr* also shows an underestimation of the apparent  $J_0$  of over 10 % for  $J_0 > 150 \text{ fA/cm}^2$  due to the neglected carrier diffusion.

The *diffusion\_corr* method leads to the same results as *uniform\_injection\_corr* for  $J_0 < 30 \text{ fA/cm}^2$  where the diffusion towards the surfaces is apparently negligible. Both methods underestimate  $J_0$  for low input  $J_0$  with a deviation of 10 % at  $J_0 = 4 \text{ fA/cm}^2$  which is dominated by other experimental uncertainties in this range. Finally, the method *diffusion\_corr* shows a significantly reduced underestimation of  $J_0$  still in the range of 5 % for  $J_0 = 500 \text{ fA/cm}^2$ .

Since the base-lifetime is calculated by subtracting the calculated surface recombination from the measured lifetime, an underestimation of  $J_0$  leads to an

underestimation of  $\tau_{\text{SRH}}$ . However, the higher  $J_0$ , the more dominating is the surface recombination and the higher is the resulting uncertainty in  $\tau_{\text{SRH}}$ . Consequently, the *Kane&Swanson* method underestimates  $\tau_{\text{SRH}}$  by over 10 % for  $J_0 > 17 \text{ fA/cm}^2$ . The method *uniform\_injection\_corr* improves the reproduction of  $\tau_{\text{SRH}}$  with a deviation of 10 % at  $J_0 = 75 \text{ fA/cm}^2$ . Finally, *diffusion\_corr* leads to a deviation below 10 % up to  $J_0 = 200 \text{ fA/cm}^2$ .

The second set of simulations applies two different  $J_0$  of  $J_0 = 50 \text{ fA/cm}^2$  or  $J_0 = 200 \text{ fA/cm}^2$  on both sides but different constant contributions of  $\tau_{\text{SRH}} = 10$  to  $1000 \mu\text{s}$ . The simulations are analyzed in a fit-range of  $\Delta n_{\text{av}} = (1 \text{ to } 2) \cdot 10^{16} \text{ cm}^{-3}$ . The apparent  $J_0$  is depicted on the left hand side of Figure 3.12, whereas the apparent  $\tau_{\text{SRH}}$  is depicted on the right hand side, both over input  $\tau_{\text{SRH}}$ .

All methods show an increasing apparent  $J_0$  towards low bulk lifetimes. For low  $J_0$  (a), *uniform\_injection* turns out to be inapplicable for low bulk lifetimes (in the case of  $J_0 = 50 \text{ fA/cm}^2$  and  $\tau_{\text{SRH}} = 110 \mu\text{s}$ , the input  $J_0$  is already overestimated by 10 %). In contrast, the iterative correction for  $\tau_{\text{SRH}}$  (*uniform\_injection\_corr* and *diffusion\_corr*) leads to a consistently reproducible  $J_0$ , down to  $\tau_{\text{SRH}} = 20 \mu\text{s}$  with a deviation below 6 %. The finite diffusion of carriers (comparison between *uniform\_injection\_corr* and *diffusion\_corr*) shows no significant influence for the low recombination active surface. Despite the mentioned increase of  $J_0$  for decreasing  $\tau_{\text{SRH}}$ , the *Kane&Swanson* method underestimates  $J_0$  by 20 %.

For the  $J_0 = 200 \text{ fA/cm}^2$  simulations, the relative behavior of the apparent  $J_0$  obtained by the methods assuming uniform injection density (*Kane&Swanson*, *uniform\_injection*, *uniform\_injection\_corr*) is similar in respect to  $\tau_{\text{SRH}}$  but the higher recombination activity of the surface leads to a higher impact of the finite carrier diffusion and thus to an absolute decrease of the curves by  $\Delta J_0 \approx 26 \text{ fA/cm}^2$ . In contrast, *diffusion\_corr* reproduces the input  $J_0$  very well with a deviation below 5 % at  $\tau_{\text{SRH}} = 20 \mu\text{s}$ . Note that in such cases, other influences such as the measurement uncertainties, remaining injection dependence of  $\tau_{\text{SRH}}$ , or the uncertainty in the intrinsic lifetime may become crucial and prevent a meaningful  $J_0$ -analysis in the experiment.

The obtained  $\tau_{\text{SRH}}$  in the fit range (right hand side of Figure 3.12) show a high correlation with the input  $\tau_{\text{SRH}}$  in the simulations for all methods. For low recombination activity of the surfaces of  $J_0 = 50 \text{ fA/cm}^2$ , all methods can be applied to extract  $\tau_{\text{SRH}}$ . The deviation of the *Kane&Swanson* method of up to 40 % is a result of Auger- and  $n_i$ -models being applied differently and the underestimated  $J_0$ , whereas the methods applying the same models as the simulation and accounting for band-gap

narrowing in the substrate (*uniform\_injection*, *uniform\_injection\_corr* and *diffusion\_corr*) show a deviation below 10 %.

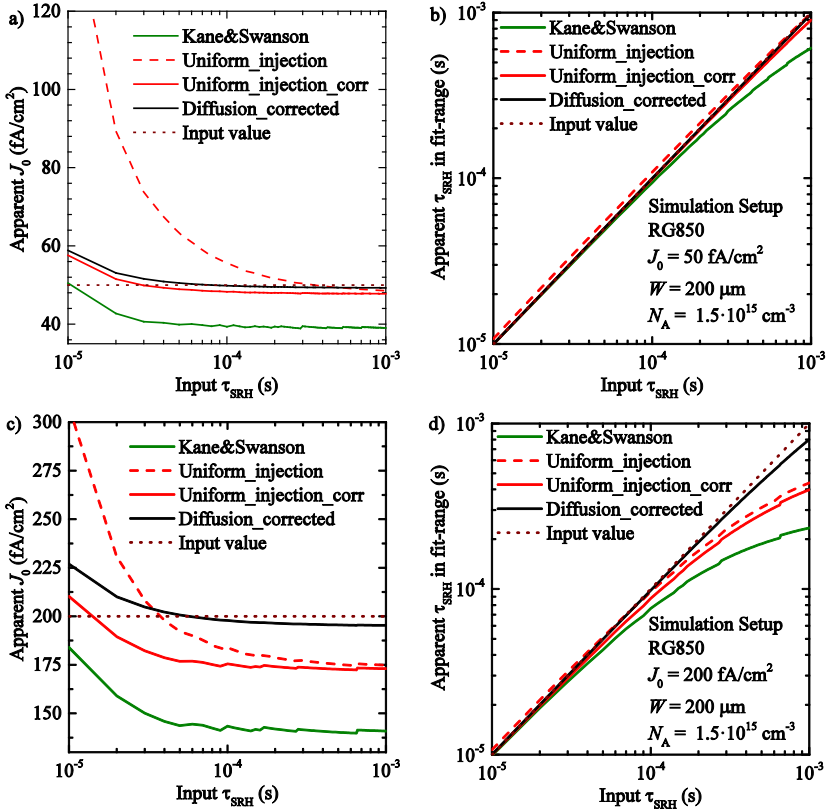


Figure 3.12 Results of the  $J_0$ -analysis on simulated data sets with different methods. Each sample is simulated with a thickness of  $W = 200 \mu\text{m}$ , base doping  $N_A = 1.5 \cdot 10^{15} \text{ cm}^{-3}$ , an injection independent  $\tau_{\text{SRH}}$ , and the implemented spectrum RG850. The analysis is carried out in a fit range of  $(1 - 2) \cdot 10^{16} \text{ cm}^{-3}$ . The obtained  $J_0$  are applied for the calculation of  $\tau_{\text{SRH}}$ . Left/right: apparent  $J_0 / \tau_{\text{SRH}}$  over input  $\tau_{\text{SRH}}$ . Above:  $J_{0,\text{input}} = 50 \text{ fA/cm}^2$ . Below:  $J_{0,\text{input}} = 200 \text{ fA/cm}^2$ .

For higher surface recombination activity of  $J_0 = 200 \text{ fA/cm}^2$ , the underestimation of  $J_0$  by the methods assuming a uniform  $\Delta n$  (*Kane&Swanson*, *uniform\_injection*, *uniform\_injection\_corr*) leads to an underestimation of  $\tau_{\text{SRH}}$  of up to 76 % for *Kane&Swanson*, 56 % for *uniform\_injection* and 60 % for the *uniform\_injection\_corr*. *Diffusion\_corr* leads to a deviation of up to 20 %. All deviations are given for the highest applied base lifetime of  $\tau_{\text{SRH}} = 1 \text{ ms}$ .

From this section can be concluded that for symmetrical lifetime samples, simulated with red-filter RG850, the evaluation methods which take into account the finite carrier diffusion and are independent from a constant contribution of  $\tau_{\text{SRH}}$  (*diffusion\_corr* and *general\_solution*) show the best reliability on all regarded combinations of parameters, such as base dopant concentration, injection density,  $\tau_{\text{SRH}}$ , and the input  $J_0$ , as published by the author in Ref. [75].

### 3.5 Experimental Comparison on Symmetrical Lifetime Samples

For an experimental comparison of the different methods, symmetrical lifetime samples (FZ-Si material,  $W = 200$  to  $230 \mu\text{m}$ ) of different base-doping are produced with alkaline textured surfaces and exposed to the same industrial-type  $\text{POCl}_3$ -diffusion (resulting in a sheet resistance of approx.  $90 \Omega/\text{sq.}$ ) and  $\text{SiN}_x$  passivation procedure. The process flow chart is depicted in Figure 3.13.

The samples are analyzed in a Sinton WCT-120 lifetime tester at the wafer center, applying the generalized measurement mode and the red-filter RG850. All data sets are analyzed in the injection range of  $\Delta n_{\text{av}} = (1 \text{ to } 1.5) \cdot 10^{16} \text{ cm}^{-3}$ . In this section, only the results of the *Kane&Swanson* method, the method *uniform\_injection* as recently implemented in the lifetime tester software, the correction of the latter method by the evaluation of an average  $\tau_{\text{SRH}}$  in the fit-range *uniform\_injection\_corr*, and the method *diffusion\_corr* with the similar correction for  $\tau_{\text{SRH}}$  are given.

For a direct comparison with the results on simulated data sets of the previous chapter, simulations with the same settings are carried out, applying  $J_0 = 208 \text{ fA/cm}^2$ . Further applied is a constant  $\tau_{\text{SRH}}$  obtained in the same fit-range from the measurement data by Eq. (3.15) for each sample individually. As shown in the previous section, the impact of this  $\tau_{\text{SRH}}$  is mainly on the correction of *uniform\_injection\_corr* and *diffusion\_corr*.

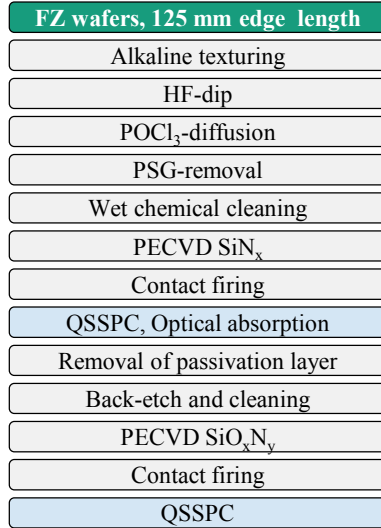


Figure 3.13 Process flow for the fabrication of the symmetrical lifetime samples to evaluate  $J_0$ .

**Results**

The fit data for each method over average injection density is shown in Figure 3.14; the inverse corrected lifetime is applied for the *Kane&Swanson* method. The respective values for the other methods are scaled with the average  $n_{i,eff}^2$  in the fit range, to compare using the same scale. In particular, this means multiplication of  $\tau_{corr}^{-1}$  or  $\tau_s^{-1}$ , respectively, with the BGN-correction factor  $f_{BGN} := n_{i,eff}^2 / \langle n_{i,eff}^2 \rangle_{Fit}$ .

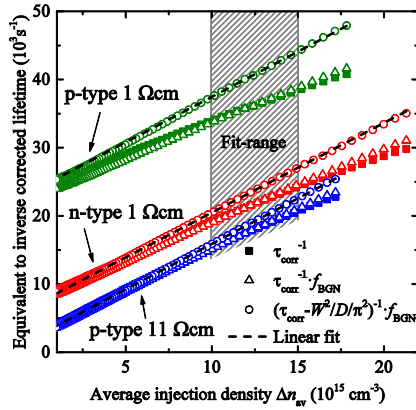


Figure 3.14: Inverse corrected lifetime equivalent versus average injection density for the different methods, testing one wafer of each base substrate. For each data-set, the slope of the data is proportional to the evaluated  $J_0$ , independent from  $\Delta n_{av}$ . The data sets of the lowly doped p-type and n-type samples differ very little and therefore only the data of the p-type sample is shown.

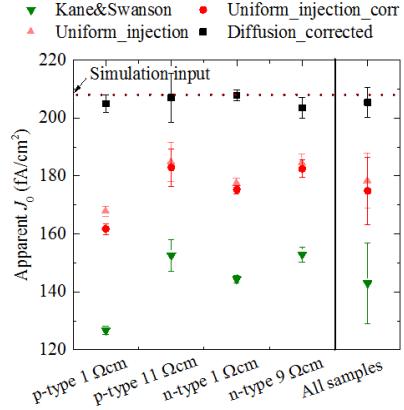


Figure 3.15: Apparent  $J_0$  resulting from the different methods in the center of the wafers; the data are evaluated by a linear fit of the respective parameter in the range of  $\Delta n_{av} = (1 \text{ to } 1.5) \cdot 10^{16} \text{ cm}^{-3}$ . Error bars give the standard deviation of the point-wise evaluated  $J_0$  over the fit range for the material related results and the standard deviation over all samples for the averaged result.

The data used for *uniform\_injection* ( $\tau_{corr}^{-1} \cdot f_{BGN}$ ) shows increased linearity in comparison to  $\tau_{corr}^{-1}$ , used for the *Kane&Swanson* method but still exhibits a decreasing slope for higher injection densities. The additionally diffusion corrected data ( $\tau_s^{-1} \cdot f_{BGN}$ ) exhibits a nearly constant slope for all injection densities (for visual comparison, straight lines are given, resulting from a fit over the whole injection range).

The resulting apparent  $J_0$  in the fit range of  $\Delta n_{av} = (1 \text{ to } 1.5) \cdot 10^{16} \text{ cm}^{-3}$  is shown in Figure 3.15: The *Kane&Swanson* method leads to significantly lower apparent  $J_0$  (deviation of 26 fA/cm<sup>2</sup> for the p-type materials) on the highly doped than on the lowly doped samples. The method *uniform\_injection* leads to higher apparent  $J_0$  than the

*Kane&Swanson* method. The correction for the influence of  $\tau_{\text{SRH}}$  (*uniform\_injection\_corr*) is only significant for the highly doped *p*-type sample ( $\Delta J_0 = 6 \text{ fA/cm}^2$ ). The difference between the apparent  $J_0$  of the *p*-type samples is reduced to  $21 \text{ fA/cm}^2$  for *uniform\_injection\_corr*. The method *diffusion\_corr* leads to higher apparent  $J_0$  than the other methods. Here, no systematic influence of the dopant concentration is observed and averaging over all samples leads to a consistent mean value of  $J_0 = 205 \text{ fA/cm}^2$  with a standard deviation of  $5 \text{ fA/cm}^2$ .

The results of a point-wise evaluated apparent  $J_0$  of the four methods over injection density together with the results of the simulation applying  $J_0 = 208 \text{ fA/cm}^2$  as input value for each sample are shown in Figure 3.16.

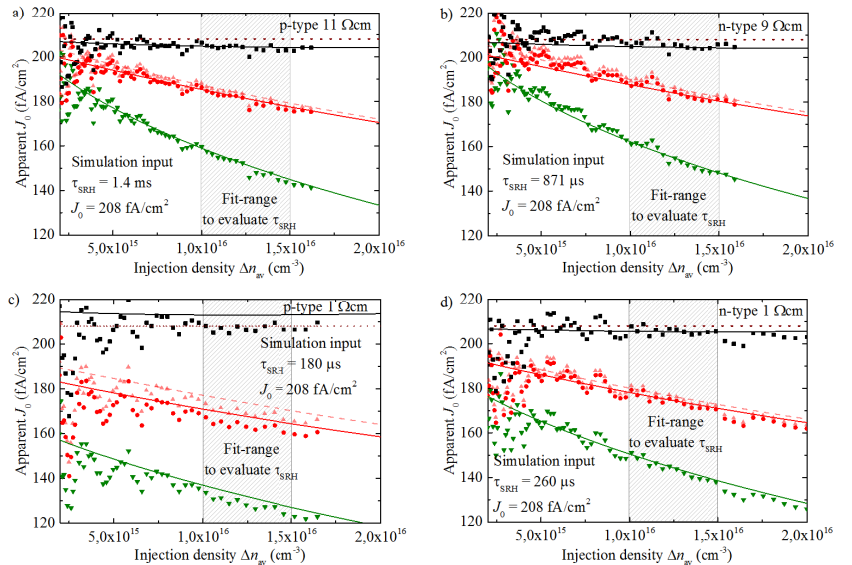


Figure 3.16: Apparent  $J_0$  over average injection density for the different methods. Points show the result of the incremental evaluation (averaged over 3 neighboring points) of the measured data sets. Lines show the same analysis on simulated data sets applying  $J_0 = 208 \text{ fA/cm}^2$  for all samples and a constant  $\tau_{\text{SRH}}$  obtained from the method *diffusion\_corr* in the fit-range for each sample.

- ▼ Kane&Swanson
- ▲ Uniform\_injection
- Uniform\_injection\_corr
- Diffusion\_corrected
- Simulation input

The four graphs show the analyzed apparent  $J_0$  for four different samples of different base-substrate. For each point, the lowest apparent  $J_0$  is given by the *Kane&Swanson* method. The positive slope of  $n_{i,\text{eff}}^2$  over  $\Delta n$  leads to higher apparent  $J_0$  for the method *uniform\_injection\_corr*. The diffusion-correction applied for the method *diffusion\_corr* increases the apparent  $J_0$  further.

For all samples and investigated evaluation methods, the apparent  $J_0$  obtained from simulation and measured data are in very good agreement. For the method *diffusion\_corr*, the measured data deviates less than 2.5 % from the simulated data in the fit range. This is a confirmation that the measurement is accurately described by the simulation and that the discussion based on the simulated data is valid. Note that it is no confirmation that the actual  $J_0$  of the surfaces is 208 fA/cm<sup>2</sup> since the systematic influences of e.g. the optical absorption factor or the measured wafer thickness do not influence the comparison between simulation and measurement significantly. For the good agreement, in the following, the simulation data are discussed which has the great advantage of being comparable with the true value of the input  $J_0$ .

The simulation applies the full Klaassen mobility model, taking into account the scattering at free carriers. As discussed in Chapter 2.1, the consideration of free-carrier scattering at zero net current is questionable. In this case, the influence of the free-carrier scattering is estimated to be minor for the regarded experimental data: the apparent  $J_0$  is reduced by approx. 1 % for the measured samples when free-carrier scattering is turned off in the applied implementation of the carrier mobility. In consequence the Klaassen model can be safely applied for the diffusion correction of the  $J_0$  evaluation.

Both methods that do not account for the finite carrier diffusion in the substrate lead to an apparent  $J_0$  that decreases with increasing injection density. The *Kane&Swanson* method underestimates  $J_0$  up to 35% in the fit range. The BGN correction (*uniform\_injection*) improves the analysis but still leads to an underestimation of  $J_0$  of up to 17 %. In contrast, *diffusion\_corr* leads to apparent  $J_0$  being reasonable independent from the fit range and the substrate: apart from the scattering of the data points towards lower injection densities, there is no significant change of the apparent  $J_0$  over injection density. The deviation between different substrates is below 2.5 %, well below the uncertainties originating in the measurement of the wafer thickness, the optical absorption factor or the assumption that the samples exhibit identical  $J_0$ .

After removal of passivation layer and highly doped region and subsequent passivation, the samples are analyzed in the same QSSPC measurement setup again to evaluate the carrier lifetime in the base substrate. The results are given in Table 3.3 together with the apparent  $J_0$  obtained in the wafer-center of the respective samples.

Table 3.3 Apparent  $J_0$  of different methods. The applied fit range is  $(1 \text{ to } 1.5) \cdot 10^{16} \text{ cm}^{-3}$ .  $\tau_{\text{SRH}}$  extracted from method *diffusion\_corr* and Auger-corrected lifetime  $\tau_{\text{corr}}$  after back etching of the emitter and subsequent passivation (both at  $\Delta n = 10^{15} \text{ cm}^{-3}$ , assumed additional uncertainty of 5 % on the apparent  $J_0$  for the evaluation of  $\tau_{\text{SRH}}$ ).

Base doping, $\rho_0$	<i>Kane&amp;Swanson</i>	<i>uniform_injection</i>	<i>uniform_injection_corr</i>	<i>diffusion_corr</i>	$\tau_{\text{SRH}}$ from $J_0$ -analysis <i>diffusion_corr</i>	$\tau_{\text{corr}}$ after back-etching and passivation
	( $fA/cm^2$ )	( $fA/cm^2$ )	( $fA/cm^2$ )	( $fA/cm^2$ )	(ms)	(ms)
<i>n</i> -type, 1 $\Omega$ cm	144	177	175	208	$0.36 \pm 0.04$	$0.35 \pm 0.03$
<i>n</i> -type, 9 $\Omega$ cm	153	184	182	204	$0.9 \pm 0.1$	$1.0 \pm 0.1$
<i>p</i> -type, 1 $\Omega$ cm	127	168	162	205	$0.17 \pm 0.03$	$0.21 \pm 0.02$
<i>p</i> -type, 11 $\Omega$ cm	153	185	183	207	$1.3 \pm 0.3$	$1.0 \pm 0.1$
Average of all samples and standard deviation	$143 \pm 14$	$178 \pm 10$	$175 \pm 11$	$205 \pm 5$		

The comparison of  $\tau_{\text{SRH}}$  obtained from the method *diffusion\_corr* with the measured  $\tau_{\text{corr}}$  of the passivated base substrate shows good agreement - *diffusion\_corr* can be used to get a good estimation of  $\tau_{\text{SRH}}$  on samples with diffused surfaces as long as the injection behavior of the base lifetime enables the evaluation of  $J_0$  in an applicable fit range.

### 3.6 Impact on $J_0$ -Analysis of Asymmetrical Samples

Another important application is the determination of  $J_0$  of one side of the wafer while the recombination properties of the other side are known or negligible. In this section, a similar simulation study as in Section 3.4 is carried out assuming asymmetrical samples. The higher recombination active surface of which  $J_0$  is to be evaluated is located at the illuminated front side. The applied methods to calculate  $J_{0,\text{front}}$  and  $\tau_{\text{SRH}}$  are listed in Table 3.2 (p. 45). All simulations in this section apply a constant  $\tau_{\text{SRH}} = 500 \mu\text{s}$ .

For the methods assuming uniform injection density in the substrate (*Kane&Swanson*, *uniform\_injection* and *uniform\_injection\_corr*),  $J_{0,\text{front}}$  is calculated by subtracting the known  $J_{0,\text{back}}$  from the measured sum of both sides  $2J_0$  analogously to Eq. (3.3):

$$J_{0,\text{front}} = 2J_0 - J_{0,\text{back}} . \quad (3.17)$$

In the case of a SRV at the rear side  $S_{\text{back}}$  that is independent from injection density,  $J_{0,\text{front}}$  can be calculated directly by  $J_{0,\text{front}} = 2J_0$ .

For a highly doped rear side,  $\tau_{\text{SRH}}$  can be directly evaluated by all methods. If at the rear side a constant  $S_{\text{back}}$  is applied,  $\tau_{\text{SRH}}$  can be calculated for the methods assuming uniform injection density by subtracting the rear-side recombination from the apparent  $\tau_{\text{SRH,App}}$  obtained from the analysis by

$$\frac{1}{\tau_{\text{SRH}}} = \frac{1}{\tau_{\text{SRH,App}}} - \frac{S_{\text{back}}}{W} . \quad (3.18)$$

The analysis method taking into account the finite carrier diffusion coefficient (*general\_solution*) can be applied directly by calculating the effective surface recombination velocity at the rear side from the given  $J_{0,\text{back}}$  by Eq. (2.31) assuming  $\Delta n = \Delta n_{\text{av}}$  and inserting into Eq. (3.2) to evaluate  $J_{0,\text{front}} \cdot \tau_{\text{SRH}}$  follows analogously to the symmetrical case from Eq. (3.16). The method *diffusion\_corr* is not applied on asymmetrical samples since the solutions Eq. (2.41) and Eq. (2.42) are only valid for symmetrical samples or samples with one totally recombination inactive surface.

## Results

In the first simulation, a highly doped rear side is applied characterized by  $J_{0,\text{back}} = 20 \text{ fA/cm}^2$ . This value is assumed to be known in the analysis. At the front-side,  $J_{0,\text{front}} = 100 \text{ fA/cm}^2$  is applied. The extracted apparent  $J_{0,\text{front}}$  and  $\tau_{\text{SRH}}$  of the different methods in dependency of  $\Delta n_{\text{av}}$  are shown in Figure 3.17.

The results are very similar to the ones in the symmetrical case (compare Figure 3.9, p. 46): the *Kane&Swanson* method leads to a strongly decreased apparent  $J_0$  for high injection densities. The method *uniform\_injection* shows a reduced decrease due to the consideration of BGN but overestimates  $J_0$  for low injection densities by up to 7 % due to the influence of the finite  $\tau_{\text{SRH}}$ . The correction for this effect (*uniform\_injection\_corr*) leads to a well reproduced  $J_0$  for low injection densities with still an underestimation of  $J_0$  of up to 10 % in the fit range. The method taking into account the carrier diffusion (*general\_solution*) reproduces  $J_0$  up to  $\Delta n_{\text{av}} = 3 \cdot 10^{16} \text{ cm}^{-3}$  with a deviation below 3 %.

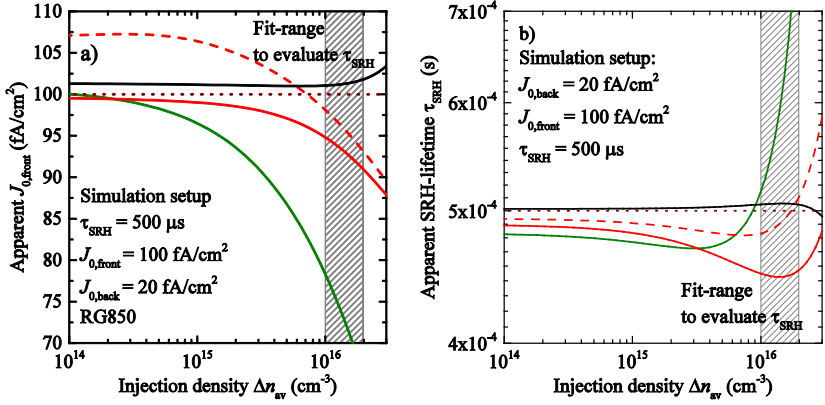


Figure 3.17 a) Apparent  $J_0$  over injection density extracted from simulation data with the different methods (known  $J_{0,back}$ ). The data are simulated with  $p$ -type base doping  $N_A = 1.5 \cdot 10^{15} \text{ cm}^{-3}$  applying  $J_{0,back} = 20 \text{ fA/cm}^2$ ,  $J_{0,front} = 100 \text{ fA/cm}^2$ , an additional recombination in the substrate characterized by  $\tau_{SRH} = 500 \mu s$ , and the spectrum of the red-filter RG850. The fit-range of  $\Delta n = (1 \text{ to } 1.5) \cdot 10^{16} \text{ cm}^{-3}$  is applied for the averaging of  $J_0$  used for the calculation of  $\tau_{SRH}$  and vice versa. b) Calculated  $\tau_{SRH}$ .

The SRH lifetime  $\tau_{SRH}$  is reproduced most accurately by the method *general\_solution* with a deviation below 5%. The other methods differ strongly depending on the applied injection range. The findings are very similar to the symmetrical case and the reader finds a discussion of the influences of the different methods there (see p. 46).

Experimentally, it is interesting to evaluate  $J_0$  from asymmetrical samples of which one side exhibits a non-diffused surface (e.g. precursors of solar cells before metallization, so-called *implied- $V_{OC}$  samples*, or samples doped by single-side doping techniques). For the analysis method *general\_solution* one can consider arbitrary cases of known surface recombination velocities at the rear side of the wafer  $S_{back}(\Delta n)$  as long as the injection dependency is known. Here we consider the case, where the rear side of the wafer is a non-diffused passivated surface described by a constant surface recombination velocity  $S_{back} = 10 \text{ cm/s}$ . The simulation applies the red-filter RG850 and a constant  $\tau_{SRH} = 500 \mu s$ . The apparent  $J_0$  and  $\tau_{SRH}$  in dependency of  $\Delta n$  are shown in Figure 3.18. Additionally an effective  $J_{0,back}$  of the rear side is shown, calculated from  $S_{back}$  and  $\Delta n_{av}$  by Eq. (2.31).

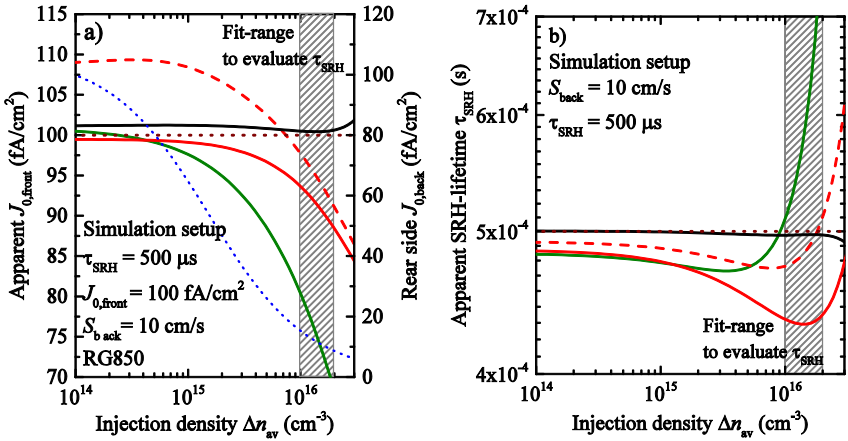


Figure 3.18 a) Apparent  $J_0$  over injection density  $\Delta n_{av}$  extracted from simulation data with the different methods. The data are simulated with  $p$ -type base doping of concentration  $N_A = 1.5 \cdot 10^{15} \text{ cm}^{-3}$ ,  $S_{back} = 10 \text{ cm/s}$ ,  $J_{0,front} = 100 \text{ fA/cm}^2$ , an additional recombination in the substrate defined by  $\tau_{SRH} = 500 \mu\text{s}$ , and the spectrum of the red-filter RG850. The fit-range of  $\Delta n = (1 \text{ to } 1.5) \cdot 10^{16} \text{ cm}^{-3}$  is applied for the averaging of  $J_0$  used for the calculation of  $\tau_{SRH}$  and vice versa. b) Calculated  $\tau_{SRH}$ .

The results are very similar to the results with diffused rear side (Figure 3.17). The differences originate in the different injection-dependent behavior of the rear side (compare  $J_{0,back}$  resulting from  $S_{back}$ ): while at low  $\Delta n$ ,  $J_{0,back}$  is high and the sample is very similar to a symmetrical sample, the effective  $J_{0,back}$  decreases strongly for increasing injection density. This results in a behavior of an asymmetrical sample with low surface recombination at the rear side with an effective  $J_{0,back}$  in the fit range of approx. 10 fA/cm<sup>2</sup>. Thus, the methods assuming uniform injection density (*Kane&Swanson*, *uniform\_injection* and *uniform\_injection\_corr*) underestimate  $J_{0,front}$  in this range even more than in the case of  $J_{0,back} = 20 \text{ fA/cm}^2$ . Additionally it is observed that *uniform\_injection* overestimates  $J_{0,front}$  at low injection densities up to 10 %. This originates in the non-diffused rear side with its similar injection dependent recombination to a constant  $\tau_{SRH}$ : the influence of a constant additional recombination on the resulting  $J_0$  increases. In contrast, the method *general\_solution* reproduces  $J_{0,front}$  with a deviation of 0.5 % in the fit-range.

Consequently, the  $\tau_{SRH}$ -data are reproduced well by *general\_solution*. The other methods differ very similar to the case of an input value of  $J_{0,back} = 20 \text{ fA/cm}^2$  (see Figure 3.17) and are not discussed therefore.

The behavior of the effective  $J_{0,\text{back}}$  over  $\Delta n$  shows the necessity of applying the general solution Eq. (3.2) instead of approximations for  $S_{\text{back}} = 0$  or  $S_{\text{back}} = S_{\text{front}}$ : It covers the range of  $S_{\text{back}} \approx S_{\text{front}}$  at  $\Delta n_{\text{av}} = 10^{14} \text{ cm}^{-3}$  to  $S_{\text{back}} < 0.2 S_{\text{front}}$  at  $\Delta n_{\text{av}} = 10^{16} \text{ cm}^{-3}$  – thus the recombination shifts from being equally distributed on both sides at low injection levels to a near negligible rear side recombination at high injection levels. This shows also that evaluating  $J_0$  of such samples, high-injection conditions are beneficial to suppress the recombination at the non-diffused surface of the base substrate and therefore the requirement of a method that leads to accurate results under such conditions.

### 3.7 Experimental Comparison on Asymmetrical Lifetime Samples

For an experimental evaluation of the  $J_0$ -analysis on highly doped asymmetrical samples (e.g. solar cells at a stage of production before metallization), asymmetrical lifetime samples and corresponding symmetrical lifetime samples are produced. The flow chart of the process sequence is depicted in Figure 3.19. The symmetrical lifetime samples to evaluate  $J_0$  of the textured side of the symmetrical samples are made of  $n$ -type Cz-silicon with a resistivity of  $\rho_0 = 5.8 \text{ } \Omega\text{cm}$  (after thermal donor elimination) and a final thickness of  $W \approx 180 \text{ } \mu\text{m}$ . The asymmetrical samples are produced by the FeDiO process [81] where a thick thermal oxide serves as protection layer in the alkaline texturization bath, as diffusion barrier during  $\text{POCl}_3$  diffusion and finally as passivation layer for the rear side. For the substrate,  $p$ -type Cz-Si with a base resistivity of  $\rho_0 = 1.7 \text{ } \Omega\text{cm}$  (after thermal donor elimination) and a final thickness of  $W \approx 165 \text{ mm}$  is used. Two different  $\text{POCl}_3$  diffusion processes are applied denoted as A and B. After contact firing the wafers are analyzed in generalized mode in the Sinton WCT120 QSSPC measurement setup with and without the application of the red-filter RG850.

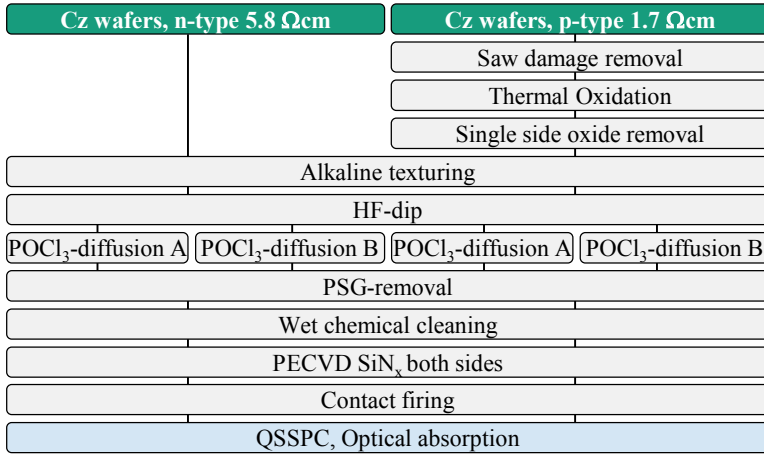


Figure 3.19: Flow chart for the fabrication of the symmetrical (left) and asymmetrical (right) lifetime samples to evaluate the apparent  $J_0$ . The samples were taken from a solar cell experiment of which the results are published by Werner et al. [5].

The apparent  $J_0$  and  $\tau_{SRH}$  of the symmetrical samples is then used as input parameters for the same simulation as in the previous chapters for the symmetrical lifetime samples. In an iterative step, the input  $J_0$  for the simulations is adapted to match the outcome of the analysis on the measured data sets to obtain a consistent simulation with the measurement data on the symmetrical references. Thus the obtained  $J_0$  represents the value which leads to consistency between measurement and simulation and is free from influences of the applied analysis method.

For the asymmetrical lifetime samples, this adapted  $J_0$  is used as input  $J_{0,front}$  for the simulations. At the rear side, a constant  $S_{rear} = 20$  cm/s is assumed in both, the simulations and the data analysis, which is assumed to be an upper limit of the SRV of the given surface.

### Results for the symmetrical samples

The measured apparent  $J_0$  of two symmetrical samples for diffusion A and B over injection density are well described by the simulated data, comparable to Figure 3.16. The best agreement of the simulated and measured apparent  $J_0$  in the fit range of  $\Delta n_{av} = (1 \text{ to } 1.5) \cdot 10^{16} \text{ cm}^{-3}$  is found with an input value of  $J_0 = 78 \text{ fA/cm}^2$  for diffusion A and  $J_0 = 214 \text{ fA/cm}^2$  for diffusion B. An experimental uncertainty of 5 % can be assumed for both values.

## Results for the asymmetrical samples

The apparent  $J_0$  obtained from the QSSPC samples on asymmetrical lifetime samples is shown in Figure 3.20. The data are analyzed and simulated applying the red-filter RG850. The results are listed in Table 3.4.

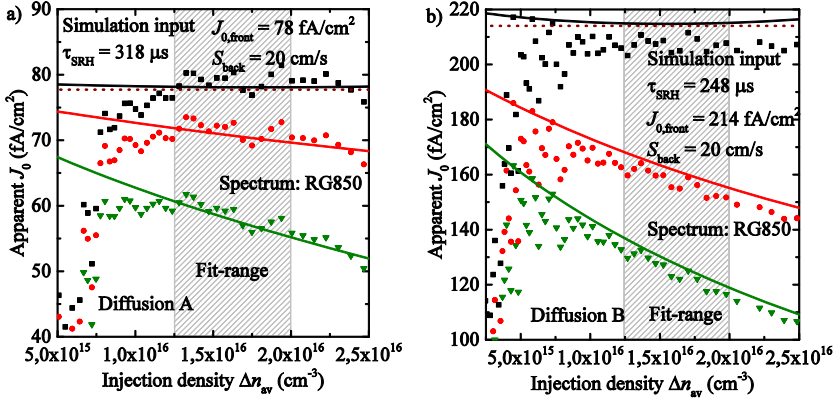


Figure 3.20: Apparent  $J_0$  of the asymmetrical lifetime samples over average injection density for the different methods applying the red-filter RG850. Points show the result of the incremental evaluation (averaged over 3 neighboring points) of the measured data sets. Lines show the same analysis on simulated data sets applying a constant  $\tau_{\text{SRH}}$  obtained from the method `general_solution` in the fit-range of the measurement and the analyzed  $J_0$  of the symmetrical samples.

- ▼ Kane&Swanson
- Uniform\_injection\_corr
- General\_solution
- Simulation input

The apparent  $J_0$  obtained from all analysis methods show a strong decrease on the measured data sets towards low  $\Delta n_{\text{av}}$  below  $1.2 \cdot 10^{16} \text{ cm}^{-3}$ . This is not the case for the analysis of the simulation data which is simulated under the assumption of an injection independent base lifetime  $\tau_{\text{SRH}}$  and rear surface recombination velocity.

For diffusion A, the analysis with the red filter (Figure 3.20, a) and the method `general_solution` reaches a plateau of  $J_0 = (79 \pm 1) \text{ fA/cm}^2$  (average and standard deviation over the fit range) at higher injection densities very well in agreement with the apparent  $J_0$  obtained from the analysis and simulation of the symmetrical lifetime sample of  $J_0 = 78 \text{ fA/cm}^2$ . Therefore the fit range for all asymmetrical samples is chosen to  $\Delta n_{\text{av}} = (1.25 \text{ to } 2) \cdot 10^{16} \text{ cm}^{-3}$ . The methods assuming a uniform injection density over the wafer (`Kane&Swanson` and `uniform_injection_corr`) show an increased underestimation of  $J_0$  for higher injection densities - in agreement with the simulations and attributed to the same effects as for the symmetrical lifetime samples (see Section 3.5).

For diffusion B analyzed with a red-filter (Figure 3.20, b), the finding is quite similar: the method *general\_solution* leads to a plateau of the apparent  $J_0$  for injection densities above  $\Delta n_{av} = 10^{16} \text{ cm}^{-3}$  at  $J_0 = (207 \pm 3) \text{ fA/cm}^2$  in agreement within the measurement uncertainties with the value obtained from the analysis and simulation of the symmetrical lifetime probes of  $214 \text{ fA/cm}^2$ . The methods assuming uniform injection show a decreased  $J_0$  well before the plateau is reached and are not suited for the analysis of this measurement therefore. The stronger increase for the sample exhibiting higher  $J_0$  can be directly attributed to the enhanced diffusion influence compared to the sample with a lower recombination active front side.

Figure 3.6 and Figure 3.7 indicate that for asymmetrical samples, the application of the flasher without red-filter together with the assumption of a uniform injection density could be a good choice. The apparent  $J_0$  obtained from the QSSPC samples on the asymmetrical lifetime samples applying the flasher in measurement and its spectrum in the simulation is shown in Figure 3.21. The results are listed in Table 3.4.

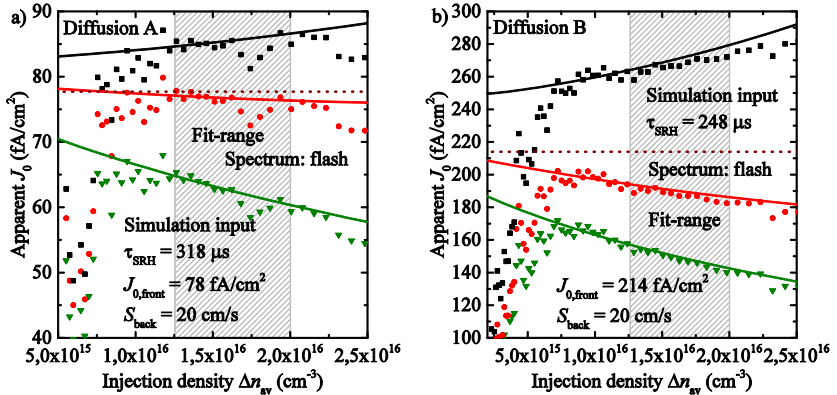


Figure 3.21: Apparent  $J_0$  of the asymmetrical lifetime samples over average injection density for the different methods applying the flasher spectrum. Points show the result of the incremental evaluation (averaged over 3 neighboring points) of the measured data sets. Lines show the same analysis on simulated data sets applying a constant  $\tau_{SRH}$  obtained from the method *general\_solution* in the fit range of the measurement and the analyzed  $J_0$  of the symmetrical samples.

- ▼ Kane&Swanson
- Uniform\_injection\_corr
- General\_solution
- ⋯ Simulation input

The incremental evaluation of  $J_0$  on the measured data-sets without red-filter leads to a different result: the method assuming a homogeneous generation profile (*general\_solution*) leads to an increased apparent  $J_0$  for increasing  $\Delta n$ . This finding confirms the necessity of a red filter to reach a sufficient uniform generation profile for the application of the diffusion corrected analysis.

For diffusion A (Figure 3.21, a), the assumption of a uniform injection density (*uniform\_injection\_corr*) leads to a plateau of the apparent  $J_0$  at  $(76 \pm 1)$  fA/cm<sup>2</sup>.

The analysis without red-filter for diffusion B (Figure 3.21, b) shows a different behavior: Although the assumption of a homogeneous generation profile (*general\_solution*) leads to an increasing apparent  $J_0$  with increasing  $\Delta n$  the assumption of a uniform injection density leads to a decreased apparent  $J_0$  with increasing  $\Delta n$ . In this case the method *uniform\_injection\_corr* leads to  $J_0 = (188 \pm 3)$  fA/cm<sup>2</sup> which is 12 % lower than the assumed value of 214 fA/cm<sup>2</sup>. Since the data are in very good agreement with the simulation, the origin of the deviation is not assumed to be measurement uncertainties but a decreased  $\Delta n$  towards the front surface which is not accounted for in the method *uniform\_injection\_corr*. This indicates that even though the assumption of a uniform injection density in the substrate is more valid without red-filter, for high  $J_0$  the application of a red-filter and the assumption of a homogeneous generation profile (*general\_solution*) lead to more reliable results.

*Table 3.4 Apparent  $J_0$  of different methods (in fA/cm<sup>2</sup>) obtained from the analysis of the symmetrical samples (left) and asymmetrical samples (right). The applied fit range is  $(1 - 1.5) \cdot 10^{16}$  cm<sup>-3</sup> for the symmetrical and  $(1.25 - 2) \cdot 10^{16}$  cm<sup>-3</sup> for the asymmetrical samples. The uncertainty represents the standard deviation of the measurement points over the fit range.*

Diffusion	Simulation input	Symmetrical sample ( <i>diffusion_corr</i> )	Optical setup	Kane&S wanson	Uniform_injection_corr	General_solution
A	78	$77 \pm 1$	RG850	$59 \pm 2$	$72 \pm 1$	$79 \pm 1$
			flasher	$63 \pm 2$	$76 \pm 1$	$84 \pm 2$
B	214	$210 \pm 2$	RG850	$125 \pm 5$	$158 \pm 4$	$207 \pm 3$
			flasher	$148 \pm 5$	$188 \pm 3$	$267 \pm 3$

Comparing the average values obtained in the fit-range (Table 3.4) one finds that the application of a red-filter together with the method accounting for the finite carrier diffusion (*general\_solution*) at high injection densities opens the possibility of evaluating  $J_0$  on single-side diffused wafers: for diffusion A one finds an apparent  $J_0 = (79 \pm 1)$  fA/cm<sup>2</sup> for the asymmetrical sample in agreement with  $J_0 = 78$  fA/cm<sup>2</sup> obtained from the simulation of the symmetrical sample. For diffusion B one finds for the asymmetrical sample  $J_0 = (207 \pm 3)$  fA/cm<sup>2</sup> while the simulation of the symmetrical sample gives  $J_0 = 214$  fA/cm<sup>2</sup>. Note that the uncertainties in this case give only the standard deviation in the fit-range and do not reflect the measurement uncertainties which are estimated to 5 % of  $J_0$ .

### 3.8 Conclusion

In this chapter, different methods for the extraction of the recombination parameter of diffused surfaces from lifetime measurements are analyzed on the example of QSSPC measurements. One result is a new analysis method taking into account the effect of band-gap narrowing due to injected carriers in the base substrate (*uniform\_injection*). In cooperation with R. A. Sinton [15] this method has been implemented into the Sinton lifetime tester software and thus already in widespread use in the photovoltaic community. On the one hand, it leads to an apparent  $J_0$  that is independent from the substrate doping; on the other hand, it enables the application of the obtained values in modern simulation tools that account for band-gap narrowing. However, the implemented version of the method is, in contrast to the *Kane&Swanson* method, not independent from a constant  $\tau_{\text{SRH}}$  in the base substrate. An iterative correction for this effect is proposed (*uniform\_injection\_corr*) that leads to the same robustness of the new method as the implemented standard method (*Kane&Swanson*).

Another result is that for higher injection densities, the finite diffusion coefficient of the injected carriers and thus a non-constant injection density over the wafer depth has to be taken into account. Methods for symmetrical and asymmetrical lifetime samples are proposed, based on the assumption of uniform carrier generation and being robust against a constant  $\tau_{\text{SRH}}$  value due to iteration (*diffusion\_corr* and *general\_solution*). It is shown that the method solves the often observed problem of decreasing apparent  $J_0$  for increasing injection densities above  $10^{16} \text{ cm}^{-3}$  – that was previously leading to a high uncertainty of the actual  $J_0$  obtained from the analysis. The method shows very good agreement with the applied values in simulation data and an increased independency of the obtained  $J_0$  from the applied fit-range and base substrate doping. It is suited to extract  $J_0$  with the slope method for symmetrical and asymmetrical samples even when the latter feature one non-diffused, passivated surface.

For all simulations carried out in this work and applying a red-filter, the methods accounting for both, BGN in the substrate and finite carrier diffusion (here denoted as *diffusion\_corr* or *general\_solution*), lead to the best reproduction of the input  $J_0$  over a broad range of injection density. Therefore it is recommended to apply this method for the analysis of QSSPC data together with the application of a red-filter for excitation in all cases.

Furthermore the new methods lead to a strongly improved reproduction of the applied  $\tau_{\text{SRH}}$ . On the one hand, evaluating  $J_0$  at higher injection densities with higher accuracy leads to the possible application of base substrates with lower  $\tau_{\text{SRH}}$  or even injection dependent  $\tau_{\text{SRH}}$ , e.g. influenced by boron-oxygen defect recombination. On the other hand the consideration of the carrier diffusion leads to a higher accuracy for the subtraction of  $J_0$  from the measured total recombination, even for comparable high  $J_0$ .

The methods *uniform\_injection\_corr* and *diffusion\_corr* have been implemented in a spread-sheet calculator and made available for download at the Sinton Instruments Inc. website and are thus easily accessible for users.

## 4 Analytical Modeling of locally contacted Solar Cells

Central results of this investigation are published in Ref. [85]. The numerical simulations are carried out in the scope of the PhD thesis of Marc Rüdiger [27] whereas all new analytical expressions and results are part of this work. The injection independent model, taken as starting point of the investigation is introduced in Section 2.5. The injection dependent approach is introduced in Section 4.2. In Section 4.3 the consideration of high-level injection effects is given and the numerical model for the comparison is briefly explained in Section 4.4. Finally the results are compared in Section 4.5.

### 4.1 Introduction

For solar cells with locally contacted rear surface, analytical modeling is a simple way to optimize required parameters, such as the metallization fraction and the size and distribution of the local contacts as well as to predict the influence of material and device properties on the cell parameters. Analytical modeling represents a fast and, once implemented, easy accessible approach by omitting time consuming, complex, multidimensional numerical simulations. One widely used recently published model ([10], see Chapter 2.5) is based on the two-diode model and applies injection independent material parameters, valid at low level injection conditions. However, devices exhibiting well passivated surfaces and high bulk carrier lifetimes may reach intermediate or even high injection level conditions under one sun illumination at open-circuit (OC) and maximum power point (MPP) [86]. In this chapter an adaption of the analytical model for injection dependent modeling as well as first adjustments of the analytical model to account for deviations from low level injection conditions are presented. The validity of the adjustments is investigated by comparison of the results to three dimensional numerical simulations.

### 4.2 Injection Dependent Model

The model from Ref. [10] applies the two diode equation (2.46). The I-V-curve is obtained from a sweep of the external voltage  $V_{\text{ext}}$ . Eq. (2.46) can be written alternatively in dependence of the junction voltage  $V_{\text{junction}}$

$$J = -J_{\text{col}} + J_{01} \left[ \exp\left\{\frac{V_{\text{junction}}}{V_{\text{th}}}\right\} - 1 \right] + J_{02} \left[ \exp\left\{\frac{V_{\text{junction}}}{2V_{\text{th}}}\right\} - 1 \right] + \frac{V_{\text{junction}}}{R_p}, \quad (4.1)$$

where the external voltage of the device is given by  $V_{\text{ext}} = V_{\text{junction}} + J R_s$  ( $J < 0$ ).

To describe intermediate or high injection levels, the injection dependence of the parameters in Eq. (4.1) has to be considered to determine ( $J_{\text{mpp}}$ ,  $V_{\text{mpp}}$ ) and  $V_{\text{OC}}$ . From

Eq. (2.28) follows the relation between the injection density  $\Delta n_{\text{junction}}$  at the edge of the junction with the voltage drop  $V_{\text{junction}}$  across it

$$V_{\text{junction}} = V_{\text{th}} \ln \left\{ \frac{\Delta n_{\text{junction}} (\Delta n_{\text{junction}} + N_{\text{dop}})}{n_{i,\text{eff}}^2} + 1 \right\}. \quad (4.2)$$

Eq. (4.1) and (4.2) allow for calculating the I-V-curve of the device by a sweep of  $\Delta n_{\text{junction}}$  and thus to apply  $\Delta n_{\text{junction}}$  directly as input parameter. The main influences of the injection density are on  $R_S$  and  $J_{01}$  of which the equations are adapted in the following.

### Series resistance

The series resistance  $R_S = R_{S,\text{front}} + R_{S,\text{base,light}}$  is composed by the series resistance contribution of the front contacts and the emitter  $R_{S,\text{front}}$  and by the contribution of the base  $R_{S,\text{base,light}}$ , which also includes the spreading resistance due to the local contacts at the rear side. The first term is nearly injection independent due to the high dopant concentrations present in the emitter, whereas the base resistance  $R_{S,\text{base,light}}$  is affected by the carrier concentration and mobility in the base.

The injection independent model applies the specific resistivity of the material without injection

$$\rho_0 = \frac{1}{q\mu_{\text{maj}}N_{\text{dop}}}, \quad (4.3)$$

with  $\mu_{\text{maj}}$  the mobility for the majority carriers.

For devices with low recombination and low base dopant concentration the injected carriers lead to a significantly enhanced specific conductivity [86] and therefore to reduced resistance losses. In a first approach, an injection dependent specific resistivity is introduced accounting for the injected majority carriers being

$$\rho_{\text{light}} = \frac{1}{q\mu_{\text{maj}}(N_{\text{dop}} + \Delta n_{\text{junction}})}, \quad (4.4)$$

by scaling the resistance per contact in the analytical model with the factor  $\rho_{\text{light}} / \rho_0$ .

### Base recombination

For the important case of Cz-grown *p*-type base Si-material, the stabilized electron lifetime at an injection density of  $\Delta n = 0.1 \cdot N_A$  for the SRH recombination at boron-oxygen defects in silicon of interstitial oxygen concentration  $[O_i]$  and boron concentration  $N_A$  is given in Eq. (2.17). This is directly applied in the injection independent model to calculate the bulk lifetime  $\tau_{\text{bulk}}^{-1} = \tau_{\text{SRH}}^{-1} + \tau_{\text{intr}}^{-1}$ . The intrinsic lifetime is calculated assuming an injection density of  $5 \cdot 10^{14} \text{ cm}^{-3}$ .

In the injection dependent consideration, the SRH recombination is calculated by Eq. (2.18). To evaluate the injection density in the bulk, we roughly estimate the injection density in a first approach by a self-consistent iteration

$$\Delta n(x) = \Delta n_{\text{junction}} \exp\left(-\frac{x}{L_{\text{eff}}(\Delta n_{\text{rear}}, \Delta n_{\text{bulk}})}\right), \quad (4.5)$$

applying Eq. (2.49),  $\Delta n_{\text{rear}} = \Delta n(W)$  and

$$\Delta n_{\text{bulk}} = \frac{1}{W} \int_0^W \Delta n(x) dx = \frac{L_{\text{eff}}}{W} (\Delta n_{\text{junction}} - \Delta n_{\text{rear}}). \quad (4.6)$$

This approach only holds at OC conditions and should be replaced by an expression for arbitrary working points for devices that leave the low-level injection regime significantly already at MPP. However, at OC the injection density is highest and injection effects are reduced at MPP so that the error of this rough estimation should be small for most devices. To evaluate Eq. (4.5) the minority diffusion coefficient  $D_{\text{min}}$  is replaced by the ambipolar diffusion coefficient  $D_{\text{amb}}$  in Eq. (2.24) and the rear side passivation is calculated by the injection dependent SRH formalism as described in the following.

### Recombination at the rear side

For the rear side of the device with  $p$ -type base-doping, parameterizations of the LLI surface recombination velocities (SRV) for the metallized area  $s_{\text{met}}$  as well as for the passivated surface  $s_{\text{pass}}$  are assumed, representing literature values for laser fired contacts [87]:

$$s_{n,\text{met}}(N_A) = S_0 + \alpha \exp[\beta (N_A + N_0)]$$

$$s_{p,\text{met}} = 10^7 \frac{\text{cm}}{\text{s}}, \quad (4.7)$$

with  $S_0 = -900 \text{ cm/s}$ ,  $\alpha = 22.1 \text{ cm/s}$ ,  $\beta = 1.29 \cdot 10^{-16} \text{ cm}^3$  and  $N_0 = 3.4 \cdot 10^{16} \text{ cm}^{-3}$  and for thermal oxide passivation [88]

$$s_{n,\text{pass}}(N_A) = s_{p,\text{pass}}(N_A) = 23 \cdot \left(\frac{N_A}{1.5 \cdot 10^{15} \text{ cm}^{-3}}\right)^{0.41} \frac{\text{cm}}{\text{s}}. \quad (4.8)$$

The subscript  $n$ ,  $p$  labels the recombination velocity for electrons or holes, respectively.

The classical analytical model applies the effective SRV Eq. (2.50) for LLI conditions by applying  $S_{\text{met}} = s_{n,\text{met}}$  and  $S_{\text{pass}} = s_{n,\text{pass}}$  and the series resistance contribution of the base and rear side  $R_{S,\text{back}}$  Eq. (2.51), and the minority carrier diffusion constant  $D_{\text{min}}$ .

In the injection dependent case we apply Eq. (2.19) for the recombination at a non-diffused back surface,  $S_{\text{met}}$  and  $S_{\text{pass}}$ , assuming one sort of trap mechanism in the middle of the band gap by  $p_1 = n_1 = n_{i,\text{eff}}$ . These values are applied for the calculation of  $S_{\text{eff}}$  in (2.50) and subsequently for the calculation of  $L_{\text{eff}}$  by Eq. (2.49). We calculate an effective base dark saturation current at any working point of the solar cell in adaption of Eq. (2.48)

$$J_{0b,\text{eff}} = \frac{q D_{\text{amb}} n_i^2}{(N_{\text{dop}} + \Delta n_{\text{junction}}) \cdot L_{\text{eff}}(\Delta n_{\text{rear}}, \Delta n_{\text{bulk}})} \quad (4.9)$$

which is then inserted in Eq. (4.1) via  $J_{01} = J_{0b,\text{eff}} + J_{0e}$ .

### 4.3 High-Level Injection Effects

Apart from replacing  $N_{\text{dop}}$  by  $(N_{\text{dop}} + \Delta n)$  and applying injection dependent parameterizations, further effects have to be considered when leaving the low-level injection regime.

We consider two effects which become of importance already at intermediate injection levels and reduce the external voltage of the device: Firstly, the different mobilities of electrons and holes may result in an electric field within the wafer to maintain charge neutrality by assisting the motion of holes. On the one hand, this results in an adaption of the effective diffusion coefficient when quasi neutrality is applied as is the case in the analytical model, and which is already considered by the application of the ambipolar diffusion coefficient. On the other hand, the impact on the device output is a drop of the electrostatic potential across the base, the *Dember voltage* [35]

$$\Delta V_{\text{demb}} = - \frac{\mu_n - \mu_p}{\mu_n + \mu_p} \frac{k_B T}{q} \ln \left( \frac{\Delta n_{\text{cont}} \cdot (\mu_n + \mu_p) + \mu_p N_A}{\Delta n_{\text{junction}} \cdot (\mu_n + \mu_p) + \mu_p N_A} \right), \quad (4.10)$$

with the carrier mobilities  $\mu_n$ ,  $\mu_p$  and the injection density at the rear contact  $\Delta n_{\text{cont}}$ . Secondly, the difference in chemical potential of the majority carriers at the junction and the metal surface due to their different concentrations at these positions [35] reads

$$\Delta V_X = \frac{k_B T}{q} \ln \left( \frac{\Delta n_{\text{junction}} + N_A}{\Delta n_{\text{cont}} + N_A} \right). \quad (4.11)$$

To evaluate these effects, in a first approach, the injection density at the metal interface is estimated by

$$\Delta n_{\text{cont}} = \Delta n_{\text{junction}} \exp \left( - \frac{W}{L_{\text{eff}} (S_{\text{eff}} = S_{\text{met}})} \right), \quad (4.12)$$

omitting the part of the device with passivated rear side by evaluating  $L_{\text{eff}}$  assuming  $S_{\text{eff}} = S_{\text{met}}$  but applying the parameters  $\Delta n_{\text{rear}}$  and  $\Delta n_{\text{bulk}}$  from the iteration applied to calculate  $\tau_{\text{bulk}}$ ,  $D_{\text{amb}}$ ,  $S_{\text{pass}}$  and  $S_{\text{met}}$ , described above. Again this estimation is, like Eq. (4.5), not accurate in non-OC conditions and should be replaced by an accurate description for modeling devices that leave the low-level injection regime significantly even at MPP.

#### 4.4 Comparison to Numerical Simulations

To validate the analytical model we perform a comparison with the three dimensional device simulator Sentaurus Device [20] using identical models for

- Auger recombination: Dzewior and Schmid as stated in Ref. [31]
- Carrier mobility: Klaassen model [20, 32, 33]
- Band gap narrowing: Schenk model [14]
- Intrinsic carrier concentration after Eq. (2.6)
- Injection dependent SRH recombination at boron-oxygen complexes after Eq. (2.18)
- Injection dependent SRH recombination at the rear interfaces after Eq. (4.7), (4.8) and (2.19).

The simulated structure is a rear surface passivated  $p$ -type Si solar cell with local point contacts. We investigate three different bulk boron doping densities  $N_A$  and point distances  $L_P$  (square pattern) between 200 and 1000  $\mu\text{m}$  at a wafer thickness of  $W = 170 \mu\text{m}$ . In the numerical model, the contact points are of quadratic shape with a side length of 80  $\mu\text{m}$ . The analytical model applies circular contacts of the same area, leading to a radius of  $r = 45.1 \mu\text{m}$ .

To test the model for high injection densities, the simulated device shows a nearly ideal front side, including non-recombination active full area transparent metal contact, which translates into the analytical model by neglecting optical shading ( $M = 0$ ) as well as any series resistance contribution from the front side. The shallow Gaussian emitter doping profile with a surface concentration of  $10^{17} \text{cm}^{-3}$  and a profile depth of 1  $\mu\text{m}$ , used in the numerical simulation, yields by Eq. (2.32) an analytically modelled dark saturation current density of 3  $\text{fA/cm}^2$ , applied in the analytical model. Thus, the recombination and series resistance are highly dominated by contributions from the rear surface and the bulk. Further details for the numerical model can be found in Ref. [86] [27]. In the numerical model, the front side shows very good light trapping with upright pyramids and a high back reflection. The cumulated generation profile obtained by the numerical raytracer is reproduced for the analytical model using the parameterization Eq. (2.53).

Two different material qualities have been considered: FZ-Si exhibiting no SRH recombination in the bulk and Cz-Si material with a high interstitial oxygen contamination of  $[O_i] = 10^{18} \text{ cm}^{-3}$ , leading to an injection dependent bulk carrier lifetime (compare Figure 3.10). The first choice (FZ-Si) represents an extreme case where nearly all series resistance contributions and recombination are dominated by the rear side of the device. It is chosen to emphasize the effects of high injection density in the substrate and thus to give a test of the injection dependent modeling and high-level injection corrections. The second choice (Cz-Si) gives a more realistic view to investigate the application of injection dependent model in practice.

$J_{02}$  is set to  $J_{02} = 0$ , thus the results regarded here are effectively of a one-diode model. Furthermore, the influence of  $R_p$  is neglected by the choice of  $R_p = 1 \text{ M}\Omega\text{cm}^2$  in the analytical model.

## 4.5 Results

### Optical generation

The cumulated generation profile obtained by the numerical raytracer together with the fit of the parameterization Eq (2.53) for the application in the analytical model are shown in Figure 4.1.

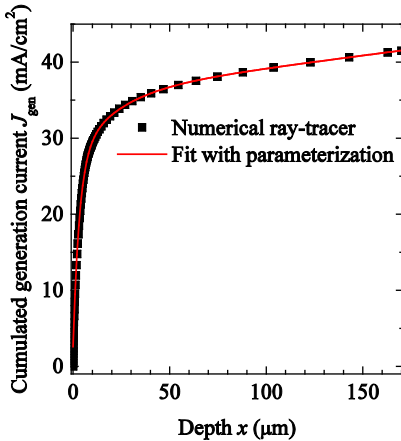


Table 4.1 Obtained parameters for the fit of Eq (2.53) to the cumulated generation current density from the raytracer.

Parameter	Value
$J_{\text{gen,front}}$	2.6 mA/cm <sup>2</sup>
$J_{\text{gen,exp1}}$	24.5 mA/cm <sup>2</sup>
$J_{\text{gen,exp2}}$	8.8 mA/cm <sup>2</sup>
$J_{\text{gen,hom}}$	5.6 mA/cm <sup>2</sup>
$L_1$	3.3 $\mu\text{m}$
$L_2$	21.6 $\mu\text{m}$

Figure 4.1 Cumulated generation profile obtained by the numerical raytracer (symbols) and the fit for the analytical model (line), Eq. (2.53), over depth.

The total generation current density obtained by the numerical raytracer is  $J_{\text{gen}}(W) = 41.50 \text{ mA/cm}^2$ . The fit of the parameterization shows excellent agreement for

the cumulated generation profiles leading to  $J_{\text{gen}}(W) = 41.53 \text{ mA/cm}^2$ . The applied fit parameters are given in Table 4.1.

### Diode characteristics

The diode characteristics for the FZ-Si devices with contact distance of  $L_p = 1 \text{ mm}$ , base substrates characterized by  $\rho_0 = 0.5 \Omega\text{cm}$  and by  $\rho_0 = 5 \Omega\text{cm}$  are shown in Figure 4.2.

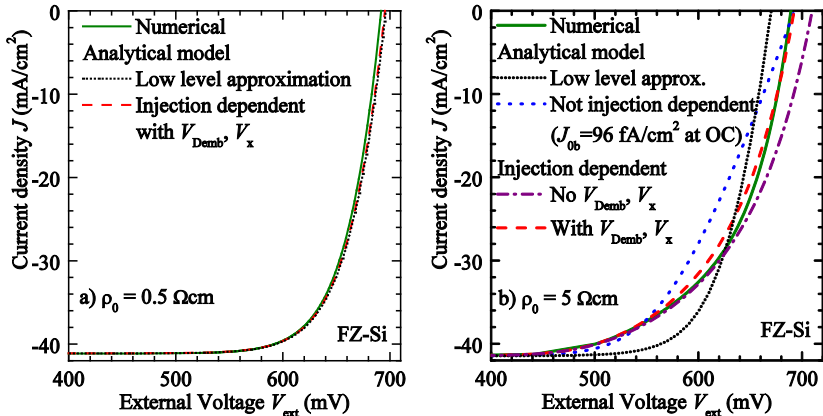


Figure 4.2 I-V-curves for the FZ-Si devices with a contact distance of  $L_p = 1000 \mu\text{m}$ . For a)  $\rho_0 = 0.5 \Omega\text{cm}$  and b)  $\rho_0 = 5 \Omega\text{cm}$ . The numerical data are compared to the analytical model assuming low-level injection conditions and injection dependent modeling. In b) two curves are shown additionally: injection independent modeling assuming a  $J_{0b}$  that reproduces  $V_{OC}$  of the numerical result and injection dependent modeling neglecting the high injection effects of the Dember-voltage and the chemical potential of the carriers at the contacts. Note that no influence of  $J_{02}$  and  $R_p$  is assumed.

While the diode characteristics are already well reproduced by the LLI-approximation for a) highly doped material, deviation of the low level approximation for b) lowly doped material is observed. The reason is, on the one hand, the overestimated series resistance due to the neglected contribution of the injected carriers to the conductivity of the substrate. On the other hand, the recombination at OC is overestimated. Consequently, the shape of the diode characteristics cannot be explained with injection independent modeling, even when assuming a  $J_{0b}$  to provide the  $V_{OC}$  of the numerical calculation (blue dotted line). The first implementations of injection dependent modeling given in Section 4.1 improve the agreement with the numerical data but lead to strong overestimation of  $V_{OC}$ . This deviation is greatly reduced by considering the high level injection corrections  $V_{\text{Dember}}$  and  $V_x$  given in Section 4.3. The incorporation of these high-level injection effects leads to an underestimation of the FF (The red curve shows still a decreased absolute current density at the same voltage in the range

---

of the expected MPP). This may occur due to the rough estimation of  $\Delta n$  at the rear side and at the contacts. However, detailed analysis of the injection density obtained by numerical simulations of this device (shown in Ref. [27]) show a strong spatial variation and point out that the series resistance of the device is strongly affected by the reduced injection density directly above the contacts. Thus the assumption of a uniform injection density at specific areas of the device which is inherent to the analytical form of Eq. (2.50) and (2.51) may be a crucial draw-back for the presented approach. However, in devices exhibiting series resistance and recombination contributions from the front side and contacts this effects may still be of minor importance and the presented model shows already an important improvement in predicting the I-V-curve of this extreme case.

### High base carrier lifetime

The diode parameters for the simulated and modelled devices without additional base recombination (FZ-Si) over contact spacing  $L_p$  are shown in Figure 4.3.

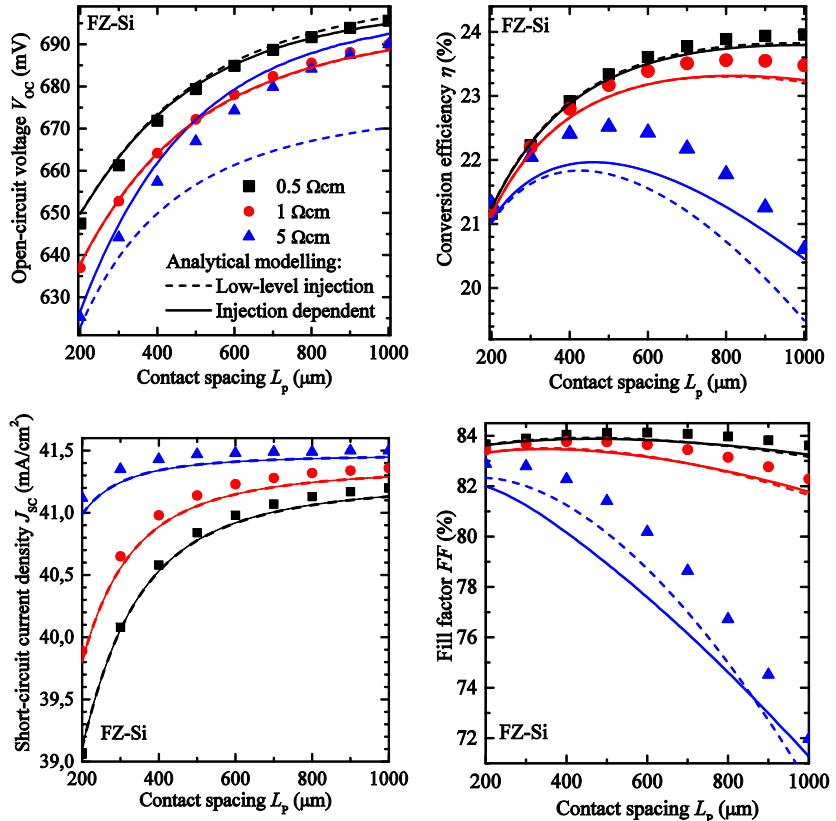


Figure 4.3 Analytically calculated  $I$ - $V$ -parameters in low level injection approximation (dashed) and with injection dependent modeling (solid lines) without additional base recombination (FZ-Si). The numerical results ([27], symbols) are shown for comparison.

The dashed lines in Figure 4.3 represent the classical analytical model assuming low level injection conditions whereas the solid lines represent the injection dependent analytical model of this work.

The short circuit current density  $J_{SC}$  is reproduced well by the analytical model for all simulated devices with a deviation below  $0.1 \text{ mA}/\text{cm}^2$ . Since the devices are in low-

level injection conditions at SC, we observe no deviation between the analytical models.

Apparently the open-circuit voltage  $V_{OC}$  of the FZ-Si devices is reproduced very well (deviation below 2 mV) by the classical analytical model for highly doped material with specific resistivity of 0.5 and 1  $\Omega\text{cm}$ , respectively. However, for lower doping densities and higher contact spacing  $L_p$ , the classical analytical model clearly underestimates  $V_{OC}$  by up to 20 mV. The agreement of the predicted  $V_{OC}$  for the FZ-Si material of the numerical and analytical results improves with the corrections (deviation below 4mV), indicating that the deviation indeed mostly origins in the departure from low level injection conditions.

The  $FF$  is reproduced by both analytical models with a deviation below 0.6 %<sub>abs</sub> for the highly doped material with specific resistivity of 0.5 and 1  $\Omega\text{cm}$ , respectively. For lower doping densities and higher contact spacing  $L_p$ , the classical analytical model underestimates the  $FF$  by up to 2 %<sub>abs</sub>. This can be contributed to the overestimated recombination and thus reduced voltage at a given working point and the underestimated conductivity of the base due to neglecting the additional conductivity of the injected carriers. The reduction is partly compensated by the reduction of the predicted  $V_{OC}$ . In Figure 4.2 can be seen, that although the  $FF$  is reproduced in a certain way, the diode characteristic of the device is not reproduced at all and thus the deviation of the classical analytical model from the numerical simulations is much higher than the difference in  $FF$  suggests. The injection dependent model underestimates the  $FF$  by up to 2.5 %<sub>abs</sub>. The origin of this deviation is discussed in the previous section.

Finally, for the predicted conversion efficiency  $\eta$  follows, that both analytical models reproduce the numerical data well for highly doped material with a deviation below 0.2 %<sub>abs</sub>. For lower doped material, the classical model deviates up to 1.1 %<sub>abs</sub> from the numerical result. The agreement of the predicted efficiency with the numerical results further improves considering injection dependence in our first approach. For the simulated 5  $\Omega\text{cm}$  device, an efficiency deviation below 0.5 %<sub>abs</sub> can be observed.

### Injection dependent base recombination

The diode parameters for the simulated and modelled devices with additional base recombination defined by  $[O_i] = 10^{18} \text{ cm}^{-3}$  (Cz-Si) over contact spacing  $L_p$  are shown in Figure 4.4.

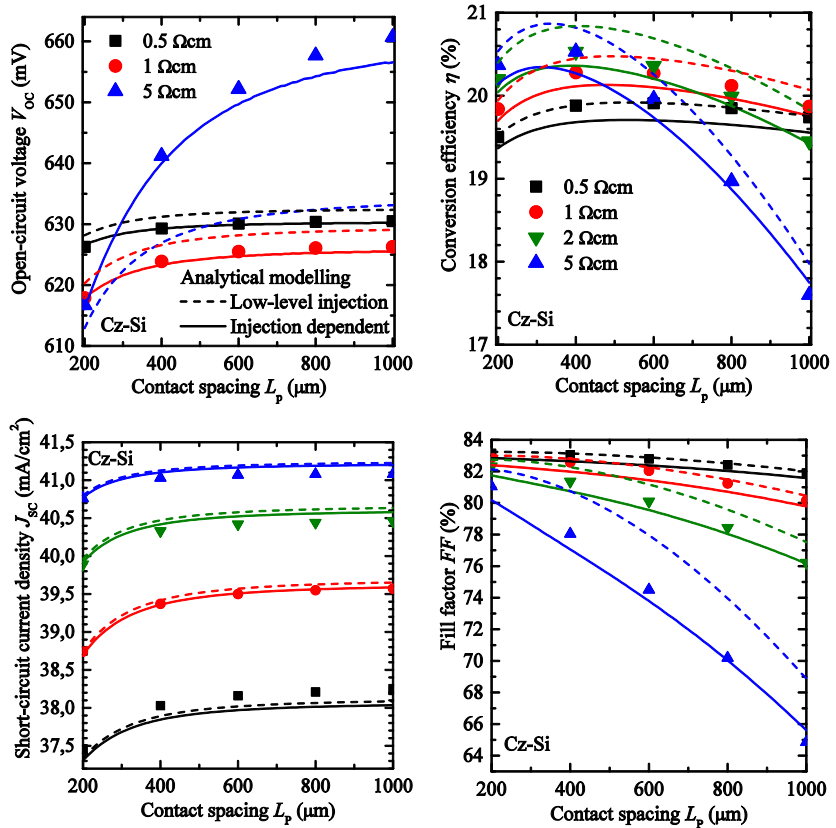


Figure 4.4 Analytically calculated open-circuit voltage, conversion efficiency, short circuit current density and fill factor in low level injection approximation (dashed) and with injection dependent modeling (solid lines) with additional base-recombination defined by  $[O_i] = 10^{18} \text{ cm}^{-3}$  (Cz-Si). The numerical results ([27], symbols) are shown for comparison. For visibility, the  $V_{oc}$ -results for the 2  $\Omega\text{cm}$  material are not shown.

The dashed lines in Figure 4.3 represent the classical analytical model assuming low level injection conditions whereas the solid lines represent the injection dependent analytical model of this work.

The short circuit current density  $J_{SC}$  is reproduced well by the analytical model for all simulated devices with a deviation below  $0.2 \text{ mA/cm}^2$ .

Similar to the FZ-Si devices, the open-circuit voltage  $V_{OC}$  is reproduced well (deviation below 3 mV) by the classical analytical model for highly doped material with specific resistivity of 0.5 and  $1 \Omega\text{cm}$ , respectively. However, for lower doping densities and higher contact spacing  $L_P$ , the classical analytical model clearly underestimates  $V_{OC}$  by up to 30 mV, due to the greatly overestimated SRH-recombination at high injection densities. The agreement of the predicted  $V_{OC}$  of the numerical and analytical results substantially improves with the corrections for highly doped material (deviation below 1mV) and for lowly doped material (deviation below 4mV). The reduced deviation for highly doped material of the Cz-Si case in respect to the FZ-Si case can be explained by the fact, that the recombination in the device is limited by the bulk SRH-recombination in the first case and by the rear surface in the latter: while the calculation of the recombination at the rear surface faces the problem of spatial variations in  $\Delta n$ , the SRH-recombination in the base is related to the average injection density in the base which is closer to the injection density estimated by Eq. (4.6).

The  $FF$  is reproduced by both analytical models with a deviation below  $0.5 \%_{\text{abs}}$  for the highly doped material with specific resistivity of 0.5 and  $1 \Omega\text{cm}$ , respectively. For lower doping densities and higher contact spacing  $L_P$ , the classical analytical model overestimates the  $FF$  by up to  $3 \%_{\text{abs}}$  which can be directly contributed to the underestimation of  $V_{OC}$ , partly compensated for by the underestimation of the series resistance due to neglecting the injected carriers (compare Figure 4.2). The injection dependent model deviates from the numerically obtained  $FF$  by up to  $1 \%_{\text{abs}}$ . The improvement in respect to the FZ-Si material can be attributed to the reduced domination of the rear side in the case of Cz-Si.

Finally, for the predicted conversion efficiency  $\eta$  follows, that both analytical models reproduce the numerical data well for highly doped Cz-Si material with a deviation below  $0.2 \%_{\text{abs}}$ . For the lowly doped material, the classical model overestimates  $\eta$  by up to  $0.3 \%_{\text{abs}}$ . In contrast, the injection-dependent model leads to an underestimation of up to  $0.3 \%_{\text{abs}}$ .

Note that these devices represent an extreme case for the model and that for realistic front side and base material, much higher agreement between the analytical model and the numerical solution is expected since the parameters  $J_{01}$  and  $R_S$  are not fully determined by the bulk and rear side, and since low level injection conditions remain preserved for lower bulk doping densities, as can already be observed for the investigated Cz-Si material. However, injection dependency is significant for strongly injection dependent recombination as is observed e.g. in compensated material or for lowly doped material with high lifetimes or in  $n$ -type silicon.

## 4.6 Conclusion

Analytical modeling shows good agreement with numerical modeling in low level injection conditions. Violation of low level injection conditions due to lower doped base material and injection dependent physical parameters, such as the SRH recombination in oxygen contaminated Cz-Si, requires injection dependent modeling. The proposed corrections lead to much better agreement of the analytical model with the numerical calculations for the simulated device with an ideal front structure. For more realistic structures, the deviations from the numerical model are expected to further decrease since the front side will contribute significantly to the saturation current and the series resistance of the solar cell leading to less relative injection dependency in these parameters and additionally to lower injection densities.

The calculation time of the analytical implementation increases for the presented additional implementations, but stays well in the range of one second on a desktop computer for a full contact distance variation (100 I-V-curves). Therefore the presented analytical model is a fast and accurate way to predict the optimum point contact spacing as well as the influence of different material parameters on the device even for devices exhibiting strongly injection dependent or high effective lifetimes and low doping densities and therefore leaving the low level injection regime. Even more it seems suited to fit experimentally obtained I-V-curves of such devices which could be challenging for numerical simulations. The comparison of the I-V-curves of the analytical models shows that injection independent modeling is not able to reproduce the diode characteristics in a meaningful way and, thus, is likely to evaluate misleading I-V-parameters by the fitting procedure.

Particularly the influence of different injection behavior of bulk defects as well as surfaces (diffused – non-diffused) can be regarded properly with the new model. The results indicate that the two diode model is also applicable at such devices as *n*-type solar cells reaching high voltages at typically lower doping densities and thus intermediate injection conditions. However, the results also show the limitations of the model: many applied analytical functions are based on spatially uniform physical quantities such as bulk lifetime, bulk conductivity, and recombination at surfaces. Sticking to the presented form of the two-diode model, non-uniform injection densities can only be considered in a way of implementing correction factors.

## 5 Recombination Velocity of Phosphorus Diffused Surfaces

*The described experiment was taken out in supervision of the master thesis of Momtazur Rahman [89] where further details about the experiment and characterization results are given. The experimental setup is stated in Section 5.2. The characterization results and modeling data are given in Section 5.3. Finally, the results are discussed and compared to literature data in Section 5.4.*

### 5.1 Introduction

To reduce the recombination activity of diffused surfaces is one of the main targets in the development of doping processes. Development in the screen-printed metal pastes for contacting, contacting schemes, passivation schemes, and solar cell concepts allow for a continuous improvement and adaption of the doping processes, which in consequence increase in complexity. For *p*-type silicon solar cells with screen-printed contacts, the general trend herein is to decrease surface dopant concentration in comparison to former processes. For other solar cell structures, such as back-contact back-junction solar cells, the different surface areas feature different constraints with respect to e.g. metallization fraction, illumination, or sheet resistance. A comprehensive quantitative understanding of the recombination properties of these diffused surfaces is crucial to minimize the experimental effort of such developments.

In this chapter, the surface recombination velocity of holes  $S_p$  at the Si-dielectric interface of phosphorus-doped surfaces is investigated in dependency of the surface dopant concentration  $n_{\text{surf}}$ . For industrial cell-structures, phosphorus-doped surfaces are often passivated by means of PECVD  $\text{SiN}_x$  or thin thermally grown  $\text{SiO}_2$  layers coated with PECVD  $\text{SiN}_x$  [90]. A general applicable parameterization of  $S_p$  for  $\text{SiN}_x$  passivated surfaces faces the problem, that the deposition and composition of these layers is generally adapted and optimized for the given surface morphology and dopant concentration. However, experience shows that a thin layer of silicon rich oxy-nitride  $\text{SiO}_x\text{N}_y$  coated with  $\text{SiN}_x$  in the same reactor (in this work, this passivation stack is denoted as *SiriON*, described by Ref. [91]) can lead to dark saturation current densities very close to the values of single  $\text{SiN}_x$ -layers that are optimized for the given surface dopant concentration and morphology. Thus in this work, *SiriON* is applied instead of  $\text{SiN}_x$  assumed to be more representative for the particular optimized or graded  $\text{SiN}_x$  layers than a  $\text{SiN}_x$  layer optimized for one specific dopant concentration.

To evaluate the effective surface recombination velocity  $S_p$  of highly phosphorus-doped surfaces, data-sets of  $J_0$  and corresponding doping profiles which exhibit a wide range of surface concentrations are needed. To increase the number of data-points and avoid increasing the experimental effort strongly due to many different types of

diffusion processes and necessary ECV profiling, a procedure based on subsequent removal of surface layers in an ozone-based etching solution [92] is applied.

## 5.2 Experimental Setup

The process sequence is shown in (Figure 5.1).

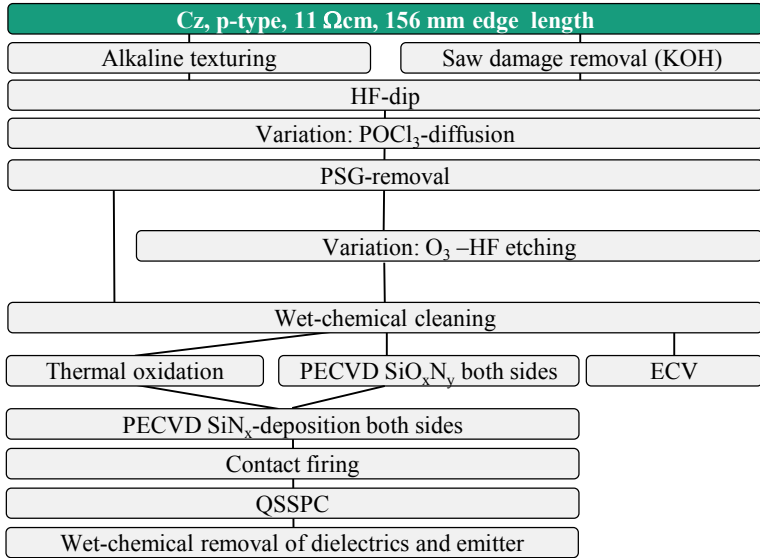


Figure 5.1 Process flow for the fabrication of the symmetrical lifetime samples to evaluate  $J_0$  and the carrier profile. Additionally, the wafer sheet resistance is measured by inductive coupling before diffusion, after PSG-removal and after removal of the passivation layer and the emitter after QSSPC.

The starting material are Cz-pulled  $p$ -type Si wafers of 156 mm edge length, an initial thickness of approximately 190  $\mu\text{m}$ , and a specific base resistance (after thermal treatment) of approximately 11  $\Omega\text{cm}$ . After alkaline texturing or saw damage removal, the wafers are exposed to three different  $\text{POCl}_3$  diffusion processes, which are denoted as diffusion A, B and C in the following. These processes are further developments of the in-situ oxidized diffusion processes described in Chapter 6 and feature a deposition phase at lower temperature and an oxidation phase at higher temperatures (compare Figure 6.1).

After removal of the phosphosilicate glass (PSG) layer, wafers of diffusion A and C are exposed to an ozone ( $\text{O}_3$ ) -based solution for different time spans (bath composition: 30 ppm  $\text{O}_3$ , 2 g/l HF, 3 g/l HCl). The etching process is described in detail by Moldovan *et al.* [92]. Half of the lifetime samples are exposed to a short thermal oxidation step [90] resulting in a thickness of the  $\text{SiO}_2$  layer of approx. 10 nm,

or directly coated with an approx. 10 nm thick  $\text{SiO}_x\text{N}_y$ -layer in a PECVD reactor. All lifetime samples are then coated with an additional  $\text{SiN}_x$ -layer in the same PECVD reactor of approx. layer thickness 60 nm. To simulate the fabrication conditions of a solar cell the wafers are exposed to a contact firing step in a fast firing belt furnace with set temperature  $T_{\text{set}} = 800 \text{ }^\circ\text{C}$  and band velocity  $v_{\text{band}} = 6 \text{ m/min}$ . The effective lifetime of the symmetrical samples (structure compare Figure 3.3) is measured in a QSSPC Sinton lifetime-tester WCT120 setup in generalized mode applying the red filter RG850.  $J_0$  is evaluated with the method *diffusion\_corr*, introduced in Chapter 3. The optical absorption factor is calculated from optical reflectance and transmission measurements, the wafer thickness is measured by differential capacitance probe, and the base dopant concentration is evaluated by means of inductive coupling after wet-chemical removing of the passivation layer and emitter. The doping profile is evaluated at both, the textured and the planar samples after removal of the PSG and pre-passivation cleaning as well as on some samples after ozone-etching.

### 5.3 Results

The resulting sheet resistances after PSG-removal as well as the standard deviations (*uniformity*) over single wafers (compare Figure 2.3) and the process boat are shown in Figure 5.2.

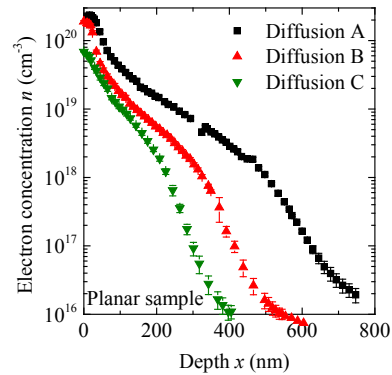
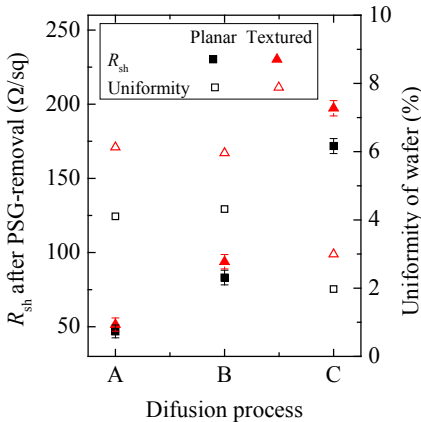


Figure 5.2: Measured sheet resistance and average standard deviation over one wafer after PSG-removal. Error bars denote the standard deviation of the mean sheet resistance of each wafer over the process boat (not fully loaded).

Figure 5.3: Carrier profiles evaluated by ECV in the center of planar wafers after removal of the PSG layer.

The sheet resistance is increased for textured surfaces compared to planar surfaces. This increase is for diffusion A approximately 9 %, diffusion B approx. 12 % and

diffusion C approx. 14 % of the sheet resistance of the planar samples. The increase can be attributed to the increased oxide growth on  $\langle 111 \rangle$ -surfaces compared to  $\langle 100 \rangle$  surfaces as observed e.g. by McIntosh *et al.* [93] and to the higher surface area per wafer and thus reduced PSG-growth towards the wafer center, as described by Rothhardt [49]. The average values of the sheet resistances over the wafers show a maximum standard deviation of approximately 1 % over the process boat (not fully loaded) while the values of each measurement spot show a maximum standard deviation of 7 % over the wafer. To take these deviations into account, in the following, all calculations are taken out for each wafer separately and all measurements are evaluated in the center of each wafer.

### Determination of individual doping profiles

The resulting doping-profiles measured by ECV at the center of planar wafers are shown in Figure 5.3.

According to the difference in sheet resistance, the doping profiles of the textured samples show slightly lower near surface doping densities (not shown here) than the ones evaluated on the planar samples. In the evaluation of the ECV measurements, the applied surface roughness of each sample is adjusted to match the locally measured sheet resistance of the emitter, compare Eq. (2.25). The applied area factors  $f_A$  are in a range of 0.99 – 1.06 for the planar and of 1.56 – 1.66 for the textured samples, well in the range of the theoretical values for ideal planar surfaces 1, and ideal random pyramidal texture 1.73 [93], and verified by optical evaluation of the surface roughness of similar samples which lead to  $1.05 \pm 0.03$  and  $1.6 \pm 0.07$ , respectively. Since ECV profiling is a destructive method and the profiles are to be used for modeling of the recombination behavior of the symmetrical lifetime samples, the profiles have to be applied to different wafers than the measured ones. Since all wafers exhibit slightly different sheet resistances, the doping profile of each wafer after PSG-removal is obtained by linearly scaling the dopant concentration profile of the corresponding ECV-sample (same surface topography and diffusion process) to match the sheet resistance measured in the center of each wafer, which requires a scaling factor between 0.93 and 1.06 for all samples. The obtained profiles are assumed to be the best guess of the doping profile of each individual lifetime sample.

To obtain the doping profiles  $n(x)$  of the finally passivated wafers, one has to consider the effects of the ozone-etching, the pre-passivation cleaning and partly also of the short thermal oxidation process. All three are regarded as simple removal of a near surface layer of silicon, neglecting redistribution of the dopant profile during thermal oxidation; the impact of this approximation is considered in the error bars of the datasets. The sheet conductivity  $\Sigma_{sh} = R_{sh}^{-1}$  of a layer of thickness  $x_{etch}$  removed from the surface is calculated by

$$\Sigma_{\text{sh}}(x_{\text{etch}}) = q \int_0^{x_{\text{etch}}} \mu(n) \cdot n(x) dx. \quad (5.1)$$

A comparison between the calculated  $\Sigma_{\text{sh}}(x_{\text{etch}})$  and the measured  $\Sigma_{\text{sh}} = \Sigma_{\text{sh,afterPSG}} - \Sigma_{\text{sh,passivated}}$  in the center of the wafer leads to the etch depth  $x_{\text{etch}}$  of each wafer and thus to the carrier profile, as e.g. applied in Ref. [94].

Figure 5.4 shows a comparison of the measured profiles on a planar sample after PSG-removal after diffusion C and after subsequent ozone-etching on similar samples, shifted by the calculated etch depth  $x_{\text{etch}}$  from Eq. (5.1).

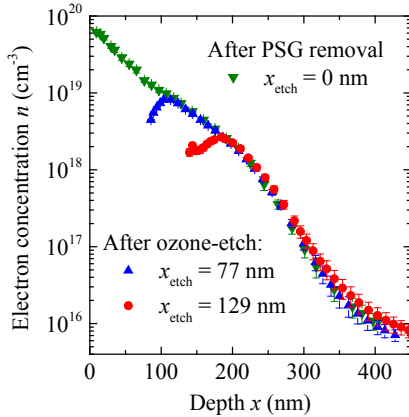


Figure 5.4: Carrier profiles after PSG-removal after diffusion C and after subsequent removal of the surface in an ozone solution, evaluated by ECV. The back-etched profiles are shifted by the calculated etch depth from measured sheet resistances in the wafer center.

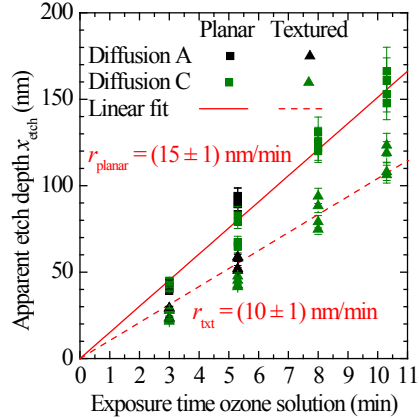


Figure 5.5: Calculated etch depth versus exposure time of the wafers in the ozone solution. The linear fits provide the etch rate  $r$  for planar and textured surfaces.

It is observed that the measured dopant concentration decreases towards the surface. The wafers can be expected to previously having exhibited a doping profile very similar to the profile of the non-etched sample and that the wet-chemical removal of a portion of the surface by ozone-etching does not change the dopant concentration in the remaining volume of the emitters. Thus the decrease of the dopant concentration towards the surface can be identified as a measurement artifact of the ECV, as reported in [94]. In consequence, the profiles of the non-etched back samples are extrapolated towards the surface and the uncertainty of this concentration value is increased.

However, apart from the near surface points, the etched back profiles show a very similar behavior as the non-etched back profiles and the calculation of the etch depth by Eq. (5.1) is regarded as accurate within the measurement uncertainties of the ECV.

In the following, the profiles of the etched back emitters are calculated by the above procedure from the profile of the corresponding non-etched back emitters which increases the accuracy of the evaluation of the surface concentration by omitting the measurement artifact of the ECV.

The etch depth of all wafers over exposure time in the ozone solution is shown in Figure 5.5. The calculated etch depth show a nearly linear behavior with the exposure time. The etch rate is calculated to  $r_{\text{planar}} = (15 \pm 1) \text{ nm/min}$  for planar and  $r_{\text{txt}} = (10 \pm 1) \text{ nm/min}$  for alkaline textured surfaces.

### Determination of $J_0$

From previous experiments and the surface roughness obtained by the ECV-profiling, it is assumed that the same carrier profile with the same surface recombination velocity leads to a  $J_0$  that is a factor of 1.6 higher on textured samples than on planar samples. In Ref. [95], highly doped, shallow emitters show a factor  $1.6 \pm 0.1$  between samples exposed to the same alkaline texturing or saw damage removal as applied in this work. Since this increase is no effect of higher emitter recombination in respect to emitter area but rather an effect of higher surface area and thus higher effective  $J_0$  determined by the QSSPC measurement, in the following all  $J_0$  of textured samples are divided by 1.6 for the application in the one-dimensional model. To account for the additional uncertainty of this procedure, the  $J_0$  uncertainty of textured samples is increased according to a surface factor of 1.55 to 1.65 in all following calculations.

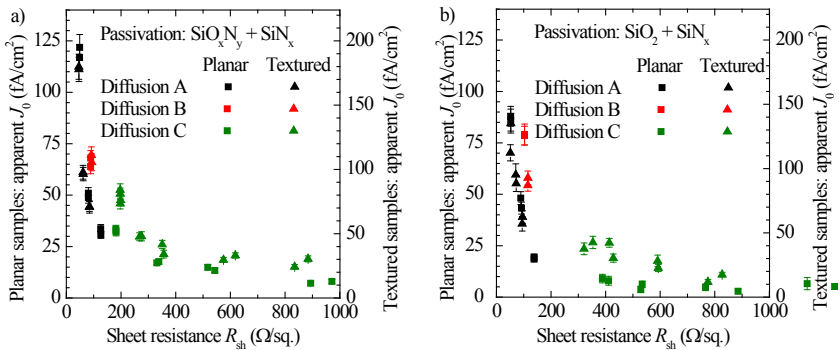


Figure 5.6: Apparent  $J_0$  over sheet resistance of the diffused emitters passivated with a thin layer of a) PECVD  $\text{SiO}_x\text{N}_y$  and b) thermally grown  $\text{SiO}_2$ , equally coated with PECVD  $\text{SiN}_x$ .  $J_0$  is evaluated by the method `diffusion_corr` (compare Chapter 3.3). The scale on the right hand side for the textured samples is reduced in respect to the planar samples by a factor of 1.6.

The apparent  $J_0$  evaluated after the method `diffusion_corr` (compare Chapter 3) over emitter sheet resistance is shown in Figure 5.6.

It is observed that for each diffusion process,  $J_0$  decreases with increasing sheet resistance. At high sheet resistances above  $100 \text{ } \Omega/\text{sq}$ , the textured samples exhibit a  $J_0$  that is increased more than 1.6 in comparison with the planar samples, pronounced for the  $\text{SiO}_2 + \text{SiN}_x$  passivated samples. This effect will be discussed in more detail below.

### Calculation of $S_p$

For each sample, the effective surface recombination velocity is calculated by Eq. (2.32) applying the individually assumed doping profile and the apparent  $J_0$ . An example of the  $S_p$  extraction is shown in Figure 5.7.

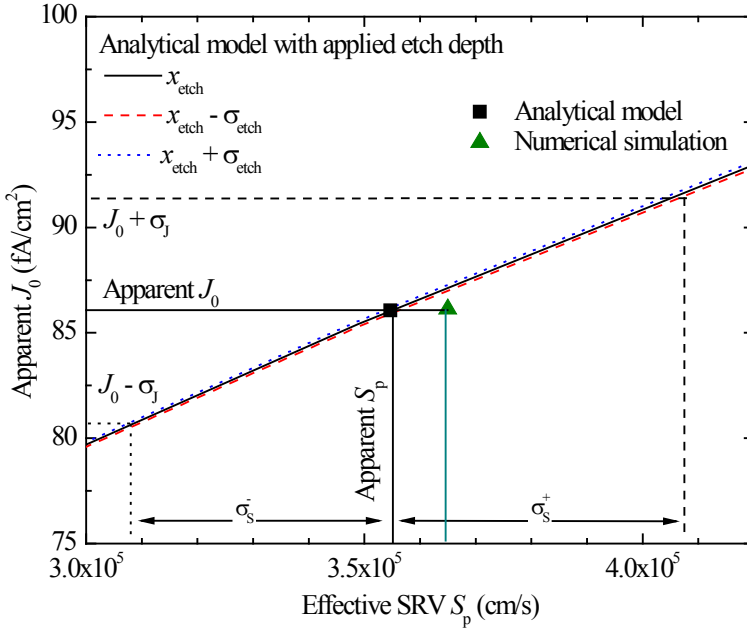


Figure 5.7: Example for the calculation of  $S_p$  from the apparent  $J_0$ : the uncertainty of  $S_p$  e.g. in positive direction  $\sigma_{S^+}$  is calculated by the simulation of the emitter applying the profile assuming an etch depth of  $x_{\text{etch}} - \sigma_{\text{etch}}$  and a  $J_0 + \sigma_j$ . For comparison, the result of a numerical simulation is shown.

The carrier profile is calculated from the etch depth and the profile assumed for the wafer after PSG-removal: to evaluate the uncertainty of  $S_p$ , the uncertainty of the etch depth  $\sigma_{\text{etch}}$  leads to three different applied profiles with etch depth  $x_{\text{etch}}$  and  $x_{\text{etch}} \pm \sigma_{\text{etch}}$ . Furthermore the uncertainty of the apparent  $J_0$ , composed by the standard deviation over the fit-range (here  $\Delta n_{\text{av}} = 1.3 \cdot 10^{16}$  to  $2.5 \cdot 10^{16} \text{ cm}^{-3}$ ) of the method *diffusion\_corr* and additional 5 % assumed for the uncertainty of the QSSPC method and setup leads to three applied dark saturation current densities:  $J_0$  and  $J_0 \pm \sigma_j$ . Note that in these

cases the measurement uncertainty is assumed to be represented by the standard deviation instead of the standard error – this procedure is based on the assumption that the uncertainties arise mainly of systematic deviation and not of statistical measurement errors, which are confirmed through repetitive measurements to be negligible in this case.

Also shown in Figure 5.7 is the result of the numerical device simulator EDNA [19]. For all extracted  $S_p$ , the result of the numerical simulation lies well within the uncertainty estimated by  $\sigma_s^+$  and  $\sigma_s^-$ .

In literature, several parameterizations of the surface recombination velocity  $S_p$  for phosphorus diffused surfaces [96-100] are found, which use

$$S_p = S_{p,1} \left( \frac{n_{\text{surf}}}{10^{19} \text{ cm}^{-3}} \right)^{\gamma_1} + S_{p,2} \left( \frac{n_{\text{surf}}}{10^{19} \text{ cm}^{-3}} \right)^{\gamma_2}, \quad (5.2)$$

with the fit parameters  $S_{p,1}$ ,  $S_{p,2}$ ,  $\gamma_1$  and  $\gamma_2$ . All extracted  $S_p$  are plotted in dependency on the surface dopant concentration  $n_{\text{surf}}$  in Figure 5.8.

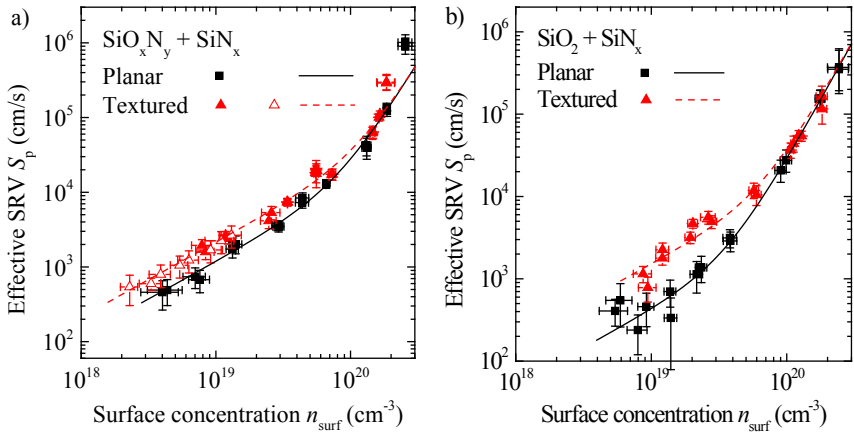


Figure 5.8: Calculated effective surface recombination velocity  $S_p$  plotted versus the electron surface concentration  $n_{\text{surf}}$  for a) SiriON and b)  $\text{SiO}_2 + \text{SiN}_x$  passivated surfaces. Closed symbols show the evaluated data of the experiment described in this chapter. Open symbols show additional data evaluated on alkaline textured SiriON passivated samples described in Chapter 6. The values for the textured samples are obtained by using  $J_{0,\text{app}} = J_{0,\text{txt}}/1.6$ . Lines show the parameterization given in Table 5.1.

The extracted  $S_p$  of the SiriON passivated samples show a monotonous increase with  $n_{\text{surf}}$ . The points with the highest surface concentration (diffusion B without ozone-etch) show a significant deviation from the parameterization function Eq. (5.2). This is attributed to near surface inactive phosphorus as reported in literature [101], which can

exhibit high recombination activity [83, 94]. Therefore, these data points are omitted for the parameterization. The texturing shows no significant influence on  $S_p$  for high  $n_{\text{surf}} > 7 \cdot 10^{19} \text{ cm}^{-3}$ . However for lower concentrations the textured samples exhibit slightly higher  $S_p$  than the planar samples. This could be an effect of the lower defect density at  $\langle 100 \rangle$  surfaces compared to  $\langle 111 \rangle$  surfaces [93] but it cannot be excluded that this is an effect of the different sample temperatures during contact firing due to the different surface morphologies or of the surface morphology itself. In case of alkaline textured, SiriON passivated surfaces the data-sets evaluated in Chapter 6 are applied as well. They fit very well to the data-sets obtained in this chapter by back-etching, although they seem to exhibit slightly lower  $S_p$  at the same concentration (not significant). Since nearly two years have passed between the generation of the two data-sets, the agreement can be regarded as very good.

The extracted  $S_p$  of the  $\text{SiO}_2 + \text{SiN}_x$  passivated surfaces do not show a deviation for the highest surface concentrations as is the case for SiriON passivation. It is assumed that the short oxidation step leads to either a transformation of the electrically inactive phosphorus or removes the near surface layer containing the inactive phosphorus by oxidation. Thus those points are included in the parameterization. Similar to the SiriON passivated samples, there is no difference between textured and planar surface observable for high surface concentrations of  $n_{\text{surf}} > 7 \cdot 10^{19} \text{ cm}^{-3}$ . However, for lower surface concentrations the deviation between the surface morphologies is clearly pronounced and well beyond measurement uncertainties. Even though an influence of the different wafer temperatures during contact firing cannot be excluded either, it is very likely that in this case the effect is due to the increased surface defect density of alkaline textured surfaces, dominated by  $\langle 111 \rangle$  planes.

The parameterization of the effective SRV is given in Table 5.1.

*Table 5.1 Parameters of Eq. (5.2) used for the parameterization shown in Figure 5.8. The exponents  $\gamma_1$  and  $\gamma_2$  are preset for all data sets and  $S_{p1}$  and  $S_{p2}$  are determined through a minimization of  $\chi^2$ . Because of the scarce data at high surface concentrations for the  $\text{SiO}_2 + \text{SiN}_x$  passivated samples,  $S_{p2}$  is determined for both surface morphologies simultaneously for these.*

Passivation	Surface	$S_{p1}$	$\gamma_1$	$S_{p2}$	$\gamma_2$
$\text{SiO}_x\text{N}_y + \text{SiN}_x$	planar	1177	1	16.3	3
	textured	2135	1	15.1	3
$\text{SiO}_2 + \text{SiN}_x$	planar	410	0.9	26	3
	textured	1497	0.9	26	3

### Influence of fixed surface charge

The analytical solution, Eq. (2.32), assumes electrical neutrality and does not account for fixed surface charges. In consequence, the obtained parameterizations represent

effective  $S_p$ , which can be applied in Eq. (2.31) or numerical device simulators to calculate  $J_0$  from a given dopant concentration profile but are expected to differ from the physical SRV. The applied passivation stacks comprise positive fixed charges near the Si-dielectric interface. For the applied SiriON passivation stacks, Seiffe *et al.* [91] extracted a surface charge density of  $Q_f = (4.1 \pm 1) \cdot 10^{11} \text{ cm}^{-2}$  on planar p-type Si wafers after contact firing and illumination. In the case of planar  $\text{SiO}_2$ -passivated surfaces, Altermatt *et al.* [11] apply  $Q_f = 7 \cdot 10^{10} \text{ cm}^{-2}$ . To estimate the influence of the assumed surface charge in this work,  $Q_f = 5 \cdot 10^{11} \text{ cm}^{-2}$  is applied, well above the reported values in literature.

$S_p$  is extracted from the measurement data as described above, but now using the numerical device simulator PC1Dmod, which is in excellent agreement with the models applied in this work (compare Appendix, Fig. A.2). Figure 5.9 shows  $S_p$  over surface dopant concentration for the textured, SiriON-passivated samples with and without the application of a surface charge.

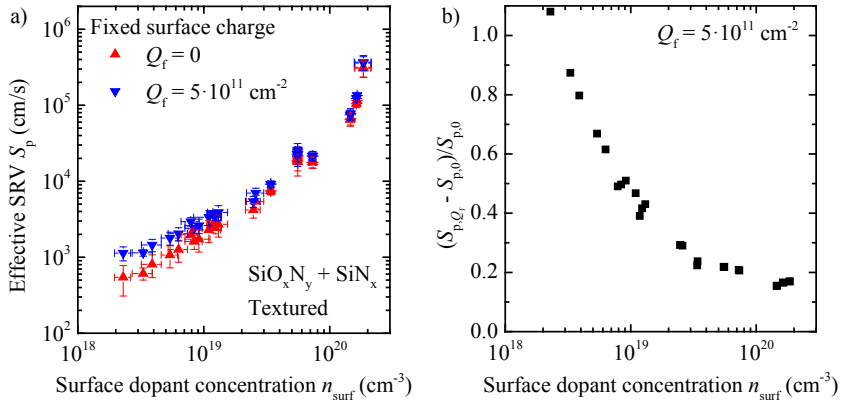


Figure 5.9 a) Calculated effective surface recombination velocity  $S_p$  plotted versus the electron surface concentration  $n_{\text{surf}}$  of the SiriON passivated, alkaline textured samples. The data are evaluated by PC1Dmod with and without the application of a fixed surface charge. b) Relative deviation of  $S_p$ , assuming a fixed surface charge or not.

At high dopant concentrations, the SRV  $S_{p,Q_f}$  calculated under the assumption of a surface charge, exceeds the SRV assuming no surface charge  $S_{p0}$  by approximately 20 %. For lower dopant concentrations, the deviation increases reaching approximately 100 % at  $n_{\text{surf}} = 2.1 \cdot 10^{18} \text{ cm}^{-3}$ . This confirms that care has to be taken when interpreting  $S_{p0}$  as SRV.

Figure 5.10 shows the extracted  $S_p$  under the assumption of  $Q_f = 5 \cdot 10^{11} \text{ cm}^{-2}$  for the given samples, analogously to Figure 5.8. The resulting parameterizations are listed in Table 5.2.

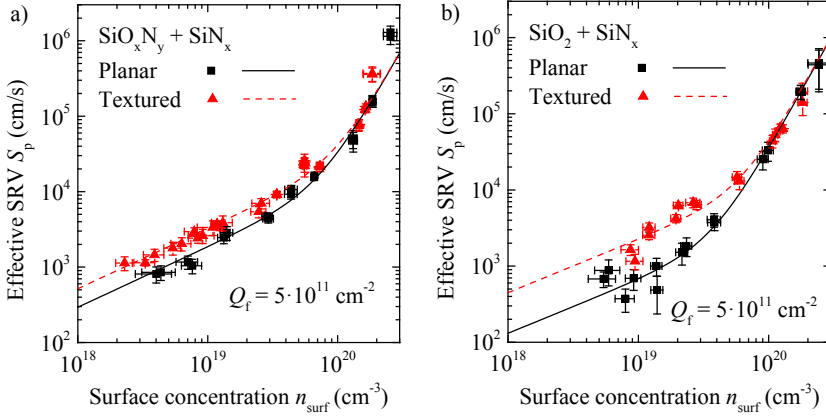


Figure 5.10: Calculated effective surface recombination velocity  $S_p$  plotted versus the electron surface concentration  $n_{\text{surf}}$ . The calculation is taken out with PCIDmod under the assumption of a fixed surface charge  $Q_f = 5 \cdot 10^{11} \text{ cm}^{-2}$ . The values for the textured samples are obtained by using  $J_{0,\text{app}} = J_{0,\text{txt}}/1.6$ . Lines show the parameterization given in Table 5.2.

Comparing Figure 5.10 and Figure 5.8, no qualitative difference is observable. This leads to the important conclusion that the discussion above is valid if the interfaces at the planar and textured surfaces exhibit the same surface charge density, independent of its absolute quantity.

Table 5.2 Parameters of Eq. (5.2) used for the parameterization of the data applying  $Q_f = 5 \cdot 10^{11} \text{ cm}^{-2}$ , shown in Figure 5.10. The exponents  $\gamma_1$  and  $\gamma_2$  were preset for all data sets and  $S_{p1}$  and  $S_{p2}$  were determined through a minimization of  $\chi^2$ . Because of the scarce data at high surface concentrations for the  $\text{SiO}_2 + \text{SiN}_x$  passivated samples,  $S_{p2}$  is determined for both surface morphologies simultaneously for these.

Passivation	Surface	$S_{p1}$	$\gamma_1$	$S_{p2}$	$\gamma_2$
$\text{SiO}_x\text{N}_y + \text{SiN}_x$	planar	1851	0.8	17.4	3.1
	textured	3257	0.8	16.8	3.1
$\text{SiO}_2 + \text{SiN}_x$	planar	657	0.7	26	3.1
	textured	2245	0.7	26	3.1

The parameterizations allow for comparing  $S_p$  for a given  $n_{\text{surf}}$  for textured and planar surfaces. Figure 5.11 depicts the ratio of  $S_p$  for the textured and planar samples under the assumption of a surface charge and without.

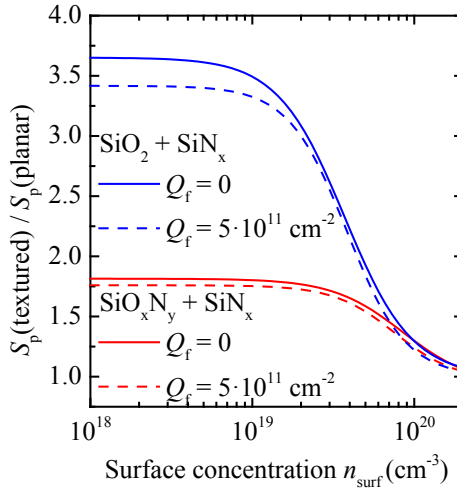


Figure 5.11: Calculated ratio of  $S_p$  for textured and planar samples under the assumption of  $Q_f = 0$  (Table 5.1) and  $Q_f = 5 \cdot 10^{11} \text{ cm}^{-2}$  (Table 5.2).

For both passivation layers, the ratio increases for decreasing surface concentration and converges to a value, which is a direct consequence of the similar choice of  $\gamma_1$  for each passivation stack. However, the influence of the assumed surface charge is small and for low surface concentrations one finds a ratio of  $3.5 \pm 0.2$  for the  $\text{SiO}_2 + \text{SiN}_x$  passivated samples and  $1.8 \pm 0.1$  for the  $\text{SiO}_x\text{N}_y + \text{SiN}_x$  passivated samples. Note that the uncertainties given here are only related to the choice of the surface charge density. To evaluate the difference between textured and planar surfaces for low dopant concentrations quantitatively, more independent data points are needed in this range.

### Comparison with literature

In literature, several parameterizations of the surface recombination velocity  $S_p$  for phosphorus diffused surfaces are found [96-100]. The applicability of these data is limited on the one hand, because the passivation schemes underwent a development in the years since evaluation of the data. On the other hand for textured surfaces, the measured  $J_0$  is taken directly for the simulation of planar surfaces [96] without taking into account, that the emitter area is increased and thus for the same  $S_p$  an increase of  $J_0$  by a factor of 1.6 to 1.7 is expected for shallow emitters [93, 95]. The so obtained  $S_p$  are effective values that do not allow for the direct comparison with the  $S_p$  of planar surfaces and may depend on the shape of the profile. In this work, the measured  $J_0$  on textured surfaces is reduced by the experimentally observed factor of 1.6 for shallow and highly doped emitters [95] before applied in the simulation.

In literature one finds effective SRV values for different passivation schemes and dopants. A good overview and reassessment for the application of Fermi-Dirac statistics is given by Altermatt *et al.* [11]. A comparison of the  $S_p$  for textured surfaces is not possible since Altermatt's  $J_0$ -data were not scaled by a surface factor prior to the one-dimensional emitter simulation. For planar samples, Altermatt applies fixed surface charges of density  $2 \cdot 10^{11} \text{ cm}^{-2}$  in the case of  $\text{SiN}_x$  and  $7 \cdot 10^{10} \text{ cm}^{-2}$  in the case of  $\text{SiO}_2$ . Since in this work the passivation layers differ and the fixed surface charge density is not known, a complete comparison of the data is not possible. However for high doping densities the influence of the fixed charges is effectively reduced and a comparison is possible.

In Figure 5.12 the data by Kerr *et al.* [97] revised by Altermat *et al.* [96] for planar samples is shown.

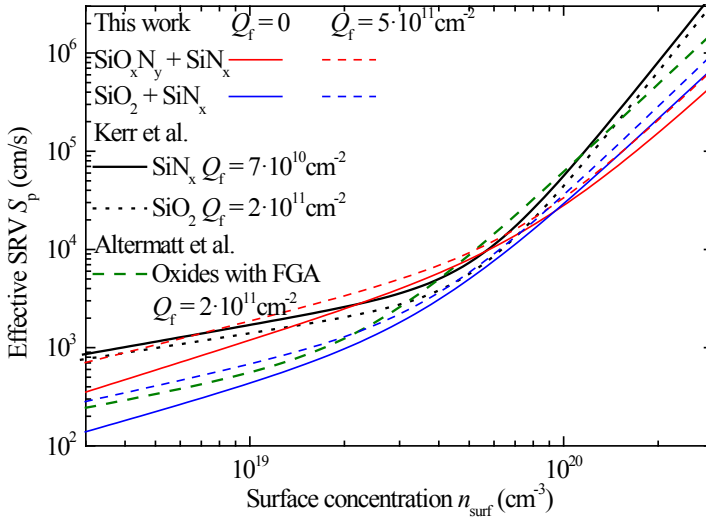


Figure 5.12: Effective surface recombination velocity  $S_p$  as a function of the surface concentration  $n_{\text{surf}}$  for planar surfaces: solid (blue and red) lines show the parameterization of this work assuming no surface charge and dashed lines assuming an upper limit of  $Q_f = 5 \cdot 10^{11} \text{ cm}^{-2}$ . Black lines give the parameterization by Altermatt *et al.* [96] of data-sets evaluated by Kerr *et al.* [97], the green dashed line shows a parameterization by Altermatt *et al.* [96] for  $\text{SiO}_2$  exposed to a forming gas anneal, obtained by evaluating data from different authors.

At high dopant concentrations  $n_{\text{surf}} > 8 \cdot 10^{19} \text{ cm}^{-3}$  all the data-sets by Kerr *et al.* and Altermatt *et al.* increase strongly with increasing surface concentration. The effective  $S_p$  evaluated in this work increase significantly less with  $n_{\text{surf}}$  in this range resulting in a deviation of a factor of 2.3 - 6 at  $n_{\text{surf}} = 2 \cdot 10^{20} \text{ cm}^{-3}$ . The literature data sets were

simulated under the assumption of a surface charge. For lower dopant concentrations  $n_{\text{surf}} < 8 \cdot 10^{19} \text{ cm}^{-3}$ , the literature data are in agreement with the parameterizations of this work under the assumption of  $0 < Q_f < 5 \cdot 10^{11} \text{ cm}^{-2}$ .

## 5.4 Conclusion

It is demonstrated that the presented procedure enables the determination of the effective surface recombination velocity  $S_p$  for a broad variation of surface concentrations  $n_{\text{surf}}$  with a comparable small number of different diffusion processes. The etch-back procedure allows for a high accuracy in the determination of  $n_{\text{surf}}$  by ECV due to the omitted measurement artifact at the surface and prevents the influence of inactive phosphorus formed near the surface.

For the two examined passivation schemes, an effective  $S_p$  is extracted as a function of  $n_{\text{surf}}$  in the range of  $n_{\text{surf}} = 3 \cdot 10^{18}$  to  $2 \cdot 10^{20} \text{ cm}^{-3}$  for planar and alkaline textured surfaces. For lower dopant concentrations, the obtained values are in good agreement with the parameterization found in literature. The extracted  $S_p$  are significantly lower than literature values at high doping densities.

The scaling of the  $J_0$  of textured surfaces to a plane prior to simulation enables the direct comparison of  $S_p$  between textured and planar surfaces. While for high doping densities  $> 8 \cdot 10^{19} \text{ cm}^{-3}$  no difference is observed, for low doping densities  $S_p$  is significantly increased at textured surfaces, especially for the passivation stack  $\text{SiO}_2 + \text{SiN}_x$  by a factor of approx.  $3.5 \pm 0.2$ . This increase is shown being nearly independent from the assumed fixed surface charge density under the assumption that both, textured and planar interfaces exhibit the same surface charge density.

The obtained parameterizations are applicable for simple device modeling, e.g. analytically with Eq. (2.32) and (2.33) or numerically without the need of applying a fixed surface charge. For the extraction of  $J_0$  and the simulation of  $S_p$ , the same physical parameter sets are applied as e.g. in the numerical simulation tools EDNA [19] and PC1Dmod [17]. Further experiments in the author's research group showed, that the passivation quality of the SiriON stack is comparable with industrially applied, graded  $\text{SiN}_x$  layers which are optimized for a given surface concentration.

## 6 In-Situ Oxidation for Advanced Doping Processes

*The experimental results of this chapter are published in Ref. [102]. Section 6.2 gives the experimental setup and details about the processes. In Section 6.3 the characterization results are reported which are compared with simulation results in Section 6.4.*

### 6.1 Introduction

For back-contact back-junction silicon solar cells, a phosphorus-doped front surface field featuring low recombination is beneficial, preventing the recombination of minority carriers generated near the front side and reducing the effect of electrical shading. Low recombination activity requires low dopant concentrations. A common way to produce such phosphorus doping is the  $\text{POCl}_3$  diffusion in a tube furnace, subsequent wet chemical removal of the PSG, wet chemical cleaning, thermal oxidation and finally wet chemical removal of the silicon dioxide layer as applied for the preliminary solar cell process (see Section 2.6). Due to its numerous wet chemical and high temperature steps, this sequence is cost intensive in industrial production and elevates the risk of contamination of the material or introducing recombination defects in the substrate due to repeated heating [103]. In this chapter a  $\text{POCl}_3$  tube furnace diffusion is developed to produce deep, low surface concentration profiles in one single process step. Thermal oxidation after  $\text{POCl}_3$ -diffusion without removing the PSG-layer is reported in literature [104-106] as well as  $\text{POCl}_3$ -diffusion processes on different temperature plateaus [107]. Here we combine in-situ oxidation with different temperature plateaus to form deep driven-in phosphorus profiles in one process step suitable for e.g. the front side of BC-BJ solar cells or both-side contacted solar cells with alternative metallization techniques.

### 6.2 Experimental Setup

The  $\text{POCl}_3$  diffusion is performed in an industrial tube furnace on 190  $\mu\text{m}$  thick  $n$ -type FZ-Si wafers with a resistivity of 9.2  $\Omega\text{cm}$  and alkaline textured surfaces for carrier lifetime measurements or planar surfaces for ECV profiling. A schematic of the diffusion process is shown in Figure 6.1. It exhibits a deposition phase in  $\text{POCl}_3$ ,  $\text{O}_2$  and  $\text{N}_2$  gas ambient and a subsequent oxidation phase in oxygen ambient at elevated temperatures. The temperature of the first plateau, the deposition temperature  $T_d$ , is varied whereas two different temperatures  $T_{\text{ox}}$  and plateau times of the oxidation phase are applied - resulting in a process with short (30 min) drive-in at high temperature  $T_{\text{ox}} = 1050$   $^\circ\text{C}$ , here denoted *Type A*, and one with long (90 min) drive-in at moderate temperature  $T_{\text{ox}} = 950$   $^\circ\text{C}$ , *Type B*. As a reference process a  $\text{POCl}_3$ -diffusion on a single temperature plateau resulting in a sheet resistance of  $R_{\text{sh}} = 147$   $\Omega/\text{sq}$  is chosen (applied for the formation of the FSF by Woehl [69]).

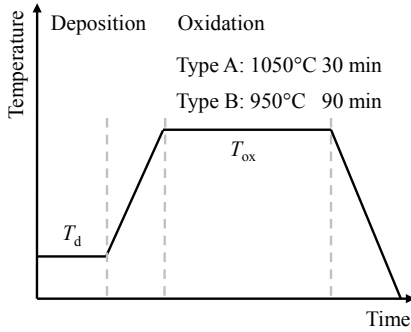


Figure 6.1 Schematic of the diffusion process.  $T_d$  is used as control parameter for the sheet resistance.

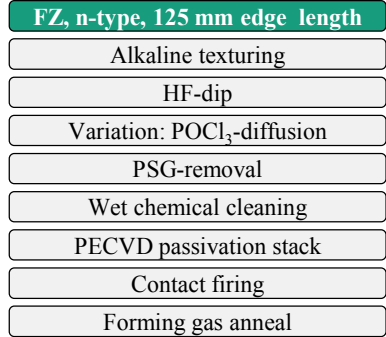


Figure 6.2 Process flow for the fabrication of the symmetrical lifetime samples to evaluate  $J_0$ .

An overview on the process sequence for the fabrication of symmetrical lifetime samples is shown in Figure 6.2. After the wet-chemical removal of the PSG and cleaning, the carrier lifetime samples are passivated with the SiriON stack deposited by PECVD, exposed to a contact firing step in a fast firing oven at a set temperature of 800 °C at a band velocity of 0.52 m/s and a subsequent forming gas anneal at 425 °C. We extract the dark saturation current densities for the FSF  $J_{0,FSF}$  from QSSPC in generalized measurement mode by the method accounting for BGN and carrier diffusion, denoted as *diffusion\_corr* in Chapter 3.3.

### 6.3 Results

The sheet resistance of the emitter  $R_{sh}$ , averaged over wafer and process boat, as a function of the deposition temperature  $T_d$  is shown in Figure 6.3. It is to note here that for reasons of IP protection it is not possible to give absolute values of  $T_d$ . Therefore  $T_d$  is linearly scaled to arbitrary units in the following figures.

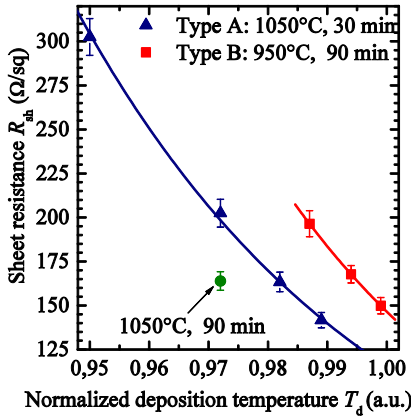


Figure 6.3: Sheet resistance  $R_{sh}$  as a function of deposition temperature  $T_d$ . Lines show exponential fits to the data. Error bars indicate standard deviation over wafer and process boat (not fully loaded).

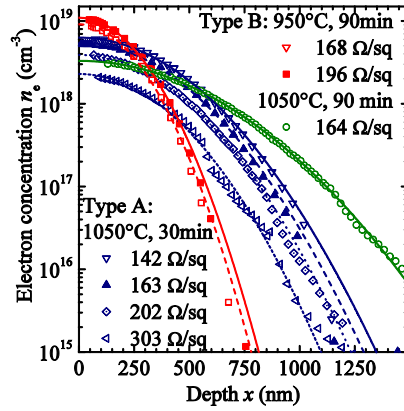


Figure 6.4: Carrier concentration profiles measured by ECV in the wafer center. Lines show gaussian fits to the data.

A high homogeneity for 125 mm and 156 mm sized wafers with a standard deviation of inline sheet resistance measurement (compare Figure 2.3) below 3 % as well as over the process boat (not fully loaded) is achieved.  $T_d$  allows excellent control of  $R_{sh}$ : for a given drive-in process,  $R_{sh}$  can be described very well by a simple exponential function of  $T_d$  of the form  $R_{sh} = R_0 \cdot \exp(T_d/T_0)$  with the fit-parameters  $R_0$  and  $T_0$  (without further physical meaning). For the same  $T_d$ , increasing the temperature or the duration of the oxidation phase leads to a decreased  $R_{sh}$ .

The measured carrier profiles are shown in Figure 6.4. All profiles are well described by Gaussian distributions of the form

$$N_{dop} = n_{surf} \exp \left\{ - \ln \left( \frac{n_{surf}}{10^{16} \text{ cm}^{-3}} \right) \cdot \left( \frac{x}{x_j} \right)^2 \right\}, \quad (6.1)$$

with the surface dopant concentration  $n_{surf}$  and the physical junction depth  $x_j$ , here defined by  $N_{dop}(x_j) = 10^{16} \text{ cm}^{-3}$ .

The Gaussian shape of the profiles can be understood physically: at low phosphorus concentrations, the diffusion of phosphorus in crystalline silicon is governed by a self-interstitial assisted diffusion mechanism [108] resulting in a concentration independent diffusion coefficient  $D_{ph}$  for lower concentrations, which is limited by the diffusivity of phosphorus atoms through the self-interstitials [109]. With increasing phosphorus

concentration, the diffusion is limited by the diffusion of the self-interstitials, resulting in a reduced effective  $D_{\text{Ph}}$  with increasing concentration. Bentzen et al. [109] evaluated  $D_{\text{Ph}}$  in dependence of the device temperature quantitatively. At the example of a diffusion temperature of 890 °C, the transition between the two limitations takes place at a phosphorus concentration of approx.  $10^{19} \text{ cm}^{-3}$  and leads to a nearly constant  $D_{\text{Ph}}$  for concentrations up to  $3 \cdot 10^{19} \text{ cm}^{-3}$ . In this experiment, the device temperature at the drive-in process is even higher than 890 °C which leads to an increased concentration of the transition point [109] and thus to a nearly constant  $D_{\text{Ph}}$  for concentration exceeding  $3 \cdot 10^{19} \text{ cm}^{-3}$ . In consequence, the phosphorus diffusion during the oxidation plateaus is well described by a constant  $D_{\text{Ph}}$ . The growth of a  $\text{SiO}_2$  layer between the PSG-layer and the silicon during temperature ramp-up under  $\text{O}_2$ -atmosphere effectively separates the diffusion source from the silicon. Finally, from Fick's second law follows a Gaussian dopant profile for a constant  $D_{\text{Ph}}$  and a finite dopant source:

$$N_{\text{dop}}(x, t) = \frac{Q}{\sqrt{\pi D_{\text{Ph}} t}} \exp\left\{-\left(\frac{x}{2\sqrt{D_{\text{Ph}} t}}\right)^2\right\}, \quad (6.2)$$

with the (area-related) dopant dose of phosphorus  $Q$ , and the time of diffusion  $t$ . Comparing Eq. (6.1) and Eq. (6.2) for the ideal diffusion leads to

$$\begin{aligned} n_{\text{surf}} &= \frac{Q}{\sqrt{\pi D_{\text{Ph}} t}} \\ x_j &= 2\sqrt{D_{\text{Ph}} t \cdot \ln\left(\frac{n_{\text{surf}}}{10^{16} \text{ cm}^{-3}}\right)}. \end{aligned} \quad (6.3)$$

Since assumptions necessary for Eq. (6.2), such as a constant diffusion temperature and coefficient, are not fulfilled in the investigated processes, it is refrained here to relate the empirical profiles to Eq. (6.2) quantitatively. However, it gives valuable insight to understand the results qualitatively. The dopant dose  $Q$ , calculated by Eq. (6.3) from the Gaussian profiles, over  $T_{\text{d}}$  is shown in Figure 6.5.

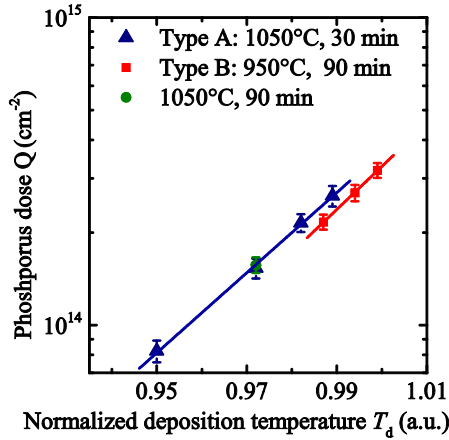


Figure 6.5: Calculated dopant dose  $Q$  from the Gaussian fit to the measured concentration profiles over deposition temperature  $T_d$ . Error bars denote the influence of the estimated uncertainty of the ECV. Lines show exponential fits, which are not further applied in this work.

The dopant dose  $Q$  increases with increasing  $T_d$  in consequence of an increased in-diffusion of phosphorus during the deposition phase. Comparing type A to type B at the same  $T_d$ , the dopant dose resulting from type A is higher. This can be explained by the influence of the higher temperature in the oxidation phase of process type A: apparently, the higher in-diffusion of phosphorus from the PSG due to higher temperatures exceeds a possible effect of the accelerated oxidation and thus the faster separation of the dopant source. Interestingly, the longer duration of the oxidation phase shows only a minor increase of  $Q$  (compare type A to the same diffusion process with duration of the oxidation plateau of 90 min). This is in agreement with the concept of separating the dopant source from the silicon at the beginning of the oxidation phase or even during heat up.

The resulting parameters from the Gaussian fit,  $n_{\text{surf}}$  and  $x_j$ , are plotted over  $T_d$  in Figure 6.6.

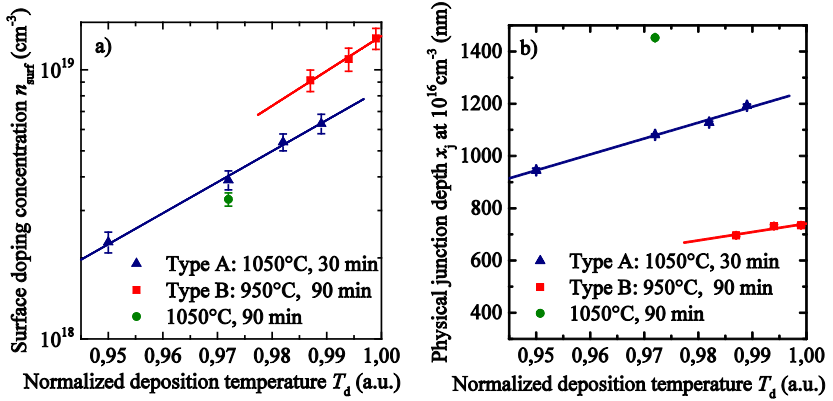


Figure 6.6: Parameters of the Gaussian fit to the measured concentration profiles over deposition temperature  $T_d$ : a) surface concentration  $n_{\text{surf}}$  b) physical junction depth  $x_j$ . Error bars denote the uncertainty of the fit plus in the case of a) the estimated uncertainty of the ECV. Lines show exponential (a) and linear (b) fits (parameters given in Table 6.1).

The surface concentration  $n_{\text{surf}}$  (Figure 6.6, a) increases with increasing  $T_d$  in consequence of an increased in-diffusion of phosphorus during the deposition phase.  $n_{\text{surf}}$  decreases with increasing  $T_{\text{ox}}$  which can be attributed, on the one hand, to a faster separation of the PSG from the silicon due to the enhanced oxidation (decreasing  $Q$ ), and, on the other hand, during the oxidation phase the diffusivity is higher at higher temperatures and leads to a deeper Gaussian profile with lower surface concentration (increasing  $D_{\text{Ph}}$ ). The latter effect is visible by comparing the Type A diffusion with the process at the same  $T_d$  but a three times longer oxidation phase:  $n_{\text{surf}}$  decreases due to the longer time of redistributing the dopant concentration (increasing  $t$ ). Finally, the described influences on  $n_{\text{surf}}$  are further enhanced by the removal of a portion of the highly doped, near surface silicon by oxidation, which increases with oxidation temperature and time.

For similar drive-in conditions, the physical junction depth  $x_j$  (Figure 6.6, b) increases with  $T_d$  because of the increased concentration gradient resulting from a higher dopant in-diffusion during the deposition phase for increased  $T_d$  (compare Eq. (6.3) with increasing  $n_{\text{surf}}$ ). However,  $x_j$  is dominated by the drive-in conditions:  $x_j$  increases with  $T_{\text{ox}}$  (increased  $D_{\text{Ph}}$ ) and, at the same  $T_{\text{ox}}$  with the duration of the oxidation phase (increasing  $t$ ).

For constant drive-in conditions,  $n_{\text{surf}}$  can be empirically described by an exponential function of  $T_d$  of the form  $n_{\text{surf}} = c_0 \cdot \exp(T_d/T_0)$ . The fit parameters are given in Table 6.1. For type A diffusion, a variation of  $T_d$  in the applied range of this experiment increases the dopant concentration by a factor of 3. For constant drive-in conditions,  $x_j$

can be empirically described by a linear function of  $T_d$ . The fit parameters of the function  $x_j = a + b \cdot T_d$  are given in Table 6.1. For the limited generality of the regarded problem, in particular the neglected dependency of gas concentrations, it is refrained from calculating uncertainties for the parameters here.

Table 6.1: Fit parameters for the surface concentration  $n_{\text{surf}} = c_0 \cdot \exp(T_d/T_0)$  and junction depth  $x_j = a + b \cdot T_d$  in dependence of the deposition temperature  $T_d$  (in K).

Diffusion type	$c_0$ (cm <sup>-3</sup> )	$T_0$ (K)	$a$ (μm)	$b$ (nm/K)
A	$1.4 \cdot 10^7$	37.7	-5.0	6.1
B	$2.9 \cdot 10^5$	32.5	-2.6	3.2

The empirical fit parameters have more practical value than easily accessible physical meanings. However, from parameter  $b$  follows, that increasing  $T_d$  by 1 K, the junction depth increases by 6.1 nm for diffusion type A and by 3.2 nm for diffusion type B. Increasing  $T_d$  by  $T_0$  increases  $n_{\text{surf}}$  by a factor of  $e$ . In the next section the parameters are applied to predict  $J_0$  and  $R_{\text{sh}}$  in dependence of the deposition temperature  $T_d$ .

The apparent  $J_0$  over  $R_{\text{sh}}$  are shown in Figure 6.7.

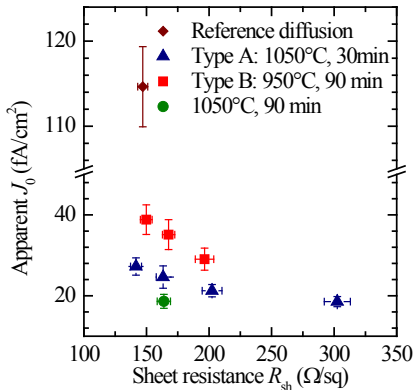


Figure 6.7: Measured  $J_0$  over sheet resistance  $R_{\text{sh}}$  (alkaline textured surfaces). The error bars denote uniformity, scattering of different samples and measurement uncertainties. The reference diffusion exhibits one single temperature plateau.

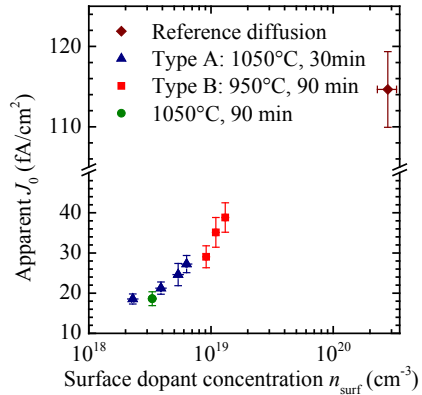


Figure 6.8: Apparent  $J_0$  over surface dopant concentration  $n_{\text{surf}}$ , obtained from the gaussian fits to the ECV-data. For the reference diffusion the concentration limit of electrically active phosphorus after Solmi et al. [110] is applied.

Compared to the reference diffusion at one single temperature plateau, all in-situ oxidized diffusions lead to dark saturation current densities from 18 to 38 fA/cm<sup>2</sup>. For each given drive-in procedure,  $J_0$  decreases with increasing  $R_{\text{sh}}$ .

An explanation of this behavior is given by the apparent  $J_0$  in dependence of the surface concentration, shown in Figure 6.8: For the investigated samples,  $J_0$  increases monotonously with  $n_{\text{surf}}$ . For the in-situ oxidized samples  $J_0$  is dominated by the surface recombination velocity for two reasons: on the one hand, the low doping prevents effective electrical shielding of the surface, on the other hand, it leads to low Auger-recombination. The reference diffusion shows a comparable high surface concentration exceeding the activation limit of phosphorus [110] – this leads to high recombination activity [94] and thus to a high  $J_0$  despite the more effective shielding of the near surface area.

## 6.4 Predictive Modeling

The parameterization of  $S_p$  described in Chapter 5 allows for the predictive modeling of the recombination behavior of the highly doped surfaces, if the doping profile is known and the recombination in the bulk of the emitter can be assumed to be dominated by the Auger mechanism. Both assumptions are valid for the  $\text{POCl}_3$ -diffusion processes with in-situ oxidization presented here. The parameters given in Table 6.1 enable for calculating the depth and surface concentration of the Gaussian profiles in dependence of  $T_d$  for each drive-in process separately.

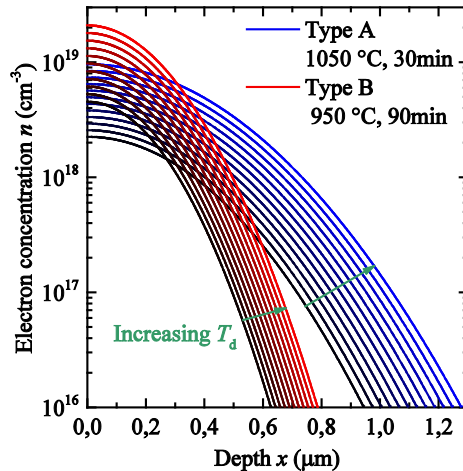


Figure 6.9: Selection of the simulated carrier profiles. The arrows show the development of the sheet resistance from 300  $\Omega/\text{sq}$  to 100  $\Omega/\text{sq}$ . Compare ECV-profiles in Figure 6.4.

The simulated variation of profiles exhibiting  $R_{\text{sh}}$  from 100  $\Omega/\text{sq}$  to 300  $\Omega/\text{sq}$  is shown in Figure 6.9.

With the parameterization of  $S_p$ , given in Table 5.1,  $J_0$  is calculated by Eq. (2.32). Figure 6.10 shows the result in dependence of a)  $T_d$ , b)  $R_{sh}$ , and c)  $n_{surf}$ . The modeling assists understanding the dependencies of the measured  $J_0$ . Additionally, the loss in short circuit current due to the recombination of carriers generated in the highly doped region is calculated by Eq. (2.33), assuming the same  $S_p$  of the textured surfaces but the generation profile of a flat surface. Since the effective incident angle of light can be assumed to differ from zero as is the case for a perfectly flat surface, the calculated  $\Delta J_{sc}$  represents a lower limit for the expected loss.

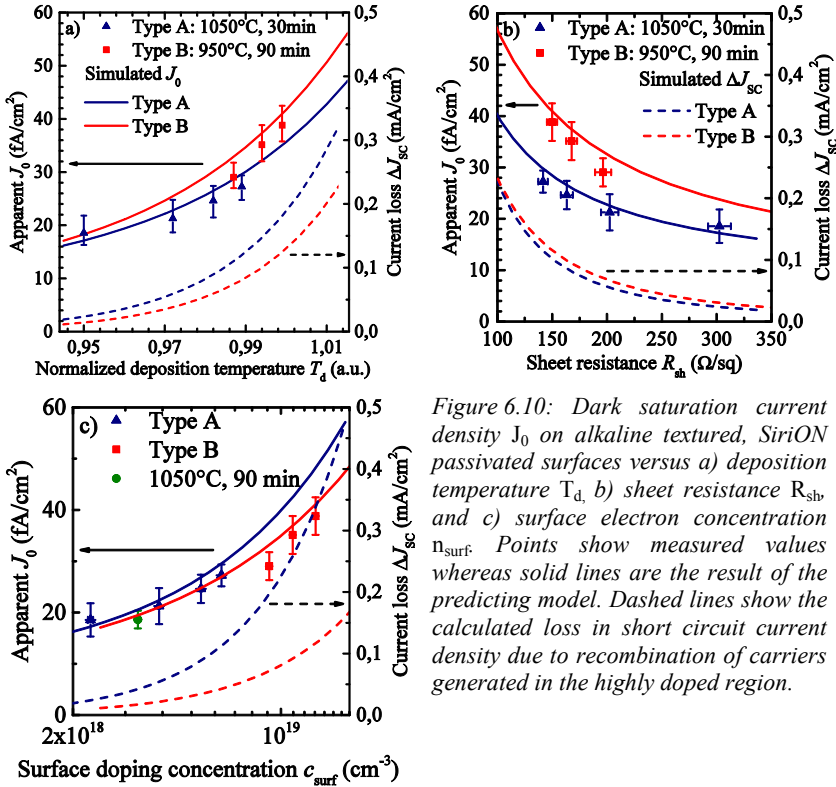


Figure 6.10: Dark saturation current density  $J_0$  on alkaline textured, SiRiON passivated surfaces versus a) deposition temperature  $T_d$ , b) sheet resistance  $R_{sh}$ , and c) surface electron concentration  $n_{surf}$ . Points show measured values whereas solid lines are the result of the predicting model. Dashed lines show the calculated loss in short circuit current density due to recombination of carriers generated in the highly doped region.

All measured apparent  $J_0$  are, in the range of their estimated uncertainty, in agreement with the simulation.

For both drive-in processes A and B,  $J_0$  increases with  $T_d$  (Figure 6.10, a). However, the simulation results show that the increase is higher for Type B than for Type A which could not be concluded from the measurement data alone.

From a practical point of view, for the development of solar cells the most interesting dependency is the variation of  $J_0$  and  $\Delta J_{SC}$  with  $R_{sh}$  (b), especially when the diffused side, e.g. the front side, is contacted. At the same  $R_{sh}$ , type B leads to a  $J_0$  that is approximately 40 % higher than that of type A. In contrast,  $\Delta J_{SC}$  is nearly identical for both types with a maximum deviation of 0.01 mA/cm<sup>2</sup>, well negligible regarding the uncertainty of the modeling procedure. This leads to the interesting fact, that for these two sets of different Gaussian profiles  $\Delta J_{SC}$  shows mainly the same functional dependence from sheet resistance.

A further important parameter for the development of solar cells with front contacted emitter is  $n_{surf}$ , since the contact resistance depends on  $n_{surf}$  [62], or, more precisely on the near surface dopant concentration, specifically for the applied metallization technique [111]. The modeling results depicted in Figure 6.10 c) show in this example, that type A leads to low  $J_0$  and  $\Delta J_{SC}$  for low  $n_{surf}$ . But when  $n_{surf} > 10^{19}$  cm<sup>-3</sup> is required it can lead to high and undesirable  $\Delta J_{SC}$  and thus, for this aspect, type B could be a better choice.

## 6.5 Conclusion

New processes to form deep driven-in phosphorus diffusion profiles with low surface concentrations in one single diffusion step are introduced. The obtained sheet resistances show high homogeneity with standard deviations below 3 % over wafers and process boat (inline sheet resistance measurement, compare Figure 2.3). The deposition temperature allows for excellent control of the sheet resistance in the investigated range of 120 to 300 Ω/sq. The surface concentration is influenced by both, the deposition temperature and drive-in process whereas the latter mainly controls the depth of the profile. For the lowly phosphorus-doped profiles, the surface concentration and thus the surface recombination velocity is the dominating parameter for the dark saturation current density  $J_0$ . The low  $J_0 = 18$  to 38 fA/cm<sup>2</sup> measured on textured test samples seem promising for the application on the front side of solar cells.

The simulation of the recombination behavior in dependence of the process parameters gives additional insight for further development of diffusion processes. For the investigated diffusion processes, the dopant profiles can be accurately described by Gaussian functions and the profile parameters can be expressed as functions of the deposition temperature. This allows for modeling the most important parameters for the application in solar cells for different processes: the surface concentration  $n_{surf}$ ,  $R_{sh}$ ,  $J_0$ , and  $\Delta J_{SC}$ .

## 7 Back-Contact Back-Junction Solar Cell with Al-Alloyed Emitter

*In Section 7.2 a new process sequence is introduced and the experimental results of the first proof-of-concept batch are given. To investigate the efficiency potential of the developed cell structure as well as the influence of the newly implemented method of structuring the emitter on the cell performance, numerical simulations are analyzed in Section 7.3. The simulations were carried out by Nico Wöhrle with the simulation software Sentaurus Device [20].*

### 7.1 Introduction

One aim of this doctoral thesis is the improvement of the solar cell manufacturing process described in Chapter 2.5. Although forming the FSF with the in-situ diffusion / oxidation step described in Chapter 5, led already to a strong reduction in process complexity and recombination at the front side (published in Ref. [102]), the complete process sequence remained complex. Moreover, the probably cost-intensive high thermal budget during the diffusion process, which is necessary in order to obtain a low phosphorus surface concentration at the cell's front side, is not regarded being optimal. In this chapter, a new process sequence is derived leading to a great reduction in process complexity and omitting the necessity of temperatures above 900 °C during oxidation. Since this process sequence emerged at the later part of this doctoral thesis, only one solar cell batch could be realized and, thus, only a proof of concept can be presented without any process optimization.

To show the potential of optimizing this new solar cell structure, two-dimensional numerical simulations are carried out. The implemented experimental results include recombination- and resistivity values as well as carrier profiles extracted from simple test structures. The simulations apply the geometric approaches to reduce the coverage fraction of the aluminum alloyed emitter, partly presented on experimental solar cell structures in this chapter.

### 7.2 Proof of Concept Cell Batch

#### 7.2.1 Desired Solar Cell Process Sequence

The phosphorus diffused surfaces of the BC-BJ solar cell have to fulfill several requirements: the FSF should exhibit a low dark saturation current density  $J_{0,FSF}$  and enable a high internal quantum efficiency at short wavelength (low  $\Delta J_{SC}$ ) – whereby both are generally achievable by low dopant concentrations. For example, Woehl [69] performed a long oxidation process after the diffusion processes for these reasons. The BSF should enable an electrical contact to the metallization with a low resistivity and, at the same time, shield the highly recombination active metal-silicon interface in order to provide a low dark saturation current density on both, the metallized  $J_{0,met}$  and the

passivated  $J_{0,BSFpass}$  silicon surface. In case of the metallized area, a low  $J_{0,met}$  is generally reached by a high near surface dopant concentration. For example, Woehl selected a comparably high BSF doping-level, that exhibited a high surface concentration of  $1.9 \cdot 10^{20} \text{ cm}^{-3}$  after the long oxidation step and a very low sheet resistance of  $2 \Omega/\text{sq}$ , corresponding to a low contact resistance, but a high recombination activity due to enhanced Auger recombination and moreover, significant free-carrier absorption.

To overcome the restrictions concerning the simultaneous doping of an appropriate FSF and BSF and to decrease the process complexity to an industrially relevant scale, a new process sequence is derived (Figure 7.1). The new process sequence results in a slightly different solar cell structure.

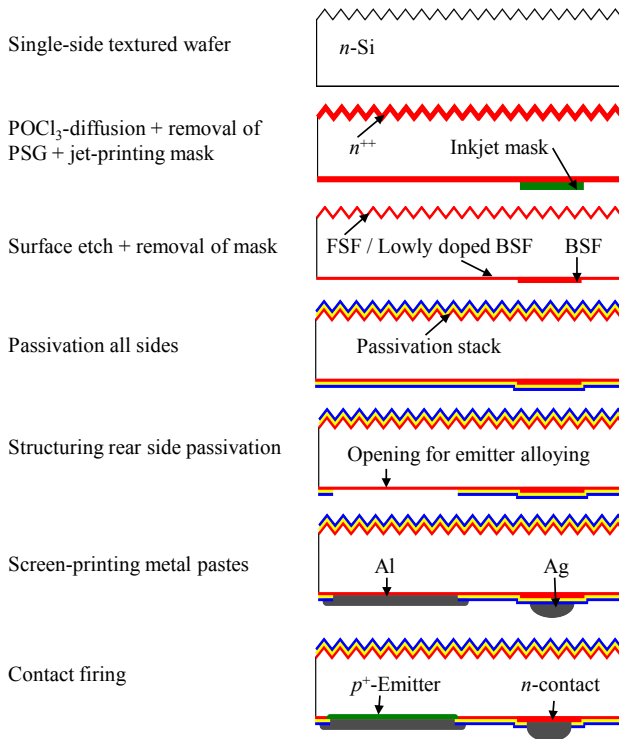
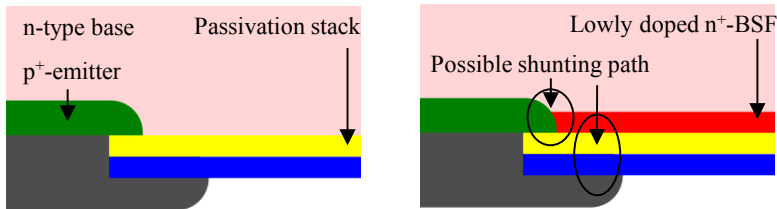


Figure 7.1 Modified solar cell process sequence in focus of this thesis. The  $n^+$ -regions (FSF and BSF) are formed in one single diffusion step, whereas the  $p^+$ -emitter forms during contact firing.

The main alteration in respect to the former sequence (see Figure 2.6) is that the BSF is formed in a  $\text{POCl}_3$  diffusion on all wafer surfaces, whereas, after diffusion, the electrical properties of the FSF are defined by careful back-etching the highly doped surface, while the BSF is locally protected by an inkjet-printed mask resin [112]. This reduces the number of tube furnace steps featuring high thermal budget by two, overcomes the necessity of diffusion barriers, and could be physically beneficial: It is expected that the double-sided phosphorus diffusion enables a more efficient gettering of impurities present in the bulk of the material than single-sided phosphorus diffusion [113]. Additionally, a possible contamination with impurities originating in the cleaning procedure or deposition of the diffusion barriers is avoided.

Apart from passivation, no deposition, thermal growth or removal of dielectric layers is necessary reducing the number of process steps greatly. Due to low reproducibility, structure definition, and industrial relevance, the screen-printing of masks is replaced by inkjet-printing of a resin [114] whose advantages like non-contact and high accuracy are more and more in question for solar cell production [115]. For simplicity of the alignment and structure definition, by applying the same resin as etching mask in an HF-based etching solution, the passivation layer is wet-chemically opened. The latter method is utilized instead of laser ablation which would be presumably the choice in industrial production.

The structure's modification forms two potential shunting paths which need to be considered (compare Figure 7.2). The first path might arise from the adjacent highly doped surfaces ( $p^+$ -emitter and lowly doped  $n^+$ -BSF). Non-ideal short circuits between  $p$ -electrode and  $n^+$ -BSF might be the second one. The impact of this design is investigated in Section 7.2.3.



*Figure 7.2 Schematic drawing of the emitter edge for a solar cell without high-doping in the gap (left) and the solar cell resulting from the new process sequence (right). For the latter, the  $n^+$ -BSF is directly adjacent to the  $p^+$ -emitter and underlies the  $p$ -electrode. The special structure leads to two possible shunting paths which are highlighted as well.*

Further restrictions of this solar cell technology are the relatively high  $J_{0e}$  of the aluminum emitter, responsible for 48 % of the overall dark saturation current density

of the best solar cell in Ref. [69]. Moreover, the internal reflection of an aluminum-alloyed rear side is low, which will be investigated in Section 7.2.4.

Additionally, there exists a specific trade-off concerning the contact firing step. While for a low  $J_{0e}$ , and low recombination losses, respectively, an approx.  $10\ \mu\text{m}$  deep Al- $p^+$ -layer (compare Figure 2.8 and Ref. [69]) and thus a high thermal budget is beneficial, for the formation of an electrically conductive Ag-contact, lower peak-temperatures and exposure times are desired and generally applied for commercial silver pastes. This influence is investigated in Section 7.2.2.

The thickness of the formed Al- $p^+$ -layer increases with decreasing ratio between contact area of Al to Si and overall Al area [69] due to the higher amount of paste available per alloying area. One option to reduce the temperature during contact firing without reducing the thickness of the emitter is the reduction of the contact coverage while maintaining metal coverage (Figure 7.3). Additionally, the latter option reduces the emitter coverage of the cell's rear side and, in consequence, the effective  $J_0$  as long as the lowly doped BSF exhibits a significantly lower  $J_0$  than the non-passivated Al-emitter, which is the case here. This is in contrast to a sole reduction in emitter width leading to a smaller pitch, which would increase the surface fraction of the highly recombination active contacted BSF (compare Figure 7.2.8 and discussion there). In this work, the cell's emitter coverage fraction  $EC$  is varied by introducing line shaped openings of the rear side dielectric layer at the same metal coverage and pitch distance. The influence of this procedure on the cell performance is extracted from simulations and discussed in Chapter 7.3.

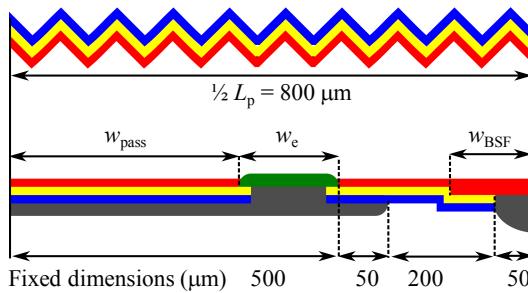


*Figure 7.3 Schematic cross section of the solar cell with structured emitter. The screen-printing of the metals is the same for all solar cells in this work. The variation is defined by the utilized inkjet masks. These feature a variation in the width of the BSF  $w_{\text{BSF}}$ , the width of the passivated area underneath the p-electrode  $w_{\text{pass}}$ , and, in consequence, lead to a variation in the width  $w_e$  of the line-shaped emitter.*

As stated in Section 2.6, another possibility is to mix defined boron content into the Al-paste. Corresponding emitters feature higher dopant concentrations at the same Al-doping profile reducing  $J_{0e}$  [72] for shallow profiles due to the enhanced field effect.

This allows for reducing the thermal budget during contact firing even further. Additionally, the specific contact resistance between the emitter and the aluminum is expected to decrease due to the higher acceptor density. In this work, AIB-powder is mixed to the Al-paste and applied to the solar cells. The simulation study in Chapter 7.3 applies Al-B-profiles fitted to experimental data.

## Experimental setup

Solar cells are fabricated according to the flow chart depicted in Figure 7.4.

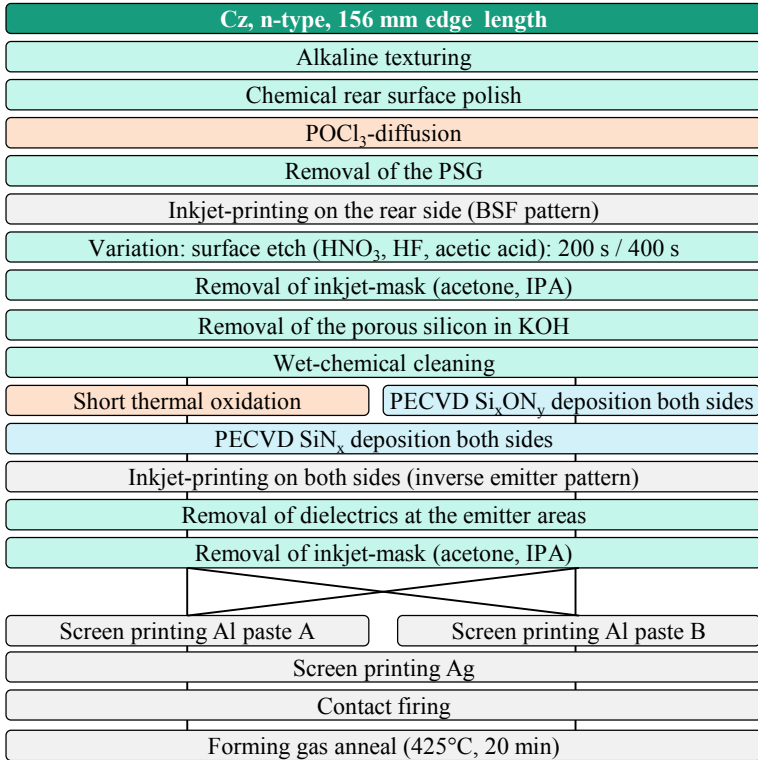


Figure 7.4: Process plan of the investigated solar cells. The high-temperature steps carried out in a tube furnace are marked orange, the PECVD depositions blue, and the wet-chemistry steps green. The Al-paste is double printed. Besides, symmetrical lifetime samples were produced, featuring the same base material, phosphorus-diffused surfaces, and passivation layers as the solar cells. The samples were diffused, etched, and passivated together with the solar cells in the same process-runs.

The substrate is *n*-type Cz-Si material with a specific resistance of  $\rho_0 = (3.5 \pm 0.4) \Omega\text{cm}$  after high-temperature treatment and the related anneal of thermal donors as well as a thickness of  $W = (156 \pm 6) \mu\text{m}$  after texturing and rear side polish.

The aim of this experiment is to investigate the feasibility of the new solar cell process sequence. Therefore three process variations are implemented:

- For passivation of the surfaces on the one hand, a short thermal oxidation is carried out, growing a  $\text{SiO}_2$  layer with a thickness of approx. 10 nm. On the other hand, an equally thin layer of  $\text{SiO}_x\text{N}_y$  [91] is deposited by PECVD on both sides of the wafers. Independent from the passivation layers in direct contact with the silicon, all wafers are PECVD-coated with a  $\text{SiN}_x$ -ARC layer featuring a thickness of approx. 65 nm on the front and 80 nm on the rear side. In the following, the solar cells are denoted as *Oxide* and *SiriON*, accordingly.
- Two different aluminum pastes are applied: Paste A is a recent Al-paste of unknown composition, which is used for manufacturing PERC-type solar cells. Paste B is a former product which is utilized for the same application, where for this batch 0.9 %<sub>weight</sub> of AlB-Powder were added, as described in Ref. [72].
- For the careful back-etching of the BSF in a solution containing  $\text{HNO}_3$ , HF, and acetic acid  $\text{CH}_3\text{COOH}$  [116], two different etching times are chosen in order to investigate lowly doped FSF/BSF regions with a high passivation quality and their possible shunting behavior. In the following, the solar cells are denoted as *ShallowEtch* and *DeepEtch*, accordingly.

Seven solar cells are located on each wafer. Table 7.1 depicts the emitter width  $w_e$ , the width of the passivated area underneath the aluminum  $w_{\text{pass}}$ , the emitter coverage fraction  $EC$ , and the width of the highly doped BSF  $w_{\text{BSF}}$  in dependence of the cell structure as used for the cell preparation (compare Figure 7.3).

*Table 7.1 Dimensions of the solar cells applied on each wafer as investigated in this work. All solar cells exhibit a pitch distance of 1.6 mm, an edge length of 5 cm, and a width of the Ag-contact of  $(97 \pm 10)$   $\mu\text{m}$ . Characterization results of solar cell 1 are not given in this work.*

Structure	Emitter $w_e$ ( $\mu\text{m}$ )	Emitter passivation $w_{\text{pass}}$ ( $\mu\text{m}$ )	EC (%)	Width BSF $2w_{\text{BSF}}$ ( $\mu\text{m}$ )
2 and 4	500	-	62	200
3	500	-	62	350
5	200	300	25	350
6	350	150	44	200
7	350	150	44	350

The emitter coverage is adjusted by varying the width of the emitter line opening at a constant pitch distance of 1.6 mm and constant aluminum coverage with an approx. width of the Al-fingers of 1.05 mm. Therefore, cells with (cells 5 to 7) and without (cells 2 to 4) passivation underneath the center of the aluminum contact are prepared. In the case of cells featuring an emitter coverage of 44 and 62%, the width of the BSF is varied as well.

An image of the rear side of a wafer is given in Figure 7.5.

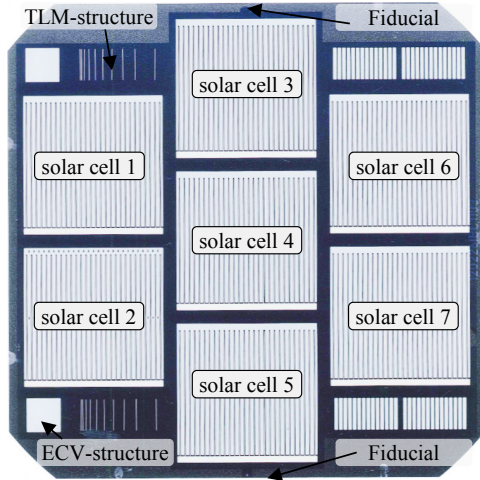


*Figure 7.5 Optical scan of the wafer's rear side. 7 different solar cell structures together with TLM-, ECV- and line resistance structures are fabricated on the same wafer. The optical system of the screen-printer uses two fiducials for the alignment of the contacts, which are defined by the inkjet-mask before opening the passivation stack. The solar cells exhibit an edge length of 5 cm (inclusive busbars).*

## 7.2.2 Analysis of Different Process Steps

### Phosphorus diffusion and etching

For phosphorus diffusion a thermal process featuring  $\text{POCl}_3$  is chosen that leads to a comparably deep profile (compare Figure 7.6) with a physical junction depth of approx. 800 nm, a surface dopant concentration that presumably exceeds the activation limit [110], and a sheet resistance of  $(33 \pm 2) \Omega/\text{sq}$ .

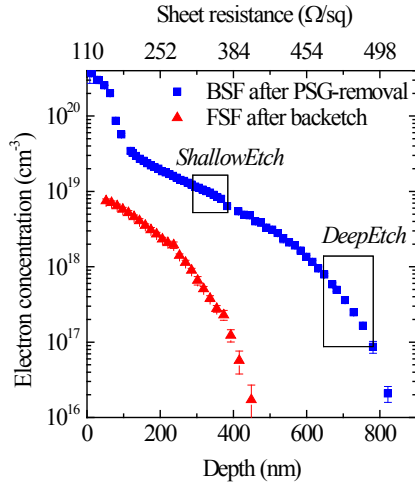


Figure 7.6 ECV measurement of the electron profile after diffusion (BSF) and subsequent back-etch (FSF) of a planar reference sample. The calculated ranges of the etch depth, utilized for the fabricated solar cells, are marked in rectangles.

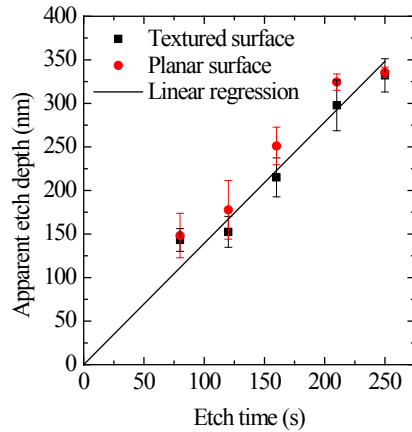


Figure 7.7 Apparent etch depth over etching time for the textured and planar samples, respectively. Error bars denote the standard deviation over the wafer (inline inductive-coupling sheet resistance measurement, compare Figure 2.3). From the linear regression an etching rate of 1.4 nm/s is extractable.

The process is chosen, first, due to its high sheet resistance homogeneity over the wafer and the process boat. Since, beforehand, the etch rate of the back-etch procedure is not evaluated, the second criterion is the high depth of the profile in order to enable a broad process window for the back-etch. The third aspect is the super-saturation of the near surface doping to ensure low resistive Ag-contacts, being less sensitive to the Ag paste composition and firing conditions. The possible disadvantages are a high peak temperature of the diffusion process of 950°C and a high expected  $J_{0,BSFpass}$ .

To find an applicable etching time, several samples with alkaline textured and with saw damage etched surface (additional wafers and symmetrical lifetime samples) are exposed to the etching solution for different time spans. The etching solution consists of HF, HNO<sub>3</sub>, CH<sub>3</sub>COOH and deionized water with volume fractions of 9:205:295:245. The resulting porous silicon at the sample surface is subsequently removed in a KOH solution with a concentration of 30g/l for 10 s. Both steps are carried out at room temperature (approx. 20 °C). The comparison of the measured decrease in conductivity with the calculated decrease in conductivity of the non-etched profile calculated by Eq. (5.1) leads to a nearly linear dependence of the etch depth upon the etch-time (Figure 7.7) and, thus, to an etching rate  $r$  of  $(1.4 \pm 0.2)$  nm/s.

For the solar cells etch-times of 200 s (*ShallowEtch*) and 400 s (*DeepEtch*) are chosen. These etch times lead to a calculated etch depth of  $(337 \pm 48)$  nm and  $(714 \pm 68)$  nm on the corresponding symmetrical lifetime samples of the solar cell batch, respectively. The respective uncertainty is the standard deviation between different samples. For the solar cell samples, after creating the porous silicon layer in the etching batch, the jet-printed resin is removed by sequentially performed dipping-processes in acetone and IPA baths. Subsequently the porous silicon layer is removed in the KOH solution for 10 s. The removal of the jet-printed resin before the application in the KOH solution is necessary, because it dissolves in alkaline solutions and potentially affects the etching of the porous silicon.

### **Influence of high temperature treatment on the bulk carrier lifetime**

The passivated lifetime samples show significant differences according on whether they are passivated with thin thermally grown  $\text{SiO}_2$  or PECVD  $\text{SiO}_x\text{N}_y$  layers. Notice that the investigated passivation layers are both additionally coated with a PECVD  $\text{SiN}_x$ -layer. The samples are fabricated in parallel to the solar cells and on the same material. They are exposed to the same process sequence as the front side of the solar cells except for being laid onto the wafer table of the inkjet printer of which the influence is regarded to be negligible. After thermal oxidation,  $\text{SiN}_x$  deposition and fast-firing, the wafers indicate effective lifetimes, which are measured with QSSPC in the wafer center, of  $\tau_{\text{corr}} = (180 \pm 60)$   $\mu\text{s}$  at  $\Delta n_{\text{av}} = 10^{15}$   $\text{cm}^{-3}$ . The PL-signal reveals a severe ring-shaped reduction in carrier lifetime from the wafer edges to the center (Figure 7.8, a). This is observed for all diffused samples which are exposed to the short thermal oxidation. In contrast, the samples fabricated according to the SiriON passivated solar cells exhibit a homogeneous distribution of high lifetime along the wafer, in fact  $\tau_{\text{corr}} = (3.1 \pm 0.1)$  ms at the same injection density.

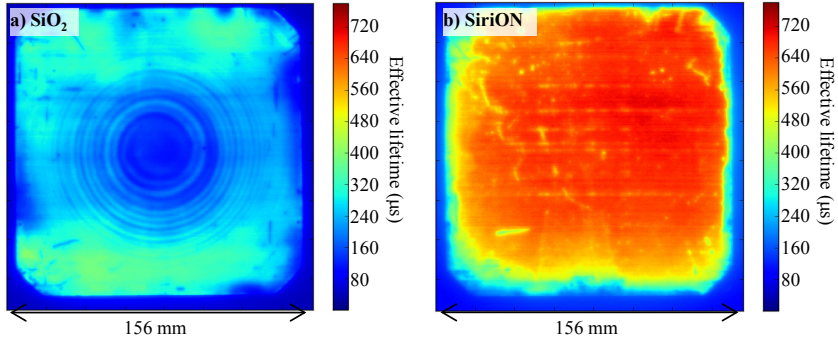


Figure 7.8. QSSPC-calibrated luminescence images of lifetime samples, fabricated in parallel to the solar cells featuring the FSF, passivated with thin thermal  $\text{SiO}_2$  (a) or SiriON (b). The images are taken at an illumination density of approx. 1 sun. Thus, sample b) is measured at high injection density and limited by Auger-recombination, whereby sample a) is measured at low injection and limited by defect recombination.

The ring-shaped reduction of the bulk carrier lifetime of Cz-Si after several high temperature steps is a commonly observed effect [117] related to the oxygen content in the Cz-Si wafers. In this experiment, a diffusion process involving a high temperature step at 950 °C and a thermal Oxidation at 840 °C is chosen. Following experiments showed that this effect can be avoided by performing a diffusion process at lower temperature or the application of different Cz-Si material, for example. Thus the reduction of the base carrier lifetime is not inherent to the solar cell manufacturing process.

### Recombination parameter of the diffused surfaces

The apparent  $J_0$  of the differently passivated symmetrical lifetime samples over the calculated etch depth is presented in Figure 7.9 for planar and textured surfaces. Despite the low bulk carrier lifetime of the  $\text{SiO}_2 + \text{SiN}_x$  passivated samples, the evaluation method *diffusion\_corr* (compare Chapter 3) enables reliable determination of  $J_0$  at high injection levels.

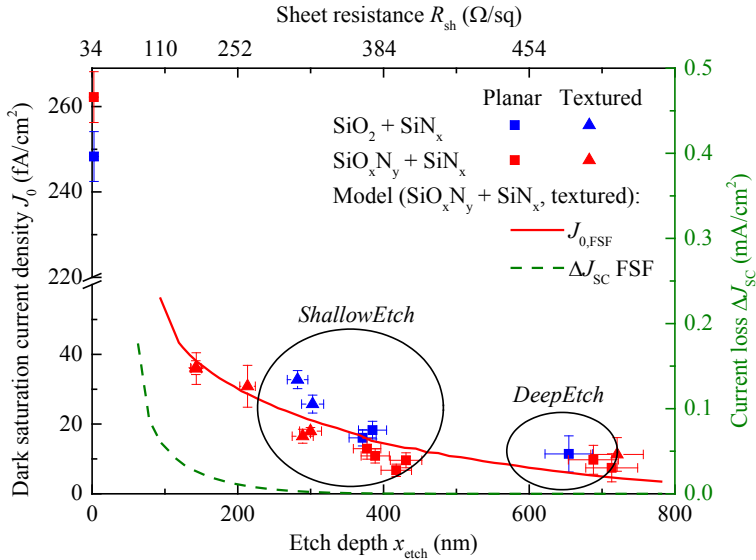


Figure 7.9. Apparent dark saturation current density extracted from QSSPC on symmetrical lifetime samples over the calculated etch depth and the measured sheet resistance (top axis). Lines correspond to the calculation after Eq. (2.32) for the parameterization of  $S_p$  after Table 5.1 (data set for alkaline textured and PECVD SiriON passivated surfaces). The loss in the cell's short circuit current density  $\Delta J_{sc}$  due to the recombination of minority carriers generated in the FSF after Eq. (2.33) is depicted as well.

For the group *ShallowEtch*, the lifetime samples indicate a reasonable low  $J_{0,FSF} < 30$  fA/cm<sup>2</sup> on textured and  $J_{0,BSF_{low}} < 20$  fA/cm<sup>2</sup> on planar surfaces. For the group *DeepEtch*, the apparent  $J_0$  of both regions is below 20 fA/cm<sup>2</sup>, and no difference between the surface topographies can be observed within the measurement uncertainties. In contrast, the planar, oxide-passivated area of the initial BSF indicates a rather high  $J_{0,BSF_{pass}}$  of  $(248 \pm 6)$  fA/cm<sup>2</sup>, and the SiriON passivated samples a comparable  $J_{0,BSF_{pass}} = (262 \pm 6)$  fA/cm<sup>2</sup>.

For comparison with the results obtained in Chapters 5 and 6, the simulation results of  $J_0$  over etch depth, which were extracted by applying Eq. (2.32) and the parameterization of Table 5.1 for textured and PECVD SiriON passivated surfaces, is shown. The measured data are in agreement with the simulation results. The calculated current loss  $\Delta J_{sc}$ , which is calculated after Eq. (2.33) for carriers generated in the FSF, shows that an excellent quantum efficiency in the short wavelength range can be achieved with the back-etched profile for etch depth higher than 100 nm.

## Contact firing

To find applicable firing conditions one group of SiriON passivated samples is exposed to a variation of contact firing processes after screen-printing. For each process two wafers are used: one to measure the temperature-time curve with two thermocouple elements placed on two different solar cell structures and the other to evaluate the resistance of the Ag-contact to the BSF with TLM on the test structures shown in Figure 7.5. The validated parameter is the normalized contact resistance  $R_C W_C$  with the contact resistance  $R_C$  and length  $W_C$  of one contact stripe. Note that the TLM-samples are fabricated accordingly to the  $n$ -contact structure of the solar cells and, thus,  $R_C W_C$  is directly applicable to the series resistance contribution to the final solar cells.

A typical temperature-time profile of the firing process is shown in Figure 7.10. A sharp temperature peak is observed, indicating that the sample does not reach an equilibrium state depending solely on the heat influx and dissipation but rather a transient state which is influenced by the exposure time in the different heat zones.

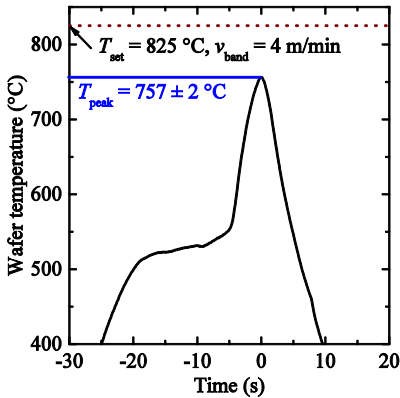


Figure 7.10 Temperature - time profile of a thermocouple element placed on a solar cell for a set temperature of  $T_{\text{set}} = 825^\circ\text{C}$  and a band velocity of  $v_{\text{band}} = 4\text{ m/min}$ .

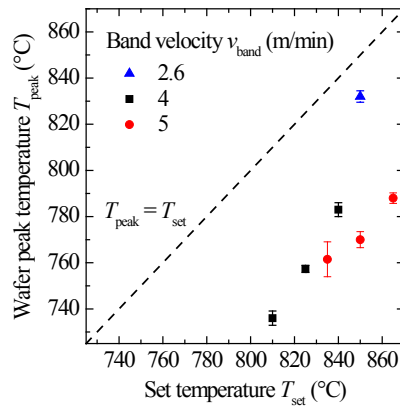


Figure 7.11 Measured peak wafer temperature  $T_{\text{peak}}$  over set temperature  $T_{\text{set}}$  for the different applied band-velocities. Error bars denote the standard deviation of the wafer peak temperature measured by two differently located sensing elements upon one wafer.

In Figure 7.11 the measured peak temperature  $T_{\text{peak}}$  versus the set temperature  $T_{\text{set}}$  for three different band-velocities is depicted. In agreement with the findings above,  $T_{\text{peak}}$  of the wafer at a given  $T_{\text{set}}$  decreases with increasing band velocity.

The corresponding normalized contact resistance of the Ag-contacts over  $T_{\text{peak}}$  is shown in Figure 7.12.

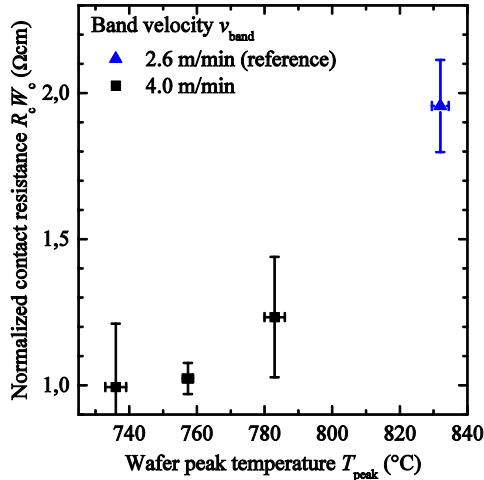


Figure 7.12: Normalized contact resistance  $R_C W_C$  of the Ag-contacts over peak wafer temperature  $T_{\text{peak}}$ . Shown are the median values over 4 to 8 samples for each contact firing condition. Error bars denote the standard deviation over the group.

In the investigated range, the normalized contact resistance increases with increasing peak temperature. At  $T_{\text{peak}} = (757 \pm 2)^\circ\text{C}$  (corresponding to  $T_{\text{set}} = 825^\circ\text{C}$ ) and  $v_{\text{band}} = 4 \text{ m/min}$  it reaches  $R_C W_C = (1.0 \pm 0.1) \Omega\text{cm}$  which is a promising value for the application in the solar cell. However, these firing conditions result in a wafer peak temperature well below  $T_{\text{peak}} = (832 \pm 3)^\circ\text{C}$ , as measured for the reference process at  $T_{\text{set}} = 850^\circ\text{C}$  and  $v_{\text{band}} = 2.6 \text{ m/min}$ . Thus, the electrical contact resistance on the modified BSF is reduced while the thermal budget during firing is decreased.

The firing parameters of the reference process were chosen in Ref. [69, 102] for the formation of an approx.  $10 \mu\text{m}$  deep Al-emitter. Cross sections of solar cells from the same wafer fired with  $T_{\text{set}} = 825^\circ\text{C}$  and  $v_{\text{band}} = 4 \text{ m/min}$  were investigated with SEM to evaluate the thickness of the  $p^+$ -region in dependence of the emitter structure. As an example, the cross-sectional SEM-image of solar cell structure 5 ( $w_e = 200 \mu\text{m}$ ) is shown in Figure 7.13. The resulting thickness of the  $p^+$ -regions over the width of the emitter opening is shown in Figure 7.14.

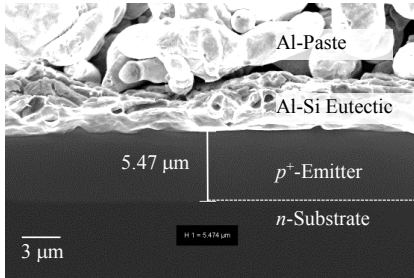


Figure 7.13: SEM image of a cross section of solar cell 5 (nominal emitter width  $w_e = 200 \mu\text{m}$ ) utilized to measure the thickness of the Al-alloyed  $p^+$ -region. The dashed line indicates the position of the  $p$ - $n$ -junction.

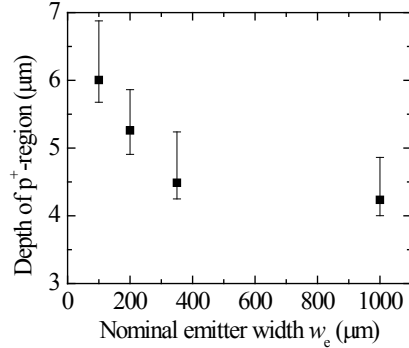


Figure 7.14 Thickness of  $p^+$ -region over width of the emitter opening in the center of the alloyed region. Error bars denote the range of deviation over the emitter region (maximum, minimum).

The depth of the  $p^+$ -region increases with decreasing emitter width  $w_e$  from  $4.2 \mu\text{m}$  for the non-structured emitter up to  $6.0 \mu\text{m}$  for the smallest contact opening of  $w_e = 100 \mu\text{m}$ . This is in agreement with the findings in Ref. [70], where the increasing thickness for smaller screen-printed structures in comparison to full-area alloying is related to the higher amount of Al-paste per emitter area available for the alloying process. A confirmation is found on the investigated samples of this work (not shown here): the formed emitter is deeper towards the center (in direction of the passivated area under the Al) than towards the outer edges (in direction of the  $n$ -contact), which leads to slightly increased error bars for the structured emitters in Figure 7.14.

Even for the non-structured emitter, the thickness of the  $p^+$ -region exceeds  $4 \mu\text{m}$  at nearly all regarded points. Figure 2.8 indicates that, for the applied paste with AIB additive,  $J_0$  starts to converge to its lower level for a profile thickness above  $4 \mu\text{m}$ . In consequence, all further investigated solar cells are exposed to the same contact firing step with a set temperature of  $825^\circ\text{C}$  and band velocity of  $4 \text{ m/min}$ .

### 7.2.3 Parallel Resistance

PECVD SiriON passivation leads to a high lifetime and low  $J_0$  on the symmetrical lifetime samples. However, all the solar cells fabricated in the experiment featuring this passivation scheme exhibit very low  $FF$ - and  $V_{OC}$ . The dark I-V-curves of the differently passivated cells are exemplarily shown in Figure 7.15. Notice that the cells are characterized by applying reverse (left) and forward bias (right).

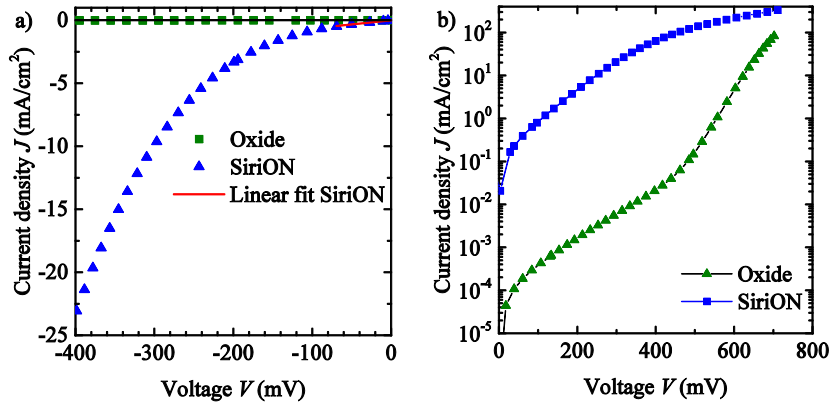


Figure 7.15 Exemplary dark I-V curves for an oxide passivated and a SiriON passivated solar cell of the same structure (EC = 62%) under reverse (a) and forward bias (b). In the case of the SiriON passivated solar cell, the data fit according to Eq. (7.1) for the estimation of  $R_p$  is shown.

According to the 1-D-model, low  $FF$  can be attributed to low  $R_p$  originating in a low electrical resistance between the  $p$ - and  $n$ -contact. As an estimation of  $R_p$ , the dark I-V curve of some samples is fitted in a small voltage range ( $V \rightarrow 0$ ) where the slope of the dark I-V-curve is reasonably constant. The parallel resistance is then calculated as the effective resistance of this structure by

$$R_p = \frac{V}{J} \Big|_{V \rightarrow 0} \quad (7.1)$$

where  $V$  is the measured voltage of the device and  $J$  the current density per cell area. The estimated  $R_p$  of several SiriON passivated solar cells is around  $100 \Omega\text{cm}^2$  (Figure 7.16). No correlation with the emitter coverage, the emitter structuring, or the etch depth is observed. In contrast, the oxide passivated solar cells show an  $R_p$  above  $10^5 \Omega\text{cm}^2$  – no influence on  $FF$  and thus cell performance is expected (compare Figure 7.26).

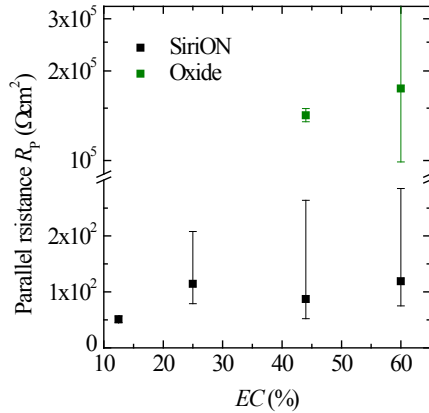


Figure 7.16: Parallel resistance extracted from the dark  $I$ - $V$  curves by Eq. (7.1). All PECVD SiriON passivated solar cells show very low  $R_p$ . No correlation with the emitter structure can be observed. All oxide passivated samples show high values above  $10^5 \Omega\text{cm}^2$ .

An analysis of SEM images of the emitter-edge region of the corresponding solar cells (Figure 7.17), gives a possible explanation of low  $R_p$  of SiriON passivated structures.

On the left hand side, a typical cross section of an oxide passivated solar cell is shown. The emitter region at the edge of the opening shows a thickness of approx.  $3.6 \mu\text{m}$ , which is comparable to the thickness of the emitter region in the center of the emitter opening. In contrast, the same emitter region of SiriON passivated solar cells (right hand side) shows a greatly reduced thickness and the eutectic layer seems to be in contact with the substrate at the outer etch. Apart from the edges, alongside the emitter opening of 8 different samples, no region of substantially reduced emitter thickness is found in the SEM-analysis neither on Oxide nor on SiriON passivated solar cells (compare Figure 7.14). Thus the effect shown in Figure 7.17 is presumably the origin of the reduced parallel resistance of the SiriON passivated solar cells.

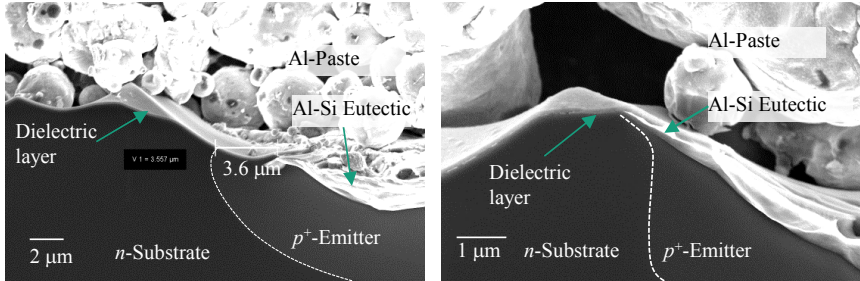
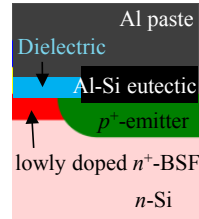


Figure 7.17 SEM scan of the cell's cross section at the edge of the emitter of an oxide passivated solar cell (upper left) and a SiriON passivated solar cell (upper right). While the eutectic layer of the oxide passivated sample is separated from the silicon base by several micrometers of emitter, at the SiriON passivated sample it has grown under the passivation layer and is in close contact to the base substrate. The latter might be a possible current path which leads to the observed low shunt resistance. Right: schematic of the regarded region.



The question remains if the observed behavior of the eutectic growth is fundamentally influenced by the thermally grown  $\text{SiO}_2$  layers or the PECVD deposited  $\text{SiO}_x\text{N}_y$  layers. Figure 7.18 shows SEM scans of the passivation layers between the metal fingers of an oxide passivated (left) and at the edge of the emitter opening of a SiriON passivated (right) solar cell.

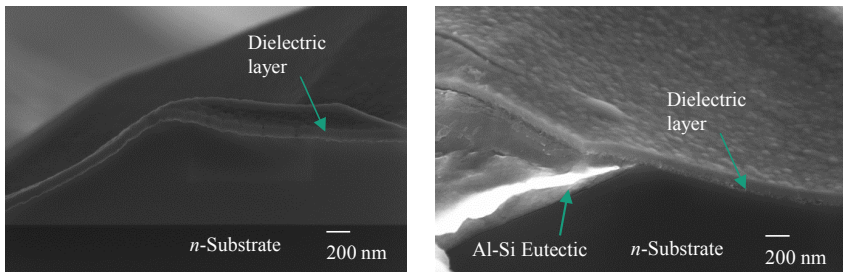


Figure 7.18 SEM scan of the passivation layer on the silicon base of an oxide passivated solar cell (left) and a SiriON passivated solar cell (right). While the first is in close contact to the base, the latter is lifted partially and shows voids at the surface.

The SiriON passivation stack seems to be partially lifted from the substrate. The voids within the passivation layer are found on all SiriON solar cells, but not on the corresponding lifetime samples fabricated alongside with the same process sequence as the cell's rear side. The effect of the reduced parallel resistance when replacing the thermal oxide passivation by PECVD  $\text{SiO}_x\text{N}_y$  was observed in the scope of this work

at three different solar cell batches with local aluminum alloyed rear emitter with and without a lowly doped BSF. Therefore, the observations made are significant. However, the present data cannot exclude that the SiriON passivation stack can be adapted to fulfil the requirements for this solar cell structure.

#### 7.2.4 Solar Cell Characteristics

The comparison in this section is taken out on the best cells per group in order to demonstrate the impact of the above described effects on the I-V-characteristics in dependence of the differently fabricated cell types. All I-V-parameters in this section are measured with a busbar shading aperture featuring an active area of  $16.65 \text{ cm}^2$ .

##### Dimensions at the rear side

Since the oxide passivated samples show a low bulk-lifetime, dependent on the location of the solar cell on the wafer, a quantitative comparison between the different layouts is not fully reliable. In consequence, for all thermally oxidized wafers, the solar cell at position 2, located at the edge of the wafer (compare Figure 7.5) exhibits the highest conversion efficiency. The I-V-parameters of the thermally oxidized solar cells are in a narrow range compared with the statistical scattering over different wafers and cell geometries. Thus, the effect of structuring the emitter on the cell's conversion efficiency is analyzed in more detail in a simulation study in Section 7.3. Care has to be taken by comparing the influence of the BSF width  $2w_{\text{BSF}}$  and the emitter coverage fraction  $EC$  on the effective recombination because  $V_{\text{OC}}$  and  $J_{\text{SC}}$  of the solar cell are assumed to be influenced by the spatially varying bulk lifetime (compare Figure 7.8).

A measure of the spatial variation of the bulk lifetime can be found by comparing the solar cells 2 and 4 which exhibit the same structure, but are located at the edge (solar cell 2) and the center of the wafer (solar cell 4). It is found for some groups that the solar cells on the wafers exhibiting the highest conversion efficiency show little variation of the I-V-parameters between cells 2 and 4. We assume that the bulk lifetime of those wafers is varying little and could be high enough to enable the validation of dimensional influences on the solar cell performance.

Table 7.2 depicts the I-V-parameters of cells in dependence of the structure. The cells are passivated with thermal oxide and located on the same well performing wafer.

By comparing cell 2 and cell 3, cell 3 exhibits a higher width of the highly doped BSF. This results in a slight decrease of  $V_{\text{OC}}$  and  $J_{\text{SC}}$ , which is expected due to the higher  $J_0$  of the BSF in comparison to the lightly doped BSF. However, the decrease is well in the range of the measurement uncertainties and cannot be quantified from this measurement since its impact depends strongly on the unknown bulk lifetime.

Table 7.2 Measured I-V-parameters of the solar cells located on the same wafer. The FSF is realized by DeepEtch, passivated with a stack consisting of a thermal SiO<sub>2</sub> and a PECVD SiN<sub>x</sub> layer. The emitter is metalized and formed with Al paste B, containing ALB.

Structure	EC (%)	2w <sub>BSF</sub> (μm)	V <sub>OC</sub> (mV)	J <sub>SC</sub> (mA/cm <sup>2</sup> )	FF (%)	η (%)
2	62	200	639	39.3	80.1	20.2
2*			646	38.6	80.5	20.1
3	62	350	638	39.2	79.9	20.0
4	62	200	640	39.3	80.0	20.1
5	25	350	627	38.3	77.2	18.5
6	44	200	641	39.2	78.7	19.7
7	44	350	641	38.9	79.4	19.8

\* independently measured at Fraunhofer ISE CalLab

Structuring the emitter (cells 5, 6, and 7) leads to a reduced FF for all solar cells. Since the parallel resistance obtained from reverse dark I-V-measurements remains high (compare Figure 7.16), this may be attributed to an increased series resistance due to the reduced contact area of the aluminum.

The solar cell exhibiting the highest conversion efficiency (cell 2, thermal oxide passivated, DeepEtch, Al-paste B) is independently measured by Fraunhofer ISE CalLab with the same aperture as used for all measurements in this chapter. Although the conversion efficiency is in very good agreement, V<sub>OC</sub> and J<sub>SC</sub> obtained by the different measurement setups differ significantly. This difference can be mainly attributed to the advanced temperature control and spectral mismatch of the calibrated measurement and gives a measure for the uncertainty of the presented I-V-parameters in this chapter.

The global I-V-parameters are influenced by heterogeneities which occur partly because of the manufacturing process, which has not been optimized for the present solar cell technology. To evaluate the influence of structuring the emitter, SR-LBIC measurements are carried out on solar cell 4, serving as a reference without emitter structuring, and solar cell 6, which exhibits the same layout at the rear side as cell 4 except for the structuring of the emitter into two stripes, whereby each stripe features a width of 350 μm. The data are acquired in an area of approximately 1 cm<sup>2</sup> in the center of the solar cell with a step width of 25 μm.

Figure 7.19 depicts EQE scans at wavelengths of the laser beam of λ = 780 nm and λ = 1064 nm. Furthermore the J<sub>SC</sub>-maps are shown, obtained by the J<sub>SC</sub> mapping analysis introduced by Padilla *et al.* [43]. Linear interpolation to λ of 300 nm to 1170 nm is performed as described in Ref. [43] to cover the full range of the AM1.5G spectrum relevant for the silicon solar cell.

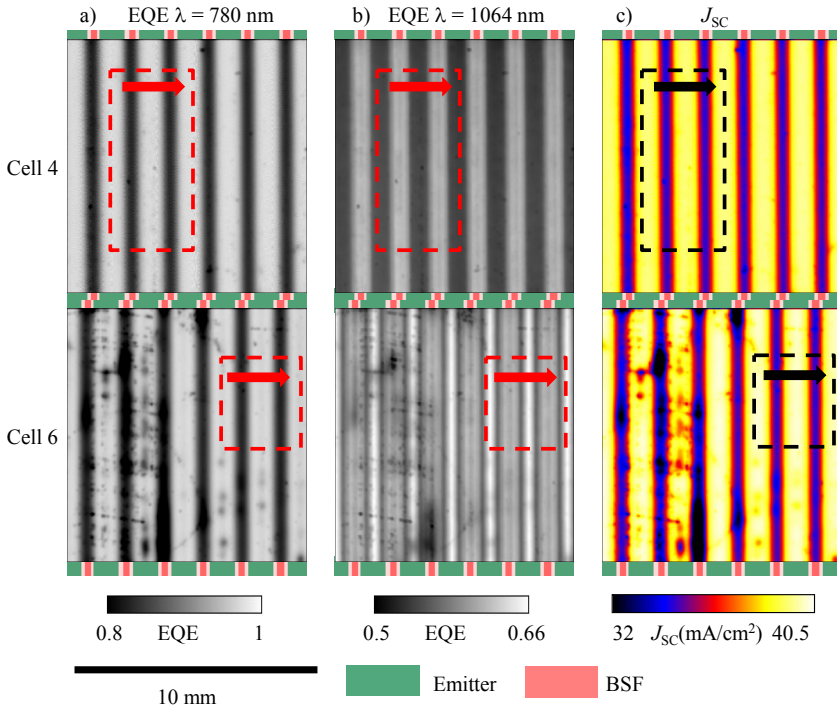


Figure 7.19 SR-LBIC scans of solar cell structure 4 (upper) and 6 (lower) located on the same wafer (global  $I$ - $V$ -parameters are given in Table 7.2). The FSF is realized by DeepEtch, passivated with a stack consisting of a thermal  $\text{SiO}_2$  and a PECVD  $\text{SiN}_x$  layer, metallized with Al-paste B. Shown are the local external quantum efficiency EQE at a wavelength of a) 780 nm, b) 1064 nm and c) the local short circuit current density  $J_{sc}$ . The regions used to obtain line-scans for the following figures by averaging the EQE parallel to the finger structure are marked with rectangles. The arrows denote the direction of the line scan's lateral dimension. To help interpreting the images, the rear electrodes of the solar cells are drawn schematically.

Several heterogeneities are observed for cell 6. These can be attributed mainly to scratches on the front side of the solar cell which influence the signal by both, optical artifacts and enhanced recombination at the front side. For each solar cell a rectangular region which shows few disturbances is chosen to obtain line-scans of the shown quantities by averaging the EQE parallel to the finger structure.

Figure 7.20 depicts the line-scans of the local EQE of solar cells 4 and 6 at a)  $\lambda = 780$  nm and b)  $\lambda = 1064$  nm.

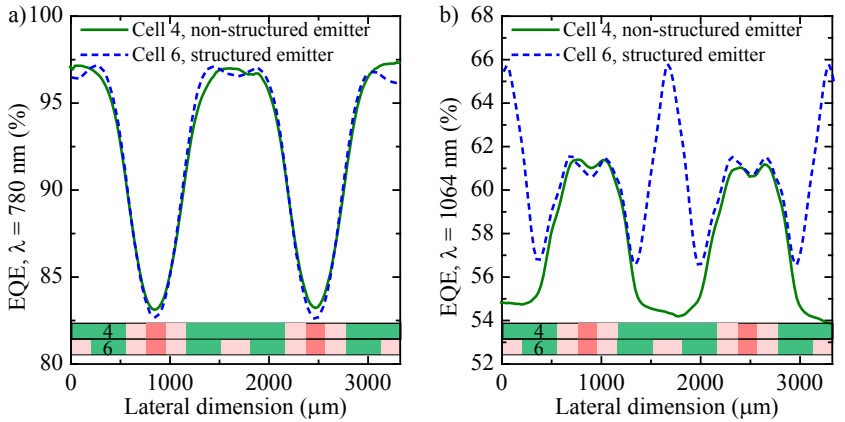


Figure 7.20 EQE line-scan average obtained by SR-LBIC measurements for solar cells 4 and 6 evaluated by averaging the EQE parallel to the finger structures (compare Figure 7.19). To assist interpretation, the rear side doping of the solar cells is drawn schematically.

■ Emitter  
■ Highly doped BSF  
■ Lowly doped BSF

For  $\lambda = 780$  nm, the absorption length in crystalline silicon is approximately  $10 \mu\text{m}$ . Thus nearly all the light is absorbed before reaching the rear side of the solar cell. Therefore, the lateral variation is dominated by the collection efficiency of the cells and not significantly influenced by the optical reflection at the rear side.

For both solar cells, it is observed that the collection efficiency is decreased above the highly doped BSF. This effect is known as *electrical shading* and depends on the recombination activity of the FSF, the base substrate, of the BSF, and of the distance to the emitter [118]. Due to its relatively high  $J_0$ , the highly doped BSF has the highest impact on the EQE within this region. As expected, no difference can be observed in this area between solar cell 4 and 6. Solar cell 4 reaches a maximum local EQE in the center of the emitter where the carriers are generated most distantly from the highly doped BSF. In contrast, solar cell 6 shows a small local minimum at the center of the emitter area. This can be explained by additional electrical shading due to the locally structured emitter: the carriers generated at the center have an additional lateral distance of  $150 \mu\text{m}$  to the emitter and an additional recombination path arising from the lowly doped BSF underneath the passivation at the rear side. However, since the lowly doped BSF exhibits a very low  $J_0$ , the additional electrical shading is small in comparison to the electrical shading in the area of the highly doped and partly contacted BSF.

For  $\lambda = 1064$  nm, the absorption length in crystalline silicon is approximately  $900 \mu\text{m}$ . It can be assumed that most photons traverse the solar cell and are multiply internally

reflected at the rear- and the front side of the solar cell. Accordingly, the average EQE of both solar cells is lower at these longer wavelength due to the photon's additional possibility of being re-emitted (escaping the solar cell), absorbed without creating electron-hole pairs, e.g. at the Al-Si eutectic or the Ag-contact, or absorbed in the Al-emitter with its low collection efficiency. Both solar cells reach an EQE of approximately 61 % at the  $n$ -doped rear side area. A small decrease in the EQE is observed directly above the highly doped BSF. This decrease can be attributed, on the one hand, to the lower internal reflectance of the screen-printed contact compared to the passivated area, and, on the other hand, to free carrier absorption within the highly doped BSF. From the edges of the emitter in direction of the emitter center the EQE decreases. This is in contrast to the EQE at shorter wavelength and can be attributed to the low internal reflectance of the aluminum alloyed rear side. For solar cell 4, the EQE reaches a plateau of approximately 55 % above the emitter area. In contrast, the EQE of solar cell 6 increases until it reaches a maximum peak of approximately 65 % in the center of the structured emitter. Since the minority collection probability of those regions was shown to be slightly decreased compared to the non-structured emitter, this increase can be directly attributed to the higher internal reflectance of the passivated rear side compared to the Al-alloyed emitter.

The results show, that, on the one hand, the collection probability at the structured emitter is slightly lower due to the enhanced path length of the minority carriers to the emitter and, on the other hand, the increased internal reflection increases the EQE for higher wavelengths.

To quantify the net effect for the solar irradiation spectrum AM1.5g, Figure 7.21 depicts the line-scan of a) the local  $J_{SC}$  for both solar cells in the same regions as used for the line-scans of the EQE as well as b) the local difference between the solar cells:  $\Delta J_{SC} = J_{SC}(\text{cell 6}) - J_{SC}(\text{cell 4})$ .

The local  $J_{SC}$  in the area of the  $n$ -doped rear side is approximately the same for both solar cells. The structured emitter shows a maximum of  $J_{SC}$  in the center between the emitter stripes which indicates that the higher internal rear side reflectance overcompensates the lower collection probability in this area. It is interesting that the local  $J_{SC}$  of solar cell 6 exceeds 40 mA/cm<sup>2</sup> in the emitter area. This shows that a structured Al-emitter together with the back-etched FSF and lowly recombination active BSF is well suited to reach very high current densities and that the limiting part of the solar cell in terms of carrier collection is in this case the highly doped BSF, which is contacted by screen-printing.

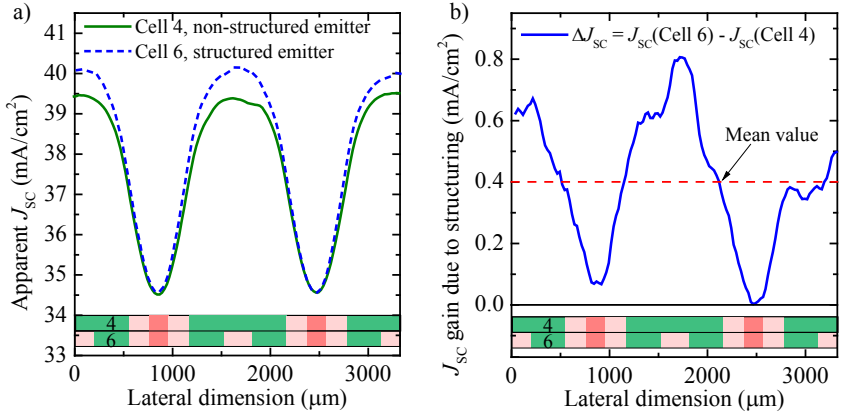


Figure 7.21 a) Local  $J_{sc}$  line-scans evaluated by LBIC measurements for solar cells 4 and 6 obtained by averaging parallel to the finger structures (compare Figure 7.19). b) Local difference  $\Delta J_{sc}$  between the two cells. In order to assist the interpretations, the rear side doping of the solar cells is drawn schematically.

■ Emitter  
■ Highly doped BSF  
■ Lowly doped BSF

The local difference of  $J_{sc}$  between both cells shows a maximum of  $0.8 \text{ mA/cm}^2$  and an average over the whole region of  $0.4 \text{ mA/cm}^2$ . Notice that the analysis has been carried out on two solar cells that were fabricated on the same wafer. Thus process-related variations as e.g. varying thickness of the ARC, difference in screen-printing, and emitter doping, are strongly reduced. Furthermore the choices of two analysis regions which show no further local defects enable the direct evaluation of the structure related effects. However, in Figure 7.21 b) it is obvious that the precision of subtracting the  $J_{sc}$  is limited and thus the increase in  $J_{sc}$  has to be attributed with a significant uncertainty. In contrast to the increased local  $J_{sc}$ , the global I-V-measurement does not show a significant difference in  $J_{sc}$  between solar cell 4 and 6. This can be understood by comparing the local  $J_{sc}$  of both solar cells in Figure 7.19: solar cell 6 is much more affected by local artifacts than solar cell 4.

The expected effect of the increased rear side reflection can be estimated by comparing the calculated photo generation of wafers with fully aluminum alloyed rear side to wafers with rear sides covered with dielectrics: the difference in photo generated current density  $J_{ph}$  is estimated by Fellmeth [4] for Si-wafers with alkaline textured,  $\text{SiN}_x$ -passivated front side and a fully aluminum alloyed rear side in respect to a rear side covered with a dielectric layer to be  $\Delta J_{ph, \max} = 1.5 \text{ mA/cm}^2$ . The reduction of  $J_{ph}$  can be approximated by a simple linear superposition of the different areas leading to

$$\Delta J_{ph} = EC \cdot \Delta J_{ph, \max} \quad (7.2)$$

This is accurate for regions with high carrier collection probability but overestimates the influence of the increased rear side reflection in regions with locally low collection probability and does not take into account the optical coupling of the different regions. The optical coupling between the regions (photons are reflected from one region and propagate to the other) is observed to increase the gain by small structures in comparison to the presented simple linear superposition. For solar cell 4, Eq. (7.2) leads to a reduction of  $J_{ph}$  due to the reduced rear side reflection of  $\Delta J_{ph} = 0.9 \text{ mA/cm}^2$  whereas for solar cell 6,  $\Delta J_{ph} = 0.6 \text{ mA/cm}^2$  is calculated. The calculated difference between solar cell 4 and 6,  $0.3 \text{ mA/cm}^2$ , is in the range of the measured difference in  $J_{sc}$  of  $0.4 \text{ mA/cm}^2$ . Note that for a fully quantitative comparison, the optical properties of the solar cells in question, in particular of the applied passivation stacks and of the emitter, have to be evaluated.

To investigate the influence of the width of the highly doped BSF, local  $J_{sc}$  maps of solar cell 3, with a BSF width of  $350 \mu\text{m}$ , and cell 4, with a BSF width of  $200 \mu\text{m}$ , are compared. Figure 7.22 depicts the line scan of the local  $J_{sc}$ , as well as the difference between the local  $J_{sc}$  of cell 4 and cell 3,  $\Delta J_{sc} = J_{sc}(\text{cell 4}) - J_{sc}(\text{cell 3})$ .

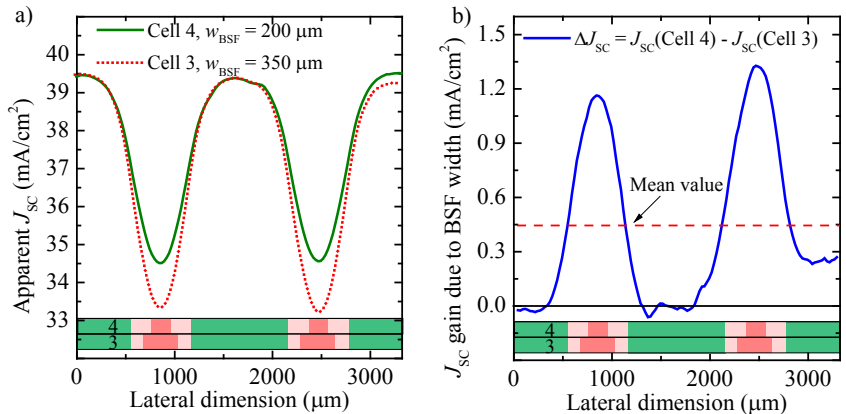


Figure 7.22 a) Local  $J_{sc}$  line-scan average evaluated by SR-LBIC measurements for solar cells 4 and 3 obtained by averaging the local  $J_{sc}$  parallel to the finger structures. b) Local difference  $\Delta J_{sc}$  between the two cells. In order to assist the interpretation the rear side doping of the solar cells is drawn schematically.

■ Emitter  
 ■ Highly doped BSF  
 ■ Lowly doped BSF

As expected, no difference of the local  $J_{sc}$  in the region of the emitter is observed. In contrast, the decrease in  $J_{sc}$  at the highly doped BSF region increases with increasing width of the BSF. The difference  $\Delta J_{sc}$  shows a maximum in the BSF-area of approx.  $1.2 \text{ mA/cm}^2$  and an average of  $0.4 \text{ mA/cm}^2$ . Again, this value has to be considered with care which can be deduced from the not fully periodic behavior of  $\Delta J_{sc}$  in

Figure 7.22 b). The effect shows the benefit of reducing the area fraction of the highly recombination active BSF which could be achieved by increasing the printing accuracy and structure definition or even applying a point-shaped Ag rear contact.

### Al-paste composition

Similar to the other recombination influences, the comparison between Al-paste A and B cannot be entirely quantified, because of the influence of the spatially varying bulk lifetime on  $V_{OC}$  and  $J_{SC}$ . Furthermore, each wafer is printed with one paste and, thus, the comparison between the pastes comprises the comparison of solar cells manufactured on different wafers which enhances the uncertainty e.g. due to different base-lifetimes, variations in ARC, and line width of the printed contacts. Table 7.3 depicts the I-V-parameters of the solar cells manufactured with Al-paste A on the wafer with the highest conversion efficiency of this group.

*Table 7.3 Measured I-V-parameters of the solar cells located on the same wafer. The FSF is realized by DeepEtch, passivated with a stack consisting of a thermal SiO<sub>2</sub> and a PECVD SiN<sub>x</sub> layer. The emitter is metalized and formed with Al paste A.*

Structure	EC (%)	$2w_{BSF}$ ( $\mu\text{m}$ )	$V_{OC}$ (mV)	$J_{SC}$ (mA/cm <sup>2</sup> )	FF (%)	$\eta$ (%)
2	62	200	636	39.3	77.4	19.3
3	62	350	634	39.0	76.1	18.8
4	62	200	634	38.9	77.1	19.0
5	25	350	612	38.2	64.7	15.1
6	44	350	630	39.0	73.3	18.0
7	44	200	633	39.2	74.0	18.4

By comparing the different cells, the finding is quite similar to the cells manufactured with Al-paste B (compare with Table 7.2) and is, therefore, not discussed. The main difference is a drop in  $FF$  for all solar cells which could be observed in the whole group manufactured with paste A. Further investigations indicate that the effect is not a difference of the series resistance, but could be rather explained by an increase in  $J_{02}$  or decrease in  $R_p$  (compare the two-diode model). Since the chemical composition of Al-paste A is unknown for the author and its characterization is not possible in the frame of the legal contract of utilization of the paste, the effect is not further investigated in this work. However, the results show that the Al-paste composition has a strong impact on the performance of the investigated solar cell technology and that adding AlB powder to the Al-paste might not only be beneficial to reduce  $J_{0e}$  but also be necessary to obtain a high  $FF$ .

### Passivation scheme

As shown in Section 7.2.3, the PECVD SiriON passivated solar cells show a very low  $R_p$ . All corresponding solar cells show  $FF$  below 53 %,  $V_{OC}$  below 400 mV and, accordingly,  $\eta$  below 6 %. As expected from the previous results (compare dark I-V and SEM images in Figure 7.16 and Figure 7.17, respectively), the  $FF$  and the  $V_{OC}$  of every single cell are both strongly reduced in comparison to solar cells passivated with thermally grown oxide layers. This can be directly attributed to the reduced  $R_p$  and was discussed in Section 7.2.3. No correlation of the measured I-V-parameters with emitter coverage or emitter-structuring is observed.

### Etch depth

Exemplary, the I-V-parameters of a solar cell with an etch depth of  $\sim 350$  nm (*ShallowEtch*) and one with  $\sim 650$  nm (*DeepEtch*) are shown in Table 7.4.

*Table 7.4 Measured I-V-parameters of two solar cells with different etch depth. The surface is passivated with thermal  $\text{SiO}_2$  +  $\text{SiN}_x$  and the regarded sample on the wafer is solar cell 2.*

	$V_{OC}$ (mV)	$J_{SC}$ (mA/cm <sup>2</sup> )	$FF$ (%)	$\eta$ (%)
ShallowEtch	638	39.2	79.7	19.9
DeepEtch	639	39.3	80.1	20.2

Within the scattering of the measurement results over different wafers of the same group, there is no significant difference observable between cells processed according to the *ShallowEtch* and the *DeepEtch*. This can be interpreted in a way that the process is robust with regard to the applied profile and etch depth.

Notice that all applied FSFs exhibit sheet resistances above 270  $\Omega$ /sq. By applying the highest measured specific resistance  $\rho_0$  of 4  $\Omega$ cm and a wafer thickness of 160 mm, an upper limit for the sheet resistance of the base substrate can be estimated to be 250  $\Omega$ /sq. Thus, the lowest sheet conductivity of the base substrate without illumination exceeds the highest sheet conductivity of the FSF and no significant influence due to the additional conductivity of the FSF on the series resistance and, thus, on the  $FF$  is expected in this case.

## 7.3 Simulation of Solar Cell Parameters

### 7.3.1 Simulation Setup

In order to give realistic or rather ideal solar cell performances, the input parameters of the simulation are chosen according to measurement results as follows. The dopant concentration profiles are depicted in Figure 7.23.

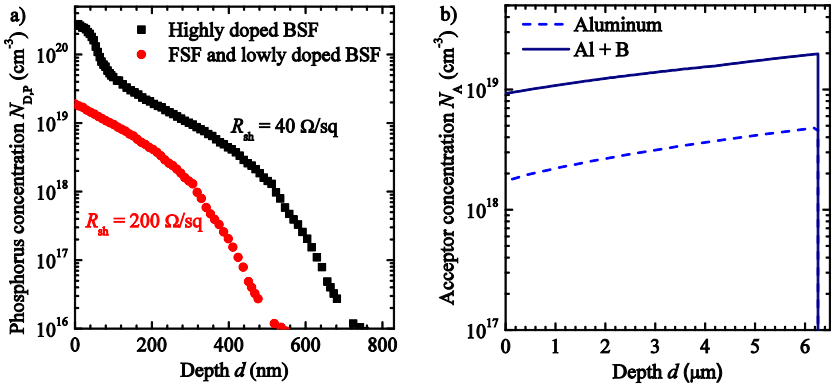


Figure 7.23. a) Applied donor concentration profiles (phosphorus).

b) Applied acceptor concentration profiles (aluminum, boron). The SRV is chosen to reproduce  $J_0$  listed in Table 7.5.

For the highly doped BSF, a profile is chosen measured on planar samples after a  $\text{POCl}_3$ -diffusion process very similar to diffusion B in Chapter 5, resulting in an average sheet resistance over test samples of  $R_{sh} = (40 \pm 2) \Omega/sq$ . The effective surface recombination velocity  $S_p$  (Table 7.5) is chosen to reproduce the measured  $J_0$  of the test structures:  $J_{0,BSFpass} = 100 \text{ fA/cm}^2$  for the passivated BSF-area,  $J_{0,BSFlow} = 21 \text{ fA/cm}^2$  for the lowly doped BSF at planar surfaces and  $J_{0,FSF} = 34 \text{ fA/cm}^2$  for the FSF at textured surfaces, accordingly.

At the Ag-Si interface, setting  $S_p$  to the thermal velocity corrected for the one-dimensional restriction of reaching the surface plane  $S_p = 3 \cdot 10^6 \text{ cm/s}$  [100] leads to a  $J_0$  of the metallized BSF of  $J_{0,met} = 146 \text{ fA/cm}^2$ . This value seems to be low for present commercially available Ag-pastes. However, Fellmeth [4] reports that  $J_{0,met}$  of screen-printed Ag-contacts on phosphorus diffused surfaces is mainly a function of the sheet resistance and that for  $R_{sh} = 40 \Omega/sq$ ,  $J_{0,met}$  is close to  $J_{0,pass}$  of the passivated surface, although in his work  $J_{0,met}$  is higher than reported here. It is assumed that the difference in  $J_{0,met}$  and  $J_{0,pass}$  is strongly related to the applied screen-printing paste and firing conditions – which are both unknown in this simulation study. To provide a conservative estimation, the SRV beneath the Ag-contact is set to  $10^7 \text{ cm/s}$  and an additional near surface recombination is introduced, leading to  $J_{0,met} = 450 \text{ fA/cm}^2$ .

For the aluminum emitter, a fit to a measured Al-profile is chosen with a depth of  $6.1 \mu\text{m}$  resulting from a calculation for a peak temperature of  $T_{\text{peak}} = 830 \text{ }^\circ\text{C}$  and, in addition, the respective boron concentration is applied (Figure 7.23). The SRV and an additional recombination within the emitter is adapted to reproduce  $J_{0e} = 200 \text{ fA/cm}^2$  as reported minimum value by Rauer *et al.* [72] for metal paste B with the same ALB additive as used for the fabrication of solar cells in this work. The exact shape of the doping profile is expected to be of minor influence because the influence of a fully contacted rear side emitter on the solar cell performance can be mainly characterized by  $J_{0e}$  and its internal light reflection.

A schematic of a symmetry element of a simulated device is shown in Figure 7.24.

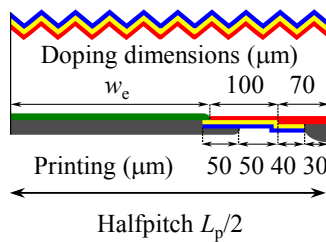


Figure 7.24. Symmetry element of the simulated solar cell structure, referred to as non-structured emitter. The width of the emitter per symmetry element is denoted as  $w_e$ .

The  $n$ -diffused back-surface dimensions are not varied and show a total width of  $340 \mu\text{m}$ . The width of the Ag-contact  $w_{\text{Ag}}$  is set to  $60 \mu\text{m}$  which is a value reached for screen-printed Ag-contacts on the front side of industrial solar cells today. The width of the highly doped BSF is set to  $140 \mu\text{m}$  giving a high alignment tolerance of  $40 \mu\text{m}$  on each side of the contact to the edge of the highly doped BSF. Unless otherwise stated, the pitch  $L_p$  is set to  $1.3 \text{ mm}$  and the outer edges of the doped emitter area are at a distance of  $960 \mu\text{m}$ , compare Figure 7.24. For the overlap of the aluminum finger over the emitter edge,  $50 \mu\text{m}$  are chosen, giving an alignment tolerance between the doped emitter edge and the BSF of  $100 \mu\text{m}$  and a distance between Al- and Ag-contacts of  $90 \mu\text{m}$ .

Table 7.5 gives the geometrical dimensions and the recombination parameters of the differently applied surfaces.

Table 7.5 Width per unit cell (half-pitch, compare Figure 7.24), applied SRV and resulting  $J_0$  of the different highly doped surfaces. Note that within the emitter and within the BSF beneath the contact, the carrier lifetime is reduced to match the chosen  $J_0$ .

	Half Width ( $\mu\text{m}$ )	SRV (cm/s)	$J_0$ (fA/cm <sup>2</sup> )
Emitter	varies	$10^7$	200
FSF	-	$5 \cdot 10^3$	34
BSF passivated	40	$5 \cdot 10^5$	100
BSF contacted	30	$10^7$	450
Lowly doped BSF	100	$3 \cdot 10^3$	21

For simplicity, the carrier generation profile applied in the numerical simulation is calculated by the ray tracer of the simulation package under the assumption of a rear side partly covered with a dielectric layer and partly with an Al-alloyed emitter. The parameters for the rear side reflectance are chosen to match the difference in  $J_{\text{Ph}}$  between the fully covered cases of  $1.5 \text{ mA/cm}^2$  (compare Section 7.2.4). The coverage fraction of the Al-alloyed emitter in the optical simulation is chosen according to  $EC$ , whereas the width of the optically simulated symmetry element is  $10 \mu\text{m}$  – according to the pyramidal structure on the front-side. Thus the optical simulation does not entirely reflect the solar cell structure. However, for photons of lower wavelength, which are dominantly absorbed before reaching the rear side, the choice of the optical simulation can be regarded as accurate. For intermediate wavelength with a high absorption probability during the first bounces, the choice of the optical simulation could lead to differences. For photons of high wavelength, which are often reflected at the cell's inner surfaces, the simulation is accurate again. The resulting uncertainty due to the choice of optical simulation are regarded as minor compared with the assumptions made on the properties of the diffused regions and of the metal contacts.

### 7.3.2 Consideration of Contact and Metal Resistivity

In the numerical simulation, the contact resistance and contributions of metal conductivity to the series resistance are ignored in order to be taken into account subsequently within an analytical formalism, similar to the procedure in Ref. [119]. Therefore, a simple diode-model is regarded (Figure 7.25). The diodes as well as internal series resistance  $R_{S,i}$  and parallel resistance  $R_{P,i}$  are already considered for the output of the numerical simulation.

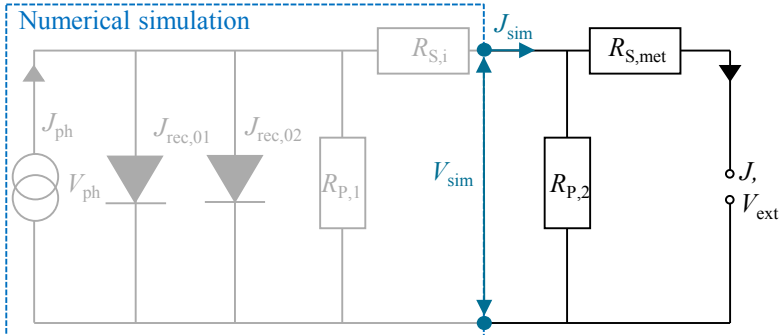


Figure 7.25. Adaption of the two diode model to consider external series resistance  $R_{S,met}$  and parallel resistance  $R_{P,2}$ . The device in the rectangle is considered as the output of the numerical simulation,  $(J_{sim}, V_{sim})$ , which does not apply the two-diode model. Notice that this procedure is in agreement with the two-diode model for  $J R_{S,i} \ll V_{ext}$  or  $R_{P,2}$  sufficiently high.

The obtained current density  $J_{sim}$  and voltage  $V_{sim}$  are then corrected to consider the series resistance contribution of metals and contacts  $R_{S,met}$  and an additional parallel resistance  $R_{P,2}$  [119]:

$$J = J_{sim} - \frac{V_{sim}}{R_{P,2}} \quad (7.3)$$

$$V_{ext} = V_{sim} - R_{S,met} \cdot J$$

The influences of the parallel resistance  $R_{P,2}$  and of the series resistance  $R_{S,met}$  on the conversion efficiency and fill factor of a solar cell are shown in Figure 7.26 and Figure 7.27, respectively. The parallel resistance  $R_{P,2}$  reduces the  $FF$  by 0.1 %<sub>abs</sub> for  $R_P \approx 10^4 \Omega\text{cm}^2$ . The series resistance  $R_{S,met}$  reduces  $\eta$  and the  $FF$  linearly for the applied model.

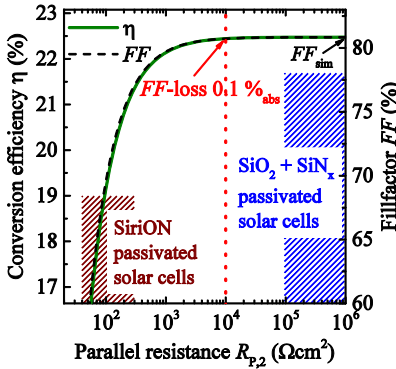


Figure 7.26 Influence of the parallel resistance  $R_{p,2}$  on the FF and the conversion efficiency after the model shown in Figure 7.25. For comparison, the measured range of  $R_p$  for the different solar cells is depicted (compare Figure 7.16).

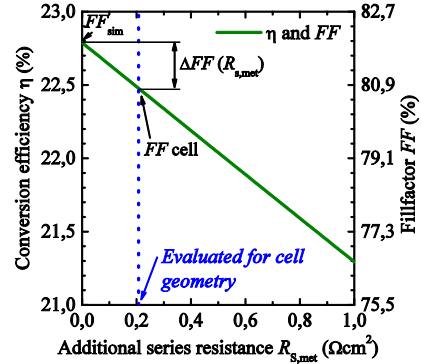


Figure 7.27 Influence of an additional series resistance  $R_{s,met}$  on FF and  $\eta$  after the model shown in Figure 7.25. As an example, the result for a solar cell with  $R_{s,met} = 208 \text{ m}\Omega\text{cm}^2$  is given (compare Table 7.7).

### Series resistance

The series resistance contributions (Table 7.6) are calculated by applying resistance data from various measurements performed in the scope of this work. The assumed finger length  $l_f = 3.8 \text{ cm}$  is very close to the finger length of the produced solar cells in this work and is dimensioned for a two busbar design of a full area solar cell with an edge length of 156 mm, as described by e.g. Hendrichs *et al.* [120]. For the calculation of the series resistance the unit cell area  $a_{\text{unit}} = l_f \cdot L_p/2$  is applied.

The series resistance contributions are calculated according to the calculation by Woehl [69], based on Refs. [62, 121-123]. The width of the Ag-contacts is set to  $w_{\text{Ag}} = 60 \mu\text{m}$  and the area of the finger cross section to  $A_{\text{Ag}} = 2.4 \cdot 10^{-5} \text{ cm}^2$ . gives a contribution to the series resistance for the lateral transport in the  $n$ -electrode of [62]

$$R_{\text{Ag,lat}} = \frac{2 \rho_{\text{Ag}} \cdot l_f}{3 A_{\text{Ag}}} a_{\text{unit}}, \quad (7.4)$$

with the specific resistivity of the screen-printed and fired silver paste  $\rho_{\text{Ag}}$ . The width of the aluminum fingers  $w_{\text{Al}}$  corresponds to the different applied geometries. The Al-thickness is assumed to be  $d_{\text{Al}} = 35 \mu\text{m}$  (double print). This leads to a contribution to the series resistance for the lateral transport in the  $p$ -electrode of [62]

$$R_{\text{Al,lat}} = \frac{2 \rho_{\text{Al}} \cdot l_f}{3 d_{\text{Al}} w_{\text{Al}}} a_{\text{unit}}, \quad (7.5)$$

with the specific resistivity of the screen-printed aluminum paste  $\rho_{Al}$ .

The contribution of the contact resistances is calculated by [122]

$$R_{S,cont} = \frac{\sqrt{R_{sh}\rho_c}}{l_f} \coth\left(\frac{w_f}{2} \sqrt{\frac{R_{sh}}{\rho_c}}\right) a_{unit}, \quad (7.6)$$

with the sheet resistance  $R_{sh}$  of the diffused area under the contact, the width of the line contact  $w_f$  and the specific contact resistance  $\rho_c$ . For the  $p$ -contact,  $w_f$  corresponds to the emitter width according to the different applied geometries. The total series resistance contribution of the contacts and lateral transport in the metal fingers

$$R_{S,met} = R_{S,cont,Ag} + R_{Ag,lat} + R_{S,cont,Al} + R_{Al,lat}, \quad (7.7)$$

is evaluated by Eq. (7.4) to (7.6) applying the parameters given in Table 7.6.

*Table 7.6 Applied parameters to evaluate the contributions to series resistance of metal and contacts, Eq. (7.4) to (7.6). The data are evaluated on different test-structures within the scope of this work.*

	Applied parameter	Origin of data
Ag-lateral	$\rho_{Ag} = 2.9 \mu\Omega\text{cm}$	Line resistance structures on Si
Ag-Si (BSF)	$\rho_{c,n} = 2 \text{ m}\Omega\text{cm}^2$ , $R_{sh} = 40 \Omega/\text{sq}$	TLM structures, $R_{sh}$ measured
Al-lateral (alloyed)	$\rho_{Al} = 28 \mu\Omega\text{cm}$	Line resistance structures on $n$ -type Si
Al-lateral (on passivation)	$\rho_{Al} = 21 \mu\Omega\text{cm}$	Line resistance structures on dielectric
Al-Si (emitter)	$\rho_{c,p} = 14 \text{ m}\Omega\text{cm}^2$ , $R_{sh} = 20 \Omega/\text{sq}$	TLM structures on $p$ -type wafers, ECV profile

In the following, for each simulated solar cell structure a different value of the series resistance is calculated and applied using the conductance data in Table 7.6 and Eq. (7.7). The resulting  $R_{S,met}$  for the simulated structures are shown in Table 7.7.

For the non-structured emitter, the total external series resistance decreases with decreasing emitter coverage. For emitter structuring, the total series resistance increases with decreasing emitter coverage. The discrepancy in the  $R_{S,met} - EC$  behavior of the differently designed cells originates from the different number of metal fingers per unit cell in the case of the non-structured emitter.

Table 7.7 Applied additional series resistance  $R_{S,met}$  for the simulated solar cell structures evaluated with Eq. (7.7). The schematic of the non-structured emitter cell is shown in Figure 7.24, and for the emitter structuring in Figure 7.29.

Simulation	$EC$ (%)	$p$ -contact and fingers ( $m\Omega cm^2$ )	$n$ -contact and fingers ( $m\Omega cm^2$ )	$R_{S,met}$ ( $m\Omega cm^2$ )
Non-structured emitter (Section 7.3.3)	79 74 66	76 71 68	149 121 93	225 192 161
Emitter structuring (Section 7.3.4 and 7.3.5)	77 31 15	69 87 129	121 121 121	190 208 250

For the non-structured emitter, the external series resistance is dominated by the  $n$ -contact whereas for lower  $EC$  the resistance of the  $p$ -contact dominates due to the reduced contact area.

### Parallel resistance

The solar cell structure in question exhibits regions where, on the one hand, the  $p$ -contact is separated from the lowly doped BSF only by the dielectric rear side passivation and, on the other hand, the emitter doping is in direct contact with the diffused surface of the lowly doped BSF (compare Figure 7.2). A parameter describing possible parasitic conductivity between the  $n$ - and  $p$ -region in the two-diode model is the parallel resistance  $R_p$ . Numerical simulations cannot calculate these parasitic effects due to their occurrence with an undefined probability. The possible conductivity between aluminum and BSF or emitter and BSF may originate from local defects in the passivation layer [124-126] or local heterogeneities of the alloying. Statistically distributed defects like blisters or even pinholes in e.g. PECVD  $SiO_xN_y/SiN_x$  stacks were already presented in this work by SEM measurements (compare Figure 7.7). Such defects might lead to a very low shunt resistance, low  $FF$ , and thus low  $\eta$ , as shown in the solar cell results (compare Section 7.2.3). In order to estimate the  $R_p$  and its impact on the  $FF$  of the simulated cells, the parallel resistance is measured on the fabricated, thermally oxide passivated solar cells and its influence on the solar cell performance is estimated by Eq. (7.3). The result shows (Figure 7.26) that the measured  $R_p$  values above  $10^5 \Omega cm^2$  (see Figure 7.16) are sufficient to prevent a measurable influence of  $R_p$  on the  $FF$  and, thus, the conversion efficiency. Consequently, no parallel conductivity is considered in the following study.

### 7.3.3 Influence of Pitch Contact Distance

By reducing the pitch distance  $L_p$  of the solar cells without structured emitter from 1.6 mm down to 1 mm, while maintaining the dimensions of the  $n$ -doped silicon fingers, the emitter coverage fraction decreases from 79 % down to 66 %. The I-V-parameters versus  $L_p$  are shown in Figure 7.28.

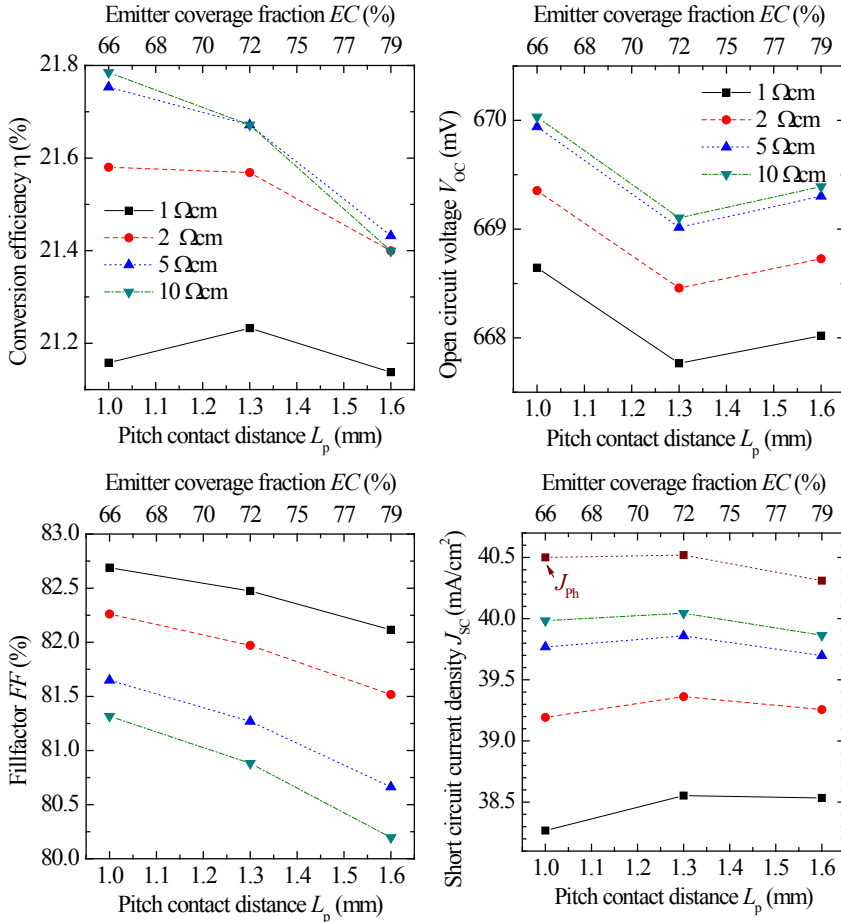


Figure 7.28. I-V-parameters as a function of the pitch distance  $L_p$  for different applied base dark resistivity  $\rho_0$ . The variation is achieved by adapting the emitter width at constant dimensions of all other areas leading to an emitter coverage given at the upper axis. To compare the collection efficiency, the photo generated current density  $J_{Ph}$  is shown as well.

The short circuit current density is influenced mainly by two effects: with increasing pitch distance and, thus, increasing emitter coverage fraction  $EC$ , the electrical shading is reduced due to the reduced area fraction of the n-doped fingers. On the other hand, rear side reflection decreases with increasing emitter coverage fraction leading to a lower photo current generated in the cell. For the highly doped base substrate with a dark specific resistance  $\rho_0 = 1 \Omega\text{cm}$ , the additional shading dominates due to the lower base carrier lifetime, leading to an increase in  $J_{SC}$  by  $0.3 \text{ mA/cm}^2$  within the pitch distance range of interest. For the lowly doped base substrate with a dark specific resistance  $\rho_0 = 10 \Omega\text{cm}$ , the effect of the rear side reflection dominates, leading to an increase in  $J_{SC}$  by  $0.1 \text{ mA/cm}^2$  within the pitch distance range of interest. Both described effects are small compared to the influence of the base substrate doping due to electrical shading above the  $n$ -finger featuring a total width of  $340 \mu\text{m}$  and recombination within the base substrate in general: while the lowly doped cells loose approx.  $0.5 \text{ mA/cm}^2$  compared to the photo current density, the highly doped samples loose up to  $2.2 \text{ mA/cm}^2$ .

Decreasing emitter coverage through the variation of the pitch distance leads to an increase of the area of the metallized n-fingers, which exhibit the highest  $J_0$  on the solar cells. In consequence, the decreased share of  $J_{0e}$  at the solar cell's  $J_{0l}$  is compensated for by an increased  $J_{0,BSFmet}$  and, thus, no significant change of  $V_{OC}$  is observed.

The decrease in  $L_p$  has two major effects on the series resistance: on the one hand, it increases the number of metal fingers and the contact area per cell area which results in a decrease in  $R_{s,met}$  by  $0.06 \Omega\text{cm}^2$ . On the other hand, the internal series resistance of the solar cell decreases by reducing the distance between the emitter and the Ag-contact. This leads to an increase in  $FF$  by  $1.3 \%_{\text{abs}}$  for the  $10 \Omega\text{cm}$  and of  $0.6 \%_{\text{abs}}$  for the  $1 \Omega\text{cm}$  substrate by reducing  $L_p$  from  $1.6 \text{ mm}$  to  $1 \text{ mm}$ .

The influence of the  $FF$  dominates the correlation between the conversion efficiency and  $L_p$ , although the absolute level of the conversion efficiency is set by the higher  $J_{SC}$  of the lowly doped base substrate. For the  $\rho_0 = (5 \text{ to } 10) \Omega\text{cm}$  material, the reduction in  $L_p$  leads to a gain in conversion efficiency of  $0.4 \%_{\text{abs}}$  resulting in a predicted conversion efficiency of  $\eta = 21.8 \%$ . It is to note that this gain is limited by the possibility to reach low recombination below the BSF-contact, at the emitter and in the base substrate. For the choice of screen printed contacts, this limitation could be crucial.

### 7.3.4 Influence of Emitter Structuring

As shown in Section 2.6 and 7.2.2, achieving a low  $J_{0e}$  and at the same time a low contact resistivity is challenging. Furthermore, the high temperature during contact firing might prevent the formation of Ag-contacts providing low resistance losses. This

limits the possible gain of a solar cell featuring a low pitch distance; another solution is regarded to increase the conversion efficiency for given  $J_{0e}$  and  $J_{0BSF}$ . The least recombination active surface of the solar cell is the passivated lowly doped BSF area. One way to raise its coverage fraction is to structure the emitter partly and to introduce one or more stripes of passivation under the Al-metallization as introduced in Section 7.1. In Ref. [69] it is shown that the aluminum on top of the applied passivation stack increases the SRV on the passivated base only marginally (increase  $< 80$  cm/s). Since for the regarded solar cell structure, the SRV at the lowly doped BSF Si-dielectric interface is assumed to be  $2.4 \cdot 10^3$  cm/s, it seems meaningful to assume the same  $J_{0,BSFpass}$  under the Al-metallization as in the non-Al covered region. Furthermore, the influence could be reduced technologically by the application of different, in particular thicker, passivation stacks. Additionally it is assumed that  $J_{0e} = 200$  fA/cm<sup>2</sup> can be achieved independently of the emitter dimensions for emitter openings featuring a width of higher than  $66 \mu\text{m}$ . Technologically this could be realized by modifying the firing parameters, the paste composition, and the printing conditions.

Three geometrical structures (Figure 7.24 and Figure 7.29) are simulated to show the potential influence of the emitter structuring on the cell performance: one without passivated area, denoted as *non-structured emitter*, one with two and one with three emitter stripes, whereas in each case the emitter stripes cover the same area fraction.

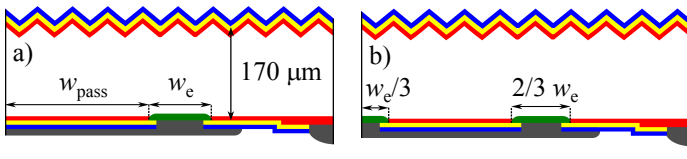


Figure 7.29. Symmetry elements of the additionally simulated solar cell structures: a) two emitter stripes and b) three emitter stripes. The total width of the emitter per symmetry element is denoted as  $w_e$ . The pitch distance of  $L_p = 1.3$  mm is the same for all simulations in this section.

The pitch contact distance is kept constant at  $L_p = 1.3$  mm. Three different emitter widths  $w_e$  and, thus, emitter coverage fractions  $EC$  are considered:  $w_e = 500 \mu\text{m}$  ( $EC = 77\%$ ),  $w_e = 200 \mu\text{m}$  ( $EC = 31\%$ ), and  $w_e = 100 \mu\text{m}$  ( $EC = 15\%$ ). The coverage of the structured emitter is calculated with two emitter stripes per Al-finger (Figure 7.29, a) and three emitter stripes per Al-finger (Figure 7.29, b).

The I-V-parameters versus  $EC$  for substrates featuring a base resistivity of  $2 \Omega\text{cm}$  and  $10 \Omega\text{cm}$  are shown in Figure 7.30.

Since the dimensions of all other surfaces are constant, the open circuit voltage is dominated by the emitter coverage fraction. A reduction of  $EC$  from  $77\%$  to  $15\%$  increases  $V_{OC}$  by  $10$  mV for all substrates and geometries.

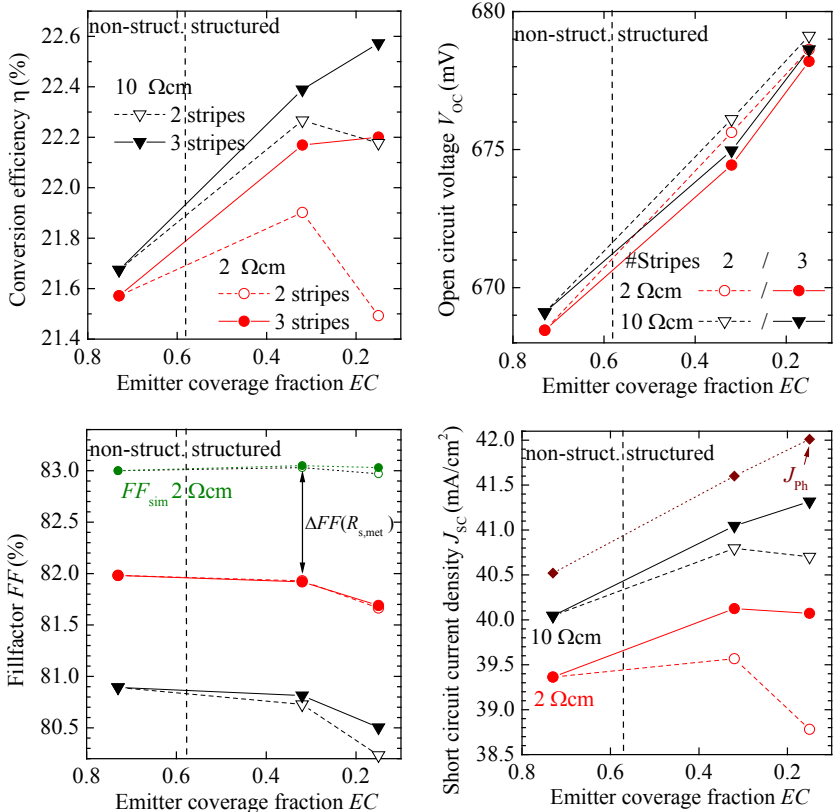


Figure 7.30. I-V-parameters versus emitter coverage fraction for two (open symbols) and three (filled symbols) emitter stripes per pitch. Two n-type substrates with different base resistivity are taken into account:  $2 \Omega\text{cm}$  and  $10 \Omega\text{cm}$ . For comparison, the calculated FF from the numerical simulation, which neglects metal and contact resistivity, is shown as well. The pitch is set to  $L_p = 1.3 \text{ mm}$ .

The photo generated current density increases with decreasing  $EC$  from 77% to 15% by  $1.5 \text{ mA}/\text{cm}^2$ . The difference between  $J_{ph}$  and  $J_{sc}$  is approx. constant for the three stripe geometry but increases significantly with decreasing  $EC$  for the two stripe geometry. This behavior shows that the two stripe geometry leads to additional electrical shading in the emitter area which is avoided by the three stripe geometry. In consequence, the three stripe geometry benefits from the higher  $J_{ph}$  for both materials and both  $EC$  whereas the two stripe geometry leads to a reduced  $J_{sc}$  for lowest  $EC = 15 \%$ .

The resulting  $FF$  from the numerical simulations ( $R_{s,met} = 0$ , green symbols) is approximatedly independent from the emitter coverage. Only for the two stripe geometry, a slight decrease is observed in comparison with the three stripe geometry which can be attributed to the series resistance contribution of holes. However, by accounting for  $R_{s,met}$ , the  $FF$  decreases by 0.3 %<sub>abs</sub> as  $EC$  decreases from 77 % down to 15 % due to the reduced Al-contact area at low  $EC$ .

Consequently, the conversion efficiency increases for the three stripe geometry by 0.9 %<sub>abs</sub> (10  $\Omega$ cm) or 0.6 %<sub>abs</sub> (2  $\Omega$ cm) when reducing  $EC$  to 15 %. The additional electrical shading and the increased series resistance due to the lower  $EC$  is effectively overcompensated by the lower  $J_{0e}$  and higher rear side reflectance. In contrast, for the two stripe geometry a decrease is observed for the reduction of  $EC$  from 31 % to 15 %. Notice here that the effect of the emitter structuring depends strongly on the achieved values of  $J_{0e}$ ,  $J_{0BSF}$ , and the base lifetime: the higher  $J_{0e}$ , the higher the benefit from structuring the emitter. On the other hand, an increase in base recombination increases the optimum number of emitter stripes to avoid electrical shading in the emitter area. Increasing  $J_{0BSF}$  leads to an increased optimum pitch and may, thus, also increase the optimum number of emitter stripes.

### 7.3.5 Influence of Base Resistivity

The effect of structuring the emitter depends strongly on the applied base resistivity. To investigate the influence of  $\rho_0$ , four different base doping densities are applied in the simulations with the different emitter structuring geometries. The I-V-parameters over the base resistivity are shown in Figure 7.31.

The emitter coverage shows the strongest influence on the open circuit voltage  $V_{OC}$  (increase up to 13 mV from  $EC = 77\%$  to 15 %) while the effect of the base resistivity is significantly smaller (increase up to 1.8 mV from  $\rho_0 = 1\ \Omega\text{cm}$  to 10  $\Omega\text{cm}$ ).

The short circuit current density  $J_{SC}$  is strongly affected by both, the base doping and the chosen geometry: higher base dopant concentrations enhance the Auger-recombination in the base and, thus, the effect of electrical shading. While high base doping leads to a decrease in  $J_{SC}$  of 1.5 mA/cm<sup>2</sup> for the non-structured emitter, the two-stripe emitter geometry with the lowest emitter coverage of 15 % leads to a decrease of 4.0 mA/cm<sup>2</sup> for the 1  $\Omega\text{cm}$  in respect to the 10  $\Omega\text{cm}$  material. The higher slope of the  $J_{SC}$  curves in respect to the  $EC = 77\%$  structure indicate the higher electrical shading of the structured emitters. This electrical shading in the emitter area could be greatly reduced by the third emitter stripe. However, three emitter stripes at moderate emitter coverage of 31 % nearly reach the collection efficiency of the non-structured emitter (compare the difference in  $J_{ph}$  and  $J_{SC}$  in Figure 7.30). The additional effect of the increased rear side reflection leads to an advantage in  $J_{SC}$  for both geometries by up to 1.3 mA/cm<sup>2</sup>.

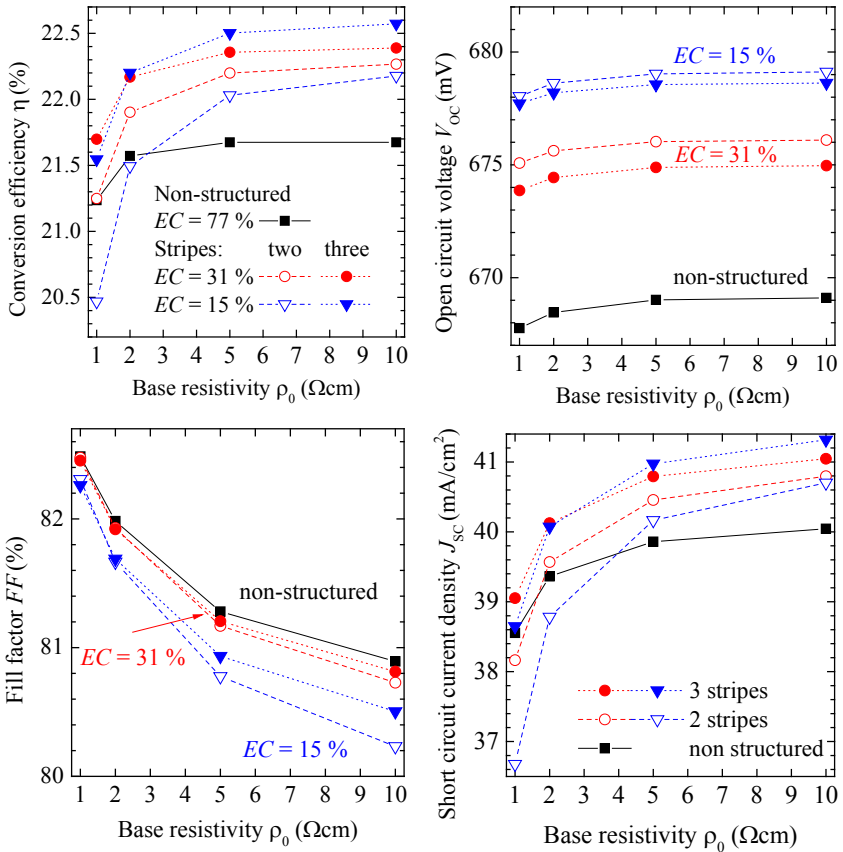


Figure 7.31.  $I$ - $V$ -parameters of the different solar cell geometries versus the base resistivity for several emitter coverages and stripe configurations. The pitch is set to  $L_p = 1.3$  mm.

The  $FF$  of the solar cell does not depend significantly on the regarded solar cell structure but increases with the base dopant concentration. This is due to the fact that the conductivity of the base substrate contributes to the series resistance of the solar cell. Note that each color in the graph is connected with one emitter coverage and, thus, the same  $R_{s,met}$ . In respect to the non-structured emitter, two effects have to be considered: on the one hand, the Al-Si contact area is proportional to  $EC$  and the series resistance contribution of these contacts increases with decreasing  $EC$ . This effect is independent from the number of emitter stripes and can be observed at low base resistivities: the reduction to  $EC = 31\%$  leads to no significant effect whereas the further reduction to  $EC = 15\%$  leads to a decrease in  $FF$  of approx.  $0.2\%_{abs}$ . On the

other hand, longer distances to the emitter increase the series resistance contribution of the holes in the solar cell. This influence is enhanced for lower base substrate dopant concentrations, higher distances between the emitter stripes (compare two stripes to three stripes for the same  $EC$ ), and for lower  $EC$ . Consequently, the highest decrease in  $FF$  compared to the non-structured emitter cell is found to be  $0.7\%_{\text{abs}}$  for the two stripe geometry with the lowest  $EC = 15\%$  and the highest  $\rho_0 = 10\ \Omega\text{cm}$ .

The conversion efficiency  $\eta$  increases with increasing base resistivity for nearly all structured emitter geometries due to the increasing  $J_{SC}$ . For the non-structured emitter, the decreasing  $FF$  leads to a broad plateau with a maximum conversion efficiency of  $\eta = 21.7\%$ , nearly reached between  $\rho_0 = 2\ \Omega\text{cm}$  and  $10\ \Omega\text{cm}$ . The two-stripe geometry shows a strong decrease in  $\eta$  for decreasing base resistivity due to electrical shading of up to  $1.7\%_{\text{abs}}$  for  $EC = 15\%$  which can be reduced by a third emitter stripe to  $1\%_{\text{abs}}$ . The three stripe geometry leads to the highest conversion efficiency for all regarded base materials, whereas the advantage over the non-structured emitter increases with a base resistivity between 5 and  $10\ \Omega\text{cm}$  leading to a maximum predicted conversion efficiency of  $\eta = 22.6\%$  at  $EC = 15\%$ .

The results show that structuring the emitter can lead to a strong dependence of the cell performance on the base resistivity due to enhanced electrical shading and that this can be avoided by reducing the distance between the emitter stripes by structuring the emitter in multiple stripes.

## 7.4 Conclusion

The newly devised solar cell process sequence shows a greatly diminished process complexity and applies exclusively technologies which are already distributed in industrial production of crystalline silicon solar cells. The main restrictions of the preliminary existing technology e.g. the formation of suitable FSF and BSF-doping profiles on the same wafer, the low alignment and structure reliability of the applied screen-printing process, the high peak firing temperature needed to form a deep emitter, as well as the high  $J_{0e}$  and  $J_{0,\text{BSFpass}}$  could be solved or, at least, greatly diminished in this work.

Experimentally, it is shown that shunting of the  $n$ - and  $p$ -type area can be avoided which was a concern regarding this type of solar cell. The application of AIB into the Al-paste as well as the reduction in emitter coverage by structuring allowed for reducing the temperature exposure during contact firing in order to obtain low resistive Ag-BSF contacts with a commercially available Ag screen printing paste and maintain sufficiently deep Al alloying. Low dark saturation current densities of the lowly doped areas could be achieved. For example, an FSF with a dark saturation current density of below  $20\ \text{fA/cm}^2$  could be fabricated by back-etching, which is ideally suited for advanced devices like the BC-BJ solar cell. The back-etching process

was exclusively developed in this work. Within the scope of this work only one solar cell batch could be realized with the developed process sequence. In this batch, the minority carrier lifetime in the substrate of the thermally SiO<sub>2</sub>-passivated samples was reduced, being related, on the one hand, to an (unnecessary) high temperature plateau during POCl<sub>3</sub> diffusion and, on the other hand, to the inadequate base material. As a consequence, it was not possible to show the full benefit of structuring the emitter on an experimental base and the conversion efficiency of the best solar cell was limited to  $\eta = 20.1\%$ , independently measured by Fraunhofer ISE CaLab. However, SR-LBIC measurements showed that structuring the emitter leads to a gain in  $J_{SC}$  of 0.4 mA/cm<sup>2</sup> for the regarded device, due to the increased reflection at the rear side. The SR-LBIC measurements show that even the moderately structured Al-emitter enables high  $J_{SC} > 40$  mA/cm<sup>2</sup> and that the remaining limitation regarding the collection efficiency of the device lies in the highly recombination active BSF, contacted by screen-printing.

In the simulation study, already achieved recombination properties of the surfaces were applied, whereas the base recombination was assumed to be intrinsic. A variation of the pitch contact distance leads to a conversion efficiency of  $\eta = 21.8\%$ . It is shown that structuring the emitter into two stripes can lead to additional electrical shading if the distance between the stripes is increased and that this effect is pronounced for low resistive base material or, more generally, for limited base carrier-lifetime. By introducing a third emitter-stripe in the center of the outer stripes, the additional electrical shading can be minimized while high voltages are maintained. With this structure a conversion efficiency of  $\eta = 22.6\%$  could be simulated, which underlines the high potential of the solar cell device. The efficiency gain by structuring the Al-emitter is calculated to up to 0.9 %<sub>abs</sub> for the simulated structure with emitter coverage of 15 % compared to 77 % of the non-structured emitter.

To sum up, the presented study shows a possible way of reaching high conversion efficiencies with a lean and industrially feasible process sequence. The presented solar cell process requires only one high temperature diffusion step without the need of further dopant sources or device temperatures above 900 °C. The contacts are applied by screen-printing and the emitter is formed by aluminum-alloying. The high  $J_{0e}$  of Al-emitters compared to B-emitters can be effectively reduced by structuring the emitter. The simulation study shows that multiple structuring of the emitter is beneficial while the optimal number of emitter stripes finally depends on e.g. the carrier lifetime in the base, the solar cell geometry, the  $J_0$  of the different surfaces, the alloying conditions, and the contact resistance between Al and emitter.



## 8 Summary

The standard method to extract the **recombination parameter**  $J_0$  and the **carrier lifetime** in the base substrate from **QSSPC measurements** of lifetime samples exhibiting diffused surfaces has been revised, adapted, and tested on simulation and measurement data sets. A key result is a new method taking into account the finite diffusion coefficient of the excess carriers in the base substrate. The method applies updated physical models, accounts for injection dependent band-gap narrowing in the substrate and leads to results that are in excellent agreement with modern simulation tools. The deviation from the input value of a numerical simulation is below 5 % for  $J_0 = (4 \text{ to } 500) \text{ fA/cm}^2$ . It enables the direct comparison of the obtained  $J_0$  on different substrates, applied injection densities and thus between different authors.  $J_0$  obtained on highly and lowly doped, *n*- and *p*-type substrates after the same process sequence differ between the substrates and from the numerically extracted value  $208 \text{ fA/cm}^2$  less than 3 % compared to the previous method which shows a 20 % deviation between the substrates and 32 % from the numerical evaluation, mainly due to neglecting the carrier diffusion. Enabling higher injection densities allows for the application of substrates exhibiting lower carrier lifetimes or higher base dopant concentrations, e.g. Cz-Si used for the production of solar cells. Furthermore it is shown that the method enables the extraction of  $J_0$  for single-side diffused wafers which is beneficial for the characterization of single-side doping techniques or samples of solar cells with passivated rear surface before metallization. In the shown example the values extracted with the developed method from asymmetrical solar cell precursors differ less than 4 % from the numerically evaluated  $J_0$  of corresponding symmetrical test structures. The method has been implemented in a spread-sheet calculator and made available for download at the Sinton Instruments Inc. website and is thus easily accessible for users.

An **analytical model for solar cells with locally contacted passivated rear surface** has been adapted to account for **injection dependent effects** and tested against numerical simulations for the case of solar cells that are mainly limited by the rear side and reach very high voltages. One result is that the analytical model shows good agreement with numerical modeling in low-level injection conditions. Violation of low level injection conditions due to lower doped base material and injection dependent physical parameters, such as the SRH recombination in oxygen contaminated Cz-Si, requires injection dependent modeling. The proposed adaptations of the model lead to a strongly improved agreement of the diode characteristics with the numerical simulation due to the consideration of injection dependent material parameters, such as resistivity, surface-, and bulk recombination and of high-level injection effects. For the case of a solar cell with ideal front side, Cz-Si with an interstitial oxygen concentration of  $[\text{O}_i] = 10^{18} \text{ cm}^{-3}$ , the developed model differs less than 4 mV in  $V_{\text{OC}}$  from the numerical simulation compared to 28 mV of the previous injection independent model.

Major deviations are expected to decrease for more realistic devices exhibiting moderate injection densities and increased contributions of injection independent parameters to the dark saturation current density and the series resistance of the solar cells. The adapted two-diode model enables a wider application range: on the one hand it seems suited for highly efficient  $n$ -type solar cells which partly reach intermediate injection densities, on the other hand the improved reproduction of the I-V-curve for solar cells exhibiting injection dependent recombination opens the possibility to extract information by fitting the model to experimentally obtained I-V-curves. The results also show the limitations of models assuming uniform injection density in highly non-uniform devices: non-uniform injection densities can only be considered by implementing correction factors which, by design, are applied to concrete points in space and are thus limited in their range of validity.

The **effective surface recombination velocity (SRV) of holes at highly phosphorus-doped surfaces** is evaluated and parameterized in dependence of the surface dopant concentration  $n_{\text{surf}}$  for two industrial relevant passivation schemes: stacks of thin thermal oxide  $\text{SiO}_2$  or PECVD deposited silicon-oxy-nitride  $\text{SiO}_x\text{N}_y$ , both covered with silicon nitride  $\text{SiN}_x$ . No difference is observed between the alkaline textured  $\langle 111 \rangle$  surfaces and planar  $\langle 100 \rangle$  surfaces for high  $n_{\text{surf}} > 8 \cdot 10^{19} \text{ cm}^{-3}$ , besides the expected increased surface area by a factor of  $\sim 1.6$ . For low  $n_{\text{surf}} < 8 \cdot 10^{19} \text{ cm}^{-3}$  the textured  $\text{SiO}_2$  surfaces show a strongly increased SRV compared to the planar surfaces which is attributed to the higher defect density of  $\text{SiO}_2$ –Si interfaces at  $\langle 111 \rangle$  surfaces. This increase is minor for the  $\text{SiO}_x\text{N}_y$  samples, which is expected, for the higher surface charge of  $\text{SiO}_x\text{N}_y$  enhances the field effect passivation. The experimental method of subsequently back-etching of the surface and the calculation of individual carrier profiles for each wafer enables to cover a wide range of  $n_{\text{surf}}$  with few diffusion processes and a high accuracy in the applied profile by avoiding the typical near surface artifacts of the profiling methods. The given parameterizations can be used for device modeling with modern simulation tools that mostly apply the same models for band-gap narrowing and intrinsic recombination.

New processes to form **deep driven-in phosphorus diffusions** with low surface concentrations in **one single POCl<sub>3</sub> diffusion step** have been developed. The obtained sheet resistances show very good homogeneity with standard deviations below 3 % over wafers and process boat. The deposition temperature allows excellent control of the sheet resistance. The surface concentration is influenced by both, the deposition temperature and drive-in process whereas the latter mainly controls the depth of the profile. The total dose of phosphorus could be correlated to the deposition temperature, whereas the influence of the drive-in process is dominantly a redistribution of the profile. The low  $J_0 = 18$  to  $38 \text{ fA/cm}^2$  measured on textured,  $\text{SiO}_x\text{N}_y/\text{SiN}_x$ -passivated samples is promising for the application on the front side of solar cells. The simulation of the recombination behavior in dependence of the process parameters gives

additional insight for further development of diffusion processes. Adaptations of the presented processes are in use for front-contacted silicon solar cells at the Fraunhofer ISE.

A short, industrially feasible sequence to produce **back-contact back-junction solar cells** featuring a **non-passivated aluminum alloyed emitter** has been developed. The presented solar cell process requires only one high temperature diffusion step without the need of diffusion masks, further dopant sources, or device temperatures above 900 °C. The contacts are applied by screen-printing and the emitter is formed by aluminum-alloying. A first experimental evaluation led to a conversion efficiency of 20.1 % (aperture area 16.25 cm<sup>2</sup>). Strategies to reduce the effect of the comparable high  $J_{0e}$  and low internal reflection of non-passivated, alloyed Al-emitters and the contact firing trade-off between optimal emitters and Ag-BSF contact formation, in particular the incorporating of B-additives to the Al-paste and the geometrical structuring of the emitter, have been successfully implemented. A simulation study based on experimentally achieved recombination parameters shows a potential conversion efficiency of a pitch variation of 21.8 % and the benefit of multiple structuring of the emitter which leads to a conversion efficiency of up to 22.6 %. Additionally, the multiple structuring of the emitter is beneficial when electrical shading is significant, e.g. due to a reduced base carrier lifetime.

## Appendix: Carrier Statistics in Highly Doped Silicon

The intrinsic carrier density  $n_{i,0}$  is fully determined by Eq. (2.1) from the intrinsic band-gap  $E_{g,0}$ , Eq. (2.4), and the densities of states  $N_C$  and  $N_V$ , Eq. (2.9), leading to  $n_{i,0} = 1.08 \cdot 10^{10} \text{ cm}^{-3}$  at  $T = 300 \text{ K}$ . However, Altmatt *et al.* [11] proposed a presently commonly accepted value of  $n_{i,0} = 9.65 \cdot 10^9 \text{ cm}^{-3}$  at  $T = 300 \text{ K}$ . Moreover, Sproul *et al.* [9] evaluated the injection dependence of  $n_i$  experimentally. Thus the parameter-set is not entirely self-consistent.

In the case of the Boltzmann approximation, this work applies Eq. (2.5). This procedure is consistent with the information of  $E_{g,0}(T)$  [8],  $n_{i,0}$  at 300 K [11] and the relative temperature dependence of  $n_{i,0}$  [9], whereas it neglects the parameterizations of the densities of states given in [8]. The motivation is, on the one hand, to apply the data which are most reliably evaluated by direct measurements ( $E_{g,0}$  and  $n_{i,0}$ ), especially the evaluated  $n_{i,0}$ . On the other hand, Schenk's band-gap narrowing model [14] gives absolute values of the energy shifts and it seems more reliable to relate these to an absolute  $E_{g,0}$  instead of to an effective band-gap that has been adapted to match the evaluated  $n_{i,0}$ . The Boltzmann approximation is applied for lowly doped silicon in this work, in particular for all base substrates.

In the case of Fermi-Dirac statistics,  $N_C$  and  $N_V$  have to be applied in Eq. (2.1) explicitly. In this work, the parameterizations of  $N_C$  and  $N_V$ , Eq. (2.9), are applied in Eq. (2.10) to evaluate  $n_{i,\text{eff}}$  by Eq. (2.1). This procedure is again consistent with the information of  $n_{i,0}$  at 300 K [11] and its relative temperature dependence [9]. The motivation is, that the evaluated  $n_i$  converges with high precision to the Boltzmann solution for low dopant concentration and without excitation (compare Figure 2.1). In numbers:  $p_0$  calculated by the Boltzmann approximation exceeds  $p_0$  calculated by Fermi-Dirac statistics by 0.004 % for a dopant density of  $N_D = 10^{16} \text{ cm}^{-3}$ . This leads to consistency of e.g. the evaluation of the base substrate of lifetime samples with the Boltzmann approximation and the modeling of the highly doped regions of the same sample with Fermi-Dirac statistics and is therefore applied for the analytical modeling of highly doped silicon in this work.

In the later part of writing this thesis, the author collaborated in the implementation of Fermi-Dirac statistics to the well-known numerical device simulator PC1D [127]. The F-D-version implemented by H. Haug [17, 18] is called PC1Dmod. In this work, PC1Dmod is applied to evaluate the accuracy of the analytical solution Eq. (2.34) and the influence of fixed surface charges on the extracted  $S_p$ . Since the procedure of the evaluation of  $n_{i,\text{eff}}$  is not given in literature, it is stated here briefly: the temperature dependent  $n_{i,0}(T)$ , Eq. (2.5), is applied as well. Instead of the parameterizations in Eq. (2.9),  $N_C$  is evaluated by

$$N_C = n_{i,0}(T) \cdot \sqrt{\frac{N_C}{N_V}} \exp\left(-\frac{E_{g,0}(T)}{2k_B T}\right). \quad (\text{A.1})$$

The temperature independent ratio  $N_C/N_V = 1.1461$  is chosen to match  $N_C(300 \text{ K}) = 2.86 \cdot 10^{19} \text{ cm}^{-3}$ , which follows from Eq. (2.9). This gives  $N_V(300 \text{ K}) = 2.49 \cdot 10^{19} \text{ cm}^{-3}$  different to the published value of  $3.1 \cdot 10^{19} \text{ cm}^{-3}$  [8]. The calculated densities of states are then applied in Eq. (2.10) and Eq. (2.11), similar to the procedure of this work. In conclusion, differently to the procedure in this work,  $E_{g,0}(T)$ , Eq. (2.4), is considered whereas from the literature values of the density of states, only  $N_C(300 \text{ K})$  is taken into account.

The relative deviation of the minority hole concentration  $p_0$  in highly phosphorus doped silicon calculated with the procedure as applied in this work and in PC1Dmod is shown in Figure A.1. Over the whole relevant range of phosphorus concentration, the deviation is below 0.35 %.

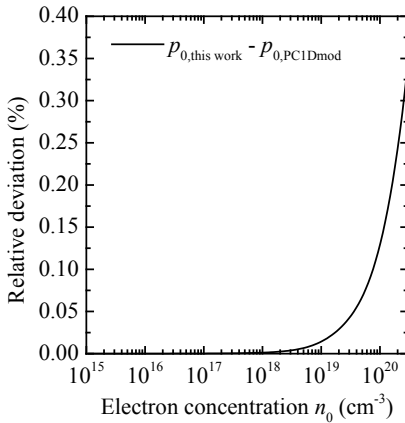


Figure A.1 Relative deviation of the equilibrium minority hole concentration  $p_0$  over electron concentration  $n_0$  at  $T = 25^\circ\text{C}$  in highly phosphorus doped silicon as calculated in this work and in PC1Dmod [17] by Fermi-Dirac statistics.

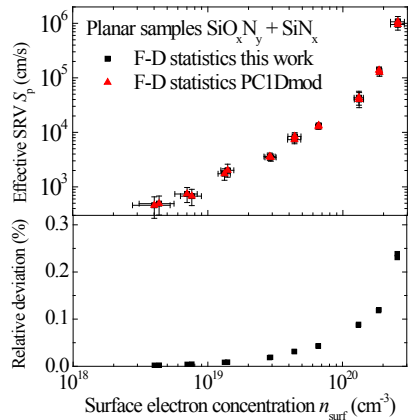


Figure A.2 Analytically extracted  $S_p$  over electron surface concentration and relative deviation of the results for one set of samples described in Chapter 5 (compare Figure 5.8). Simulated at  $T = 300 \text{ K}$ .

The calculated effective  $S_p$  (compare Chapter 5) and their relative deviation between the calculation procedures are shown in Figure A.2. In agreement with the minority hole concentrations, the deviation between the carrier statistics in PC1Dmod and in this work results in a deviation of less than 0.3 %. In consequence the calculations presented in this work are equivalent to the procedure in PC1Dmod and can be applied

there. Notice that PC1D has shown high consistency with other simulation tools [17], such as EDNA [19] and Sentaurus Device [20].

## Bibliography

- [1] I. Adopted, "CLIMATE CHANGE 2014 SYNTHESIS REPORT," 2014.
- [2] H.-M. Henning, "Energiesystem Deutschland 2050," Fraunhofer-Institute for Solar Energy Systems, Freiburg 2013.
- [3] pvXchange. (2015, 15/04/24). *PV price index*. Available: <http://www.pvxchange.com/priceindex/priceindex.aspx>
- [4] T. Fellmeth, "Silicon Solar Cells for the Application in Low Concentrator Systems-Development and Characterization," Dissertation, Mathematisch-Naturwissenschaftliche Fakultät, Eberhard Karls Universität, Tübingen, 2015.
- [5] S. Werner, E. Lohmüller, S. Maier, A. Kimmerle, A. Spribille, S. Wasmer, F. Clement, and A. Wolf, "Process optimization for the front side of p-type silicon solar cells," in *Proceedings of the 29th European Photovoltaic Solar Energy Conference and Exhibition*, Amsterdam, The Netherlands, 2014, pp. 1342-7.
- [6] S. M. Sze, *Physics of Semiconductor Devices*, 2nd ed. New York: John Wiley & Sons, 1981.
- [7] M. A. Green, "Silicon Solar Cells: Advanced Principles and Practice," *Bridge Printery: Sydney*, 1995.
- [8] M. A. Green, "Intrinsic concentration, effective densities of states, and effective mass in silicon," *Journal of Applied Physics*, vol. 67, pp. 2944-54, 1990.
- [9] A. B. Sproul and M. A. Green, "Intrinsic carrier concentration and minority-carrier mobility of silicon from 77 to 300 K," *Journal of Applied Physics*, vol. 73, pp. 1214-25, 1993.
- [10] A. Wolf, D. Biro, J. Nekarda, S. Stumpp, A. Kimmerle, S. Mack, and R. Preu, "Comprehensive analytical model for locally contacted rear surface passivated solar cells," *Journal of Applied Physics*, vol. 108, p. 124510, 2010.
- [11] P. P. Altermatt, A. Schenk, F. Geelhaar, and G. Heiser, "Reassessment of the intrinsic carrier density in crystalline silicon in view of band-gap narrowing," *Journal of Applied Physics*, vol. 93, pp. 1598-604, 2003.
- [12] J. Pankove, "Influence of degeneracy on recombination radiation in germanium," *Physical Review Letters*, vol. 4, p. 20, 1960.
- [13] A. Neugroschel, J. Wang, and F. Lindholm, "Evidence for excess carrier storage in electron-hole plasma in silicon transistors," *IEEE ELECTRON DEVICE LETTERS*, vol. 6, pp. 253-255, 1985.
- [14] A. Schenk, "Finite-temperature full random-phase approximation model of band gap narrowing for silicon device simulation," *Journal of Applied Physics*, vol. 84, pp. 3684-95, 1998.

- 
- [15] A. L. Blum, J. S. Swirhun, R. A. Sinton, and A. Kimmerle, "An Updated Analysis to the WCT-120 QSSPC measurement system using advanced device physics," in *Proceedings of the 28th European Photovoltaic Solar Energy Conference and Exhibition*, Paris, France, 2013, pp. 1521-1523.
- [16] A. Kimmerle, P. Rothhardt, A. Wolf, and R. A. Sinton, "Increased reliability for  $J_0$ -analysis by QSSPC," *Energy Procedia*, vol. 55, pp. 101-6, 2014.
- [17] H. Haug, A. Kimmerle, J. Greulich, A. Wolf, and E. S. Marstein, "Implementation of Fermi–Dirac statistics and advanced models in PC1D for precise simulations of silicon solar cells," *Solar Energy Materials and Solar Cells*, vol. 131, pp. 30-6, 2014.
- [18] H. Haug, J. Greulich, A. Kimmerle, A. Wolf, and E. S. Marstein, "PC1Dmod 6.1 - state-of-the-art models in a well-known interface for improved simulation of Si solar cells," *Solar Energy Materials and Solar Cells*, vol. in press, 2015.
- [19] K. R. McIntosh and P. P. Altermatt, "A freeware 1d emitter model for silicon solar cells," in *Proceedings of the 35th IEEE Photovoltaic Specialists Conference*, Honolulu, Hawaii, USA, 2010, pp. 1-6.
- [20] Synopsys, "Sentaurus TCAD," release E-2010.12 ed. Zürich, Switzerland.
- [21] D. Yan and A. Cuevas, "Empirical determination of the energy band gap narrowing in highly doped n+ silicon," *Journal of Applied Physics*, vol. 114, p. 044508, 2013.
- [22] D. Yan and A. Cuevas, "Empirical determination of the energy band gap narrowing in p<sup>+</sup> silicon heavily doped with boron," *Journal of Applied Physics*, vol. 116, p. 194505, 2014.
- [23] A. Richter, S. W. Glunz, F. Werner, J. Schmidt, and A. Cuevas, "Improved quantitative description of Auger recombination in crystalline silicon," *Physical Review B*, vol. 86, pp. 1-14, 2012.
- [24] T. Trupke, M. A. Green, P. Würfel, P. P. Altermatt, A. Wang, J. Zhao, and R. Corkish, "Temperature dependence of the radiative recombination coefficient of intrinsic crystalline silicon," *Journal of Applied Physics*, vol. 94, pp. 4930-7, 15 Oct 2003.
- [25] W. Shockley and W. T. J. Read, "Statistics of the recombinations of holes and electrons," *Physical Review*, vol. 87, pp. 835-42, 1952.
- [26] R. N. Hall, "Electron-hole recombination in germanium," *Physical Review*, vol. 87, p. 387, 1952.
- [27] M. Rüdiger, "Analysis and Simulation of Crystalline Silicon Solar Cells," Dissertation, Fachbereich Physik, Universität Konstanz, Konstanz, 2013.
- [28] K. Bothe, R. Sinton, and J. Schmidt, "Fundamental boron-oxygen-related carrier lifetime limit in mono- and multicrystalline silicon," *Progress in Photovoltaics: Research and Applications*, vol. 12, pp. 1-10, 2004.

- [29] S. W. Glunz, S. Rein, J. Y. Lee, and W. Warta, "Minority carrier lifetime degradation in boron-doped Czochralski silicon," *Journal of Applied Physics*, vol. 90, pp. 2397-404, 2001.
- [30] S. Rein and S. W. Glunz, "Electronic properties of the metastable defect in boron-doped Czochralski silicon: Unambiguous determination by advanced lifetime spectroscopy," *Applied Physics Letters*, vol. 82, pp. 1054-56, 2003.
- [31] P. P. Altermatt, "Models for numerical device simulations of crystalline silicon solar cells—a review," *Journal of Computational Electronics*, vol. 10, pp. 314-30, 2011.
- [32] D. B. M. Klaassen, "A unified mobility model for device simulation - I. Model equations and concentration dependence," *Solid-State Electronics*, vol. 35, pp. 953-9, 1992.
- [33] D. B. M. Klaassen, "A unified mobility model for device simulation - II. Temperature dependence of carrier mobility and lifetime. ," *Solid State Electronics*, vol. 35, pp. 961-7, 1992.
- [34] F. Schindler, M. Forster, J. Broisch, J. Schön, J. Giesecke, S. Rein, W. Warta, and M. C. Schubert, "Towards a unified low-field model for carrier mobilities in crystalline silicon," *Solar Energy Materials and Solar Cells*, vol. 131, pp. 92-99, 2014.
- [35] P. Würfel, *Physics of Solar Cells - From Principles to New Concepts*, 2005.
- [36] D. Kane and R. Swanson, "Electron-hole collisions in concentrator solar cells," in *Photovoltaic Specialists Conference, 1988., Conference Record of the Twentieth IEEE*, 1988, pp. 512-517.
- [37] S. S. Li and W. R. Thurber, "The dopant density and temperature dependence of electron mobility and resistivity in n-type silicon," *Solid-State Electronics*, vol. 20, pp. 609-616, 1977.
- [38] E. Bremner, T. Ambridge, and C. Elliott, "An automatic plotting system for the electrochemical characterization of n-type gallium arsenide," *Journal of Physics E: Scientific Instruments*, vol. 6, p. 326, 1973.
- [39] T. Ambridge, J. L. Stevenson, and R. M. Redstall, "Applications of Electrochemical Methods for Semiconductor Characterization I. Highly Reproducible Carrier Concentration Profiling of VPE "Hi-Lo"," *Journal of the Electrochemical Society*, vol. 127, pp. 222-228, 1980.
- [40] P. Blood, "Capacitance-voltage profiling and the characterisation of III-V semiconductors using electrolyte barriers," *Semiconductor science and technology*, vol. 1, p. 7, 1986.
- [41] D. K. Schroder, *Semiconductor material and device characterization*, 3rd ed. Hoboken, New Jersey, USA: John Wiley & Sons, 2006.
- [42] W. Warta, J. Sutter, B. F. Wagner, and R. Schindler, "Characterization of High-Efficiency Silicon Solar Cells with Rear Side Contacts," in *2nd World*

- Conference on Photovoltaic Energy Conversion*, Vienna, Austria, 1998, pp. 1650 - 1653.
- [43] M. Padilla, B. Michl, B. Thaidigsmann, W. Warta, and M. C. Schubert, "Short-circuit current density mapping for solar cells," *Solar Energy Materials and Solar Cells*, vol. 120, Part A, pp. 282-8, 2014.
- [44] W. Shockley, "Research and investigation of inverse epitaxial UHF power transistors," *Report No Al-TOR-64-207 Air Force At. Lab. Wright-Patterson Air Force Base Ohio*, 1964.
- [45] H. H. Berger, "Contact resistance and contact resistivity," *Journal of the Electrochemical Society*, vol. 119, pp. 507-14, 1972.
- [46] M. von Ardenne, "Das Elektronen-Rastermikroskop," *Zeitschrift für Physik*, vol. 109, pp. 553-572, 1938/09/01 1938.
- [47] G. Miller, D. Robinson, and J. Wiley, "Contactless measurement of semiconductor conductivity by radio frequency-free-carrier power absorption," *Review of Scientific Instruments*, vol. 47, pp. 799-805, 1976.
- [48] M. Spitz, U. Belledin, and S. Rein, "Fast inductive inline measurement of the emitter sheet resistance in industrial solar cell fabrication," in *Proceedings of the 22nd European Photovoltaic Solar Energy Conference*, Milan, Italy, 2007, pp. 47-50.
- [49] P. Rothhardt, "Co-Diffusion for Bifacial n-Type Solar Cells," Dissertation, Fakultät für Mathematik und Physik, Albert-Ludwigs-Universität Freiburg, Freiburg, 2014.
- [50] J. O. Schumacher, P. P. Altermatt, G. Heiser, and A. G. Aberle, "Application of an improved band-gap narrowing model to the numerical simulation of recombination properties of phosphorus-doped silicon emitters," *Solar Energy Materials and Solar Cells*, vol. 65, pp. 95-103, 2001.
- [51] A. Cuevas, M. Stocks, D. Macdonald, and R. Sinton, "Applications of the quasi-steady-state photoconductance technique," in *Proceedings of the 2nd World Conference on Photovoltaic Energy Conversion*, Vienna, Austria, 1998.
- [52] A. Cuevas, R. Merchán, and J. C. Ramos, "On the systematic analytical solutions for minority-carrier transport in nonuniform doped semiconductors: application to solar cells," *IEEE Transactions on Electron Devices*, vol. 40, pp. 1181-3, 1993.
- [53] A. Richter, J. Benick, A. Kimmerle, M. Hermle, and S. W. Glunz, "Passivation of phosphorus diffused silicon surfaces with Al<sub>2</sub>O<sub>3</sub>: Influence of surface doping concentration and thermal activation treatments," *Journal of Applied Physics*, vol. 116, p. 243501, 2014.
- [54] R. A. Sinton and A. Cuevas, "Contactless determination of current-voltage characteristics and minority-carrier lifetimes in semiconductors from quasi-steady-state photoconductance data," *Applied Physics Letters*, vol. 69, pp. 2510-2, 1996.

- [55] M. J. Kerr, "Surface, emitter and bulk recombination in silicon and development of silicon nitride passivated solar cells," PhD Dissertation, Australian National University, 2002.
- [56] H. Nagel, C. Berge, and A. G. Aberle, "Generalized analysis of quasi-steady-state and quasi-transient measurements of carrier lifetimes in semiconductors," *Journal of Applied Physics*, vol. 86, pp. 6218-21, 1999.
- [57] J. R. Haynes and W. Shockley, "The mobility and life of injected holes and electrons in germanium," *Physical Review*, vol. 81, pp. 835-43, 1951.
- [58] K. L. Luke and L.-J. Cheng, "Analysis of the interaction of a laser pulse with a silicon wafer: determination of bulk lifetime and surface recombination velocity," *Journal of Applied Physics*, vol. 61, pp. 2282-93, 1987.
- [59] A. B. Sproul, "Dimensionless solution of the equation describing the effect of surface recombination on carrier decay in semiconductors," *Journal of Applied Physics*, vol. 76, pp. 2851-4, 1994.
- [60] A. Cuevas and R. A. Sinton, "Prediction of the open-circuit voltage of solar cells from the steady-state photoconductance," *Progress in Photovoltaics: Research and Applications*, vol. 5, pp. 79-90, 1997.
- [61] R. A. Sinton, H. Tathgar, S. Bowden, and A. Cuevas, "On the problem of determining the bulk lifetime of unpassivated silicon wafers," in *Proceedings of the 14th Workshop on Crystalline Silicon Solar Cells and Modules*, Winter Park, Colorado, USA, 2004, pp. 1-4.
- [62] A. Goetzberger, B. Voß, and J. Knobloch, *Sonnenenergie: Photovoltaik*. Stuttgart: Teubner Studienbücher Physik, 1994.
- [63] K. R. McIntosh, "Lumps, humps and bumps: Three detrimental effects in the current-voltage curve of silicon solar cells," Dissertation, Centre for Photovoltaic Engineering, University of New South Wales, Sydney, Australia, 2001.
- [64] A. L. Fahrenbruch and R. H. Bube, *Fundamentals of solar cells*. New York: Academic Press, 1983.
- [65] B. Fischer, "Loss analysis of crystalline silicon solar cells using photoconductance and quantum efficiency measurements," Dissertation, Fachbereich Physik, Universität Konstanz, Konstanz, 2003.
- [66] H. Plagwitz and R. Brendel, "Analytical model for the diode saturation current of point-contacted solar cells," *Progress in Photovoltaics: Research and Applications*, vol. 14, pp. 1-12, 2006.
- [67] R. H. Cox and H. Strack, "Ohmic contacts for GaAs devices," *Solid State Electronics*, vol. 10, pp. 1213-8, 1967.
- [68] R. Brendel and U. Rau, "Injection and collection diffusion lengths of polycrystalline thin-film solar cells," *Solid State Phenomena*, vol. 67-68, pp. 81-8 1999.

- [69] R. Woehl, "All-Screen-Printed Back-Contact Back-Junction Silicon Solar Cells with Aluminum-Alloyed Emitter," Dissertation, Technische Fakultät, Albert-Ludwigs-Universität Freiburg, Freiburg, 2011.
- [70] R. Woehl, R. Keding, M. Rüdiger, H. Gentischer, F. Clement, J. Wilde, and D. Biro, "20% efficient screen-printed and aluminium-alloyed back-contact back-junction cells and interconnection scheme of point-shaped metalized cells," in *Proceedings of the 37th IEEE Photovoltaic Specialists Conference*, Seattle, Washington, USA, 2011, pp. 48-52.
- [71] F. Huster, "Investigation of the alloying process of screen printed aluminium pastes for the BSF formation on silicon solar cells," in *Proceedings of the 20th European Photovoltaic Solar Energy Conference*, Barcelona, Spain, 2005, pp. 1466-9.
- [72] M. Rauer, C. Schmiga, M. Glatthaar, and S. W. Glunz, "Alloying from screen-printed aluminum pastes containing boron additives," *IEEE Journal of Photovoltaics*, vol. 3, pp. 206-11, 2013.
- [73] M. Rüdiger, M. Rauer, C. Schmiga, M. Hermle, and S. W. Glunz, "Accurate modeling of aluminum-doped silicon," in *Proceedings of the 1st International Conference on Silicon Photovoltaics*, Freiburg, Germany, 2011, pp. 527-32.
- [74] J. Schmidt, N. Thiemann, R. Bock, and R. Brendel, "Recombination lifetimes in highly aluminum-doped silicon," *Journal of Applied Physics*, vol. 106, p. 093707, 2009.
- [75] A. Kimmerle, J. Greulich, and A. Wolf, "Carrier-Diffusion Corrected J0-Analysis by QSSPC for Increased Consistency," *Solar Energy Materials and Solar Cells*, vol. Accepted for publication, 2015.
- [76] D. E. Kane and R. M. Swanson, "Measurement of the emitter saturation current by a contactless photoconductivity decay method (silicon solar cells)," in *Proceedings of the 18th IEEE Photovoltaic Specialists Conference*, Las Vegas, Nevada, USA, 1985, pp. 578-83.
- [77] J. Nekarda, "Laser Fired Contacts (LFC) - Charakterisierung, Optimierung und Modellierung eines Verfahrens zur lokalen Rückseitenkontaktierung dielektrisch passivierter Silizium-Solarzellen," Dissertation, Fachbereich Physik, Universität Konstanz, Konstanz, 2012.
- [78] A. Cuevas, "Modelling silicon characterisation," *Energy Procedia*, vol. 8, pp. 94-99, 2011.
- [79] A. F. Thomson, Z. Hameiri, N. E. Grant, C. J. Price, D. Yan, and J. Spurgin, "Uncertainty in photoconduance measurements of the emitter saturation current," *IEEE Journal of Photovoltaics*, vol. 3, pp. 1200-7, 2013.
- [80] A. Cuevas, "The effect of emitter recombination on the effective lifetime of silicon wafers," *Solar Energy Materials and Solar Cells*, vol. 57, pp. 277-90, 1999.

- [81] H. Mäckel and K. Varner, "On the determination of the emitter saturation current density from lifetime measurements of silicon devices," *Progress in Photovoltaics: Research and Applications*, pp. 1-17, 2012.
- [82] K. L. Luke, O. von Roos, and L.-J. Cheng, "Quantification of the effects of generation volume, surface recombination velocity, and diffusion length on the electron-beam- induced current and its derivative: determination of diffusion lengths in the low micron and submicron ranges," *Journal of Applied Physics*, vol. 57, pp. 1978- 84, 1985.
- [83] B. Min, A. Dastgheib-Shirazi, P. P. Altermatt, and H. Kurz, "Accurate Determination of the Emitter Saturation Current Density for Industrial P-Diffused Emitters," in *Proceedings of the 29th European Photovoltaic Solar Energy Conference and Exhibition*, Amsterdam, The Netherlands, 2014, pp. 463 - 466.
- [84] A. Thomson, N. Grant, K. F. Chern, and T. Kho, "Improved Diffused-region Recombination-current Pre-factor Analysis," *Energy Procedia*, vol. 55, pp. 141-148, 2014.
- [85] A. Kimmerle, M. Rüdiger, A. Wolf, M. Hermle, and D. Biro, "Validation of analytical modelling of locally contacted solar cells by numerical simulations," *Energy Procedia*, vol. 27, pp. 219-26, 3-5 Apr 2012.
- [86] M. Rüdiger, C. Schmiga, M. Rauer, M. Hermle, and S. W. Glunz, "Efficiency potential of n-type silicon solar cells with aluminum-doped rear p<sup>+</sup> emitter," *IEEE Transactions on Electron Devices*, vol. 59, pp. 1295-303, 2012.
- [87] D. Kray and S. W. Glunz, "Investigation of laser-fired rear-side recombination properties using an analytical model," *Progress in Photovoltaics: Research and Applications*, vol. 14, pp. 195-201, 2006.
- [88] A. Cuevas, M. Stuckings, J. Lau, and M. Petracic, "The recombination velocity of boron diffused silicon surfaces," in *Proceedings of the 14th European Photovoltaic Solar Energy Conference*, Barcelona, Spain, 1997, pp. 2416-9.
- [89] M. Rahman, "Experimental Characterization of Recombination Properties at Diffused Surfaces for Industrial Silicon Solar Cell Concepts," Master, Institute of Micro and Nanomaterials, University Ulm, Ulm, 2014.
- [90] S. Mack, A. Wolf, C. Brosinsky, S. Schmeisser, A. Kimmerle, P. Saint-Cast, M. Hofmann, and D. Biro, "Silicon surface passivation by thin thermal oxide/PECVD layer stack systems," *IEEE Journal of Photovoltaics*, vol. 1, pp. 135-45, 2011.
- [91] J. Seiffe, L. Gautero, M. Hofmann, J. Rentsch, R. Preu, S. Weber, and R. A. Eichel, "Surface passivation of crystalline silicon by plasma-enhanced chemical vapor deposition double layers of silicon-rich silicon oxynitride and silicon nitride," *Journal of Applied Physics*, vol. 109, p. 034105, 2011.
- [92] A. Moldovan, K. Birmann, J. Rentsch, M. Zimmer, T. Gitte, and J. Fittkau, "Combined Ozone/HF/HCl Based Cleaning and Adjusted Emitter Etch-Back for Silicon Solar Cells," in *Solid State Phenomena*, 2013, pp. 305-309.

- [93] K. R. McIntosh and L. P. Johnson, "Recombination at textured silicon surfaces passivated with silicon dioxide," *Journal of Applied Physics*, vol. 105, p. 124520, 2009.
- [94] A. Kimmerle, A. Wolf, U. Belledin, and D. Biro, "Modelling carrier recombination in highly phosphorus-doped industrial emitters," *Energy Procedia*, vol. 8, pp. 275-281, 2011.
- [95] A. Kimmerle, "Herstellung und Charakterisierung hochohmiger Emmitter für Hocheffizienz solarzellen," Diplom, Fakultät für Mathematik und Physik, Albert Ludwigs Universität, Freiburg, 2011.
- [96] P. P. Altermatt, J. O. Schumacher, A. Cuevas, S. W. Glunz, R. R. King, G. Heiser, and A. Schenk, "Numerical modeling of highly doped Si:P emitters based on Fermi-Dirac statistics and self-consistent material parameters," *Journal of Applied Physics*, vol. 92, pp. 3187-97, 2002.
- [97] M. J. Kerr, J. Schmidt, A. Cuevas, and J. H. Bultman, "Surface recombination velocity of phosphorus-diffused silicon solar cell emitters passivated with plasma enhanced chemical vapor deposited silicon nitride and thermal silicon oxide," *Journal of Applied Physics*, vol. 89, pp. 3821-6, 2001.
- [98] A. Cuevas, P. A. Basore, G. Giroult-Matlakowski, and C. Dubois, "Surface recombination velocity of highly doped n-type silicon," *Journal of Applied Physics*, vol. 80, pp. 3370-5, 1996.
- [99] S. W. Glunz, S. Sterk, R. Steeman, W. Warta, J. Knobloch, and W. Wetting, "Emitter dark saturation currents of high-efficiency solar cells with inverted pyramids," in *Proceedings of the 13th European Photovoltaic Solar Energy Conference*, Nice, France, 1995, pp. 409-12.
- [100] R. R. King, R. A. Sinton, and R. M. Swanson, "Studies of diffused phosphorus emitters: saturation current, surface recombination velocity, and quantum efficiency," *IEEE Transactions on Electron Devices*, vol. 37, pp. 365-71, 1990.
- [101] A. Armigliato, D. Nobili, M. Servidori, and S. Solmi, "SiP precipitation within the doped silicon lattice, concomitant with phosphorus predeposition," *Journal of Applied Physics*, vol. 47, pp. 5489-5491, 1976.
- [102] A. Kimmerle, R. Woehl, A. Wolf, and D. Biro, "Simplified Front Surface Field Formation for Back Contacted Silicon Solar Cells," *Energy Procedia*, vol. 38, pp. 278-82, 2013.
- [103] R. J. Falster, M. Cornara, D. Gambaro, M. Olmo, and M. Pagani, "Effect of high temperature pre-anneal on oxygen precipitates nucleation kinetics in Si," *Solid State Phenomena*, vol. 57, pp. 123-128, 1997.
- [104] A. Cuevas, "A good recipe to make silicon solar cells," in *Proceedings of the 22nd IEEE Photovoltaic Specialists Conference*, Las Vegas, Nevada, USA, 1991, pp. 466-70.
- [105] Y. Komatsu, A. Stassen, P. Venema, A. H. G. Vlooswijk, C. Meyer, and M. Koorn, "Sophistication of doping profile manipulation - emitter performance

- improvement without additional process step," in *Proceedings of the 25th European Photovoltaic Solar Energy Conference and Exhibition*, Valencia, Spain, 2010, pp. 1924-9.
- [106] P. A. Basore, J. M. Gee, M. E. Buck, W. K. Schubert, and D. S. Ruby, "Simplified high-efficiency silicon cell processing," in *Proceedings of the 7th International Photovoltaic Science and Engineering Conference*, Nagoya, Japan, 1993, pp. 61-4.
- [107] Y. Komatsu, G. Galbiati, M. Lamers, P. Venema, M. Harris, A. F. Stassen, C. Meyer, M. van den Donker, and A. Weeber, "Innovative diffusion processes for improved efficiency on industrial solar cells by doping profile manipulation," in *Proceedings of the 24th European Photovoltaic Solar Energy Conference*, Hamburg, Germany, 2009, pp. 1-5.
- [108] A. Ural, P. B. Griffin, and J. D. Plummer, "Fractional contributions of microscopic diffusion mechanisms for common dopants and self-diffusion in silicon," *Journal of Applied Physics*, vol. 85, pp. 6440-6446, 1999.
- [109] A. Bentzen, A. Holt, J. S. Christensen, and B. G. Svensson, "High concentration in-diffusion of phosphorus in Si from a spray-on source," *Journal of Applied Physics*, vol. 99, p. 064502, 2006.
- [110] S. Solmi, A. Parisini, R. Angelucci, A. Armigliato, D. Nobili, and L. Moro, "Dopant and carrier concentration in Si in equilibrium with monoclinic SiP precipitates," *Physical Review B*, vol. 53, pp. 7836-41, 1996.
- [111] R. Hoenig, M. Duerrschnabel, W. van Mierlo, Z. Aabdin, J. Bernhard, J. Biskupek, O. Eibl, U. Kaiser, J. Wilde, and F. Clement, "The Nature of Screen Printed Front Side Silver Contacts-Results of the project MikroSol," *Energy Procedia*, vol. 43, pp. 27-36, 2013.
- [112] N. Mingirulli, R. Keding, J. Specht, A. Fallisch, D. Stüwe, and D. Biro, "Hot-melt inkjet as masking technology for back-contacted cells," in *Proceedings of the 34th IEEE Photovoltaic Specialists Conference*, Philadelphia, 2009, pp. 1064-8.
- [113] J. Schön, M. C. Schubert, W. Warta, H. Savin, and A. Haarahltonen, "Analysis of simultaneous boron and phosphorus diffusion gettering in silicon," *Physica Status Solidi A*, vol. 207, pp. 2589-92, 2010.
- [114] D. Biro, D. Erath, U. Belledin, J. Specht, D. Stüwe, A. Lemke, M. Aleman, N. Mingirulli, J. Rentsch, R. Preu, R. Schlosser, B. Bitnar, and H. Neuhaus, "Inkjet printing for high definition industrial masking processes for solar cell production," in *Proceedings of the 17th International Photovoltaic Science and Engineering Conference*, Fukuoka, Japan, 2007.
- [115] D. Stüwe, D. Mager, D. Biro, and J. G. Korvink, "Inkjet Technology for Crystalline Silicon Photovoltaics," *Advanced Materials*, 2014.
- [116] A.-K. Volk, U. Jaeger, J. Rentsch, and R. Preu, "A novel approach for mask-free selective emitter technology combining laser doping and wet chemical etch

- back," in *Proceedings of the 26th European Photovoltaic Solar Energy Conference and Exhibition*, Hamburg, Germany, 2011, pp. 884-9.
- [117] N. Meilwes, J.-M. Spaeth, V. Emtsev, and G. Oganessian, "On the nature and structures of different heat treatment centres in n-and p-type silicon," *Semiconductor science and technology*, vol. 9, p. 1346, 1994.
- [118] M. Hermle, F. Granek, O. Schultz-Wittmann, and S. W. Glunz, "Shading effects in back-junction back-contacted silicon solar cells," in *Proceedings of the 33rd IEEE Photovoltaic Specialists Conference*, San Diego, USA, 2008.
- [119] J. M. Greulich, "Simulation and characterization of novel large-area silicon solar cells for industrial production," Dissertation, Fakultät für Mathematik und Physik, Albert-Ludwigs-Universität Freiburg im Breisgau, Freiburg im Breisgau, 2013.
- [120] M. Hendrichs, R. Keding, A. Spribille, T. Fellmeth, S. Nold, F. Clement, A. Wolf, and D. Biro, "Optimization of multi-layer metallization design for large-area back-contact back-junction solar cells," in *Proceedings of the 29th European Photovoltaic Solar Energy Conference and Exhibition*, Amsterdam, The Netherlands, 2014, pp. 412-6.
- [121] A. Mohr, "Silicon concentrator cells in a two-stage photovoltaic system with a concentration factor of 300x," Dissertation, Fakultät für Angewandte Wissenschaften, Universität Freiburg, Freiburg, 2005.
- [122] A. Mette, "New concepts for front side metallization of industrial silicon solar cells," Dissertation, Fakultät für Angewandte Wissenschaften, Universität Freiburg, Freiburg, 2007.
- [123] S. Kluska, "Analyse von hocheffizienten rückseitig kontaktierten Silicium-Solarzellen," Diplomarbeit, Fakultät für Mathematik und Physik, Universität Freiburg, Freiburg im Breisgau, Germany, 2009.
- [124] P. Saint-Cast, F. Tanay, M. Aleman, C. Reichel, J. Bartsch, M. Hofmann, J. Rentsch, and R. Preu, "Relevant pinhole characterisation methods for dielectric layers for silicon solar cells," in *Proceedings of the 24th European Photovoltaic Solar Energy Conference*, Hamburg, Germany, 2009, pp. 2084-7.
- [125] C. Reichel, M. Reusch, F. Granek, M. Hermle, and S. W. Glunz, "Decoupling charge carrier collection and metallization geometry of back-contacted back-junction silicon solar cells by using insulating thin films," in *Proceedings of the 35th IEEE Photovoltaic Specialists Conference*, Honolulu, Hawaii, USA, 2010.
- [126] R. Keding, R. Bock, A. Bochow, K. Katkhouda, D. Stüwe, C. Reichel, F. Clement, R. Woehl, H. Reinecke, and T. Geppert, "Study of the electrical insulation of dielectric passivation layers and stacks for back-contact back-junction silicon solar cells," in *Proceedings of the 28th European Photovoltaic Solar Energy Conference and Exhibition*, Paris, France, 2013, pp. 1321-6.
- [127] D. A. Clugston and P. A. Basore, "PC1D version 5: 32-bit solar cell modeling on personal computers," in *Proceedings of the 26th IEEE Photovoltaic Specialists Conference*, Anaheim, California, USA, 1997, pp. 207-10.

## List of Publications

### Refereed journal publications

- A. Wolf, D. Biro, J. Nekarda, S. Stumpp, **A. Kimmerle**, S. Mack, and R. Preu, "Comprehensive analytical model for locally contacted rear surface passivated solar cells," *Journal of Applied Physics*, vol. 108, p. 124510, 2010.
- T. Fellmeth, A. Born, **A. Kimmerle**, F. Clement, D. Biro, and R. Preu, "Recombination at Metal-Emitter Interfaces of Front Contact Technologies for Highly Efficient Silicon Solar Cells," *Energy Procedia*, vol. 8, pp. 115-121, 2011.
- S. Mack, A. Wolf, C. Brosinsky, S. Schmeisser, **A. Kimmerle**, P. Saint-Cast, M. Hofmann, and D. Biro, "Silicon surface passivation by thin thermal oxide/PECVD layer stack systems," *IEEE Journal of Photovoltaics*, vol. 1, pp. 135-45, 2011.
- **A. Kimmerle**, A. Wolf, U. Belledin, and D. Biro, "Modelling carrier recombination in highly phosphorus-doped industrial emitters," *Energy Procedia*, vol. 8, pp. 275-281, 2011.
- F. Schindler, M. C. Schubert, **A. Kimmerle**, J. Broisch, S. Rein, W. Kwapil, and W. Warta, "Modeling majority carrier mobility in compensated crystalline silicon for solar cells," *Solar Energy Materials and Solar Cells*, vol. 106, pp. 31-6, 2012.
- **A. Kimmerle**, M. Rüdiger, A. Wolf, M. Hermle, and D. Biro, "Validation of analytical modelling of locally contacted solar cells by numerical simulations," *Energy Procedia*, vol. 27, pp. 219-26, 3-5 Apr 2012.
- **A. Kimmerle**, R. Woehl, A. Wolf, and D. Biro, "Simplified Front Surface Field Formation for Back Contacted Silicon Solar Cells," *Energy Procedia*, vol. 38, pp. 278-82, 2013.
- H. Haug, **A. Kimmerle**, J. Greulich, A. Wolf, and E. S. Marstein, "Implementation of Fermi–Dirac statistics and advanced models in PC1D for precise simulations of silicon solar cells," *Solar Energy Materials and Solar Cells*, vol. 131, pp. 30-6, 2014.
- P. Saint-Cast, M. Padilla, **A. Kimmerle**, and C. Reichel, "An analytical model for interdigitated back contact solar cells," *IEEE Journal of Photovoltaics*, vol. 4, pp. 114-21, 2014.
- B. Min, H. Wagner, A. Dastgheib-Shirazi, **A. Kimmerle**, H. Kurz, and P. P. Altermatt, "Heavily doped Si:P emitters of crystalline Si solar cells: recombination due to phosphorus precipitation," *physica status solidi (RRL) – Rapid Research Letters*, vol. 8, pp. 680-684, 2014.

- **A. Kimmerle**, P. Rothhardt, A. Wolf, and R. A. Sinton, "Increased reliability for J0-analysis by QSSPC," *Energy Procedia*, vol. 55, pp. 101-6, 2014.
- A. Richter, J. Benick, **A. Kimmerle**, M. Hermle, and S. W. Glunz, "Passivation of phosphorus diffused silicon surfaces with Al<sub>2</sub>O<sub>3</sub>: Influence of surface doping concentration and thermal activation treatments," *Journal of Applied Physics*, vol. 116, p. 243501, 2014.
- **A. Kimmerle**, J. Greulich, and A. Wolf, "Carrier-Diffusion Corrected J0-Analysis of Charge Carrier Lifetime Measurements for Increased Consistency," *Solar Energy Materials and Solar Cells*, in press (2015).
- H. Haug, J. Greulich, **A. Kimmerle**, A. Wolf, E. S. Marstein, "PC1Dmod 6.1 - State-Of-The-Art Models in a Well-Known Interface for Improved Simulation of Si Solar Cells", *Solar Energy Materials and Solar Cells*, in press (2015).

### Conference contributions

- S. Werner, U. Belledin, **A. Kimmerle**, A. Fallisch, A. Wolf, and D. Biro, "Doping- and carrier concentration profile characterisation of highly phosphorus-doped emitters," in *Proceedings of the 25th European Photovoltaic Solar Energy Conference and Exhibition*, Valencia, Spain, 2010, pp. 1942-7.
- U. Jäger, S. Mack, **A. Kimmerle**, A. Wolf, and R. Preu, "Influence of doping profile of highly doped regions for selective emitter solar cells," in *Proceedings of the 35th IEEE Photovoltaic Specialists Conference*, Honolulu, Hawaii, USA, 2010.
- U. Jäger, P. Oesterlin, **A. Kimmerle**, and R. Preu, "Beam shaping - the key to high throughput selective emitter laser processing with a single laser system," in *Proceedings of the 35th IEEE Photovoltaic Specialists Conference*, Honolulu, Hawaii, USA, 2010.
- **A. Kimmerle**, A. Wolf, U. Belledin, and B. Biro, "Modelling carrier recombination in highly phosphorus-doped industrial emitters," *1st International Conference on Silicon Photovoltaics*, Freiburg, Germany, 2011.
- T. Fellmeth, A. Born, **A. Kimmerle**, F. Clement, D. Biro, and R. Preu, "Recombination at metal-emitter interfaces of front contact technologies for highly efficient silicon solar cells," *1st International Conference on Silicon Photovoltaics*, Freiburg, Germany, 2011.
- F. Schindler, M. C. Schubert, **A. Kimmerle**, J. Broisch, S. Rein, W. Kwapil, and W. Warta, "Modeling majority carrier mobility in compensated crystalline silicon for solar cells," *2nd International Conference on Silicon Photovoltaics*, Leuven, Belgium, 2012.

- **A. Kimmerle**, M. Rüdiger, A. Wolf, M. Hermlé, and D. Biro, "Validation of analytical modelling of locally contacted solar cells by numerical simulations," *2nd International Conference on Silicon Photovoltaics, Leuven*, Belgium, 2012.
- **A. Kimmerle**, R. Woehl, A. Wolf, and D. Biro, "Simplified Front Surface Field Formation for Back Contacted Silicon Solar Cells," *3rd International Conference on Silicon Photovoltaics*, Hamelin, Germany, 2013.
- E. Navarrete, **A. Kimmerle**, B. Thaidigsmann, R. Woehl, J. R. Ramos-Barrado, and D. Biro, "Evaluation of Fire-Through Aluminum Pastes for Local Contact Formation in Silicon Solar Cells," in *Proceedings of the 28th European Photovoltaic Solar Energy Conference and Exhibition*, Paris, France, 2013, pp. 1839-1841.
- A. L. Blum, J. S. Swirhun, R. A. Sinton, and **A. Kimmerle**, "An Updated Analysis to the WCT-120 QSSPC measurement system using advanced device physics," in *Proceedings of the 28th European Photovoltaic Solar Energy Conference and Exhibition*, Paris, France, 2013, pp. 1521-1523.
- S. Werner, E. Lohmüller, S. Maier, **A. Kimmerle**, A. Spribille, S. Wasmer, F. Clement, and A. Wolf, "Process optimization for the front side of p-type silicon solar cells," in *Proceedings of the 29th European Photovoltaic Solar Energy Conference and Exhibition*, Amsterdam, The Netherlands, 2014, pp. 1342-7.
- **A. Kimmerle**, P. Rothhardt, A. Wolf, and R. A. Sinton, "Increased reliability for J0-analysis by QSSPC," *4th International Conference on Silicon Photovoltaics*, 's-Hertogenbosch, The Netherlands, 2014.
- H. Haug, **A. Kimmerle**, J. Greulich, A. Wolf, and E. S. Marstein, "Implementation of Fermi–Dirac statistics and advanced models in PC1D for precise simulations of silicon solar cells," *4th International Conference on Silicon Photovoltaics*, 's-Hertogenbosch, The Netherlands, 2014.
- **A. Kimmerle**, J. Greulich, and A. Wolf, "Carrier-Diffusion Corrected J0-Analysis of Charge Carrier Lifetime Measurements for Increased Consistency," *5th International Conference on Silicon Photovoltaics, Constance*, Germany, 2015.
- H. Haug, J. Greulich, **A. Kimmerle**, A. Wolf, E. S. Marstein, "PC1Dmod 6.1 - State-Of-The-Art Models in a Well-Known Interface for Improved Simulation of Si Solar Cells", *5th International Conference on Silicon Photovoltaics*, Constance, Germany, 2015.

## List of Constants, Symbols, and Acronyms

Constant	Description	Value
$h$	Planck constant	$6.62607 \times 10^{-34} \text{ J s}$
$k_B$	Boltzmann constant	$1.3806 \times 10^{-23} \text{ J K}^{-1}$
$q$	elementary charge	$1.602 \times 10^{-19} \text{ C}$

Symbol	Description	Typical unit
$[O_3]$	ozone concentration	ppm
$[O_i]$	interstitial oxygen concentration	$\text{cm}^{-3}$
$a_{\text{unit}}$	unit cell area	$\text{mm}^2$
$B_{\text{low}}$	radiative recombination coefficient	1
$d$	thickness of emitter region	$\mu\text{m}$
$D_{\text{amb}}$	ambipolar diffusion coefficient	$\text{cm}^2/\text{s}$
$D_{\text{min}}$	minority carrier diffusion constant	$\text{cm}^2/\text{s}$
$D_n, D_p$	diffusion coefficient for electrons / holes	$\text{cm}^2/\text{s}$
$E$	electric field	$\text{Vcm}^{-1}$
$E_C$	minimum potential in the conduction band	eV
$EC$	emitter coverage fraction	%
$E_{\text{fn}}$	quasi Fermi level of electrons	eV
$E_{\text{fp}}$	quasi Fermi level of holes	eV
$E_{\text{g},0}$	band-gap for undoped silicon	eV
$E_t$	energy potential of a defect state	eV
$E_V$	maximum potential in the valence band	eV
$f$	metallization fraction of the rear side	1
$f_A$	Area factor to account for non-planar areas in the evaluation of ECV measurements	1
$f_{\text{BGN}}$	BGN correction factor to scale the inverse lifetime for the $J_0$ -analysis	1
$f_{\text{corr}}$	correction factor for $n_{i,0}(T)$	1
$FF$	fill factor	%
$G_{\text{av}}$	average photo generation	$\text{cm}^{-3}\text{s}^{-1}$
$g_{\text{eeh}}/g_{\text{chh}}$	Coulomb enhancement factors	1
$G_L$	local generation rate	$\text{cm}^{-3}\text{s}^{-1}$
$J_0$	recombination parameter / dark saturation current density	$\text{fA}/\text{cm}^2$
$J_{0,\text{BSFlow}}$	$J_0$ of the lowly doped BSF	$\text{fA}/\text{cm}^2$
$J_{0,\text{BSFpass}}$	$J_0$ of the passivated highly doped BSF	$\text{fA}/\text{cm}^2$

Symbol	Description	Typical unit
$J_{0,front/back}$	recombination parameter of the front / rear side	fA/cm <sup>2</sup>
$J_{0,FSF}$	$J_0$ of the FSF	fA/cm <sup>2</sup>
$J_{0,met}$	$J_0$ of the metallized, highly doped BSF	fA/cm <sup>2</sup>
$J_{01}, J_{02}$	first / second diode saturation current density	fA/cm <sup>2</sup>
$J_{0b}$	dark saturation current density of the base	fA/cm <sup>2</sup>
$J_{0b,eff}$	effective base dark saturation current density	fA/cm <sup>2</sup>
$J_{col}$	photogenerated current density at junction	mA/cm <sup>2</sup>
$J_{gen}$	local cumulated generation	mA/cm <sup>2</sup>
$J_{gen,exp1,2}$	exponentially decreasing generation terms	mA/cm <sup>2</sup>
$J_{gen,front}$	front side generation	mA/cm <sup>2</sup>
$J_{gen,hom}$	homogeneous generation term	mA/cm <sup>2</sup>
$J_{mpp}$	current density at maximum power point	mA/cm <sup>2</sup>
$j_n, j_p$	electron / hole current density	Acm <sup>-2</sup>
$J_{ph}$	collected photo current at junction	mA/cm <sup>2</sup>
$J_{rec}$	recombination current density	A/cm <sup>2</sup>
$J_{SC}$	short circuit current density	mA/cm <sup>2</sup>
$J_{sim}$	device current density from numerical simulation	mA/cm <sup>2</sup>
$L$	diffusion length of minority carriers	cm
$L_1, L_2$	absorption length of exponentially decreasing generation	μm
$L_{eff,OC/SC}$	effective diffusion length at OC / SC conditions	cm
$l_f$	finger length	mm
$L_p$	pitch contact distance	μm
$M$	optical shading at front-side	1
$n$	electron concentration	cm <sup>-3</sup>
$n_0$	electron concentration in equilibrium	cm <sup>-3</sup>
$n_1, p_1$	SRH densities	cm <sup>-3</sup>
$N_A$	acceptor concentration	cm <sup>-3</sup>
$N_C$	effective density of states in the conduction band	cm <sup>-3</sup>
$N_D$	donor concentration	cm <sup>-3</sup>
$N_{dop}$	dopant concentration	cm <sup>-3</sup>
$n_{i,0}$	intrinsic carrier density for undoped silicon	cm <sup>-3</sup>
$n_{i,eff}$	effective intrinsic carrier density	cm <sup>-3</sup>
$n_{surf}$	ionized surface donor concentration	cm <sup>-3</sup>
$N_V$	effective density of states in the valence band	cm <sup>-3</sup>
$p$	hole concentration	cm <sup>-3</sup>
$p_0$	hole concentration in equilibrium	cm <sup>-3</sup>
$P_{light}$	power density of the incident light	W/m <sup>2</sup>
$Q$	total dopant dose density	cm <sup>-2</sup>
$Q_f$	fixed surface charge density	cm <sup>-2</sup>

Symbol	Description	Typical unit
$r$	etch rate	nm/s
$R_{AG,lat}$	$R_S$ contribution $n$ -fingers	$m\Omega cm^2$
$R_{Al,lat}$	$R_S$ contribution $p$ -fingers	$m\Omega cm^2$
$R_C$	contact resistance	$\Omega$
$r_{cont}$	contact radius	$\mu m$
$R_{intr}$	intrinsic recombination rate	$cm^{-3}s^{-1}$
$R_P$	parallel resistance	$\Omega cm^2$
$R_{P,2}$	resistance of shunting path outside the simulated domain	$\Omega cm^2$
$r_{planar / text}$	etch rate on planar / textured surfaces	nm/min
$R_S$	series resistance	$m\Omega cm^2$
$R_{S,back}$	global dark series resistance of the rear contact	$m\Omega cm^2$
$R_{S,base,light}$	$R_S$ contribution of the substrate under illumination	$m\Omega cm^2$
$R_{S,cont}$	$R_S$ contribution metal-semiconductor interface	$m\Omega cm^2$
$R_{S,front}$	$R_S$ contribution of the front contacts and the emitter	$m\Omega cm^2$
$R_{S,i}$	internal $R_S$ without contact and metal resistances	$m\Omega cm^2$
$R_{S,met}$	$R_S$ contribution from contacts and line resistances of metal fingers	$m\Omega cm^2$
$R_{sh}$	sheet resistance	$\Omega/sq$
$R_{spread}$	spreading resistance	$\Omega$
$R_{SRH}$	SRH recombination rate	$cm^{-3}s^{-1}$
$R_{surface}$	surface recombination rate	$cm^{-2}s^{-1}$
$S$	surface recombination velocity	cm/s
$S_{eff}$	effective recombination velocity	cm/s
$S_{front / back}$	SRV of the front / rear side	cm/s
$S_{met}$	surface recombination velocity of the metallized area	cm/s
$s_n, s_p$	LLI SRV for electrons / holes	cm/s
$S_p$	effective SRV for holes neglecting space charges	cm/s
$S_{pass}$	surface recombination velocity of the passivated area	cm/s
$T$	temperature	$^{\circ}C$
$t$	time	s
$T_d$	set temperature of the deposition plateau	$^{\circ}C$
$T_{ox}$	set temperature of the oxidation plateau	$^{\circ}C$
$T_{peak}$	device peak temperature during contact firing	$^{\circ}C$
$T_{peak}$	wafer peak temperature during contact firing	$^{\circ}C$
$T_{set}$	set temperature of fast firing oven	$^{\circ}C$
$v_{band}$	band velocity of fast firing oven	m/min
$V_{ext}$	external voltage	mV
$V_{junction}$	voltage drop across the junction	mV

Symbol	Description	Typical unit
$V_{\text{mpp}}$	external voltage at maximum power point	mV
$V_{\text{OC}}$	open circuit voltage	mV
$V_{\text{sim}}$	external voltage from numerical simulation	mV
$V_{\text{th}}$	thermal voltage	mV
$W$	wafer thickness	$\mu\text{m}$
$w_{\text{Ag}}$	width of $n$ -electrode	$\mu\text{m}$
$w_{\text{BSF}}$	half width of the highly doped BSF	$\mu\text{m}$
$W_{\text{C}}$	length of one contact stripe for TLM	cm
$w_{\text{e}}$	emitter half width	$\mu\text{m}$
$w_{\text{pass}}$	half width of passivated area underneath the Al	$\mu\text{m}$
$x_{\text{etch}}$	thickness of removed layer	nm
$x_{\text{j}}$	physical junction depth	nm
$\Delta E_{\text{C}}$	conduction band component of BGN	eV
$\Delta E_{\text{g}}$	band-gap narrowing	eV
$\Delta E_{\text{V}}$	valence band component of BGN	eV
$\Delta J_{\text{SC}}$	short circuit current loss	$\text{mA}/\text{cm}^2$
$\Delta n$	excess carrier density	$\text{cm}^{-3}$
$\Delta n_{\text{av}}$	average excess carrier density	$\text{cm}^{-3}$
$\Delta n_{\text{bulk}}$	average injection density in the substrate	$\text{cm}^{-3}$
$\Delta n_{\text{cont}}$	injection density at the rear contact	$\text{cm}^{-3}$
$\Delta n_{\text{front / back}}$	injection density at the front / rear side	$\text{cm}^{-3}$
$\Delta n_{\text{junction}}$	injection density at the junction (base-side)	$\text{cm}^{-3}$
$\Delta n_{\text{rear}}$	injection density at the rear side	$\text{cm}^{-3}$
$\Delta V_{\text{demb}}$	dember potential	mV
$\Delta V_{\text{X}}$	chemical potential difference	mV
$\Sigma_{\text{sh}}$	sheet conductivity	S
$\alpha_{\text{i}}$	time modes of the carrier decay	$\text{cm}^{-1}$
$\gamma_{\text{inj}}$	injection factor for rear side recombination in OC / SC conditions	1
$\eta$	conversion efficiency	%
$\lambda$	light wavelength	nm
$\mu_{\text{maj}}$	mobility of the majority carriers	$\text{m}\Omega\text{cm}^2$
$\mu_{\text{n}}, \mu_{\text{p}}$	electron / hole mobility	$\text{cm}^2\text{V}^{-1}\text{s}^{-1}$
$\rho$	specific resistance	$\Omega\text{cm}$
$\rho_0$	specific resistance without excitation	$\Omega\text{cm}$
$\rho_{\text{Ag,Al}}$	specific resistance of Ag / Al fingers on the solar cell	$\mu\Omega\text{cm}$
$\rho_{\text{c}}$	specific contact resistance	$\text{m}\Omega\text{cm}^2$
$\rho_{\text{light}}$	specific conductance under illumination	$\Omega\text{cm}$

Symbol	Description	Typical unit
$\sigma_{\text{etch}}$	standard error for etch depth	nm
$\sigma_j$	standard error for $J_0$	fA/cm <sup>2</sup>
$\sigma_n, \sigma_p$	specific conductivity of electrons / holes	$\Omega^{-1}\text{cm}^{-1}$
$\sigma_s$	standard error for SRV	cm/s
$\sigma_0$	specific conductivity	$\Omega^{-1}\text{cm}^{-1}$
$\tau_{\text{Aug}}$	Auger minority carrier lifetime	s
$\tau_b$	base substrate / bulk carrier lifetime	s
$\tau_{\text{corr}}$	Auger-corrected effective lifetime	s
$\tau_d$	defect lifetime	s
$\tau_{\text{eff}}$	effective carrier lifetime	s
$\tau_{\text{intr}}$	intrinsic carrier lifetime	s
$\tau_{n0}, \tau_{p0}$	SRH capture time constants	s
$\tau_p$	minority hole lifetime	s
$\tau_s$	surface lifetime	s

Acronym	Description
Ag	silver
Al	aluminum
AlB	aluminum-boride
AM1.5g	air mass 1.5 solar irradiation spectrum
ARC	anti-reflective coating
BC-BJ	back-contact back-junction
BGN	band-gap narrowing
BSF	back surface field
CH <sub>3</sub> COOH	acetic acid
Cz	Czochralski
ECV	electrochemical capacitance voltage
EQE	external quantum efficiency
F-D	Fermi-Dirac
FGA	forming gas anneal
FSF	front surface field
FZ	float-zone
HF	fluoric acid
HLI	high-level injection conditions
HNO <sub>3</sub>	nitric acid
IPA	isopropanol

---

Acronym	Description
KOH	potassium hydroxide
LLI	low-level injection conditions
M-B	Maxwell-Boltzmann
MPP	maximum power point
N <sub>2</sub>	nitrogen
O <sub>2</sub>	oxygen
OC	open circuit
PECVD	plasma-enhanced chemical vapor deposition
PL	photoluminescence
POCl <sub>3</sub>	phosphor-oxychloride
PSG	phosphosilicate glass
QSSPC	quasi-steady-state photo conductance decay
SC	short circuit
SEM	scanning electron microscope
SiN <sub>x</sub>	(non-stoichiometric) silicon nitride
SiO <sub>2</sub>	thermally grown silicon di-oxide
SiO <sub>x</sub>	(non-stoichiometric) silicon oxide
SiO <sub>x</sub> N <sub>y</sub>	silicon rich oxy-nitride
SiriON	passivation stack consistent of a thin layer of SiO <sub>x</sub> N <sub>y</sub> covered by ARC SiN <sub>x</sub>
SRH	Shockley-Read-Hall
SR-LBIC	Spectrally resolved light beam induced current measurements
SRV	surface recombination velocity
TLM	transfer-line method

---



## **Acknowledgment**

I thank all people who supported me during the time of writing this thesis. Especially I thank

Prof. Eicke R. Weber for his supervision, support, and helpful advice. Prof. Leonhard Reindl for the co-examination.

The Reiner Lemoine Stiftung not only for their generous financial support through a doctoral scholarship.

My supervisors at the Fraunhofer ISE, Dr. Robert Woehl and Dr. Andreas Wolf, together with Dr. Daniel Biro and Dr. Ralf Preu for their numerous advises and for enabling the work.

Dr. Marc Rüdiger, Dr. Johannes Greulich, Nico Wöhrle, and Dr. Halvard Haug for their numerical simulations and advice.

The whole PVTEC team for numerous processes and for having managed all the special requests. Elisabeth Schäffer for countless solar cell characterizations.

Dr. Daniel Biro, Dr. Tobias Fellmeth, Dr. Johannes Greulich, Dr. Ulrich Jäger, Roman Keding, Elmar Lohmüller, Dr. Sebastian Mack, Milan Padilla, Dr. Elena Navarrete, Dr. Marc Rüdiger, Dr. Armin Richter, Dr. Philip Rothhardt, Dr. Pierre Saint-Cast, Florian Schindler, Dr. Benjamin Thaidigsmann, Sabrina Werner, Dr. Robert Woehl, and Dr. Andreas Wolf for many discussions and joint publications at the ISE.

Prof. Pietro Altermatt, Adrienne Blum, Dr. Halvard Haug, Dr. Byungsul Min, and Dr. Ron Sinton for numerous discussions and joint publications.

Dr. Johannes Greulich, Steffi Klawitter, Dr. Sebastian Mack, Roman Keding, Milan Padilla, Andrew Thomson, Sabrina Werner, Nico Wöhrle and Dr. Andreas Wolf for proofreading.

Florian Bodny, Momtazur Rahman, Lena Nowotny, Julius Schmitt, Armin Hartmann, Steffi Klawitter, Rabin Basnet, Qurat-UI-Ain, and Samer Mourad for the trust they put into my supervision of their work.

Finally Bettina Kläsle, for her patience, encouragement and love over the years and my sons Jonah and Theo for cheering me up every day.

Novel concepts or advanced metallization techniques for crystalline silicon solar cells promise higher conversion efficiencies. Simultaneously, optimizing the highly doped surfaces increases in complexity. The present dissertation focuses on the characterization, modeling, and formation of such highly doped surfaces. In addition, an industrially feasible process sequence for solar cells exhibiting exclusively highly doped surfaces is devised.

ISBN 978-3-8440-3820-0



9

783844

038200

**SHAKER**  
**VERLAG**